NNT : 2024AIXM0621

THÈSE DE DOCTORAT

Soutenue à Aix-Marseille Université
le 17 décembre 2024 par

Loïc Corso

Tungsten crystalline evolution under helium irradiation: bubble formation and evolution steps

Discipline
Physique et sciences de la matière

Spécialité
Matière Condensée et Nanosciences

École doctorale
ED352 : Physique et Science de la matière

Laboratoire/Partenaires de recherche
IRFM - Institut de Recherche sur la Fusion Magnétique, CEA Cadarache

CINaM - Centre Interdisciplinaire de Nanoscience de Marseille

Composition du jury

Rémi Lazzari CNRS / INSP	Rapporteur
David Babonneau CNRS / Institut P'	Rapporteur
Jonathan Mougenot Université Sorbonne Paris Nord / LSPM	Examinateur
Matt Thompson Australian National University	Examinateur
Marie-France Barthe CNRS / CEMHTI	Présidente du jury
Frédéric Leroy Aix-Marseille Université / CINaM	Directeur de thèse
Elodie Bernard CEA / IRFM	Co-directrice de thèse
Stefano Curiotto CNRS / CINaM	Co-encadrant de thèse
Martiane Cabié Aix-Marseille Université / CP2M	Membre invitée
Céline Martin Aix-Marseille Université / PIIM	Membre invitée

Affidavit

Je soussigné, Loïc Corso, déclare par la présente que le travail présenté dans ce manuscrit est mon propre travail, réalisé sous la direction scientifique de Frédéric Leroy, dans le respect des principes d'honnêteté, d'intégrité et de responsabilité inhérents à la mission de recherche. Les travaux de recherche et la rédaction de ce manuscrit ont été réalisés dans le respect à la fois de la charte nationale de déontologie des métiers de la recherche et de la charte d'Aix-Marseille Université relative à la lutte contre le plagiat.

Ce travail n'a pas été précédemment soumis en France ou à l'étranger dans une version identique ou similaire à un organisme examinateur.

Fait à Aix-en-Provence, le 22 octobre 2024



Cette œuvre est mise à disposition selon les termes de la Licence Creative Commons Attribution - Pas d'Utilisation Commerciale - Pas de Modification 4.0 International.

Liste de publications et/ou brevets et participation aux conférences

1) Liste des publications et/ou brevet réalisées dans le cadre du projet de thèse :
   1. L. Corso, S. Curiotto, F. Cheynis, P. Muller, E. Bernard, M. Cabie, C. Martin, and F. Leroy, Real-time helium bubble growth in tungsten by in-situ GISAXS, Nucl. Mater. Energy **42**, 101894 (2025)
      DOI: https://doi.org/10.1016/j.nme.2025.101894

   2. L. Corso, S. Curiotto, E. Bernard, M. Cabie, C. Martin, L. Martinelli, F. Cheynis, P. Muller, and F. Leroy, Tungsten evolution under helium irradiation: Shape of bubbles by TEM and in-situ GISAXS analysis, Nuclear Materials and Energy 37, 101533 (2023).
      DOI: https://doi.org/10.1016/j.nme.2023.101533

   3. S. Curiotto, P. Müller, F. Cheynis, L. Corso, E. Bernard, and F. Leroy, Size-dependent diffusion of 3D nanovoids in a bcc solid, Applied Physics Letters 123, 241603 (2023). DOI: https://doi.org/10.1063/5.0175752

2) Participation aux conférences et écoles d'été au cours de la période de thèse :
   1. Conférence internationale MATERIAUX, Lille (France), 24-28 octobre 2022 (Poster : L. Corso, S. Curiotto, E. Bernard, et F. Leroy, Evolution cristalline du tungstène sous irradiation hélium par GISAXS in-situ : nucléation et croissance des bulles d'hélium)

   2. 19th International Conference on Plasma-Facing Materials and Components for Fusion Applications (PFMC), Bonn (Allemagne), 22-26 mai 2023 (Poster : L. Corso, S. Curiotto, E. Bernard, M. Cabie, C. Martin, L. Martinelli, F. Cheynis, P. Muller, and F. Leroy, Tungsten evolution under helium irradiation shape of bubbles by TEM and in situ GISAXS analysis)

   3. 26th International Conference on Plasma Surface Interaction (PSI), Marseille (France), 12-17 mai 2024 (Poster : L. Corso, S. Curiotto, E. Bernard, M. Cabie, C. Martin, and F. Leroy, Helium irradiated tungsten: real-time bubbles growth processes by in-situ Grazing Incidence Small Angle X-ray Scattering at the ESRF synchrotron)

   4. 17th International Conference on Surface X-ray and Neutron Scattering (SXNS), Grenoble (France), 15-18 July (Oral: L. Corso, S. Curiotto, E. Bernard, M. Cabie, C. Martin, and F. Leroy, Helium bubbles growth in tungsten by in-operando GISAXS)

Résumé

La fusion nucléaire se présente comme une possible source d'énergie abondante, sûre et décarbonée. Pour permettre son développement la communauté internationale, concentre ses efforts sur la construction, dans le sud de la France, de ITER, le plus grand réacteur de fusion (tokamak) jamais construit. Son but est de démontrer la faisabilité scientifique et technologique de la génération d'un gain net d'énergie grâce aux réactions de fusion nucléaire. Dans les tokamaks, un plasma de deutérium et tritium chauffé à plus d'une centaine de millions de kelvin est confiné grâce à des champs magnétiques intenses. Cependant, certains ions du plasma échappent à ce confinement et interagissent avec la première barrière physique, la première paroi. Le divertor, se situant sur cette premiere paroi est un composant essentiel, assurant l'efficacité du réacteur en extrayant l'excès de chaleur et de particules. Cette irradiation très intense reçue par le divertor entraîne d'importants dommages à la surface et aussi plus profondément dans le matériau. Cela affecte les propriétés et la durée de vie des matériaux, et donc l'efficacité du réacteur. Le tungstène (W) a été choisi comme matériau exposé au flux de particules le plus intense (principalement des neutrons, des ions de deutérium (D), de tritium (T) et d'hélium (He)). Il a été prouvé que l'interaction avec l'hélium affecte significativement la surface, limitant ainsi la durée de vie du composant. Également, la rétention en tritium radioactif est augmentée, ce qui présente un danger au regard de la sûreté. Comprendre l'impact de l'He sur les propriétés du W est donc d'une importance primordiale.

Dans un premier temps, les bases en science de la fusion sont présentées. La structure et le fonctionnement des tokamaks ainsi que les limites de cette technologie (régime pulsé, approvisionnement en ressources) et les solutions envisagées pour les surmonter sont abordés. Enfin, la mesure de leur performance par le « triple produit » est présentée avec un regard sur les performances atteintes jusqu'à aujourd'hui. Il est montré que le seuil de break-even (seuil où l'énergie produite compense les pertes) est proche et devrait être dépassé pour le tokamak ITER. Les raisons poussant au choix du tungstène comme matériau faisant face au plasma sont détaillées. Malgré ses avantages, quelques interrogations subsistent en particulier concernant son interaction avec l'hélium.

Dans le second chapitre, les connaissances actuelles sur l'interaction entre l'hélium et le tungstène sont présentées. Une fois les atomes d'hélium introduits dans le tungstène, leur interaction répulsive avec les atomes de tungstène constitue la force motrice pour l'agglomération de l'hélium sous forme de bulles au sein même du matériau tungstène. Dans certaines conditions, le fuzz (des nano-filaments de tungstène à la surface) peut se former. Il est envisagé que sa formation résulte de l'éclatement successif des bulles à la surface de l'échantillon. La température a été

rapportée comme un paramètre clé dans l'évolution des bulles. Par exemple, à basse température, les bulles sont signalées comme sphériques, tandis qu'à haute température (> 1223 K), elles sont rapportées comme facettées. Aucun consensus n'a été atteint concernant la description précise de la forme des bulles facettées ni sur le mécanisme de croissance des bulles qui reste encore en débat. Cela est en partie dû aux nombreux paramètres pouvant influencer la formation et l'évolution des bulles rendant les études difficilement comparables et également par le manque de dispositifs expérimentaux pouvant accéder à la dynamique des processus en temps réel durant l'implantation. Dans ce contexte, nous avons utilisé des techniques de nanoscience pour étudier séparément l'effets de différents facteurs sur la formation et l'évolution des bulles. Nous nous sommes intéressés à l'influence de la température, de l'orientation cristalline et de l'énergie d'implantation. Nous avons utilisé des échantillons monocristallins méticuleusement préparés. Nous avons introduit l'hélium dans le matériau grâce à une implantation ionique dont les paramètres (l'énergie, le flux, la température, …) sont bien contrôlés. En temps réel, pendant l'implantation nous avons caractérisé la formation et l'évolution des bulles par diffusion centrale des rayons X en incidence rasante (GISAXS).

Le troisième chapitre présente les installations expérimentales utilisées. La première partie du chapitre explique le principe du GISAXS. Ensuite est présenté le dispositif INS2, situé sur la ligne BM32 du synchrotron européen à Grenoble (ESRF). La seconde partie du chapitre est consacrée à la microscopie électronique en transmission (MET) qui est la seconde technique la plus utilisée dans ces travaux.

Dans le chapitre 4, l'étude de la forme des bulles à haute température est présentée. Afin de se rapprocher de l'équilibre thermodynamique des bulles d'hélium, la forme des bulles a été caractérisée. Nous avons montré la présence de bulles facettées exposant des facettes {110} et {100} de taille similaire. En utilisant le théorème de Wulff et les résultats expérimentaux des deux techniques (MET et GISAXS), nous obtenons un rapport d'énergie de surface de $\gamma_{100}/\gamma_{110} = 1{,}03 \pm 0{,}03$. La forme d'équilibre des bulles a été comparée à la forme d'équilibre du tungstène sous vide. D'importantes différences ont été observées. Cela prouve que l'hélium engendre une modification des propriétés physico-chimique du tungstène.

Enfin, le chapitre 5 se concentre sur l'évolution des bulles. A basse température, aucune évolution spécifique des bulles n'a été observée, tandis qu'à haute température, la taille des bulles augmente. L'évolution temporelle de la taille des bulles mesurée par GISAXS a permis d'accéder à la cinétique de croissance. Une comparaison avec des modèles analytiques de processus de croissance suggère que le mécanisme de croissance des bulles est la migration-coalescence. Également, nous montrons que la croissance des bulles facettées est limitée par le mouvement des bulles lui-même entravé par la nucléation de marche à la surface des facettes des bulles.

Mots clés : Hélium, Tungstène, Nano-bulles, GISAXS, Nanoscience, Croissance

Abstract

Nuclear fusion, as a carbon-free, abundant and safe energy source, is actively pursued by the international community by focusing its efforts with ITER currently being built in Cadarache. ITER is the largest fusion reactor (tokamak) ever built. Its aim is to demonstrate the scientific and technological feasibility of generating a net energy gain through nuclear fusion reactions. In tokamaks, a plasma of deuterium and tritium is heated to over a hundred million kelvin to fuse and generate a helium, a neutron and a massive quantity of energy. Intense magnetic fields are used to confine the plasma away of the first physical barrier. However, some particles from the plasma escape this confinement and interact with the first wall. In particular, the divertor, an essential component for the reactor's efficiency that extracts excess of heat and particles, is subject to intense heat load and particles (deuterium, tritium, helium and neutron) fluxes. This irradiation can lead to important damages at the surface and deeper in the bulk, affecting the properties and life span of the materials, hence the efficiency of the reactor. Tungsten (W) has been chosen as the plasma facing material in ITER and recent tokamaks. The interaction with He has been proven to significantly affect the component in surface and in bulk, thereby limiting the component's lifespan. In addition, after exposure to helium, the retention of radioactive tritium in the material increases resulting in a risk for the safety. Understanding the impact of He on the properties of W is therefore of prime importance.

First, the basics of fusion science is presented. The structure and principle of tokamaks, as well as the limitations of this technology (pulsed operation, resource supply), and potential solutions to overcome these challenges are discussed. Then, the measurement of their performance through the "triple product" is introduced, with a look at the achievements reached to date. It is shown that the break-even threshold (where the energy produced compensates for losses) is close and should be surpassed for the ITER tokamak. Finally, the reasons for choosing tungsten as the material facing the plasma are detailed. Despite its advantages, some questions remain, which will be the subject of this study.

In the second chapter, the current knowledge on the interaction between helium and tungsten is presented. Once helium atoms are introduced into tungsten, their repulsive interaction with tungsten atoms is the driving force for the agglomeration of helium into bubbles within the tungsten material. Under certain conditions, fuzz (nano-filaments of tungsten on the surface) can form. It is suggested that its formation results from the successive bursting of bubbles at the surface of the sample. Temperature has been reported as a key parameter in the evolution of the bubbles. For instance, at low temperatures, bubbles are reported to be spherical, while at high temperatures (> 1223 K), they are reported to be faceted. No consensus has been reached regarding the

precise description of the shape of faceted bubbles nor on the bubble growth mechanism. This is partly due to the large number of parameters that can influence bubble formation and evolution, making studies difficult to compare, as well as the lack of experimental setups able to access to the dynamics of processes in real-time during implantation. In this context, we have used nanoscience techniques to separately study the effects of various factors on bubble formation and evolution. We have focused on the influence of temperature, crystallographic orientation, and implantation energy. We have used well-prepared single crystals, helium was introduced into the material by ionic implantation with well-controlled parameters (energy, flux, temperature…). We have characterized the bubble formation and evolution in real time during implantation by grazing incidence small angle X-ray scattering (GISAXS).

The third chapter presents the experimental setups used. The first part of the chapter explains the principle of GISAXS. Then, the INS2 setup located at the BM32 beamline of the European Synchrotron Radiation Facility (ESRF) is presented. The second part of the chapter is focused on transmission electron microscopy (TEM), which is the second most used technique in this work.

In chapter 4, the study of bubble shapes is presented. In particular, at very high temperatures helium bubbles approach the thermodynamic equilibrium. We have shown the presence of faceted bubbles exhibiting {110} and {100} facets of similar size. By applying Wulff's theorem and experimental results from both techniques (TEM and GISAXS), we have obtained a surface energy ratio of $\gamma_{100}/\gamma_{110} = 1.03 \pm 0.03$. The equilibrium shape of bubbles was compared to the equilibrium shape of tungsten crystal in vacuum. Large differences have been observed, that strongly suggests a modification of the thermodynamic properties of tungsten by helium.

Finally, chapter 5 focuses on bubble evolution. At low temperatures, no specific bubble evolution was observed, whereas at high temperatures, the size of bubbles increases. The time evolution of bubbles size measured by GISAXS has allowed us to access to their growth kinetics. A comparison with analytical growth process models suggests that the mechanism responsible for bubble growth is bubble migration-coalescence. We have also shown that the growth of faceted bubbles is limited by the motion of the bubbles, hindered by the nucleation of ledges at the bubble facet surface.

Keywords : Helium, Tungsten, Bubbles, GISAXS, Nanoscience, Growth

Résumé étendu

La demande mondiale en énergie est en constante augmentation depuis la fin de l'ère préindustrielle. Cette augmentation est en partie due à la croissance de la population mondiale, au développement économique des pays émergents et à l'utilisation de plus en plus fréquente de la technologie dans les pays développés. La demande en énergie a été soutenue par l'utilisation massive des énergies dites « fossiles » telles que le charbon, le gaz et le pétrole. Aujourd'hui, ces énergies sont toujours les plus utilisées, leur part dans le mix énergétique mondial s'élève à plus de 75%. Le dioxyde de carbone (CO_2) émis par l'utilisation d'énergies fossiles a été identifié comme le principal responsable du réchauffement climatique.

Les accords de Paris sur le climat prévoient de limiter ce réchauffement à 2 °C d'ici 2050, par rapport à l'ère préindustrielle. Dans ce cadre, il apparaît nécessaire de réduire notre dépendance aux énergies carbonées pour diminuer les émissions de gaz à effet de serre, un exemple d'accord supranational dans ce sens est le « Green deal » européen. Il vise à ramener les émissions nettes de CO_2 du continent européen à zéro. Cela passera en partie par l'électrification des procédés, par exemple dans le transport, le chauffage des habitations ou l'industrie. Il est notamment prévu l'abandon de l'utilisation du charbon comme source d'énergie. Un mix électrique décarboné est donc nécessaire. Les énergies renouvelables, telles que le solaire, l'hydraulique et l'éolien, font partie de la solution. Cependant, le désavantage majeur de ces énergies est leur intermittence. Ces énergies sont alors secondées par des énergies pilotables qui sont parfois le charbon, le pétrole ou le gaz émetteurs de CO_2 ou le nucléaire, décarboné mais sujet à vives inquiétudes concernant le risque d'accident et la gestion des déchets. De ce fait, une électricité issue d'une énergie décarbonée, abondante, intrinsèquement sûre et acceptée par la population doit compléter le mix électrique.

La fusion thermonucléaire est une voie prometteuse pour produire cette électricité. À la différence de la fission nucléaire ayant lieu dans les centrales actuelles, le principe de la fusion nucléaire consiste à faire fusionner deux noyaux légers pour en former un plus lourd.

Dans le premier chapitre de cette thèse, les bases en science de la fusion sont présentées. La réaction de fusion envisagée sur Terre est celle de deux isotopes de l'hydrogène, le deutérium (D) et le tritium (T), produisant un hélium (He) et un neutron (n) très énergétique.

$$D + T \rightarrow He + n$$

Pour permettre la fusion de deux noyaux, la répulsion Coulombienne entre deux charges de même signe doit être surpassée. Cela est possible en chauffant un gaz jusqu'à des températures de l'ordre de la centaine de millions de degrés Celsius. A ces températures là le gaz passe dans le quatrième état de la matière, le plasma. La vitesse et donc l'énergie cinétique des particules du plasma sont telles que la fusion est possible.

Afin que ce processus restitue plus d'énergie que ce qu'il en consomme, il faut que les réactions de fusion libèrent suffisamment d'énergie pour compenser les pertes et maintenir le plasma en combustion. Cette condition est décrite par le critère de Lawson :

$$n_i \cdot T_i \cdot \tau_E > 5 \times 10^{21} \text{ keV.s.m}^{-3}$$

Où n_i est la densité du plasma, T_i la température du plasma (en keV) et τ_E la durée de confinement de l'énergie.
Dans la gamme de température nécessaire pour la fusion, aucun matériau ne peut résister au plasma, il faut donc le confiner sans le toucher par une barrière physique. Cela est possible grâce à des champs magnétiques dans des « tokamaks ». Les tokamaks sont constitués d'un ensemble de bobines magnétiques qui permettent de confiner et d'optimiser la forme du plasma pour accroître ses performances.

Le tokamak ITER issu d'une collaboration internationale, est en cours de construction dans le sud de la France. ITER a pour but de démontrer la faisabilité scientifique et technologique de la production nette d'énergie à partir des réactions de fusion. Le seuil de break-even (seuil où l'énergie produite par les réactions de fusion compense les pertes) devrait être dépassé pour le tokamak ITER.

L'approvisionnement des réactifs (deutérium et tritium) est crucial pour l'utilisation de la fusion. Le deutérium est un isotope non radioactif de l'hydrogène naturellement abondant dans l'eau. En revanche, le tritium un autre isotope de l'hydrogène, est lui radioactif et naturellement très peu présent sur Terre (seulement quelques traces). La durée de demi-vie du tritium est de 12,3 ans et sa décroissance en hélium 3 non radioactif s'effectue par l'émission d'un β^- (un électron). La production de tritium est envisagée au sein même des réacteurs de fusion en tirant avantage de la réaction entre du lithium et des neutrons :

$$^6Li + {}^1n \rightarrow {}^3T + {}^4He$$
$$^7Li + {}^1n \rightarrow {}^3T + {}^4He + {}^1n$$

Des composants contenant du lithium seront alors disposés autour du plasma et les neutrons issus de la réaction de fusion serviront à la génération de tritium.

Un verrou crucial à l'heure actuelle concerne les matériaux de la première paroi. En particulier le tungstène utilisé pour le divertor, la partie de la première paroi la plus sollicitée par des flux de chaleur et de particules (deutérium, tritium, hélium et neutron) émanant du plasma. Malgré ses avantages (point de fusion élevé, faible érosion, bonne conductivité thermique…) quelques interrogations persistent, notamment concernant son interaction avec l'hélium produit par la réaction de fusion. Il a été rapporté que l'hélium affecte considérablement la microstructure du tungstène à la fois en surface et dans le volume. Ces modifications engendrent de considérables dégradations des propriétés thermomécaniques du tungstène. En particulier, des poussières de tungstène peuvent être générées piégeant du tritium sous une forme dispersible. Ce point est crucial au regard de la sûreté de l'installation. La compréhension des mécanismes en jeu dans l'interaction entre l'hélium et le tungstène est ainsi primordiale pour permettre le développement de la fusion.

Dans le second chapitre, les connaissances actuelles sur l'interaction entre l'hélium et le tungstène sont présentées. Dans certaines conditions, il a été rapporté que des nano-filaments de tungstène à la surface peuvent se former sur plusieurs micromètres de profondeur. Le mécanisme de formation de ces filaments appelés « fuzz » n'est pas encore totalement compris. La présence de fuzz a été rapportée dans des conditions d'irradiation particulières, l'énergie des ions implantés doit être d'au moins 20 eV, et la température entre 900 K (~ 625 °C) et 2000 K (~ 1725 °C). En outre, une fluence minimale doit être atteinte pour permettre l'apparition de fuzz. Ce seuil de fluence a été estimé à 1×10^{24} m^{-2}. A plus basse énergie, la formation de fuzz est inhibée car à ces énergies-là, l'hélium ne parvient pas à pénétrer à travers la surface, il est rétrodiffusé. Lorsque la température est inférieure à 900 K, des nano-bulles d'hélium sont formées sous la surface et au-dessus de 2000 K des trous micrométriques sont observés à la surface. La piste privilégiée par la communauté scientifique pour expliquer l'apparition de fuzz est que sa formation résulte de l'éclatement successif de nano-bulles à la surface de l'échantillon, tel qu'illustré sur la figure ci-dessous.

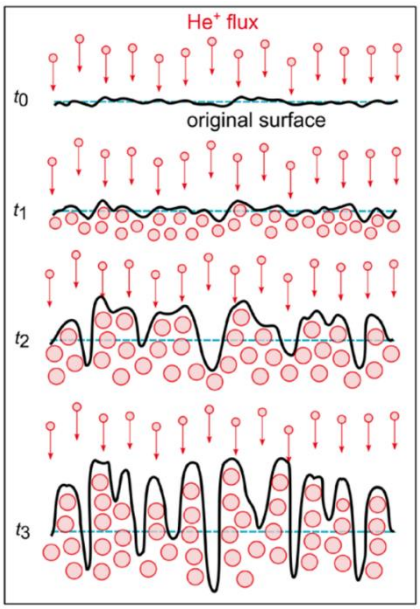

Image I : Représentation schématique de la formation du fuzz. Lors de l'augmentation de la fluence dans le temps (t_0 à t_3), i) des nano-bulles se forment proche de la surface, ii) croissent puis, iii) éclatent en surface. La répétition de ces étapes déplace les atomes de tungstène en surface générant une structure filandreuse (fuzz).

D'intenses efforts sur le plan expérimental comme sur la modélisation ont été réalisés pour comprendre la formation des nano-bulles. Cela a permis d'identifier les raisons de la formation des bulles dans le tungstène. Une fois les atomes d'hélium introduits dans le matériau, la forte répulsion avec les atomes de tungstène constitue la force motrice pour l'agglomération de l'hélium sous forme de bulles au sein même du matériau tungstène. Il a été montré que les atomes d'hélium présents dans la matrice de tungstène diffusent entre les sites tétraédriques de la maille du tungstène avec une énergie d'activation de seulement 0,06 eV. Cela leur permet d'être très mobiles et ce même à température ambiante. Une partie de l'hélium peut alors atteindre la surface et être libéré. Les atomes d'hélium toujours dans la matrice de tungstène, vont alors avoir tendance à s'agglomérer formant des clusters d'hélium pour diminuer les interactions avec le tungstène. Les clusters ainsi formés restent mobiles et continuent d'absorber des atomes d'hélium seuls ou des clusters. Une fois la pression dans le cluster suffisamment grande, un atome de tungstène peut être éjecté de son site cristallographique en position interstitielle formant une paire de Frenkel. Ce mécanisme est appelé « trap mutation », il permet au cluster d'hélium de se lier à la lacune et de stabiliser l'ensemble. Dans le cas où des lacunes sont déjà présentes dans le matériau, les clusters d'hélium peuvent aussi s'y lier. Le cluster d'hélium est alors peu mobile voire complètement immobilisé selon la température. L'ensemble cluster d'hélium-lacune est appelé une bulle. La bulle continue d'absorber des atomes d'hélium et croît par trap-mutation expulsant des atomes de tungstène en position interstitielle qui restent liés à la surface de la bulle. Il a été montré dans la littérature que par dynamique moléculaire, le voisinage du nuage d'interstitiel avant la formation d'une boucle peut être un site préférentiel pour la nucléation d'une nouvelle bulle. Une

fois que le nombre d'interstitiels est suffisamment grand, ils peuvent se réorganiser et former une boucle de dislocation qui est alors libérée et diffuse dans le matériau.

La température a été rapportée comme un paramètre clé dans l'évolution des bulles. Par exemple, à basse température, les bulles sont signalées comme sphériques, tandis qu'à haute température (> 1223 K), elles sont rapportées comme facettées. Aucun consensus n'a été atteint concernant la description précise de la forme des bulles facettées ni sur le mécanisme de croissance des bulles qui reste encore en débat. Cela est en partie dû au fait que les études dans les machines de fusion sont difficilement comparables entre elles. De nombreux paramètres peuvent influencer la formation et l'évolution des bulles, par exemple l'état de surface, la température, le flux, la fluence, l'énergie des ions, la microstructure… Or ces paramètres sont difficilement contrôlables dans une machine de fusion. De plus, le manque de dispositifs expérimentaux *in-situ* ou *in-operando* (également dans les études en laboratoire), pouvant accéder à la dynamique des processus en temps réel de l'implantation rend la compréhension des processus très complexe.

Dans ce contexte, nous proposons d'utiliser des techniques de nanoscience pour étudier séparément l'effet de différents facteurs sur la formation et l'évolution des bulles. Nous nous sommes intéressés à l'influence de la température, de l'orientation cristalline de la surface et de l'énergie d'implantation. Nous avons utilisé des échantillons monocristallins méticuleusement préparés. L'état de surface des échantillons est caractérisé par microscopie à électron lents (LEEM) et par spectroscopie Auger. La première technique nous permet de nous assurer que la rugosité en surface est minimale, c'est-à-dire que des terrasses atomiques s'étendent sur la surface. La seconde technique nous permet de nous assurer de la pureté de l'échantillon, il est notamment attendu que le carbone, couramment observé dans une matrice de tungstène et que l'oxygène présent dans l'oxyde natif formé à la surface de l'échantillon soit à des niveaux (i.e. concentration) indétectables. L'hélium est introduit dans les échantillons par implantation ionique dont les paramètres (énergie, flux, température…) sont bien contrôlés. En temps réel de l'implantation, nous avons caractérisé la formation et l'évolution des bulles par diffusion centrale des rayons X en incidence rasante (GISAXS). En complément, des analyses post-mortem par microscopie électronique en transmission (MET) ont été réalisées. L'avantage de la première technique est que la dynamique des phénomènes peut être suivie et l'information obtenue est statistique (i.e. intégrée sur tout l'échantillon). La seconde technique bien que faiblement statistique, donne une image directe des bulles dans l'échantillon, ce qui en fait un formidable outil en complémentarité de l'utilisation du GISAXS où l'information obtenue dans l'espace réciproque doit être traduite dans l'espace directe.

Le chapitre 3, vise à décrire le principe des techniques expérimentales et les bancs expérimentaux utilisés dans ce travail. La première partie du chapitre est centrée sur la diffusion des rayons X en incidence rasante (GISAXS). Avant de rentrer dans le

formalisme mathématique permettant de décrire théoriquement la diffusion des rayons X, les éléments clés permettant de comprendre et analyser un cliché GISAXS sont présentés. Les points abordés dans cette sous-partie sont ensuite démontrés dans la partie traitant de la théorie. Le point de départ de ce formalisme est la diffusion d'une onde électromagnétique à travers une interface plane d'épaisseur infinitésimale fine entre deux milieux homogènes et infinis de part et d'autre de l'interface. La diffusion des rayons X est régie par les équations de Maxwell qui permettent d'établir un système dit de « référence » qui n'est autre que le champ électromagnétique au sens de Fresnel. Le signal GISAXS est issue de la perturbation de ce système idéal. Par exemple, dans le cas des bulles d'hélium enterrées dans une matrice de tungstène, le signal GISAXS provient de la différence de l'indice de réfraction (due à une différence de densité électronique) au niveau des bulles d'hélium. Du fait que l'interaction entre la matière et les rayons X est faible, en première approximation il est possible de considérer que l'intensité de l'onde incidente n'est pas affectée par la perturbation (pas d'absorption ni de réflexion ou réfraction de l'onde), il s'agit de l'approximation de Born (BA). Ainsi, l'onde incidente arrivant sur la perturbation interagit avec, puis une onde sphérique est émise sans interagir avec le milieu. L'intensité de l'onde diffusée est alors proportionnelle au module au carré de la transformée de Fourrier de la perturbation de l'indice de réfraction. L'approximation de Born est valide pour une incidence élevée de l'onde électromagnétique mais perd en validité lorsque l'incidence est plus rasante comme dans c'est le cas du GISAXS. Ainsi, les multiples réflexions et réfractions de l'onde doivent être prises en compte. Cela est traité dans le cadre de l'approximation de Born de l'onde distordue (DWBA). L'amplitude de l'onde diffusée est alors une somme de 5 termes décrivant les différents phénomènes de réflexion et réfraction considérés comme illustré sur le schéma suivant :

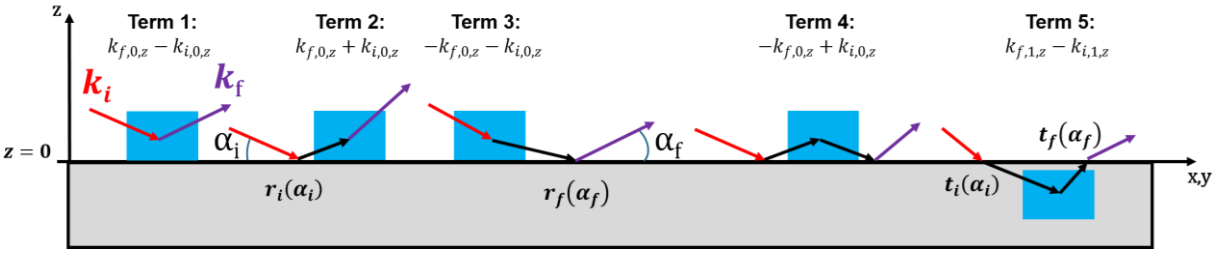

Image II : Représentation schématique des différents phénomènes de réflexion et réfraction considérés dans le cadre de l'approximation de Born de l'onde distordue (DWBA).

i) Le premier terme est le terme de Born qui correspond à la diffusion de l'onde par la perturbation comme si elle était seule dans le vide (approximation de Born).

ii) Le second terme correspond à un processus en deux temps, d'abord la réflexion de l'onde sur la surface de référence puis la diffusion par la perturbation.

iii) Le troisième terme correspond également à un processus en deux temps, où l'onde incidente est d'abord diffusée par la perturbation avant que l'onde diffusée soit réfléchie sur la surface de référence.

iv) Le quatrième terme correspond à un processus en trois temps. D'abord l'onde est réfléchie sur la surface de référence puis diffusée par la perturbation. L'onde diffusée est à son tour réfléchie sur la surface de référence avant d'atteindre le détecteur.

v) Le cinquième et dernier terme est particulièrement important pour traiter le cas d'objets enterrés comme des bulles. Il correspond à un processus en trois temps, où l'onde incidente est d'abord réfractée par la surface de référence puis diffusée par la perturbation et enfin, l'onde diffusée est également réfractée à la surface de référence avant d'atteindre le détecteur.

L'approximation de Born de l'onde distordue (DWBA) permet notamment d'expliquer l'apparition sur les clichés expérimentaux des éléments tels que la tige spéculaire (aussi traitée par l'approximation de Born) et le pic de Yoneda. Lorsque la théorie est appliquée au cas d'objets enterrés (par exemple des bulles d'hélium), l'intensité de l'onde diffusée est alors proportionnelle au module au carré du facteur de forme de l'objet, moyennant une correction sur le vecteur d'onde liée au phénomène de réfraction de l'onde transmise dans le matériau.
Le banc expérimental INS2, situé sur la ligne BM32 du synchrotron européen de Grenoble (ESRF), a été utilisé pour suivre par GISAXS *in-operando* la formation et l'évolution de bulles en temps réel pendant l'implantation. Ce banc expérimental offre la possibilité de maintenir un vide poussé même à des températures très élevées (1773 K a été atteint au cours de cette étude). A la suite de cette sous-partie, une description détaillée du protocole de préparation des échantillons est donnée. En quelques mots, la surface « modèle » des échantillons telle que décrite précédemment (rugosité et contamination chimique minimales) est obtenue par cyclage de recuit sous oxygène et flash haute température sous ultra vide.

La seconde partie du chapitre 3 est ensuite consacrée à la microscopie électronique à transmission (MET). D'abord, la procédure d'extraction de la lame fine par faisceau d'ions focalisés (FIB) est décrite. Ensuite, la particularité de l'observation des bulles est abordée. Les grosses bulles dont le diamètre est supérieur à 5 nm sont aisément observables dans des conditions d'observation « standard ». Concernant les plus petites bulles dont le diamètre est inférieur à 5 nm, des conditions d'observation particulières sont nécessaires. L'observation des petites bulles nécessite de limiter la contribution de la matrice de tungstène en utilisant le microscope en mode d'imagerie champ clair. L'échantillon est également sorti d'un éventuel axe de zone (condition cinématique). Dans ces conditions, les plus petites bulles sont alors visibles en variant la focalisation, elles apparaissent claires pour une sous-focalisation et foncées pour une sur-focalisation.

Ces techniques expérimentales ont permis d'étudier l'influence sur la formation et l'évolution des bulles de i) la température : les échantillons ont été maintenus à la température ambiante, 523 K, 873 K ou 1273 K pendant l'implantation. ii) l'orientation cristalline des échantillons, des surfaces orientées (100), (110) et (111) ont été

utilisées et iii) l'énergie d'implantation des ions de 400 eV ainsi que 2 keV ont été utilisées. Ces énergies se situent respectivement en dessous et au-dessus du seuil de création de défauts par l'hélium dans le tungstène situé autour de 500 eV. Un récapitulatif de ces conditions est montré sur la figure suivante :

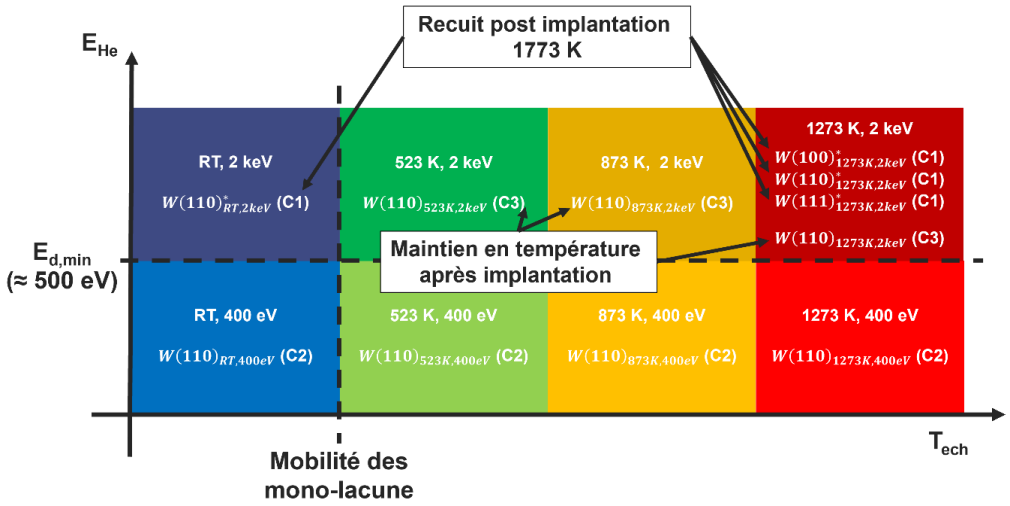

Image III : Résumé des différentes conditions expérimentales étudiées

Dans le chapitre 4, les mesures GISAXS couplées à celles de la microscopie électronique ont permis d'établir la forme des bulles en fonction des conditions d'implantation. Pour chaque échantillon, l'analyse de la population de bulle a été réalisée selon la méthodologie suivante : i) une première analyse sommaire basée sur les observations par microscopie électronique à transmission (MET) permet d'établir grossièrement la forme des bulles et la taille de celles-ci. Ensuite, ii) les mesures GISAXS effectuées à la fin de l'implantation sont comparées qualitativement avec les mesures MET. Enfin, iii) une analyse poussée des mesures GISAXS est réalisée pour déterminer avec le plus de précision la forme et la taille des bulles.

Les mesures MET pour les implantations effectuées entre la température ambiante et 873 K, (indépendamment de l'énergie d'implantation utilisée), indiquent que la population de bulles est composée en majorité de petites bulles sphériques (rayon de l'ordre du demi-nanomètre) et de plus rares, grosses bulles de forme sphéroïdale (sphère allongée dont le grand rayon mesure plusieurs nanomètres). L'analyse qualitative des mesures GISAXS est en accord avec ce résultat. La diffusion diffuse générée par les bulles ne correspond ni à celle d'objets purement sphériques, ni à celle d'objets de forme purement sphéroïdales, mais bien d'une combinaison de ces deux formes. Pour chaque échantillon, des mesures GISAXS ont été réalisées en tournant l'échantillon sur lui-même, permettant de sonder toutes les directions (avec un pas de 1°) dans le plan de la surface de l'échantillon. Cela permet d'identifier une éventuelle anisotropie de forme. Il a été ainsi constaté que les bulles sphéroïdales sont allongées dans la direction [001] et contractées dans la direction $[1\bar{1}0]$. La formation de bulles allongées pourrait résulter de la coalescence statique après grossissement de bulles sphériques ayant été formées proches l'une de l'autre.

L’analyse plus fine des mesures GISAXS nécessite l’utilisation d’un logiciel tel que Born Again, fitGISAXS ou IsGISAXS permettant de simuler et reproduire des clichés expérimentaux. Dans cette étude le logiciel IsGISAXS a été utilisé pour déterminer la distribution en taille des bulles et la proportion relative entre les bulles sphériques et sphéroïdales. Le principe est de fournir en valeurs d’entrée des coupes d’un cliché expérimental et un modèle décrivant la population de bulles (ici, de nombreuses petites bulles sphériques et une faible proportion de grandes bulles sphéroïdes). Les valeurs de taille, de distribution, et de proportion relative des bulles sont alors ajustées pour reproduire au mieux le cliché expérimental. Dans notre étude, les valeurs de départ sont celles mesurées par MET. Le modèle à deux espèces (bulles sphériques et bulles sphéroïdales) permet de reproduire convenablement les clichés expérimentaux et d’en déduire des informations quantitatives sur les bulles présentes. A basse énergie (400 eV), l’analyse fine des clichés GISAXS montre que la température entre l’ambiante et 873 K, n’impacte que très peu les bulles formées. Les formes, tailles et proportions des bulles sont quasiment identiques pour ces trois échantillons. A haute énergie (2 keV), la taille des bulles semble encore une fois relativement identique à celle mesurée à basse énergie pour des températures relativement faibles (≤ 523 K). De plus, d’après les mesures par MET et GISAXS, la proportion de bulles sphériques/sphéroïdales semble avoir été modifiée et indique que les bulles présentes à la fin de l’implantation à haute énergie sont préférentiellement sphériques (par rapport aux cas basse énergie). Ceci pourrait s’expliquer par le fait qu’à haute énergie, des lacunes sont directement générées par les ions incidents lors de l’implantation. Comme ces lacunes sont très peu mobiles à température ambiante et 523 K, l’implantation à haute énergie permet de nucléer des bulles éloignées les unes des autres. Dans le cas d’une implantation à basse énergie, la nucléation des bulles se fait majoritairement au voisinage des bulles préexistantes. La coalescence statique entre bulles est alors inhibée à haute énergie du fait d’une distance entre bulles plus grande. Pour l’échantillon implanté à 873 K et haute énergie, les images MET montrent des bulles sphériques globalement plus grosses dont le rayon mesure plusieurs nanomètres et des structures en « collier de perles ». Ces structures sont vraisemblablement issues de la coalescence des bulles. Bien que les bulles soient relativement espacées les unes des autres du fait des mono-lacunes générées par l’implantation. A cette température, les mono-lacunes sont mobiles et peuvent soit être annihilées en surface ou par recombinaison avec un atome de tungstène interstitiel ou être absorbée par une bulle d’hélium la faisant grossir et permettre la coalescence avec une bulle voisine.

Pour les échantillons implantés à 1273 K (indépendamment de l’énergie d’implantation), les images MET comme les clichés GISAXS montrent la présence de bulles facettées. Cela se traduit sur les clichés GISAXS par des tiges latérales inclinées par rapport à la direction verticale (perpendiculaire à la surface des échantillons). L’angle d’inclinaison correspond à celui entre le plan cristallographique de la facette et celui de la surface de l’échantillon. Par exemple, pour une facette {100} dans l’échantillon orienté {110} l’angle de la tige générée par la facette est alors de 45°. Pour les trois orientations cristallines (100), (110) et (111) étudiées, les bulles

formées présentent des facettes {100} et {110}. L'apparition de facettes est rendue possible lorsque dans un milieu tel que la matrice de tungstène, l'énergie de surface noté γ est anisotrope. Les facettes à la surface de la bulle sont alors formées afin de minimiser l'énergie de surface pour le volume de la bulle. Ce principe est connu sous le nom de théorème de Wulff. Lorsque l'équilibre thermodynamique est atteint, l'anisotropie de l'énergie de surface peut être obtenue. Dans ce sens, trois échantillons d'orientation différente implantés à 1273 K et 2 keV ont été recuits sous ultra vide jusqu'à 1773 K. Cette température permet d'activer la mobilité des atomes de tungstène en surface de la bulle et ainsi d'approcher l'équilibre thermodynamique. Après recuit, des bulles facettées de plusieurs dizaines de nanomètres sont observées. Toutes les bulles (indépendamment de l'orientation cristallographique) sont facettés par les mêmes plans (100) et (110) (voir figure ci-dessous).

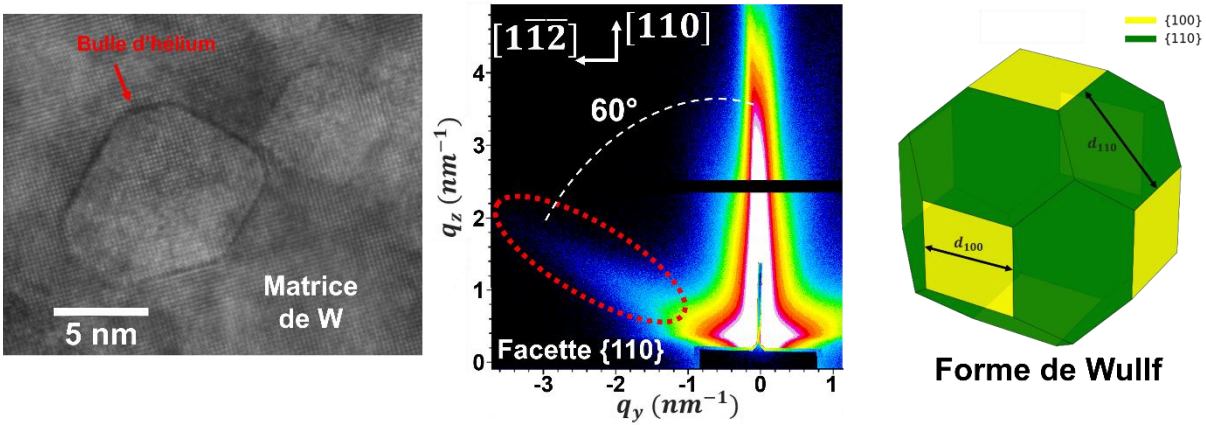

Image IV: A gauche : Image directe d'une bulle d'hélium facettée, formée à haute température. Au milieu : cliché GISAXS typique de bulles facettées. A droite : la forme de Wulff associée aux bulles d'hélium dans le tungstène déterminée par MET et GISAXS.

Selon le théorème de Wulff, la taille des facettes est liée à l'anisotropie d'énergie de surface. Nous trouvons une anisotropie entre les plans (100) et (110) de $^{\gamma_{100}}/_{\gamma_{110}} = 1.03$. Cette valeur a été comparée à celle du tungstène pur qui vaut entre 1.13 et 1.23 selon les études. La différence obtenue à l'issue de notre expérience montre que potentiellement l'hélium a un impact important sur les propriétés thermodynamiques du tungstène.

Enfin, dans le chapitre 5, la dynamique de croissance des bulles a été étudiée. La cinétique de croissance des bulles a été obtenue grâce aux mesures GISAXS *in-operando*. Elles révèlent qu'aux basses températures (≤ 873 K) le système évolue peu alors qu'à haute température (≥ 1273 K), la taille des bulles augmente pendant l'implantation et même après en l'absence d'implantation. (voir figure ci-dessous)

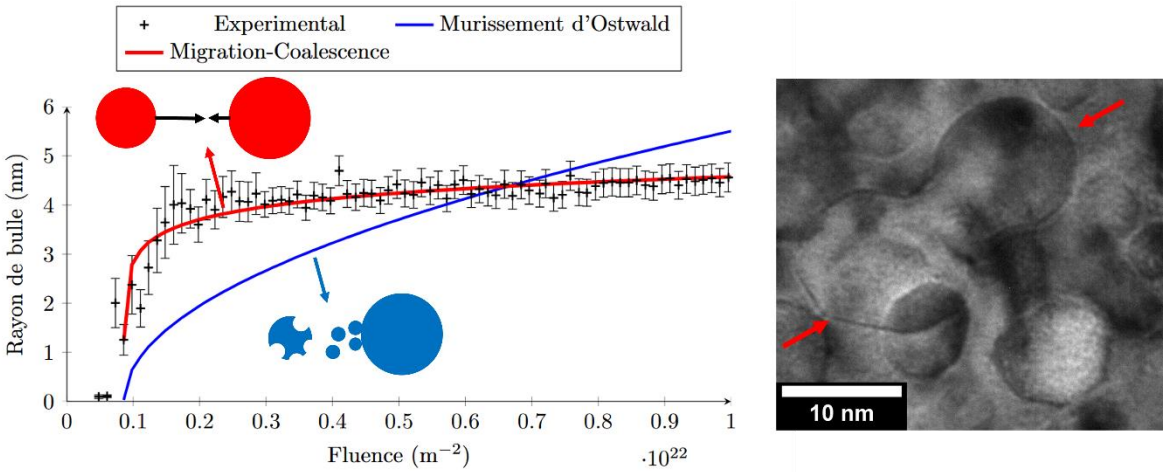

Image V : A gauche : La cinétique de croissance obtenue par GISAXS *in-operando* à haute température (en noir). La prédiction avec un mécanisme de croissance par murissement d'Ostwald est en bleu et celle par migration coalescence en rouge. A droite : image par MET de deux bulles qui coalescent.

La cinétique de croissance des bulles obtenue a été comparée à des modèles analytiques de processus de croissance tels que le murissement d'Ostwald et la migration-coalescence. La cinétique de croissance du rayon $R(t)$ des bulles prédite par le murissement d'Ostwald ($R(t) \propto t^{\frac{1}{2}}$) ne permet pas d'expliquer nos données expérimentales. Il reste le mécanisme de migration-coalescence. La migration d'une bulle implique que les atomes de tungstène à la surface de la bulle se déplacent. Pour cela trois processus élémentaires limitants peuvent être formulés, i) la diffusion des atomes de tungstène sur la surface de la bulle, ii) la diffusion par la phase vapeur à travers la bulle et iii) la diffusion par le volume à travers la matrice de tungstène entourant la bulle. Aucun de ces processus classiques ne permet de retrouver l'évolution temporelle du rayon des bulles obtenue expérimentalement. Les bulles semblent croître moins vite que ces prédictions. Nous proposons que cela vient du fait que les bulles sont facettées. La migration des bulles dans un tel cas nécessite de considérer un dernier processus élémentaire : iv) la nucléation d'une marche sur les facettes à la surface des bulles. Avec ce dernier mécanisme, l'évolution temporelle de la taille des bulles est convenablement reproduite. Le coefficient de diffusion des bulles peut alors être obtenu et nous montrons que celui-ci décroît exponentiellement avec le rayon.

En résumé, l'approche nanoscience basée sur des mesures en temps réel de l'implantation a permis de caractériser précisément la forme et les mécanismes de croissance des bulles pour différentes conditions d'implantation. L'orientation cristallographique des échantillons ne semble pas impacter la présence des bulles. En revanche la température et la présence de lacunes peut considérablement impacter la population de bulles. Ces résultats obtenus dans des échantillons modèles peuvent maintenant servir de base pour augmenter en complexité avec l'ajout de joints de grains dans la microstructure ou la présence d'impuretés pour se rapprocher d'un

composant face au plasma réel. Également, nous pensons que ces résultats permettront d’améliorer les modèles de simulation traitant de l’évolution des bulles.

Remerciements

Cette thèse a commencé à toute allure et je vois qu'elle se finit de la même manière. Ce fut très stimulant et à la hauteur de mes espérances. Bien que personnelle, cette thèse n'aurait pas été possible sans la contribution de beaucoup de collaborateurs que je souhaite remercier ici.

Tout d'abord, je tiens à remercier Elodie Bernard et Frédéric Leroy tous deux co-directrice et co-directeur de cette thèse. Je vous remercie de m'avoir proposé de travailler avec vous. Vous m'avez fait confiance pour mener à bien ces travaux et ce fut très agréable d'apprendre à vos côtés.

Merci aussi à Stefano Curiotto qui a co-encadré cette thèse. Je te remercie pour tes enseignements et ton aide sur la manip quand ça ne veut pas ! Je me rappelle bien de cette source d'Or …

Je vous remercie tous les trois de m'avoir accompagné de multiples fois dans l'espace-temps un peu bizarre de l'ESRF et d'avoir enduré les manips à mes côtés.

Je souhaite maintenant remercier Martiane Cabié pour son grand professionnalisme dans la préparation de mes lames minces. Sans aucun doute, j'affirme que sans la qualité de ton travail, une bonne partie des résultats présentés ici n'existerait pas.

Merci également à Céline Martin pour sa bienveillance et son aide dans mon travail.

Merci à Lucio Martinelli qui s'est montré toujours disponible pour nous venir en aide sur BM32. Et ce, peu importe l'heure de la journée (ou de la nuit …), ni du jour de la semaine (ou du week-end …). Merci à toi.

Je voudrais remercier Damien Chaudanson et Alexandre Altié pour votre aide au microscope. Grâce à vous j'ai pu m'exercer sans limitation donc merci.

Merci également à Fabien Cheynis et Pierre Müller pour nos échanges très instructifs et votre accueil dans le groupe.

Je voudrais remercier Laurence Azcona qui m'a grandement aidé à plusieurs reprises pendant ma thèse.

Je remercie toute l'équipe du GCFPM, pour votre professionnalisme et votre bonne humeur à savoir : Mathilde, Hélène, Adrien, Nicolas, Caroline, Alan, Mehdi, Marianne,

Stéphane, Floriane, Etienne, Jonathan, James, Djogo, Sacha, Pierre et les expatriés de Paris : Mickael et Olivier. Ce fut très agréable de faire partie de ce groupe.

Merci enfin à mes co-bureaux, Maxime et Amélia, c'était un plaisir de partager ce bureau avec vous.

Pour le mot de la fin, je voudrais te remercier toi, Chloé Fresiers pour ton support et ta joie au quotidien.

Contents

List of figures 25

List of tables 28

Introduction 29

1. Basis of the thermonuclear fusion 31
- **1.1. Thermonuclear fusion reaction** 32
  - 1.1.1. Nuclear reactions 32
  - 1.1.2. The deuterium-tritium reaction 34
  - 1.1.3. The supply of reactants 35
- **1.2. Fusion devices** 36
  - 1.2.1. Concepts 36
  - 1.2.2. Performance 39
  - 1.2.3. International thermonuclear experimental reactor (ITER) 41
- **1.3. Plasma facing materials** 43
  - 1.3.1. Specifications 43
  - 1.3.2. Tungsten components 44
- **1.4. Thesis motivation** 46

2. Helium in tungsten materials: State of the art 49
- **2.1. Alteration of materials** 51
  - 2.1.1. Helium sources 51
  - 2.1.2. Displacement damage caused by elastic collision 52
  - 2.1.3. Helium-induced nanostructures 52
- **2.2. Helium aggregation and bubbles formation** 57
  - 2.2.1. Trap mutation mechanism 57
  - 2.2.2. Loop punching mechanism 58
- **2.3. Bubble distribution in the material** 60
  - 2.3.1. Surface orientation effects 60
  - 2.3.2. Segregation at grain boundaries 61
- **2.4. Morphologies of bubbles** 63
  - 2.4.1. Helium inventory 63
  - 2.4.2. Shape of Helium bubbles 64
  - 2.4.3. Growth mechanism 66

3. Experimental techniques 69
- **3.1. Preamble** 71
- **3.2. GISAXS : Grazing Incidence Small Angle X-Ray Scattering** 73
  - 3.2.1. Practical elements 73
  - 3.2.2. The principle 80

3.2.3. ESRF – BM32 – INS2 99
3.3. Sample preparation 101
3.3.1. Samples characteristics 101
3.3.2. Preparation of clean W crystal 102
3.4. Transmission electron microscopy 106
3.4.1. Thin lamella preparation 106
3.4.2. Bubble characterisation 108
3.5. Overview of the experimental conditions 114
4. Helium bubbles characterization 119
4.1. Low temperature implantations 121
4.1.1. Room temperature 121
4.1.2. 523 K implantations 128
4.1.3. 873 K implantations 135
4.2. High temperature implantation and annealing 137
4.2.1. Non-annealed samples implanted at 1273 K 137
4.2.2. Annealed samples implanted at 1273 K 141
4.3. Equilibrium shape of bubbles 146
4.3.1. The Wulff theorem 146
4.3.2. Effect of pressurized He on the W surface energy 149
4.3.3. Form factor of the equilibrium shape of bubbles 151
5. Growth of bubbles 157
5.1. Low temperatures 159
5.2. High temperature 162
5.2.1. Experimental observations 162
5.2.2. Growth mechanism 164
5.2.3. Bubble diffusion coefficient 169
Conclusion 171
Appendix 173
References 177

List of figures

Figure 1: Binding energy per nucleon. 32
Figure 2: Evolution of the cross section for different fusion reactions. 34
Figure 3: Schematic representation of the tokamak concept. 37
Figure 4: Schematic representation of the Stellarator concept. 38
Figure 5: Triple product as an indicator of the plasma performance. 40
Figure 6: Poloidal cross-section of the ITER tokamak. 42
Figure 7: ITER divertor. 44
Figure 8: Particles flux profiles according to simulations along the outer vertical target of the ITER divertor. 51
Figure 9: Helium induced modification of the W microstructure. 53
Figure 10: Experimental window for the formation of He-induced fuzz in W 54
Figure 11: TEM micrographs of W fuzz. 55
Figure 12: Schematic representation of the fuzz formation mechanism. 55
Figure 13: SEM micrograph of a W surface after He-plasma exposure. 56
Figure 14: Sequential TEM micrographs of irradiated W sample. 58
Figure 15: Molecular dynamics simulations of the influence of a dislocation loop on the bubble nucleation. 59
Figure 16: Bubble repartition in a W polycrystalline sample. 61
Figure 17: TEM micrograph of grain boundaries decorated by bubbles. 62
Figure 18 TEM micrographs of facetted bubbles located at the grain boundaries. 65
Figure 19: Different elementary processes for the motion of a bubble. 67
Figure 20: GISAXS geometry. 73
Figure 21: Beam path of light in a medium depending on refractive index. 75
Figure 22: Penetration depth of X-ray in W for 10 keV and 18 keV X-ray energy. 76
Figure 23: Simulated GISAXS patterns within the DWBA of monodisperse objects. 77
Figure 24: Transmission coefficient in intensity. 78
Figure 25: Simulated GISAXS patterns within the DWBA of ponodisperse objects. 78
Figure 26: Typical GISAXS pattern of W single crystal before He implantation. ... 79
Figure 27: Schematic representation of the geometry to determine the boundary conditions of the electromagnetic field. 82
Figure 28: Schematic representation of the Fresnel system. 84
Figure 29: Schematic representation of the Born expansion. 88
Figure 30: Schematically representation of a rough interface. 91
Figure 31: Schematic representation of the multiple reflection and refraction events considered by the DWBA. 95
Figure 32: Schematic representation of a buried bubble 97
Figure 33: Schematic representation of the INS2 set-up. 99

Figure 34: Picture of the INS2 set-up. 99
Figure 35: Picture of W single crystalline samples used in this these. 101
Figure 36: Schematic representation of the LEEM-PEEM set-up. 102
Figure 37: Chemical and morphological characterization of the sample after preparation. 103
Figure 38: GIXD diffractogram of Au/W(110) at 1373 K. 104
Figure 39: LEEM micrographs of AU/W(110). 105
Figure 40: SEM images of the lamella preparation by FIB. 107
Figure 41: Schematic representation of the main components of a transmission electron microscope. 108
Figure 42: Schematic representation of the formation of the diffracted pattern and the image by TEM.. 109
Figure 43: Schematic representation of the use of the SAD aperture. 110
Figure 44: High resolution TEM micrograph of a helium bubble. 111
Figure 45: TEM micrograph of He bubbles in under-focus and over-focus observation. 112
Figure 46: Summary of the different experimental parameters explored in this study. 114
Figure 47: TEM micrograph of $W110\ RT, 400eV$. 121
Figure 48: GISAXS patterns at $\alpha i = 0.47°$ of $W110\ RT, 400eV$. 123
Figure 49: Background subtraction of GISAXS data. 124
Figure 50 : GISAXS pattern after background subtraction with extracted intensity profiles. 125
Figure 51: Simulated GISAXS patterns for different proportion between small spherical bubbles and large elongated bubbles. 126
Figure 52: GISAXS fit of $W110\ RT, 400eV$. 127
Figure 53: TEM micrographs of $W110\ 523K, 400eV$ and $W110\ 523K, 2keV$. 128
Figure 54: GISAXS patterns at $\alpha i = 0.47°$ for $W110\ 523K, 400eV$. 129
Figure 55: GISAXS pattern of $W110\ 523K, 2keV$ recorded with αi =0,2°. 130
Figure 56: GISAXS patterns of $W110\ 523K, 2keV$ with incident angle αi of 0,2° before implantation, at the beginning of implantation and 7 minutes later. 131
Figure 57: GISAXS fit of $W110\ 523K, 400eV$. 132
Figure 58: GISAXS fit of $W110\ 573K, 2keV$. 133
Figure 59: TEM micrographs of $W110\ 873K, 400eV$ and $W110\ 873K, 2keV$. 135
Figure 60: GISAXS patterns recorded at $\alpha i = 0.47°$ for $W110\ 873K, 400eV$ and $\alpha i = 0.6°$ for $W110\ 873K, 2keV$. 136
Figure 61: TEM micrographs of $W110\ 1273K, 400eV$ and $W110\ 1273K, 2keV$.. 138
Figure 62: TEM, STEM and EELS analysis of a He bubble. 139
Figure 63: GISAXS patterns recorded at $\alpha i = 0.47°$ for $W110\ 1273K, 400eV$ and $\alpha i = 0.6°$ for $W110\ 1273K, 2keV$. 140
Figure 64: TEM micrograph of $W100\ 1273K, 2keV\ *$. 141
Figure 65: Schematic representation of the formation of 3D iso-intensity surface map by GISAXS. 142

Figure 66: GISAXS 3D iso-intensity surface maps and patterns recorded at $\alpha i = 0.6°$ for $W1001\ 273K, 2keV*$, $W110\ 1273K, 2keV*$ and $W111\ 1273K, 2keV*$. 143
Figure 67: GISAXS patterns for $W100\ 1273K, 2keV*$ after post implantation annealing up to 1773 K with an incident angle αi of 0.2° and 0.6°. 144
Figure 68: SEM micrograph of $W110\ 1273K, 2keV*$. 145
Figure 69: γ-plot in the zone axis [001]..... 147
Figure 70: Wulff construction deduced by GISAXS. 148
Figure 71: Energetic ratio deduced by DFT or MD simulations for various surface orientations and corresponding Wulff constructions. 150
Figure 72: Schematic representation of the decomposition of the bubble shape. 151
Figure 73: Schematic representation of a cube and a truncated square based pyramid. 152
Figure 74: Simulated GISAXS patterns of the equilibrium shape of bubbles for $W100\ 1273K, 2keV*$, $W110\ 1273K, 2keV*$ and $W111\ 1273K, 2keV*$. 155
Figure 75: GISAXS patterns recorded at $\alpha i = 0.47°$ for $W110\ RT, 400eV$ during implantation. 159
Figure 76: GISAXS patterns recorded at $\alpha i = 0.47°$ for $W110\ 523K, 400eV$ during implantation. 160
Figure 77: GISAXS patterns recorded at $\alpha i = 0.47°$ for $W110\ 873K, 400eV$ during implantation. 160
Figure 78: GISAXS patterns recorded at $\alpha i = 0.47°$ for $W110\ 1273K, 400eV$ during implantation. 162
Figure 79: GISAXS patterns recorded at $\alpha i = 0.6°$ for $W100\ 1273K, 2keV*$ and $W1101273K, 2keV*$ during implantation..... 163
Figure 80: Bubble radius evolution in W100 $1273K, 2keV*$ and W110 $1273K, 2keV*$ by in-situ GISAXS analysis during implantation. 167
Figure 81: TEM micrograph of two bubbles coalescing in W110 $1273K, 2keV$. .. 169
Figure 82: TEM micrograph of W110 $1273K, 2keV$. 170
Figure 83: Bubble diffusion coefficient evolution during the bubble growth. 170

List of tables

Table 1: Main plasma parameters and dimensions for the ITER tokamak. 41
Table 2: Main physical properties of tungsten. 44
Table 3: Optical properties of W for 10 and 18 keV X-ray energies. 75
Table 4: Experimental parameters of the three experimental campaigns. 117
Table 5: Fitted parameters for $W110\ RT, 400eV$ after implantation. 126
Table 6: Fitted parameters for $W110\ 523K, 400eV$ and $W110\ 523K, 2keV$ after implantation. 134
Table 7: Facet length of bubbles in $W100\ 1273K, 2keV\ *$, $W110\ 1273K, 2keV\ *$ and $W111\ 1273K, 2keV\ *$ after 2 keV He implantation at 1273 K and annealed up to 1773 K by GISAXS. 145
Table 8: Energetic ratio between {100} and {110} W surfaces with pressurized He.. 148
Table 9: Bubble diffusion coefficient regarding the elementary processes of the bubble motion. 166
Table 10: Fit parameters for the ledge nucleation limited growth. 168

Introduction

The demand for energy is constantly increasing, partly due to the growth in the world's population, the economic development of emerging countries and the increasing use of technology in developed countries. Currently, fossil fuels, which are responsible for global warming through their carbon dioxide (CO2) emissions, account for about 75% of global energy consumption [1]. The Paris climate agreements aim to limit global warming to 2°C by 2050, highlighting the need to reduce our dependence on carbon-based energy sources to decrease greenhouse gas emissions. In Europe, the "Green Deal," adopted in 2022, has the ambitious goal of achieving climate neutrality by 2050. A part of the solution is the electrification of transport and heat production for domestic or industrial use. However, this requires clean electricity production. To that end, renewable energies such as solar, hydro, and wind power are being extensively developed in Europe, but their major drawback is their intermittency. As a result, these energy sources are often supported by on-demand energies, such as fossil fuels (coal, oil, gas) that emit CO2, or nuclear power, while being carbon-free, also raises public concerns about accident risks and waste management. Therefore, a new energy source that is decarbonised, abundant, intrinsically safe and accepted by the populations is needed.

Thermonuclear fusion is the potential source to produce this electricity. Unlike nuclear fission in the current power stations, the principle of nuclear fusion is to fuse two light nuclei to form a heavier one. This process takes place in the core of stars.

Most of the research in the field is driven by the ITER project based on an international collaboration. Additionally, recently, with records being broken, fusion has generated a great public interest. This has stimulated new investments in private research, giving rise to new actors in the field. Start-ups such as Helion Energy, Renaissance Fusion, Commonwealth Fusion Systems or General Fusion, are born, promising to produce electricity from fusion reactions within the next decades.

1. Basis of the thermonuclear fusion

1.1. Thermonuclear fusion reaction 32
1.1.1. Nuclear reactions 32
1.1.2. The deuterium-tritium reaction 34
1.1.3. The supply of reactants 35

1.2. Fusion devices 36
1.2.1. Concepts 36
1.2.2. Performance 39
1.2.3. International thermonuclear experimental reactor (ITER) 41

1.3. Plasma facing materials 43
1.3.1. Specifications 43
1.3.2. Tungsten components 44

1.4. Thesis motivation 46

1.1. Thermonuclear fusion reaction

1.1.1. Nuclear reactions

Thermonuclear fusion reactions have the potential to produce high amount of energy, without accident risk neither high activity nor long life radioactive wastes. Fusion reactions can occur when, overcoming the Coulomb barrier, two light nuclei fuse into a heavier nucleus. This process seen in the core of stars as our sun is the opposite of nuclear fission reactions that consists in breaking a heavy nucleus into lighter nuclei currently used on earth to produce electricity.

During a nuclear reaction a mass difference between reactants and products is observed, the Einstein's theory of relativity states that the mass deference is transformed in energy. This energy corresponds to the binding energy between nucleons in a nucleus and is given by the famous Einstein's formula:

$$E = \Delta m c^2 \quad (1)$$

With Δm is the masse difference beween reactants and products and c the speed of light in vacuum.
It arises from this formula that even a small mass difference could generate a massive amount of kinetic energy. The aim of using nuclear reactions (both fission and fusion) is to use this kinetic energy (i.e. heat) to produce electricity. The Figure 1 shows the nuclear energy binding curve per nucleon. Light nucleus can release energy by fusion reactions and heavy nucleus by fission reactions.

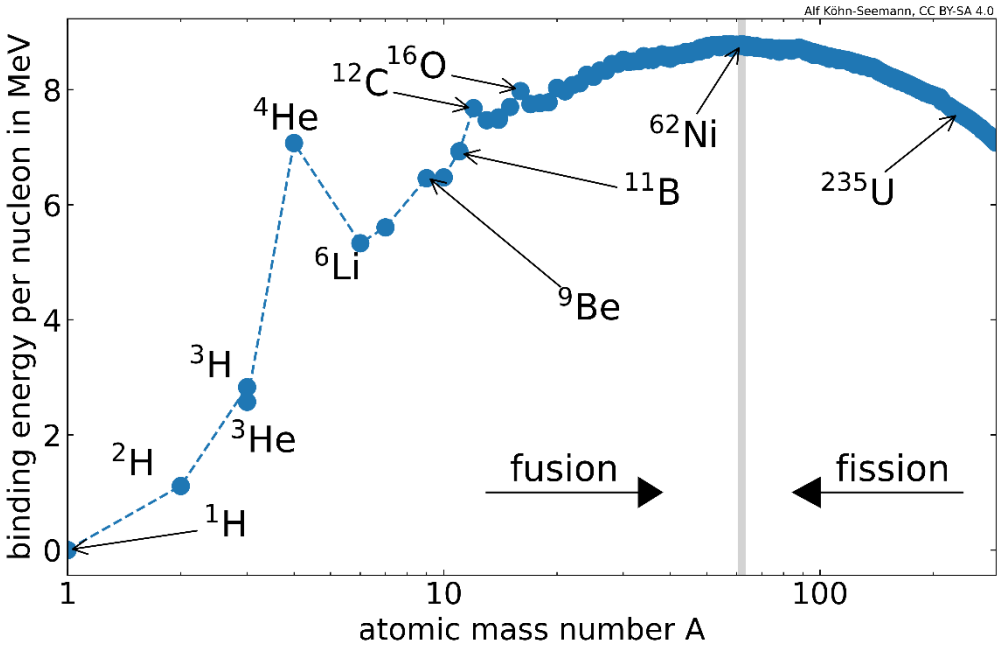

Figure 1: Binding energy per nucleon from ref. [2].

In order to fuse, as nuclei are positively charge, the Coulomb repulsion must be overcome. To that end, nuclei are accelerated to collide with a high velocity and surpass the Coulomb barrier. The velocity v of nuclei is related to the temperature by the relation:

$$v = \sqrt{\frac{3k_B T}{m}} \tag{2}$$

With k_B the Boltzmann constant ($k_B = 1.3806 \times 10^{-23}$ m^2.kg.s^{-2}.K^{-1}), T the temperature and m the mass of the nucleus.

The temperature range for fusion is of several millions of kelvins. At those temperatures, the electrostatic forces which bond electrons to nuclei are overcome leading to unbound electrons and nuclei. This fourth state of matter is a plasma. Despite that electrons and nuclei are unbound, the overall charge of a plasma is zero. At those temperatures, no material can resist, thus it is necessary to confine the plasma without touching it with a physical barrier. As it will be seen below, a solution is for example to use powerful magnets to confine the plasma thanks to magnetic fields.

In fusion science, the average kinetic energy of particles in a plasma is given by $E_v = \frac{3}{2} k_B T$. Also, it is frequent to give the temperature in unit of energy i.e. in electronvolts instead of kelvins. The temperature in kelvin is hence given by: $T\ (in\ K) = \frac{T(in\ eV)}{k_B}$. For example, a plasma temperature of 100 eV corresponds to $T = \frac{100eV}{k_B} = 1.16 \times 10^6$ K. In such a plasma the kinetic energy of particles is $E_v = \frac{3}{2} \cdot 100\ eV = 150\ eV$ and for an electron, the velocity is thus $v = \sqrt{\frac{3 \cdot 100\ eV}{9.1 \times 10^{-31}}} \approx 7.2 \times 10^6$ m.s^{-1}.

1.1.2. The deuterium-tritium reaction

The cross-section of a reaction can be assimilated to the reaction probability. Figure 2 shows the dependence of the cross section for different fusion reactions (with the highest cross section) according to the temperature (or the kinetic energy).

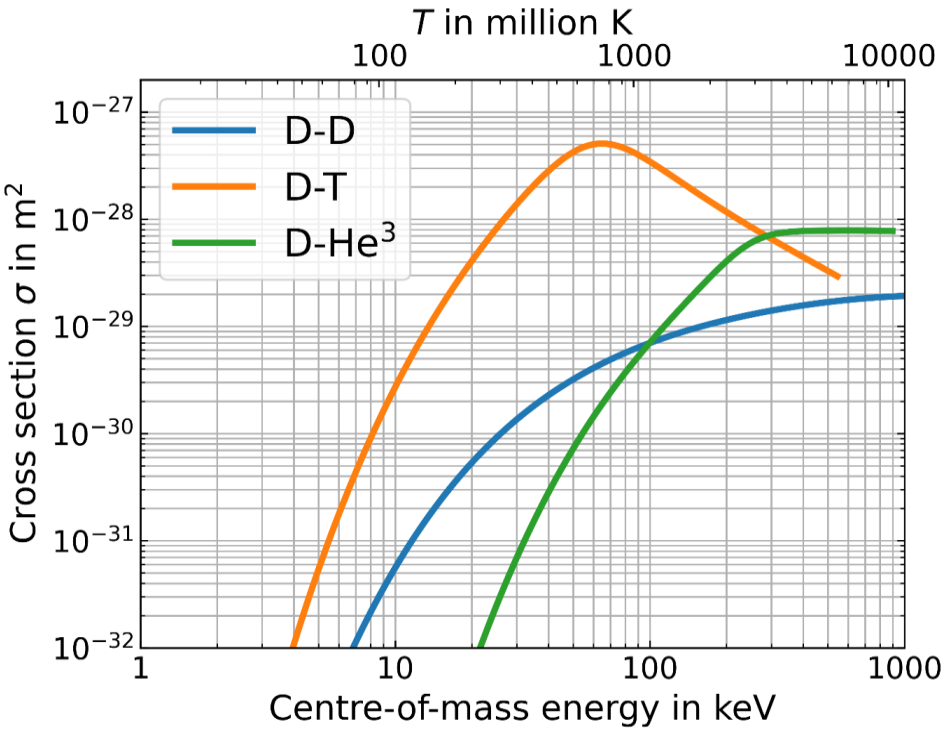

Figure 2: Evolution of the cross section for different fusion reactions from ref. [2].

The most favourable reaction, i.e. the one with the highest cross section at the lower temperature, involves two hydrogen isotopes, deuterium (D) and tritium (T), to form a helium (He) (also termed α-particle) and a neutron (n) (see Eq. (3)).

$$^{2}D^{+} + {}^{3}T^{+} \rightarrow {}^{4}He^{2+}\ (3.5\ MeV) + {}^{1}n\ (14.1\ MeV) \qquad (3)$$

The energy released by this reaction is 17.6 MeV, of which 3.5 MeV (20%) is carried by the He ions and 14.1 MeV (80%) by neutrons. As neutral particles, neutrons will escape the magnetic confinement and impact with the first materials facing the plasma to which they will transfer their energy as heat. This reaction is actively pursued by the community as being the most promising reaction to produce electricity. It offers several advantages: i) the product of the D-T reaction is non-radioactive and ii) runaway reaction is avoided due to the extreme difficulty to gather the operational conditions. Hence, in case of any disturbance the D-T plasma is cooled in few seconds and the reaction is stopped.

1.1.3. The supply of reactants

Procurement of deuterium is relatively easy. Deuterium is very abundant on Earth, and it can be extracted from sea water. The main drawback of this fusion reaction is the difficulty in supply of tritium. In addition, being a radioactive element, its use and handling are real challenges. As all hydrogen isotopes, tritium is very mobile in most materials, but the use of a radioactive elements implies a very precise confinement and monitoring of inventories.

Tritium is an unstable isotope of hydrogen. It is a radioactive element that decays by a weak β^- emission (corresponding to an electron) with an average energy of 5.7 keV (see Eq. (4(3))).

$$^3T \rightarrow {}^3He + e^- \tag{4}$$

The half-life of tritium is 12.3 years [3] meaning that 5.5% of the storage naturally decay every year. This is the main reason why only traces are naturally measured on earth. Nevertheless, artificially tritium is produced as a byproduct of CANada Deuterium Uranium (CANDU) fission reactors. Each CANDU reactor can produce 130 g per years. This quantity is sufficient for research purpose but it will be largely insufficient for an industrial operation [4]. To overcome the problem, it is proposed to generate the tritium in-situ by taking advantage of the reaction between a lithium and a neutron:

$$^6Li + {}^1n \rightarrow {}^3T + {}^4He \tag{5}$$
$$^7Li + {}^1n \rightarrow {}^3T + {}^4He + {}^1n \tag{6}$$

The goal is to include lithium directly in the plasma-facing components, in order to use neutrons produced by fusion reactions to generate tritium. Those components are called breeding blankets and massive efforts of research and development are currently being made.

1.2. Fusion devices

1.2.1. Concepts

To achieve fusion, as seen previously, the D-T plasma must remain confined and heated to millions of K. The Lawson's criterion [5] describes the conditions for which the fusion energy generated by the process compensates the energy losses. It implies a minimum to the triple product time – density – temperature that is required to achieve net production of energy:

$$n_i \cdot T_i \cdot \tau_E > 5 \times 10^{21} \text{ keV.s.m}^{-3} \quad (7)$$

Where, n_i is the ion density, T_i the plasma temperature (in keV) and τ_E the energy confinement time.

In stars, thanks to the action of the gravitational force, the density and the confinement time are extremely high which allows the temperature to remain relatively low (the temperature of the sun core is "only" 15 millions K). On Earth, two alternatives exist:
i) fusion by inertial confinement, where extremely high temperature and density are obtained, but the confinement time is very low. ii) fusion by magnetic confinement, where both temperature and confinement time are high, but the density is low.

Inertial fusion

Fusion by inertial confinement uses lasers to heat and compress a spherical capsule filled with D-T gas. So that adequate conditions are obtained in the plasma, compression of the capsule must be perfect on the spherical surface. Some examples of such devices are the National ignition facility (NIF) [6] and the Laser Mega Joule [7]. This approach has led to the best performance ever reached. In 2022, the energy produced by fusion in the NIF device was higher to the energy applied by lasers on the capsule. The power balance achieved was $Q = \frac{P_{fusion}}{P_{heating}} = 1.5$ [4]. Nevertheless, many challenges remain before industrialisation. Reproduction of this results is not an easy task and the energy cost to generate the lasers have not been considered in the power balance.

So far, the most mature technology for the future fusion power plants is based on magnetic confinement.

Magnetic fusion

“Tokamak” that stands from the Russian acronym for "toroidal chamber with magnetic coils" is the most common concept of fusion device. The Figure 3 represents a schematic view of a tokamak.

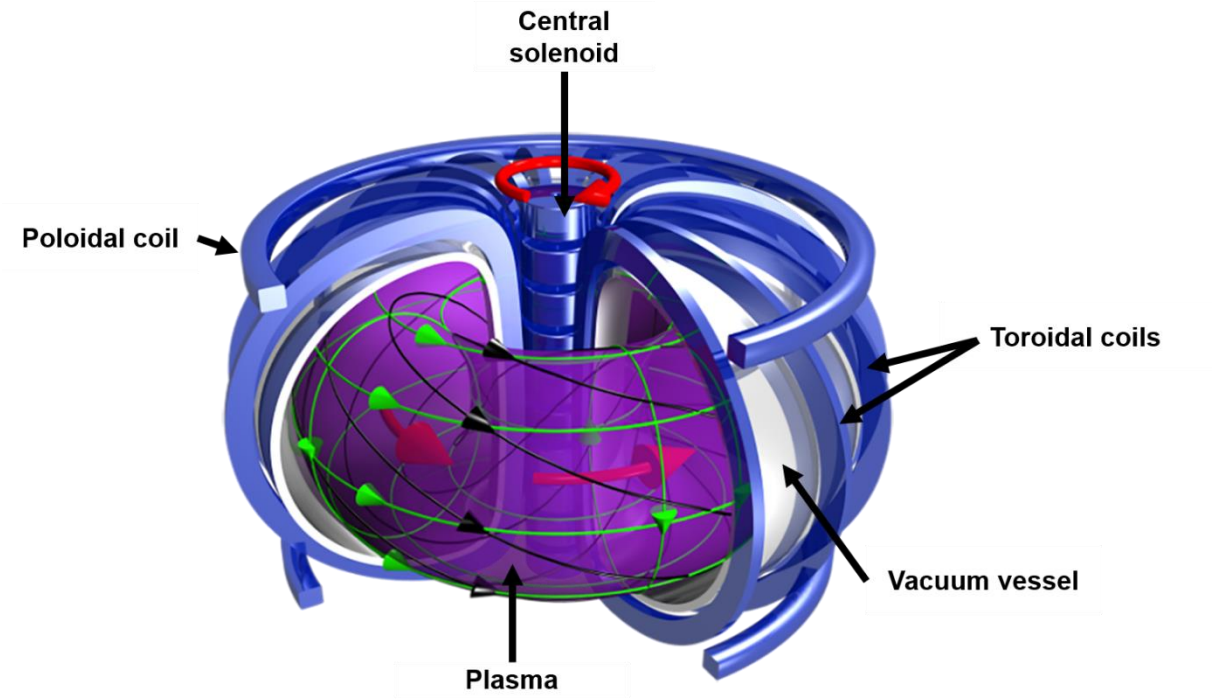

Figure 3: Schematic representation of the tokamak concept. From ref. [8]

In a tokamak the deuterium-tritium plasma is confined thanks to intense magnetic fields generated by a series of toroidal coils.
The toroidal coils generate a magnetic field (green lines) that gives to the device a torus shape. The toroidal field allows to partially confine plasma particles inside the vacuum vessel. Nevertheless, with such magnetically configuration, a gradient of the toroidal magnetic field along the radius of the torus exists and due to the gyration of particles along the magnetic lines, particles are drifting in the vertical direction. Thus, particle are not completely confined. To compensate the drift, a current (red arrows) is generated by the central solenoid (acting as an electrical transformer) in the plasma. An additional magnetic field is thus induced by the current through the plasma that twists the circular field lines (green lines) in helicoidal field lines (black lines) around the torus. With this geometry, plasma particles are confined. Finally, poloidal coils are added to control the plasma shape and its position in order to optimise the plasma performance.

Another concept of magnetic devices has been proposed to avoid the drift of particles. This second possibility consists to place twisted the coils called helicoidal as shown Figure 4. In this case the device is a stellarator.

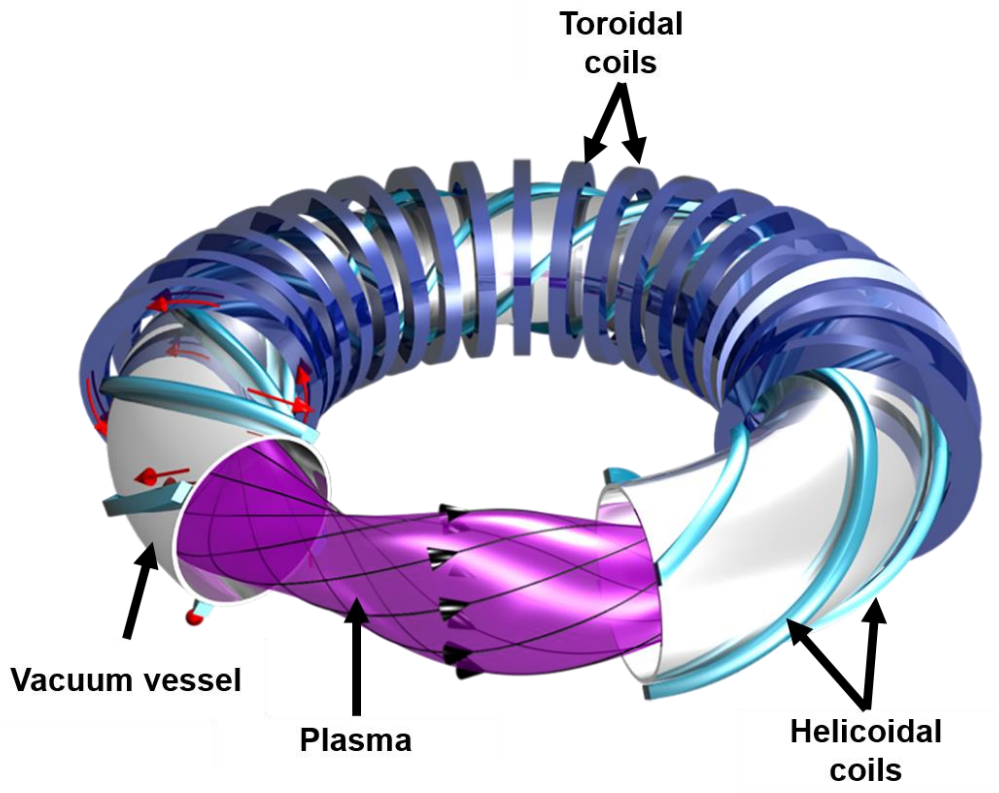

Figure 4: Schematic representation of the Stellarator concept. From ref. [8]

Due to the central solenoid, a tokamak is a pulsed device with plasma pulses limited in time. In absence of a central solenoid, the stellarator is therefore a steady-state device. The main stellarators currently in operation are for example Wendelstein 7-X [9] (W7-X, in Germany) and the large helical device [10] (LHD, in Japan). Nevertheless, the main drawback of the stellarator that limit its development is the complexity to shape the coils.

For an interested reader, a clear presentation of less common magnetic devices can be found in standard books like in ref. [11].

In a tokamak, a discharge can be summarized by the following steps:

i) Pre-fill of the vacuum vessel in deuterium and tritium gases.
ii) Increase in temperature, using the ohmic heating thanks to the current through the plasma and eventually additional heating by high-frequency electromagnetic waves or neutral beam injection (by increasing the collision between plasma particles).
iii) Continuous supply of deuterium and tritium to allow fusion reactions to be maintained.

The discharge ends when the central solenoid is discharged. Nevertheless, the discharge can be brutally interrupted by the loss of confinement caused by numerous

events. The most frequent event that can precipitate the end of the discharge is called a disruption that consists in the loss of heat by radiation due to impurities in the plasma. Let us note that the discharge time should not be confused with the energy confinement time used in the Lawson's criterion. The energy confinement time τ_E corresponds to the length of time for which particles are confined, in other words, it corresponds to the time needed for the plasma to lose its energy after shutting down of all input power.

In normal operation, the length of a discharge is limited by the central solenoid. That is the reason why all recent tokamaks use additional heating to relieve the central solenoid. The most common way is by using high-frequency electromagnetic waves. The principle is to deliver energy at a frequency in resonance with particles, that way, their velocity is enhanced. For frequency in resonance with electron exclusively, the term electron cyclotron resonance heating (ECRH) is used, in the case of resonance with ions exclusively ion cyclotron resonance heating (ECRH) is used. Another high-frequency heating system called lower hybrid current drive (LHCD) can be found, in this case both ions and electrons are accelerated.

Copper magnets (resistive magnets) were used in tokamaks until the 90s. Another limitation of the discharge can arise from the heating of magnets due to the intense current flow (in kA) in the coils. Nowadays, recent tokamaks like WEST [12] (France), JT-60SA [13] (Japan), EAST [14] (China) or KSTAR [15] (South Korea) are equipped with supra-conducting magnet allowing longer discharges.

1.2.2. **Performance**

When fusion reactions occur, α-particles produced remain confined by the magnetic fields and release their energy back in the plasma (corresponding to 20% of the energy produced) while neutrons, not affected by the magnetic confinement release their energy in form of heat in materials facing the plasma (corresponding to 80% of the energy produced).
When the Lawson's criterion is satisfied, the thermal losses are completely compensated by the heating induced by α-particles. In this regime additional heating power can be shut down, this is known as the "ignition". The gain of power $Q = \frac{P_{fusion}}{P_{heating}}$ tends to infinity if the ignition is reached.

Another important step is the "break-even" with an amplification factor $Q = 1$. The break-even is reached when the additional heating power is equal to the fusion power.

Figure 5 shows the triple product reached with the different magnetic devices.

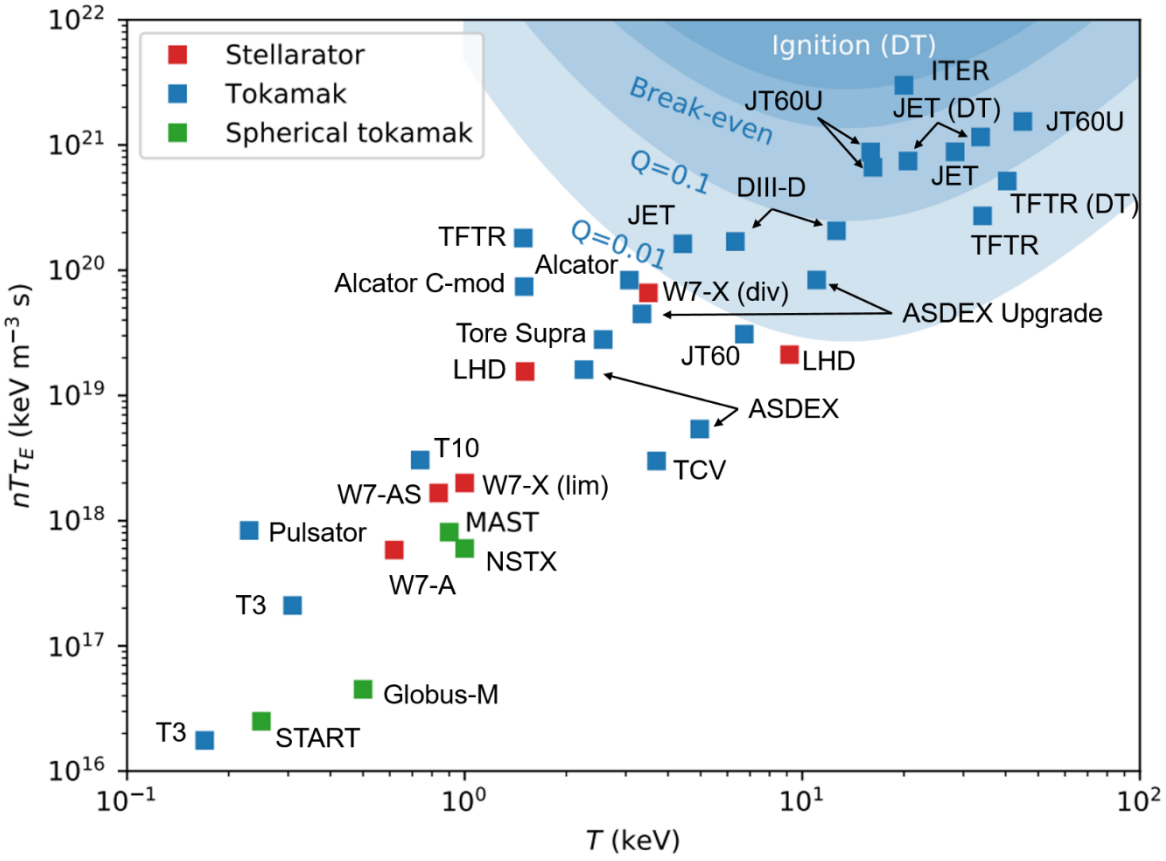

Figure 5: Triple product as an indicator of the plasma performance. From ref. [16]

The best performance has been achieved with the Joint European Torus [17] (JET, in United Kingdom) in 1997. During a pulse the maximum of 16 MW of fusion power have been obtained with 24 MW injected power in the plasma [18] ($Q = 0.67$).

1.2.3. International thermonuclear experimental reactor (ITER)

ITER for “International Thermonuclear Experimental Reactor” is an international scientific project that aims to demonstrate the scientific and technological feasibility of fusion. The ITER organization has been created in 2006 by China, the European Union, India, Japan, South Korea, Russia and the United States. Switzerland and the United Kingdom are also members of ITER through their participation to Euratom (the European atomic energy community) and several countries like Australia, Canada, Kazakhstan and Thailand have progressively joint the project as partners.

The tokamak ITER is currently under construction in the south of France. The ITER design has been adopted in order to reach and go beyond the break-even. A power gain $Q = 10$ with D-T plasma is expected. To that end, ITER will take advantage of the scale law observed in light of a large database crossing many different tokamaks. It stands that the energy confinement time τ_E (i.e. the plasma performance) increases with the major radius (distance from the center of the solenoid central to the center of the plasma), the magnetic field intensity and the plasma current according to the following empirical relation [19,20]:

$$\tau_E \propto R^{1.97} \cdot B_T^{0.15} I_p^{0.93} \quad (8)$$

Where R is the major radius (in m), B_T the magnetic field intensity (in T) and I_p the plasma current (in MA).

The dimensions of ITER will hence be the largest tokamak ever build. Table 1 summarized the main plasma parameters and dimensions of ITER.

Total fusion power	500 MW
Gain power Q	10
Major radius	6.2 m
Plasma volume	837 m^3
Plasma Surface	678 m^2
Plasma current	15 MA
Magnetic field	5.3 T
Plasma discharge duration	> 400 s

Table 1: Main plasma parameters and dimensions for the ITER tokamak from ref. [20].

A poloidal view of ITER is shown Figure 6. The large size of ITER can be visualized with the human scale at the bottom of the figure. For comparison, the second largest tokamak being build is JET with a major radius $R = 3$ m.

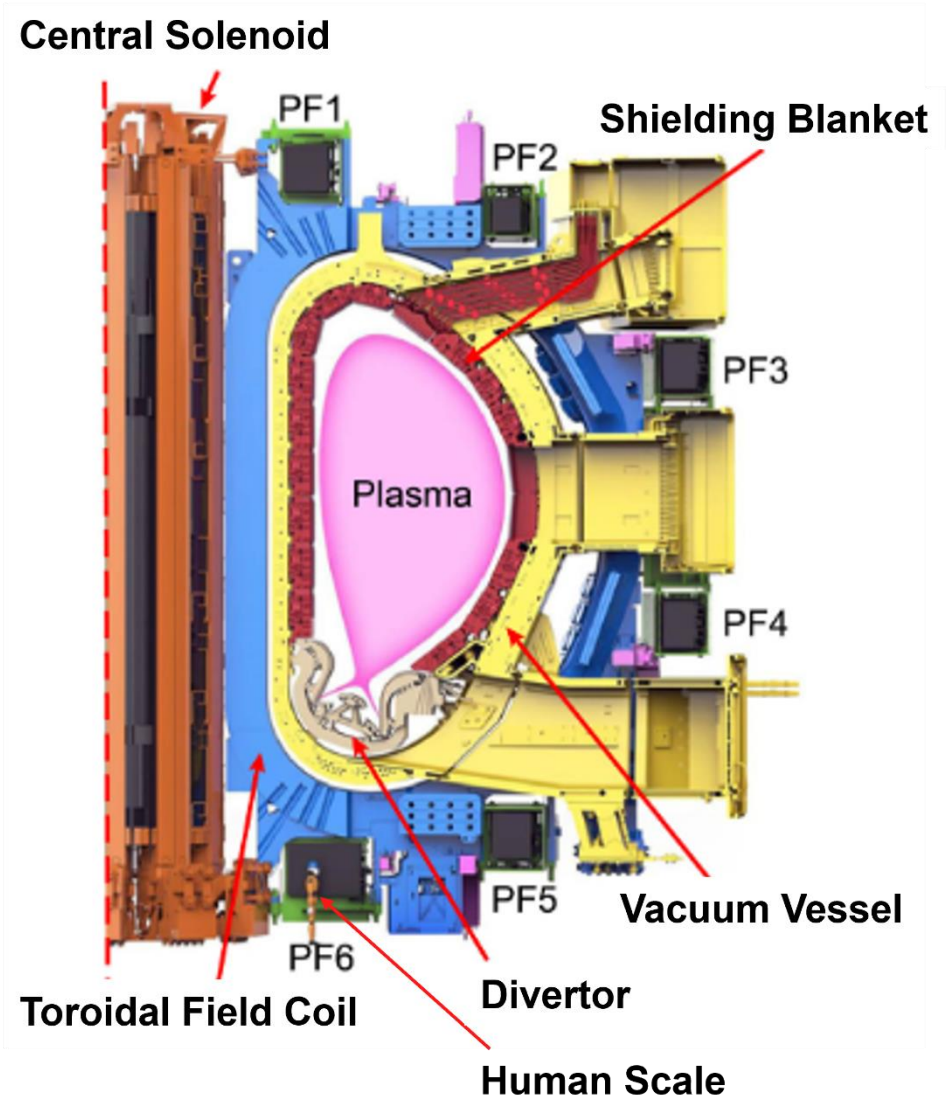

Figure 6: Poloidal cross-section of the ITER tokamak highlighting the main components and their size. PF is for Poloidal Field Coils. From ref. [21].

The main components are also pointed with red arrows. The role of the central solenoid and the different magnets (in the case of ITER supraconducting) have already been mentioned above. The shielding blanket and the divertor are key components as interacting with the plasma. In the figure is also represented a typical plasma shape of ITER. The plasma shape is not a perfect torus but instead, the plasma is D-shaped with a X-point where magnetic lines crosses before intersecting the divertor. This configuration is optimized to enhance the plasma performance. It allows to extract impurities and ashes from the fusion reaction and to guide those particles to the divertor.

1.3. Plasma facing materials

1.3.1. Specifications

The first physical barrier facing the plasma must sustain intense heat load and particles bombardment emanating from the plasma (e.g. neutrons, tritium, deuterium and helium ions escaping the confinement or charge-exchange neutral particles). In ITER the shielding blanket components must sustain up to nearly 5 $MW.m^{-2}$ [22,23]. Higher heat load are expected on divertor components, heat load of 10 $MW.m^{-2}$ in normal operation are expected [24]. This value corresponds to the heat fluxes on the thermal shield of a space shuttle re-entering in the atmosphere. The heat flux on the divertor can increase up to 20 $MW.m^{-2}$ during transient events like edge localized mode (ELM) caused by magnetic instabilities. In addition, due to open magnetic lines, the divertor is bombarded with extremely high particle fluxes up to 10^{24} $m^{-2}.s^{-1}$ [24]. The choice of material composing the plasma facing components (PFC) is therefore crucial. The requirements for a good PFC are listed below:

- High melting point: Surface of components can reach 1273 K continuously and even higher during transient events.
- High thermal conductivity: In normal operation 10 $MW.m^{-2}$ must be extracted.
- Conductor of charges: Arcing could occur due to the accumulation of charge coming from the plasma.
- Low sputtering: Erosion of the component must be minimized in order to reduce the plasma contamination by atoms from the wall. This could have a detrimental effect on the plasma temperature and leads to a disruption (sudden lose of thermal and magnet energy stored in the plasma).
- Mechanical resistivity: Temperature of the component are expected to frequently vary, in addition magnetic forces are exerted on the component and finally disruption can apply a huge force on the component. Its physical integrity must be preserved.
- Low retention of tritium: safety requirements impose to limit the amount of tritium trapped in the first wall. For ITER the maximum tritium inventory allowed in the first wall is 700 g.
- Low activation: neutrons bombardment can lead to transmutation of elements. Plasma facing material must be chosen to avoid generation of long-life activated species.

The initial choice of plasma facing material was carbon fibre composite (CFC). However, due to the chemical affinity between carbon and hydrogen isotopes, high erosion rates have been observed. This erosion has led to the production of dust capable of accumulating hydrogen isotopes in a mobilizable form, which is a serious safety issue. The best candidate that has been chosen for the ITER design is tungsten (W) to equip both the divertor and the shielding blankets. Due to its high atomic number

(Z=74) the amount of tungsten expelled in the plasma core must be minimal. Less than 10^{-5} atomic concentration is necessary to reach the ignition [25].

1.3.2. Tungsten components

The main physical properties of tungsten are summarized in Table 2.

Atomic number (Z)	74
Atomic mass (M)	183.55 u
Crystalline structure	Body centered cubic (bcc)
Lattice constant	3.1652 Å
Density	19.246 g.cm^{-3}
Melting point	3695 K (3422 °C)

Table 2: Main physical properties of tungsten from ref. [26].

Tungsten (W) has been chosen as the plasma facing material in ITER for its very high melting point (3695 K), low sputtering yield in fusion environment and low tritium retention [27,28]. The current adopted design for the ITER divertor is shown Figure 7. Actively cooled tungsten (W) monoblocks by pressurized water flowing in a copper pipe through the monoblocks are assembled in plasma facing units. Those units are themselves inserted into the inner/outer target or the dome part of a cassette. Finally, the divertor is composed of 54 cassettes.

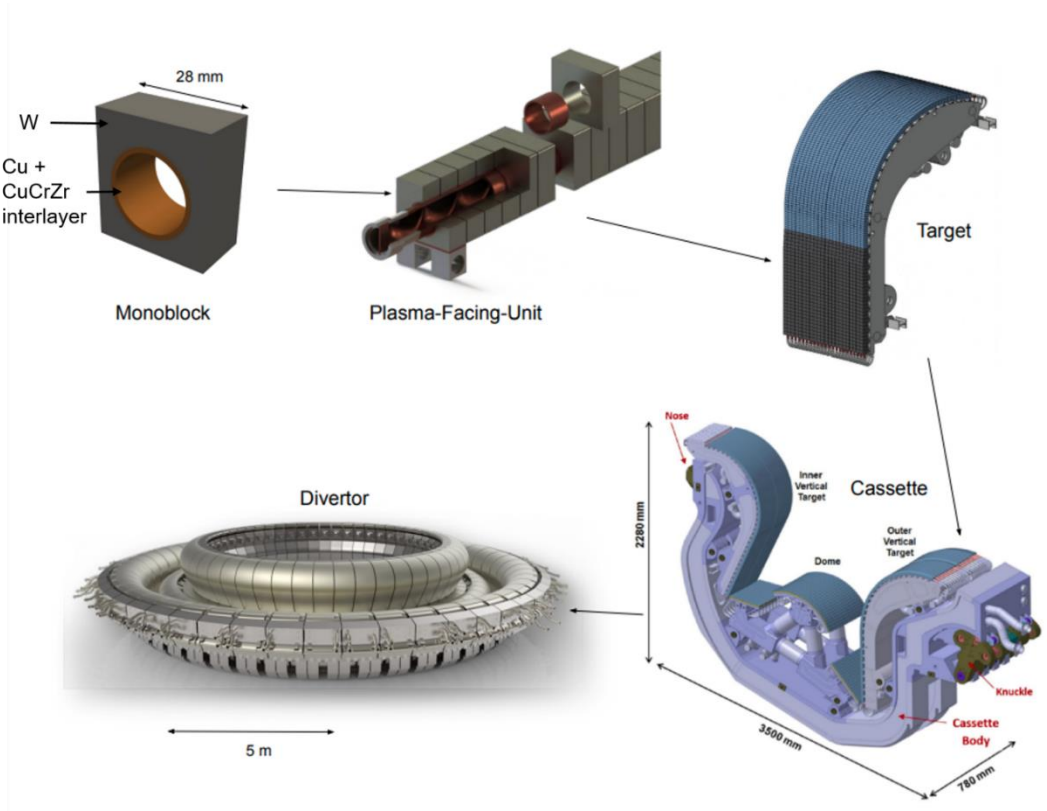

Figure 7: ITER divertor. The elementary W monoblock (top left) is assembled in a plasma facing unit (top midle), then inserted in the target (top right) or the dome (not

represented here) part of a cassette (bottom right) and finally assembled to form the divertor (bottom left). Reproduced from ref. [29].

Since the adoption of tungsten as plasma facing material by the international community, tungsten components have been manufactured and inserted in existing fusion devices. In particular, the divertor of WEST and EAST are equipped with ITER-like components.

1.4. Thesis motivation

Despite the many advantages of tungsten, the intense bombardment by deuterium, tritium and helium ions and neutrons coming from the plasma can significantly affect the component integrity, and therefore modify the properties it was chosen for. Important surface and bulk damage were reported after exposure to plasmas. In particular, the interaction with helium has been proven to reversibly affect the surface and bulk of components. At the surface, tungsten microstructure is altered, micrometer size tungsten filaments can be formed under helium irradiation. In addition, buried nanobubbles affecting the physical properties of tungsten (recrystallization, thermal conductivity …) have been reported. The presence of bubbles can also locally increase the amount of tritium trapped in the component, which could be an issue to comply with the total inventory limit specified for safety. Tritium decaying as He, it is also needed to understand how He accumulation in the metallic structure will impact its mechanical properties.

Until now, most of the efforts to address the effect of helium exposure on tungsten have been performed using a broad range of experimental conditions, as the number of experimental parameters is extremely large considering the sample characteristics (W-grade, temperature, crystal orientation, defects…) along with He exposure conditions (ion energy, flux, fluence, material temperature…). A study that would systematically address the influence of each parameter is unachievable. In addition, most of the present results is provided by post-mortem characterisation of samples, making characterization of the dynamics of the mechanisms impossible. In this context, significant modelling efforts have been performed the last ten years, that are lacking experimental data at the fundamental state to be validated.

In this work, we propose to characterize helium bubbles in tungsten using nanoscience methods and techniques. Our purpose is to answer the following questions:

- What is the impact of temperature, implantation energy and crystalline orientation on the formation of bubbles?
- What are the processes involved in the evolution of the bubbles?
- Do He bubbles evolve only during He exposure or not?

Our approach aims at filling the gap between experimental studies and modelling. To that end, we have studied the dynamics mechanisms involved in the bubbles in real time during implantation. Grazing incidence small angle X-ray scattering (GISAXS) technique has been used in real time during implantation of tungsten single crystalline samples carefully prepared. This innovative approach allows to study as closely as possible the processes at play in model samples and to track the bubbles formation and evolution during and after He implantation with a statistical point of view.

The present manuscript starts with a general overview of the experimental and modelling studies mentioned previously. In the chapter 3 will be presented the main experimental techniques used in this study. Their principle will be presented as well as the set-up. In the fourth chapter, those techniques have been used to characterize the bubbles population for different sets of irradiation conditions. Finally in the chapter 5, the mechanism involved in the growth of bubbles will be addressed.

2. Helium in tungsten materials: State of the art

2.1. Alteration of materials **51**
2.1.1. Helium sources 51
2.1.2. Displacement damage caused by elastic collision 52
2.1.3. Helium-induced nanostructures 52

2.2. Helium aggregation and bubbles formation **57**
2.2.1. Trap mutation mechanism 57
2.2.2. Loop punching mechanism 58

2.3. Bubble distribution in the material **60**
2.3.1. Surface orientation effects 60
2.3.2. Segregation at grain boundaries 61

2.4. Morphologies of bubbles **63**
2.4.1. Helium inventory 63
2.4.2. Shape of Helium bubbles 64
2.4.3. Growth mechanism 66

In ITER, the tungsten divertor must sustain an extreme heat load of 10 $MW.m^{-2}$ in steady state and a high particles (deuterium, tritium helium and neutron) flux of 10^{24} $m^{-2}.s^{-1}$ escaping from the plasma. Helium bombardment is responsible for important degradation of the component integrity which represents a risk for the tokamak operation. Many alterations of the thermomechanical properties and integrity of the tungsten based divertor have been reported. A detailed understanding of the mechanisms of tungsten degradation is hence crucial.

This chapter provides an overview of the current knowledge of the interactions between helium and tungsten.

The first part will deal with the different helium sources and their contributions to the tungsten degradation processes.

Then in the second part, the physics of the microstructure degradation of a material under irradiation will be discussed. The case of elastic collisions between He ions and W atoms will be discussed and an overview of the reported He-induced microstructure degradation will be given.

The third part will focus more particularly on the current understanding of He aggregation processes and bubbles formation in W. The mechanisms of bubble formation will be presented and supported by simulation works reported in the literature.

Finally, the last part will be dedicated to remaining open questions regarding the main bubble characteristics. In particular the He inventory in bubbles and their shape/size evolution under irradiation.

2.1. Alteration of materials

2.1.1. Helium sources

He is the product of the D-T fusion reaction. The 3.5 MeV He ions produced by the fusion reaction are confined by the magnetic fields and most of ions are slowed down to energies in the range 20-100 eV at the divertor proximity for steady state plasma scenario [24,30,31].

Figure 8 shows the flux of He that would reach the divertor in ITER for a fusion gain $Q = 10$ plasma scenario ($10^{20} - 10^{21}$m^{-2}.s^{-1}). During pure He operations, the flux of He is expected to be even higher: in the range $10^{22} - 10^{23}$m^{-2}.s^{-1}.

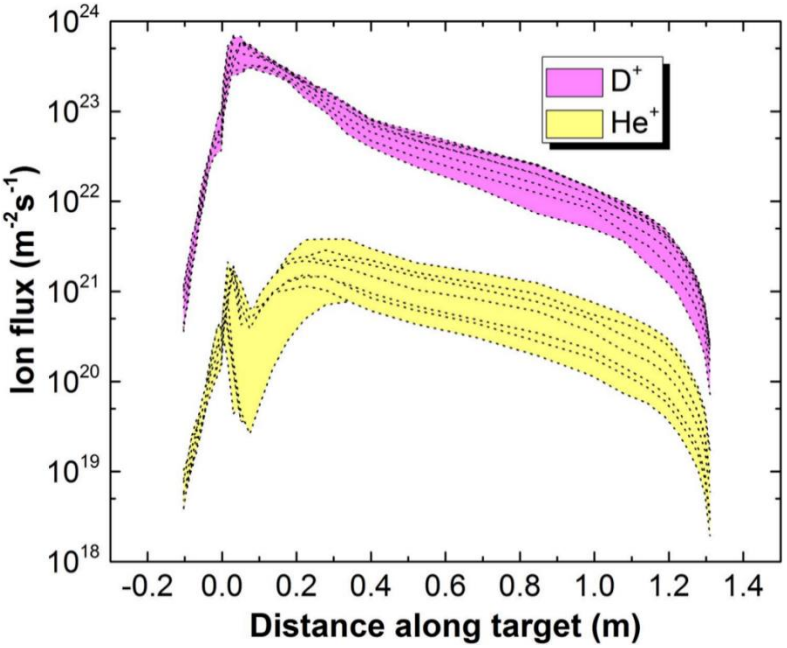

Figure 8: Particles flux profiles according to simulations along the outer vertical target of the ITER divertor. The flux profile of the ions mixing D^+ and T^+ is represented in purple as D^+. The flux profile of He ions is represented in yellow as He^+. Dotted lines correspond to different neutral pressure at the divertor. Reproduced from ref. [24].

He can also be indirectly produced by the decay of the trapped T in the materials. In addition, He can be produced by transmutation reactions occurring under neutron irradiation. Delaporte-Mathurin during his PhD study [29] has estimated those indirect sources for typical ITER operating conditions and performed a conservative comparison with the direct ion implantation flux. He has concluded that indirect sources are negligible compared to the direct ion implantation.

In conclusion, He is mainly introduced in the divertor by ion irradiation coming from the plasma.

2.1.2. Displacement damage caused by elastic collision

The bombardment of W atoms by He particles can be assimilated to elastic collisions where the kinetic energy of the target atom and the projectile is conserved (no energy dissipation through chemical reaction, heat or shape change). In that case, the maximum energy transferred to a W atom during collision is given by [32] $T = 4\frac{M_{He}M_W}{(M_{He}+M_W)^2}\,E_i$ where M_{He} and M_W are the atomic masses of He and W, and E_i is the incident ion energy. The damage generation resulting from this collision is related to the threshold displacement energy (TDE) which corresponds to the energy needed to displace the target atom from its position to an interstitial site. Commonly, the expulsed atom is called self-interstitial atom (SIA) and the couple vacancy-SIA is known as a "Frenkel pair". For polycrystalline W, the TDE is estimated to 90 eV [33]. Defining a more precise value of the TDE requires the definition of the bombardment direction relatively to the crystallographic directions of the target. The evaluation of the TDE in W by molecular dynamics simulations for several orientations have been reported in [34]. The smallest value of TDE is 42 eV for the <100> direction and the average value over 329 directions is 85 ± 5 eV, comparable to the 90 eV for polycrystalline W. The large discrepancy between the lowest and the average value of the TDE highlights the anisotropy of the material regarding the bombardment direction. In the less resistant direction (i.e. <100>) the incident ion energy required to generate a Frenkel pair is thus $E_i = 504$ eV which is well above the maximum energy expected at the ITER divertor. The collision of the majority of He ions with W atoms is then not supposed to generate damages at the surface component.

2.1.3. Helium-induced nanostructures

Despite the low He energy (<100 eV), He bombardment has been reported to generate a variety of microstructure alterations in W components (see reviews in refs. [35,36]). Depending on the irradiation conditions, the most dramatical degradation observed in W is the formation of a nanotendrils layer, so-called "fuzz" (shown in Figure 9a), that can extend up to several micrometres at the surface components. Also, large voids of micrometre scale can possibly be formed under He exposure (see Figure 9b) and finally, He nanobubbles in the first dozens of nanometers below the W surface have been reported (Figure 9c).

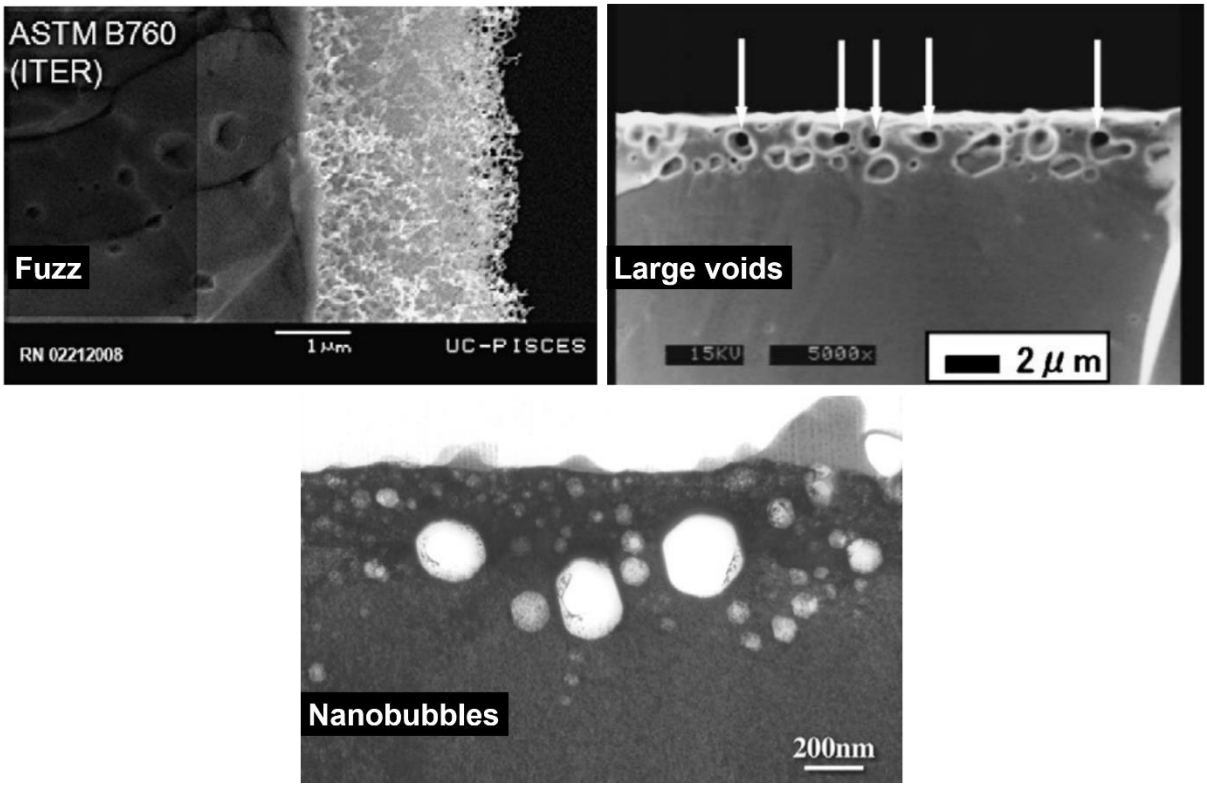

Figure 9: Helium induced modification of the W microstructure. Top left is a SEM micrograph of a W-ITER grade sample with a fuzz layer formed at its surface after exposure to a 60 eV He plasma at 1120 K, during ~1h (flux = $5x10^{22}$ $m^{-2}.s^{-1}$), reproduced from [37]. Top right is a SEM micrograph of a W sample exposed to 10 eV He plasma with a flux of $9.4x10^{22}$ $m^{-2}.s^{-1}$(Fluence is $6.8x10^{26}m^{-2}$). Large micrometer size voids pointed with white arrows are visible, reproduced from [38]. At the bottom, a TEM micrograph of He nanobubbles formed in a W ITER grade sample exposed to 30 eV He plasma at 1800 K (Flux is $1.4x10^{23}$ $m^{-2}.s^{-1}$and Fluence is $1.0x10^{27}$ m^{-2}), reproduced from [39].

These modifications of W at the surface and sub-surface can alter the physical properties of the W components and compromise the plasma performances [24]. To point out some examples, in presence of a fuzz layer, arcing is enhanced creating dust and massive sputtering of W atoms into the plasma [40,41]. This dramatically cool down the plasma temperature and so compromise the plasma efficiency. Neu et al. [25] have calculated that the atomic proportion of W in the plasma must be kept below 10^{-4} to achieve ignition in ITER. In addition, the thermomechanical properties of W such as the thermal conductivity [42,43], hardness [44,45] or recrystallization [46] are jeopardized after He irradiation. Another major concern with He-exposed W is that He bubbles and W-dust formed after erosion increase the T retention in a mobilizable form, which is critical regarding nuclear safety [47–50].

In fusion devices results on fuzz formation conditions are partly contradictory hence, no clear understanding of the fuzz formation mechanisms has been established. In Alcator C-Mod [51,52], and in ASDEX-Upgrade [53–55] W fuzz has been successfully

formed during He-plasma operation. While in JET [55] and WEST [56] tokamaks no evidence of W fuzz has been observed during He-campaign. These discrepancies are due to the high complexity of the tokamak environment, many experimental parameters considering the sample characteristics (surface state, crystal orientation, W-grade, defects) or the irradiation parameters (temperature, ion energy, flux, fluence) can affect the W response. In addition, the tokamak environment is very constrained and in-situ characterization of the microstructure is impossible.

A theoretical description of the fuzz formation is hence not available yet. However, numerous studies in plasma linear devices such as PISCES (Plasma Interaction with Surface and Components Experimental Simulator) [37,57,58] or NAGDIS (NAGoya DIvertor Simulator) [59–61] have permitted to identify a "window" (shown in Figure 10) in which the fuzz is formed [62].

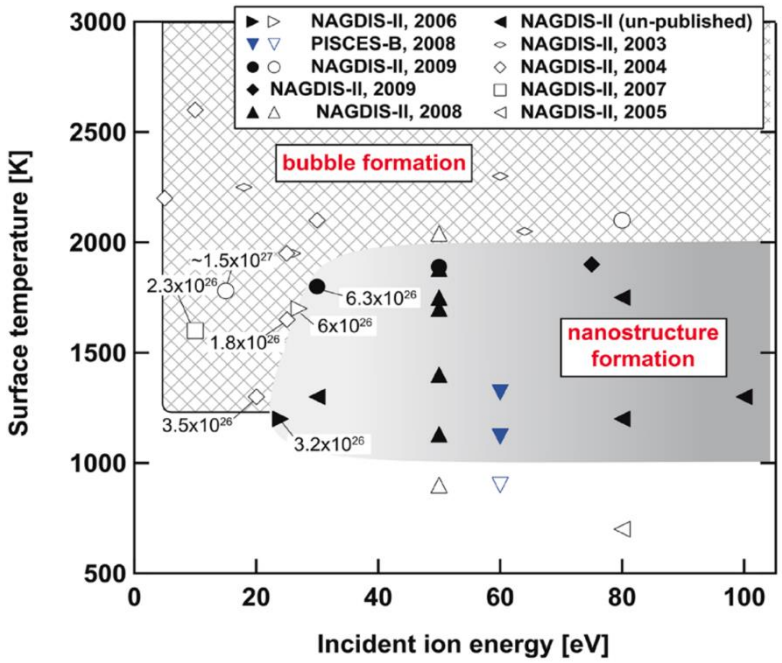

Figure 10: Experimental window for the formation of He-induced fuzz in W. Reproduced from [62]

Fuzz formation occurs only for temperatures in the range 900 K to 2000 K and a minimum He ion energy of 20 eV is necessary. In addition, it is also established that the formation of fuzz as well as the large voids are induced by prior agglomeration of He atoms into buried nanobubbles. Figure 11 shows for instance, the presence of He bubbles in the W fuzz tendrils reported in [63]. Below 900 K, only nanobubbles are observed [39,64] and above 2000 K micrometre voids are reported [38].

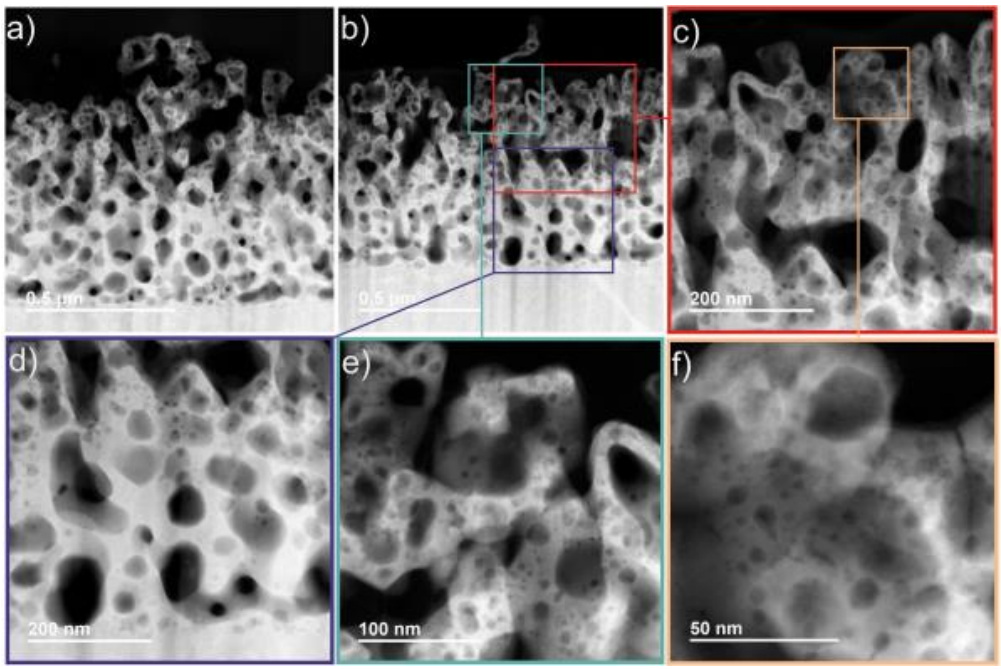

Figure 11: TEM micrographs of W fuzz formed after He exposure (80-100 eV, $1x10^{20}m^{-2}.s^{-1}$ at 1150 K) from [63]. He nanobubbles are present in the fuzz tendrils.

The proposed mechanism for fuzz formation is summarized in Figure 12. During He implantation, He nanobubbles are first formed, then grow by expelling W atoms to the surface (as it will be detailed in section 2.2) and finally burst generating protrusions at the surface which by accumulation form nanotendrils.

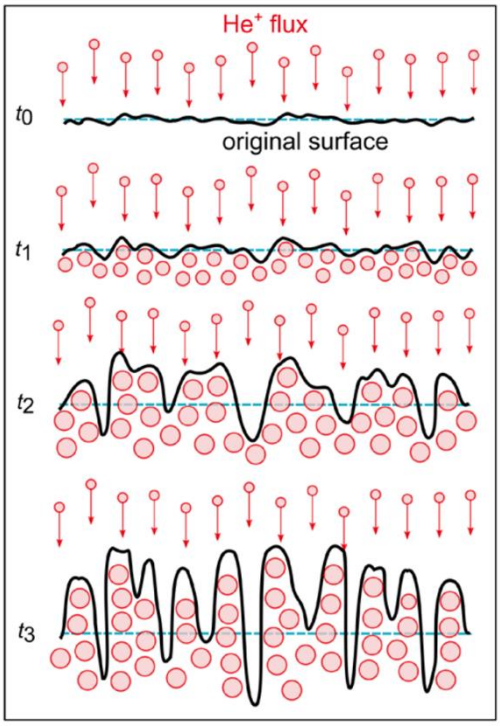

Figure 12: Schematic representation of the fuzz formation mechanism in W under He irradiation. As the fluence of He increases with time (t_0 to t_3), successive cycles of i)

bubbles formation, ii) growth by expelling W to the surface and then iii) bursting; displace W atoms in filament structure forming the fuzz. Reported from ref. [65].

The operating window for creating observable bubbles is extremely large. The incident energy of He ions must exceed 20 eV to avoid total reflexion at the W surface. This energy threshold has been estimated for various crystal orientations and temperature [66,67]. In addition, a minimal flux between $3x10^{16}$ and $7x10^{16}$ $m^{-2}.s^{-1}$ is needed to allow retention of He in W samples [68]. In fusion devices, the normal operation conditions lie in this window, hence the formation of bubbles is expected. In absence of fuzz, bubbles alone are responsible for surface degradation. Holes due to bubbles bursting on samples surface (see Figure 13) are frequently reported [69–72].

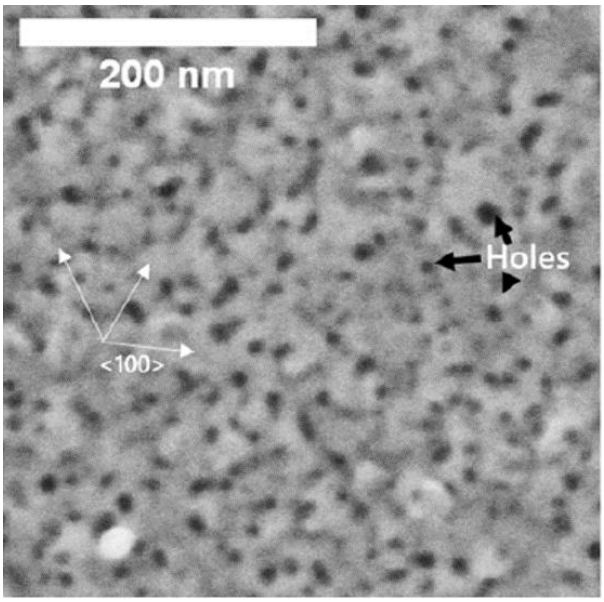

Figure 13: SEM micrograph of a W surface after He-plasma exposure. Black areas are holes formed after bubble bursting. Reproduced from ref. [72].

He bubbles formation is thus the first step of a potential critical evolution of W microstructure, having huge impact on the W components lifetime and safety (T retention). Therefore, understanding the fundamental mechanisms of He-bubble formation and evolution is of prime importance for the development of commercial fusion power plants.

2.2. Helium aggregation and bubbles formation

2.2.1. Trap mutation mechanism

Aggregation of He atoms in bubbles is driven by the low solubility of He in W. According to atomistic simulations, the W-He interaction is repulsive [73,74], He atoms are then pushed in interstitial positions. The tetrahedral interstitial site has been identified to be the most stable position by Becquart et al. [75] using *ab-initio* simulations. They have also found that interstitial He atoms rapidly diffuse through the W matrix, with a very low migration energy barrier of 0.06 eV [75].

As soon as two single He atoms get close, they form a He cluster. Indeed, the binding energy between He atoms in W has been calculated up to a group of 5 He atoms (He_5) in ref. [76] and extended up to the formation of He_{10} in ref. [77,78]. In all cases, the energetic is favourable to the formation of larger clusters. The clusters remain mobile as shown by Zhou et al. [79] by Molecular Dynamics simulations (MD) and will grow by absorbing single He atoms or He clusters. When the local pressure due to the large number of He in the cluster is high enough, a W atom is expelled from its crystallographic position as self-interstitial atom (SIA). The pressure inside the cluster is reduced by the generated vacancy, which stabilises the cluster. This mechanism can be found in the literature as the “self-trapping” mechanism. He-vacancy clusters are less mobile and frequently termed “bubbles”. You et al. [80] have studied this process and shown that the formation energy of a vacancy close to the cluster is significantly reduced when the number of atoms occupying the cluster is larger. In addition, they have estimated that minimum 5 He atoms in the cluster are necessary for self-trapping [81]. The nucleated bubble grows by repeated absorption of mobile He atoms/clusters. Once enough He atoms have been incorporated, the He-vacancy cluster (He_n-V, with V for vancancy) “trap mutates” i.e. evolves from a He_n-V to a He_n-V_2 by expelling a SIA W.

Li et al. [82] have studied the interaction between He_nV_m clusters and SIA atoms. They have pointed out that the binding energy between a He_nV_m cluster and a SIA decreases with He to vacancy ratio, the recombination of SIA and a vacancy is thus unlikely to occur in over-pressurised clusters. The energetics of He-W interaction in presence of pre-existing vacancies in the W matrix has been calculated by Becquart [76]. They have shown that absorption of a He atom on a He-vacancy cluster is always easier than the absorption of a vacancy to the same cluster. This is due to the low stability of pure vacancies assembly [83]. Finally, the stability of He clusters in presence of impurities has been studied in [84]. Except for rhenium (Re), most impurities can trap He atoms and thus nucleate bubbles.

2.2.2. **Loop punching mechanism**

As the bubble grows by repeated self-trapping and trap-mutation events, many SIA are generated that remain close to the bubble. MD simulations performed by Kobayashi et al. [85] have shown that the tensile field at the periphery of the cloud enhances the nucleation of new bubbles. They have also found, consistently with other modelling studies [86–88], the spontaneously reorganisation of the SIA cloud into a prismatic dislocation loop with a Burgers vector $b = \frac{1}{2} < 111 >$. The dislocation loop accumulates SIA as they are produced by the bubble growth, then detaches from the bubble surface and diffuses along the $< 111 >$ direction. This mechanism, called loop punching is expected to repeat if He atoms are continuously absorbed by the bubble. To support this modelling result, Iwakiri et al. [89] claim to have experimentally reported this mechanism. They have observed, by in-situ TEM, the formation of defects in W samples during irradiation by 250 eV He ions at RT. They have also recorded sequential micrographs (see Figure 14) showing the loop punching mechanism from a bubble called “platelet”.

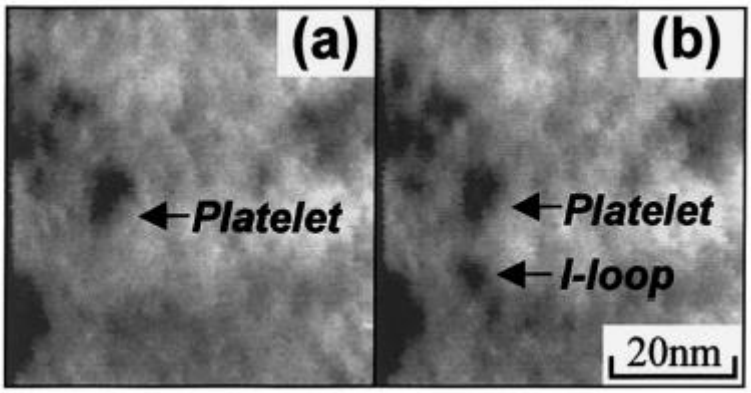

Figure 14: Sequential TEM micrographs of irradiated W sample to 250 eV He ions at RT. The black contrast is due to defects (SIA atoms) generated by the bubble growth. In (a) the cloud of defect is surrounding the bubble. In (b) a loop is punched from the bubble surface.

The internal pressure inside the bubble seems to be the driving parameter for the loop punching and hence the growth of bubbles. The pressure threshold for the detachment of the loop is dependent on the bubble growth speed. Sandoval et al. [90] have found that for high growth speed (high He fluxes), multiple loops nucleate and a significant pressure increase is needed to punch the first loop. While at low-speed growth, a single loop is formed and punched very quickly (lower pressure increases needed). In addition, Kobayashi et al. [85] have found that new bubbles are nucleated at the neighbourhood of the traveling loop. As shown in their MD simulations (Figure 15), bubbles (purples dots) are organised along $< 111 >$ directions that correspond to the path followed by the punched loop (rounded by the black dashed circle).

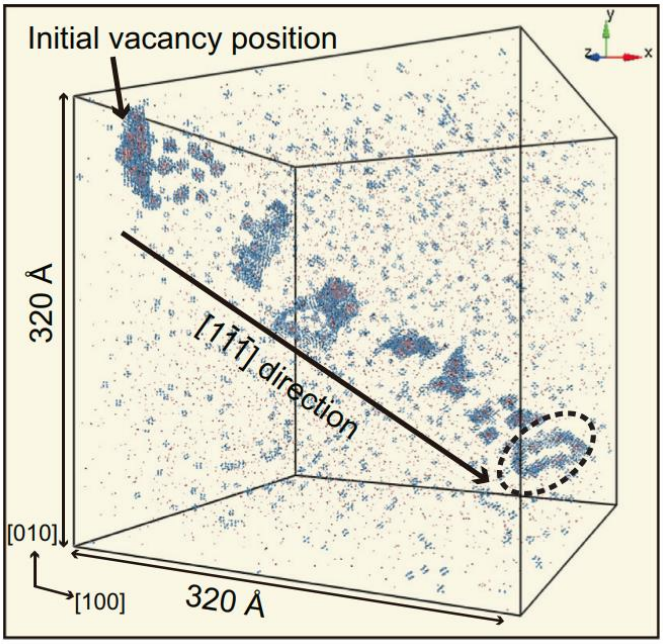

Figure 15: MD simulations after 6 ns at 2000 K. Displaced W atoms are represented in blue, He atoms in purple and the punched dislocation loop is indicated by the black dashed circle. Nucleated bubbles are organised along a $< 111 >$ direction corresponding to the path followed by the punched loop. Reported from [85].

2.3. **Bubble distribution in the material**

The bubble distribution in the material is influenced by the ability for a bubble to be nucleated. As seen previously, organised network of bubbles along the [111] direction in the material is possible because of the loops emitted by the growth of pre-existing bubbles. In this section will be presented other sources of atypical distribution of bubbles.

2.3.1. **Surface orientation effects**

Surface orientation has been reported to play a role on the depth and size distribution of bubbles. MD simulations performed by Hammond and Wirth [91] suggest that the {111} and {211} oriented surfaces will enhance the concentration of bubbles in the first nanometers below the surface. This behaviour is explained by the fact that formation of ad-atoms on {111} and {211} surface is possible thanks to only one He atom in the first atomic layers while at least three He atoms are required to generate an ad-atom on the {110} surface. The formation of close surface bubbles is thus enhanced in the case of {111} and {211} surfaces because trap mutation can occur with only one single He atom. The formation of bubbles is then independent of the surface orientation for depths more than 3 nanometers.
Experimentally, Ialovega et al. [72] have exposed polycrystalline samples to 75 eV He-plasma at 1053 K (flux is 2.3×10^{22} $m^{-2}.s^{-1}$ and fluence is 3.0×10^{23} m^{-2}). They have observed holes due to bubbles bursting for different grains. They have found higher density of holes on the surface of a {111} oriented grain compared with the surface of a {100} oriented grain. This indicates a higher density of bubbles near the surface of {111} oriented grains in agreement with the previous simulated work.
In addition, they have analysed the repartition of bubbles by TEM (see Figure 16).

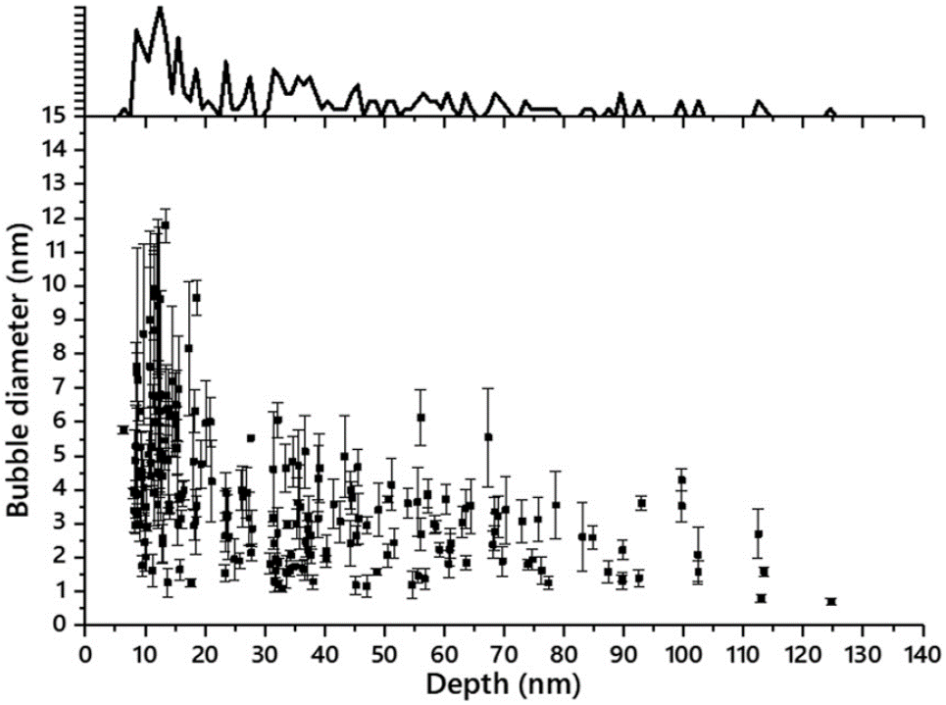

Figure 16: Bubble repartition in a W polycrystalline sample exposed to 75 eV He-plasma at 1053 K (flux is 2.3×10^{22} $m^{-2}.s^{-1}$ and fluence is 3.0×10^{23} m^{-2}). Error bars correspond to the difference of the major and minor diameters. Reproduced from ref. [72].

After a denuded zone in the first 5 nanometers below the surface due to bursting events, the maximum of the bubble density is in the range 10-15 nm with bubble diameter in the range 1 - 12 nm. Then the typical bubbles density and size decrease with the depth up to one hundred of nanometers deep where no more bubble can be detected.

2.3.2. **Segregation at grain boundaries**

Segregation of He bubbles at grain boundaries (GB) have been reported by Donovan et al. [92] after exposure of W polycrystalline samples to 47 eV He ions at 1270 K. They have observed by SEM holes corresponding to He bubbles bursting at the surface, preferentially located at GB. El-Atwani *et al.* [93] have also observed below the surface by TEM, preferential bubble formation at GB after irradiation by 2 keV He ions at 1223 K. Figure 17 is a TEM image of W nano-grains where GB are decorated by large bubbles while inside grains, only small bubbles are visible.

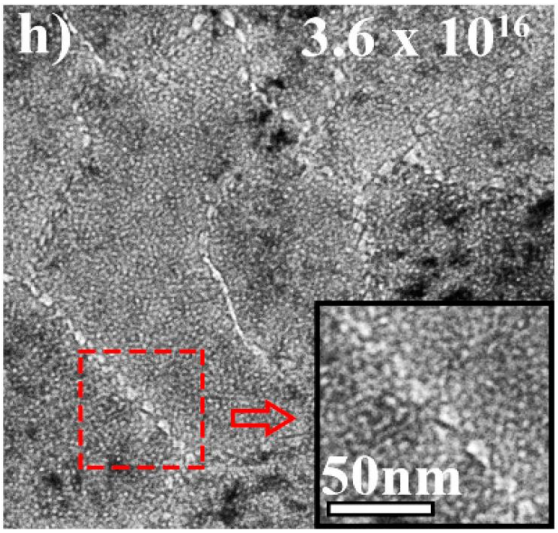

Figure 17: TEM micrograph of a nanocrystalline-grained W after 2 keV He ions bombardment at 1223 K (Flux 8.8×10^{17} m^{-2} and dose 3.6×10^{20} m^{-2}). Reported from [93].

This behaviour has been extensively studied by Hammond's team [94–97]. They have described the attraction of a He cluster towards the GB by a "drift" force that is applied on He clusters by the GB. This drift force results from the elastic inclusion theory detailed in ref. [94] and is inversely proportional to the power four of the distance between the GB and He cluster. The fundamental cause of this drift force is the difference of W density near a GB, this modifies the diffusion energy of He clusters toward GB, which biases the diffusion of clusters to GB [95]. They have also shown that once the cluster has reached the GB the strong influence of the drift force tends to immobilize the cluster [95] and enhance trap mutation [96]. This result is consistent with other simulation studies that have reported a relatively high segregation energy (1.37 eV) that locks He atoms in the GB [98].

In a fusion device, Bernard et al. [99] have exposed W polycrystalline samples to charge-exchange (CX) He from the LHD He-plasma. Despite the relatively low He energy (~500 eV), they have observed in deep regions, at 70 nm below the surface and exclusively at GB, the presence of small bubbles. This non-typical case has also been observed by Wang et al. [100] after exposure to 80 eV He-plasma of a hot-rolled sample (high GB density) and a recrystalized one (low GB density). They have reported the presence of small bubbles very deep inside the samples for both type of microstructures. The bubbles are deeper in the recrystallized sample. A possible explanation is that the low density of GB allows He atoms to diffuse far away by in-grain diffusion until they are finally trapped by a GB under the effect of the drift force.

The drift force arises also in presence of a free surface [101] and can be generalized to many defects with excess volume [102] i.e. in presence of lattice dilatation. The manifestation of the drift force is to increase the binding energy of He cluster to the defect. For example, Kurtz et al. [103] have shown in Fe, that the binding energy of He on GB increases with the excess volume.

2.4. Morphologies of bubbles

2.4.1. Helium inventory

He inventory in bubbles is a crucial issue: He pressure, which is closely related to the He inventory inside the bubble, has been identified as the key parameter for the loop punching mechanism. Also, bubbles act as a trap for hydrogen isotopes. Miyamoto et al. [49] have clearly identified by electron energy loss spectroscopy (EELS) that He bubbles are trapping sites for deuterium. Ialovega et al. [48] have shown that the deuterium retention in He pre-implanted W at 1053 K (75 eV He plasma with a flux of 2.3×10^{22} $m^{-2}.s^{-1}$ and fluence of 3.0×10^{23} m^{-2}) is much higher (3 times) compared to non-He implanted W. In addition, they have shown that in case of cycling deuterium loading and heating to 1350 K, a part of the He has been desorbed during the first temperature increase meanwhile the implanted deuterium retention has increased and reached up to 8 times the non-He irradiated W. They have concluded that more deuterium is trapped when less He remains in bubbles. This result is consistent with atomistic simulations [104,105] that show that the binding energy between H atoms and He_nV_m clusters increases when the He content is low.

For a spherical bubble and considering that the bubble is in thermodynamic equilibrium, the pressure can be estimated using the Young-Laplace relation $P = \frac{2\gamma}{r}$ [106] with γ the surface energy of W and r the bubble radius. Typically γ is around 3.3 $J.m^{-2}$ [107] and r is few nanometers. For example, it gives $P \sim 1.3\ GPa$ for a bubble with a radius of 5 nm. This is a rough estimation of the pressure as bubbles could exhibit elongated shapes or facetted shapes (see the next section).

In principle the pressure inside a bubble can be obtained if the He inventory is locally determined and knowing the equation of state of He in the pressure regime of bubbles. Despite the fact that the state law of He in GPa regime is not well known, empirical expressions have been proposed from numerical simulations. Hammond et al. [108] have first obtained a power law relation between the number of He atoms n_{He} and the number of vacancies n_V in a bubble as $n_{He} = 5n_V^{0.86}$. This relation has then been upgraded into the expression [109]:

$$n_{He} = \frac{16.08 n_V}{\left(21.8150 n_V^{2/9} - 5.7637 n_V^{1/3} + 2.2631 n_V^{4/9} - 0.1988 n_V^{5/9} + 0.0260 n_V^{2/9}\right)^{1/2}}$$

On the experimental side He inventory has been experimentally measured using EELS technique as demonstrated by Ialovega et al. [72] and Miyamoto et al. [49]. The He density n in a bubble with a diameter d is given by [110]: $n = \frac{1}{\sigma_{2p}} \frac{I_p}{I_z d}$ where I_z is the zero loss intensity (i.e. electrons that have passed through the sample without

interaction), I_p the intensity of the electronic transition in He (i.e. electrons interacting with He) and σ_{2p} the inelastic scattering cross-section for the He transition. The EELS measurement of the He content is however dependent on the model used to extract the intensity of the He peak (I_p) which is superimposed with the W plasmon signal.

The exact measurement of the pressure and He inventory as well as the definition of a non-empirical equation of state for He in bubbles are still on-going research.

2.4.2. Shape of Helium bubbles

In numerical models the shape of helium bubbles based on experimental observations at low temperature [111,112] is generally associated to a sphere. However, at high temperature, faceted shapes have been observed. For example, Wang et al. [100] have reported faceted bubbles in fuzz tendrils after implantation of W samples with 80 eV He ions at 1173 K. El-Atwani et al. [64] have reported the faceting of bubbles located at the grain boundary of irradiated W samples with 2 keV He ions at 1223 K (Figure 18) and Ohno et al. [39] have shown faceted bubbles in a grain of a polycrystalline sample after 30 eV He plasma exposure at 1800 K in NAGDIS-I.

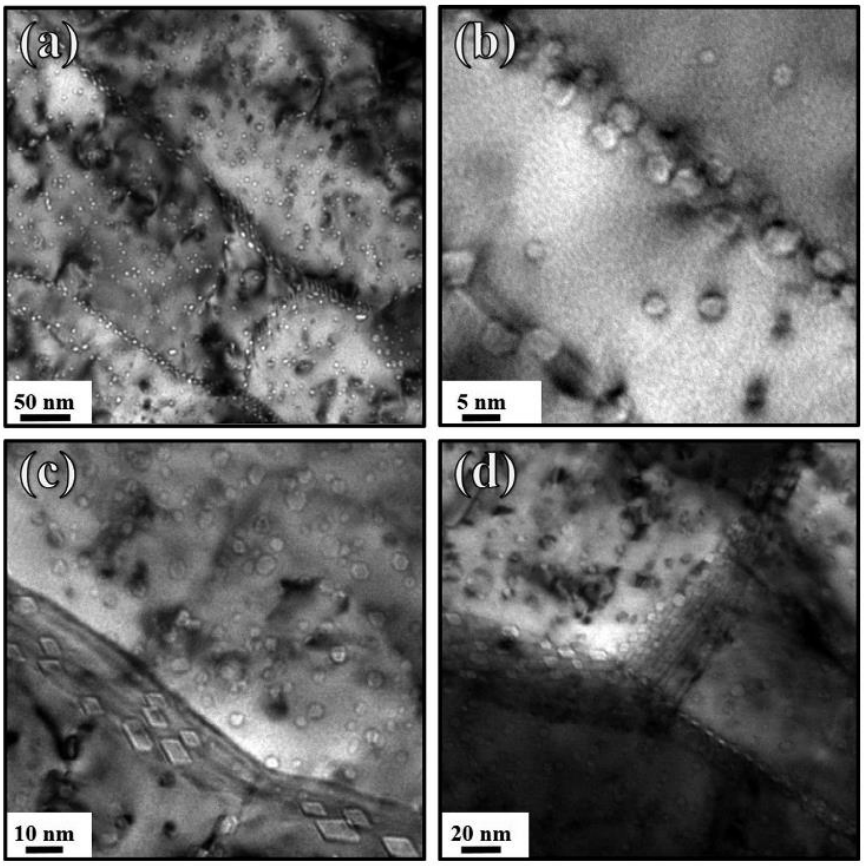

Figure 18 TEM micrographs of polycrystalline W irradiated at 1223 K with 2 keV He ions and a fluence of (a and b) 3.6×10^{19} m^{-2} and (c and d) 4.0×10^{20} m^{-2}. Facetted bubbles located at the grain boundaries are visible while bubbles inside grains remain spherical. Reproduced from ref. [64].

Huang et al. [113] have shown that taking into account the faceting of bubbles, the prediction of the equilibrium pressure inside the bubble can't be estimated by the Young-Laplace relation.

The temperature has been identified in ref. [114] as the driving parameter for the transition between spherical bubbles at low temperature and facetted bubbles at high temperature. The temperature threshold seems to be in the range 1073-1223 K. However, the clear identification of the facetted shape of bubbles in W is not an easy task. Until now, results are partially in disagreement due to a wide range of parameters (manufacturing parameters, polycrystalline material, large/low defect content, oxidized W surface, non-controlled atmosphere, different temperature…) which strongly limits the global interpretation of results.

Harrison et al. [115] have reported that He implantation at a temperature higher than the faceting threshold i.e. 1073 K and 1273 K, could form non facetted He-bubbles. However, {110} facets have been observed in polycrystalline W implanted and annealed up to 1273 K [116]. Similarly, Ialovega and co-workers [72] have proposed a 3D shape of bubbles composed exclusively of {110} facets after He implantation at 1073 K and annealing up to 1350 K. Finally, Bergstrom et al. [117] have compared in

details density functional theory (DFT) calculations and transmission electron microscopy (TEM) images of small bubbles (< 5 nm diameter) in a polycrystalline sample implanted at 1223 K. They have concluded that it is a more complex shape composed of {110}, {111}, {013} and {112} facets.
The differences among the literature results are probably inherent to different implantation conditions and to non-controlled parameters used for He implantation in W. The characterisation of the facetted shape of bubbles in W remains an open question that will be treated in Chapter 4.

2.4.3. Growth mechanism

The growth of bubbles is at the heart of the proposed mechanism for the fuzz formation. The temperature has shown to play an important role in the growth of bubbles. For example, Bernard et al. [99] have exposed identical W samples to the same He plasma in LHD meanwhile maintaining different temperatures from 338 K to 873 K. They have seen by TEM a strong increase of the mean radius of bubbles with a decrease of the bubble density for temperature higher than 723 K. This result is also a proof that bubble growth cannot be described only by agglomeration of He injected in the material. In this sense, increase of the bubbles size due to post-implantation annealing has been reported in ref. [116]. Two additional mechanisms have been proposed: migration-coalescence (MC) and Ostwald ripening (OR).

The growth of gas bubbles in metals have been intensively studied since the 60s because bubbles are responsible of swelling of metallic compounds under nuclear fission environment. Intense theoretical and experimental investigations have been pursued to determine which of migration-coalescence and Ostwald ripening is the governing mechanism.

Migration coalescence

Barnes and Mazey [118] have first observed the migration and coalescence of bubbles in copper by transmission electron microscopy (TEM) in presence of a temperature gradient. Intense theoretical work [119–122] has then been perused to address the motion of bubbles observed by Barnes and Mazey.
Other experimental investigations in different metals like in uranium dioxide (UO2) [123] or in aluminium [124] have shown direct evidence for the Brownian motion of gas bubbles in absence of external forces (such as created by a thermal gradient).

A great synthesis of the theoretical descriptions of the motion of gas bubbles in metals with and without external forces has been published by Nichols [125]. In brief, the migration of a bubble requires the displacement of the surrounding metal atoms. Three different elementary processes have been considered to address this motion:

i) The surface diffusion process by which metal atoms diffuse on the bubble surface.

ii) The volume diffusion process, where atoms diffuse through the metal matrix around the bubble.
iii) The vapour diffusion process that consists in the sublimation of atoms at one side of the bubble and the condensation at the opposite side

Figure 19 shows a schematic representation of such processes.

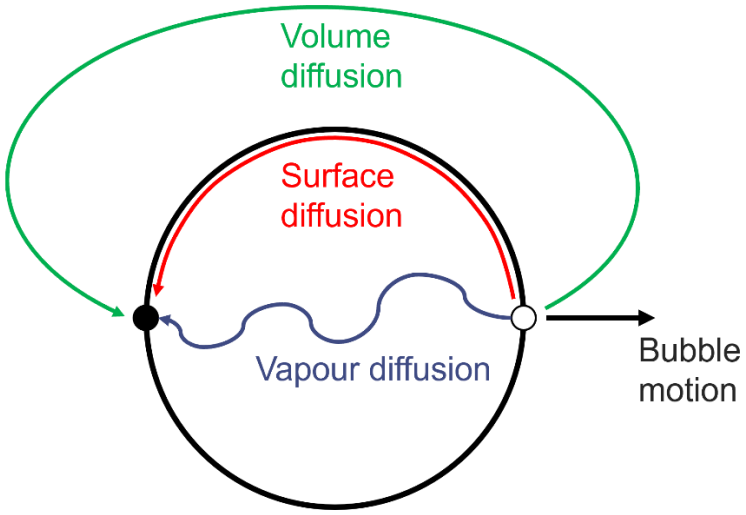

Figure 19:Schematic representation of different elementary processes for the motion of a bubble.

However, as observed by Willertz and Shewmon [126] in gold, the motion of faceted bubbles is much slower than predicted by those processes. Similar observations by Oldfield and Brown in UO2 and Goodhew and Tyler in vanadium [127] in zirconium (Zr) and in niobium-zirconium alloy [128]. In this case, an additional diffusion process should be considered: iv) the ledge nucleation limited diffusion [126,129] where the limiting step is the nucleation of an ad-vacancy nucleus on the bubble facet. Let us note that at the operating temperature of ITER (1273 K) the bubbles in W are also expected to develop facets [72,114,116,117].

Ostwald Ripening

The second proposed mechanism for bubble growth is Ostwald ripening (OR). It consists in a flux of He atoms from small bubbles towards larger bubbles. The driving force arises from the reduction of the free energy of the gas in larger bubbles. Greenwood and Boltax have derived a theoretical description of this process [130].

Both mechanisms have been observed by Schroeder *et al.* [131] in steels. The temperature seems to be the key parameter leading to a transition between MC at low temperature and OR at high temperature has been reported [132]. In steels again, more recently Cui *et al.* [133] has observed both mechanisms simultaneously.

In W, only coalescence has been observed experimentally at 1273 K by in situ TEM [134]. In this sense, kinetic Monte Carlo (KMC) simulations integrating the MC mechanism, it has been shown that, between 1003 K and 1433 K, bubbles migrate, burst at the surface and leave holes [70]. In addition, Molecular dynamic simulations have shown that single He atoms can escape from He-clusters only when the temperature reaches 2000 K [85] or 2100 K [78] suggesting that the OR mechanism is suppressed below this temperature.
However, Teo *et al.* [135] have found for polycrystalline W exposed to 20 eV He plasma at 573 K and 1073 K that OR seems to be the mechanism underlying the bubbles growth during post-implantation annealing up to 998 K since no bubble motion has been seen by TEM. Unfortunately, the shrinkage of bubbles has not been observed neither, leaving the results questionable.

The growing mechanism of bubbles in W is thus still unclear and will be treated Chapter 5.

3. Experimental techniques

3.1. Preamble 71

3.2. GISAXS : Grazing Incidence Small Angle X-Ray Scattering 73
3.2.1. Practical elements 73
3.2.2. The principle 80
3.2.3. ESRF – BM32 – INS2 99

3.3. Sample preparation 101
3.3.1. Samples characteristics 101
3.3.2. Preparation of clean W crystal 102

3.4. Transmission electron microscopy 106
3.4.1. Thin lamella preparation 106
3.4.2. Bubble characterisation 108

3.5. Overview of the experimental conditions 114

This chapter is dedicated to the presentation of the experimental principle and set-up used in this study. The reasons for choosing an approach combining microscopy and X-ray techniques are first given in a preamble.

Then, the first section will focus on the GISAXS technique. Theoretical foundations of the X-ray scattering in grazing incidence geometry are provided in order to give all elements required to analyse an experimental GISAXS pattern. The INS2 set-up of the BM32 beamline of the European synchrotron radiation facility (ESRF) in Grenoble has been used to perform all the GISAXS measurements. The set-up is presented.

The second section describes the sample preparation required prior GISAXS experiments. Detailed about the samples will be given and the preparation protocol for GISAXS experiments is described.

The third section focuses on TEM technique. After describing the protocol to prepare samples to TEM analysis, a brief introduction to the microscope structure and to the principle are provided. The specificity of the bubble observation is then given in order to observe small bubbles down to 1 nm in diameter.

Finally, the last section presents an overview of the different experiments performed during this thesis.

3.1. Preamble

Characterization of nano-size objects or interfaces are usually performed by electron microscopy as transmission electron microscopy (TEM) and scanning electron microscopy (SEM) or by near field microscopy as atomic force microscopy (AFM). Those techniques provide direct observations in real space and a specific characterization on selected areas is possible. Nevertheless, some limitations exist. For AFM and SEM, the analysis is restricted to the surface and the characterization of buried objects as He bubbles is impossible. For TEM, the technique is limited by the small-probed volume, which yields to low statistics and challenging questions on the homogeneity in the whole samples and therefore pertinence of observed phenomena. In addition, making different lamellas is a time-demanding task. At last, measurements are generally performed as post-mortem characterization giving access only to the final state and after a heavy sample preparation process, which can induce modifications in the material, as it will be seen in section 3.3.1.
The use of X-ray techniques can overcome those limitations. Especially, grazing incidence small angle X-ray scattering (GISAXS) offers many advantages for the observation of buried bubbles, for example:

i) The technique is non-destructive neither perturbative.
ii) The grazing incidence offers a high sensitivity to the bubbles zone located a few nanometers below the sample surface.
iii) The measurement is sensitive to the morphology, i.e. the shape and the size of the bubbles.
iv) The technique probes a large area, typically several dozens of millimeters square that gives statistical information.
v) The dynamics of bubbles growth can be recorded by in-situ or in-operando measurements, i.e. in real time during annealing or He implantation.

The main drawbacks of GISAXS technique are:

i) The necessary use of a synchrotron radiation source to collect enough signal from the small amount of probed matter.
ii) Information is collected in the reciprocal space and must be transposed to the real space by modelling.
iii) Focus on a specific area in the sample e.g. a specific grain boundary or a group of bubbles is not possible due to the large beam size.

The GISAXS technique is a very powerful tool by its non-destructive and non-perturbative aspects. In addition, the in-operando measuring capabilities make the GISAXS technique particularly suitable for the characterization of bubbles and their evolution in real time during He irradiation. Likewise, microscopy techniques such as TEM, providing direct images of bubbles, are great complementary tools to help in the interpretation of the GISAXS data.

Thus, in this work, both “classical” (electron and near field microscopies) and GISAXS techniques have been used for their complementarity.

3.2. GISAXS : Grazing Incidence Small Angle X-Ray Scattering

The GISAXS principle will be theoretically described in the sub-section 3.2.2, however, the mathematical formalism required is heavy. For a reader not interested in understanding the fundamental aspects of the GISAXS technique, a brief overview of the key points required to interpret GISAXS measurements is given in the sub-section 3.2.1. The final sub-section is focused on presenting the experimental set-up.

3.2.1. Practical elements

This section aims at summarising the practical elements that must be kept in mind for the interpretation of GISAXS measurements.

GISAXS geometry

The GISAXS geometry is presented in Figure 20.

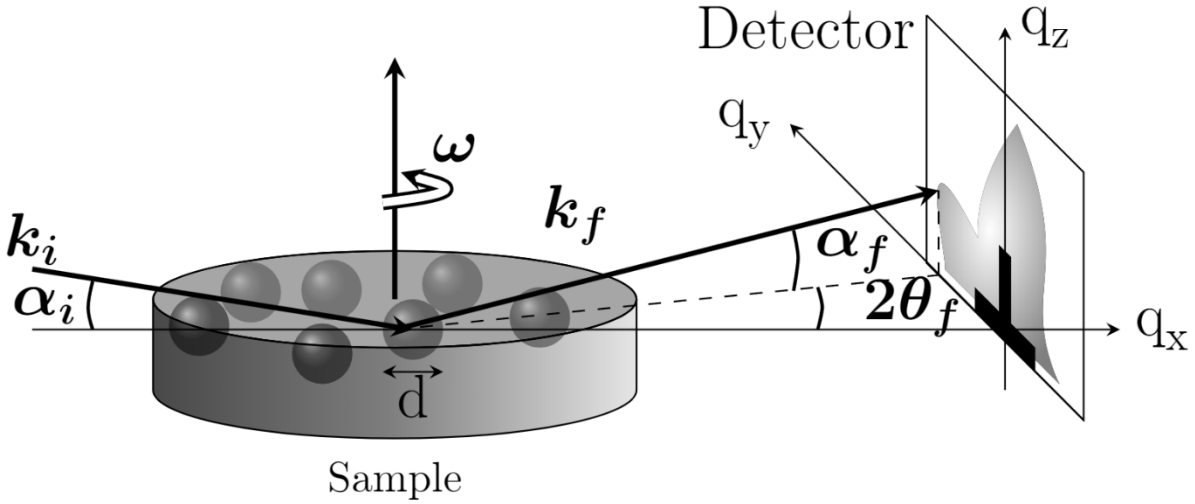

Figure 20: GISAXS geometry. $\boldsymbol{k_i}$ and $\boldsymbol{k_f}$ are the incident and scattered wave vectors. The angles α_i and α_f are the incident and exit out-of-plane angles. The in-plane exit angle is $2\theta_f$ and the angle ω is the sample azimuthal angle. A T-shaped beam stop is placed between the sample and the 2D detector to hide the direct and reflected X-ray beams to prevent the degradation of the detector.

The angle convention for the GISAXS technique is to define angles with respect to the sample surface plane. Angles in GISAXS geometry are small, the incident angles of the X-ray beam with respect to the analysed surface α_i is generally below 1° and the exit angles α_f (out-of-plane) and $2\theta_f$ (in-plane) are in the range of only few degrees.
The X-ray scattering at small angles is fully elastic thus, the incident and scattered wave vectors modulus are conserved, $|k_i| = |k_f| = k_0 = \frac{2\pi}{\lambda}$, where λ is the x-ray

wavelength. The wave vector transfer is defined as: $\boldsymbol{q} = \boldsymbol{k_f} - \boldsymbol{k_i}$ and its coordinates can be expressed using the incident and exit angles as:

$$q_x = k_0\left[\cos\left(2\theta_f\right)\cos\left(\alpha_f\right) - \cos(\alpha_i)\right] \quad (9)$$

$$q_y = k_0 \sin\left(2\theta_f\right)\cos\left(\alpha_f\right) \quad (10)$$

$$q_z = k_0\left[\sin(\alpha_i) + \sin\left(\alpha_f\right)\right] \quad (11)$$

The refractive index n of X-rays is expressed as:

$$n = 1 - \delta - i\beta \quad (12)$$

where δ is related to the dispersion of X-rays and is β related to the absorption of x-rays by the medium.

The real part of n is lower than 1 which can conduct to total external reflexion of the incident beam (see the scheme in the bottom right of Figure 21). Indeed, the Snell-Descartes law that relates the incident angle α_i to the transmitted angle α_t within the GISAXS angles convention is:

$$\cos(\alpha_i) = Re(n)cos(\alpha_t)$$

Considering that the incident angle α_i and the transmitted angle α_t are small ($\alpha_{i,t}$ <<1), we can expand the cosines (neglecting absorption) as:

$$1 - \frac{\alpha_i^2}{2} = (1 - \delta)(1 - \frac{\alpha_t^2}{2})$$

So:

$$\frac{1 - \frac{\alpha_i^2}{2}}{1 - \frac{\alpha_t^2}{2}} < 1$$

Hence:

$$\alpha_i > \alpha_t$$

The Figure 21 represents a scheme of the beam path depending on the value of the refractive index.

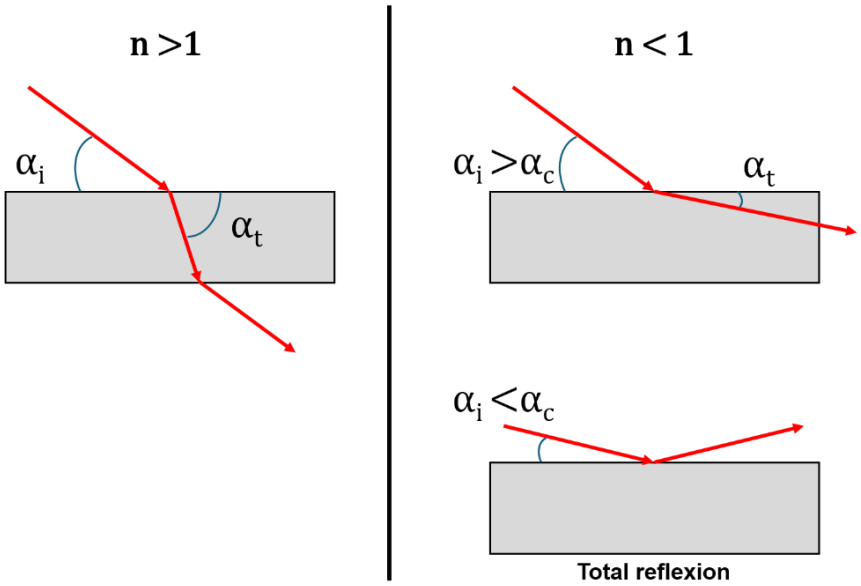

Figure 21: Beam path in a medium with a refractive index higher than unity (left) and lower than unity (right). The particular case of total X-ray reflexion is represented in bottom right.

The total external reflexion occurs when α_i is lower than a critical angle given by:

$$\alpha_c = \sqrt{2\delta} \tag{13}$$

δ and β (and so α_c) depend on the material and the X-ray wavelength (i.e. energy) used. The values of δ and β for many materials and wavelength are available using online databases [136]. For example, in Table 3 is shown δ, β and α_c for 10 keV and 18 keV X-ray energies (used in this study) in W.

X-ray energy	δ	β	$\alpha_c = \sqrt{2\delta}$
10 keV ($\lambda = 0.124\ nm$)	2.79×10^{-5}	1.78×10^{-6}	0.43°
18 keV ($\lambda = 0.068\ nm$)	9.88×10^{-6}	8.65×10^{-7}	0.26°

Table 3: Optical properties of W for 10 and 18 keV X-ray energies.

The penetration depth of X-ray in a material can be tuned by varying the incident angle, the penetration depth of X-ray is given by the expression:

$$\Lambda(\alpha_i) = -\frac{1}{2k_0 Im\left(\sqrt{\alpha_i^2 - \alpha_c^2 - 2i\beta}\right)} \tag{14}$$

The graph in Figure 22 shows the evolution of the penetration depth of X-ray for an incident angle up to 1.0°. For both X-ray energies, the penetration depth below the critical angle (vertical dashed line on Figure 22) is in the order of one nanometer, then

a net increase of the penetration depth is visible when the incident angle reaches the critical angle and the penetration of X-ray can reach few dozens of nanometers.

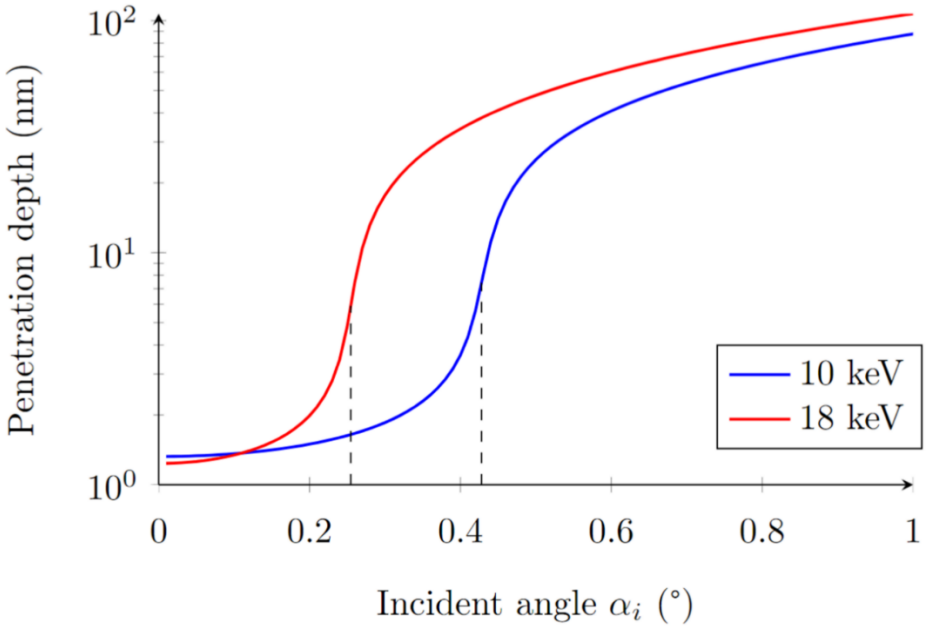

Figure 22: Penetration depth of X-ray in W for 10 keV (blue) and 18 keV (red) X-ray energy. Vertical dashed lines represent the depth at the critical angle.

GISAXS pattern

The GISAXS signal results from the variations of the electronic density in the material. In our case, the GISAXS signal arises from the local drop of the electronic density inside the He-bubbles with respect to the W-matrix. The main advantage of the GISAXS technique is to probe the shape and size of nano-objects.

For buried objects, as buried He-bubbles, the GISAXS intensity should be theoretically described by the distorted wave born approximation (DWBA). The DWBA, contrary to the simpler Born approximation (BA), considers multiple reflection or refraction events of the incident and scattered waves. Indeed, at very low angles used in GISAXS geometry, phenomenon of refraction and reflexion of X-rays at the material surface are significant and cannot be neglected. In the framework of the DWBA, the GISAXS intensity arising from a buried object such as a He-bubble is:

$$I(\boldsymbol{q}) \propto |t_i|^2 \left|t_f\right|^2 |F(\boldsymbol{q})|^2 e^{\frac{z_0}{\Lambda}} \quad (15)$$

The terms $|t_i|^2$ and $\left|t_f\right|^2$ are the Fresnel transmission coefficients in intensity for the incident and exit X-ray beam, $F(\boldsymbol{q})$ is the form factor of the buried bubble and $e^{\frac{z_0}{\Lambda}}$ an attenuation term due to the absorption of X-ray by the medium.

The form factor is defined as the Fourier transform of the bubble shape:

$$F(\boldsymbol{q}) = \int_{bubble} d\boldsymbol{r}\, e^{i\boldsymbol{q}\cdot\boldsymbol{r}}$$

For simple geometrical shapes the form factor can be found in ref. [137].

The Figure 23 shows simulated GISAXS patterns for monodisperse spheres with radius $R = 4$ nm (Figure 23a) and square based pyramids with base side $2R = 8$ nm and the angle between faces and the base equal to 45°. For anisotropic shapes as pyramids, scattering differs with respect to the X-ray beam orientation. As example, X-rays are aligned along either a face (Figure 23b) or an edge (Figure 23c) of the pyramids.

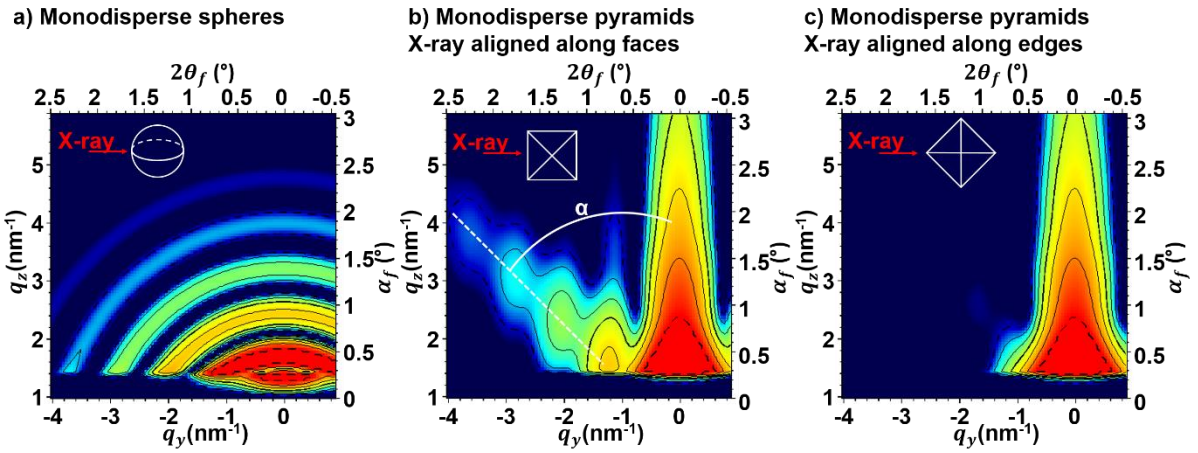

Figure 23: Simulated GISAXS patterns within the DWBA of monodisperse spheres with radius $R = 4$ nm (a) and square based pyramids (b and c) with side $2R = 8$ nm and α the angle between faces and the base. Objects are located 10 nm below the surface and probe by 18 keV X-rays with an incident angle $\alpha_i = 0.6°$. The incident X-ray beam is aligned along a face (b) or an edge (c) of pyramids.

For spheres, the pattern is composed of successive zero and non-zero intensity rings centred at the reciprocal space origin. The intensity of the non-zero rings decreases with the distance to the origin. For pyramids, an elongated vertical lobe is visible with a continuous decrease in intensity. In addition, for X-ray beam aligned along a face (Figure 23b), a lateral streak is visible at an angle of 45° corresponding to the angle between faces and the base of the pyramid. The lateral rod is less intense when the incident X-ray beam is aligned along the edges of the pyramids (Figure 23c).

For all GISAXS patterns, a horizontal line called the Yoneda peak located at $\alpha_f = \alpha_c$ ($= 0.26°$ in the example) is visible. At this line ($\alpha_f = \alpha_c$) the intensity presents a maximum (see for instance a slight deformation of the rings in Figure 23a) and below this line (i.e. $\alpha_f < \alpha_c$), a small intensity is transmitted.

Figure 24 shows the evolution of the transmission coefficients in intensity ($|t_i|^2$ and $|t_f|^2$) with respect to the incident or exit angles (α_i and α_f). The transmission coefficients in intensity can exceed 1 (up to 4 at the critical angle) giving rise to a net increase of the intensity at the critical angle (so called Yoneda peak) and below the critical angle the transmitted coefficients drop drastically to 0 since the incident and reflected beams interfere destructively.

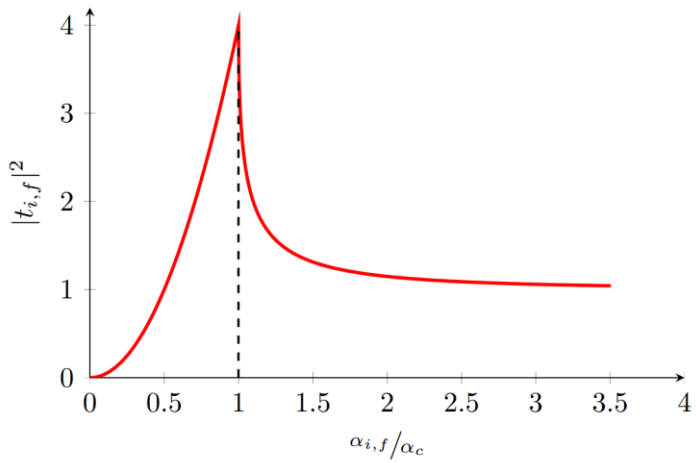

Figure 24: Incident or exit transmission coefficient (neglecting the absorption) in intensity as function of the incident or exit angle over the critical angle.

The size polydispersity of the objects also plays a role. Figure 25 shows simulated patterns for polydisperse spheres and pyramids according to a log normal distribution with geometric standard deviation $\sigma_g = 1.9$.

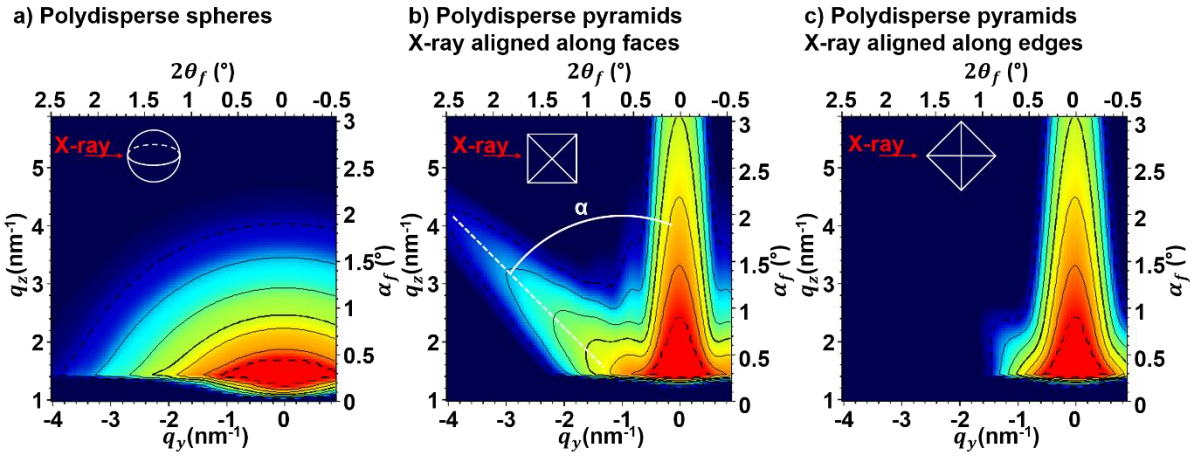

Figure 25: Simulated GISAXS patterns within the DWBA of polydisperse spheres with radius $R = 4$ nm (a) and square based pyramids (b and c) with side $2R = 8$ nm and α the angle between faces and the base. Objects are located 10 nm below the surface and probe by 18 keV X-rays with an incident angle $\alpha_i = 0.6°$. The incident X-ray beam is aligned along a face (b) or an edge (c) of pyramids.

The scattered intensity is smoothed by the polydispersity. For spheres (Figure 25a), the intensity gradually decreases, without discontinuous rings. The same effect is visible in the streak generated by the facets of pyramids (Figure 25b and c).

The last feature that worth to be mentioned is the existence on experimental patterns of an intense vertical rod called the specular rod localized at $q_y = 0$ nm^{-1}. The specular rod arises from the (specular) reflection of the X-ray on the sample surface. The specular rod is due to the out-of-plane profile of the electron density. An experimental pattern recorded on a sample before He implantation is shown in Figure 26.

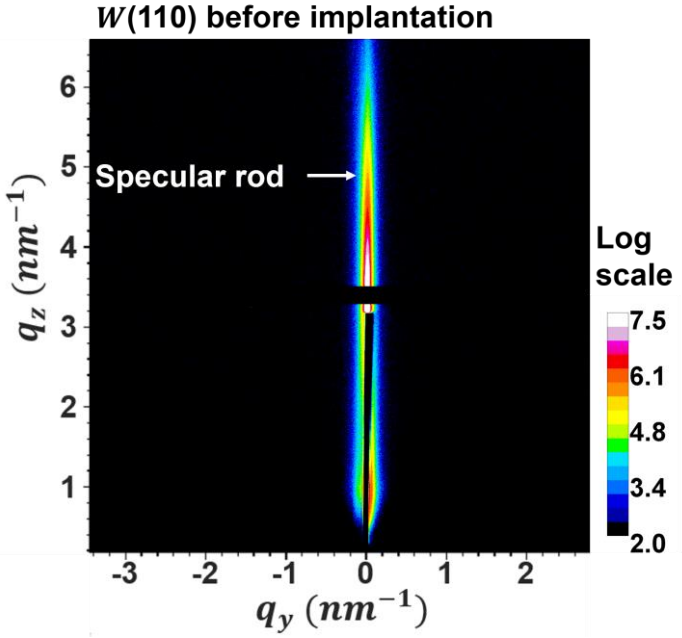

Figure 26: Typical GISAXS pattern of W single crystal just before He implantation. The vertical rod is due to the specular reflection of X-ray on the sample surface.

Qualitatively, the horizontal width of the specular rod is related to the surface roughness, the thinner the rod the flatter the surface.

3.2.2. The principle

In the following, theoretical concepts regarding the propagation of an electromagnetic wave will be presented. The aim of this section is to understand in depth the GISAXS theoretical framework in order to demonstrate the three features mentioned above: i) the specular rod, ii) the Yoneda peak and iii) the intensity dependence regarding the form factor, that is to say Eq.(15).

First, the propagation equations of an electromagnetic wave will be derived. Those concepts will allow us to define the Fresnel coefficients for the reflectivity and the transmission at a perfectly plane interface. Then, the Green formalism will be introduced and applied to solve the propagation equations. In the framework of the so-called Born approximation (BA) the GISAXS intensity will be derived and the presence of the specular rod will be proven.

Then, to treat the existence of the Yoneda peak, a correct evaluation of the transmitted and reflected waves in grazing incident geometry is required. To that ends, the distorted wave Born approximation (DWBA) which is an extension of the Born approximation (BA) will be presented. The DWBA takes into-account the multiple reflection-refraction events that can occur with grazing incidence.

Finally, in the framework of the DWBA, the GISAXS intensity for buried objects in a material will be derived and the exact formulation of Eq. (15) will be found.
Additional information on those concepts can be found in standard books [138–140] or in the review ref. [137].

X-ray propagation in 3D space

The theoretical principle of X-ray scattering is based on the electromagnetic wave propagation described by the Maxwell equations in absence of charges and currents:

$$\nabla \times \boldsymbol{E} = -\frac{\partial \boldsymbol{B}}{\partial t} \ (\mathrm{Maxwell-Faraday}) \tag{16}$$

$$\nabla \times \boldsymbol{H} = \frac{\partial \boldsymbol{D}}{\partial t} \ (\mathrm{Maxwell-Ampere}) \tag{17}$$

$$\nabla \cdot \boldsymbol{D} = 0 \ (\mathrm{Maxwell-Gauss}) \tag{18}$$

$$\nabla \cdot \boldsymbol{B} = 0 \ (\mathrm{Maxwell-Gauss\ for\ magnetism}) \tag{19}$$

Where $\boldsymbol{E}$ is the electric field, $\boldsymbol{H}$ the magnetic field, $\boldsymbol{D}$ the electric induction and $\boldsymbol{B}$ the magnetic induction.
$\boldsymbol{E}$ and $\boldsymbol{D}$ and $\boldsymbol{H}$ and $\boldsymbol{B}$ are related by the following relations:

$$\boldsymbol{E} = \varepsilon(\boldsymbol{r})\varepsilon_0 \boldsymbol{D} \qquad\qquad \boldsymbol{B} = \mu_0 \boldsymbol{H}$$

With $\varepsilon(\boldsymbol{r})$ the relative dielectric constant (also called permittivity) of the medium and ε_0 and μ_0, the dielectric and magnetic constant in vacuum respectively.

The propagation equations for $\boldsymbol{E}$ and $\boldsymbol{H}$ are derived by applying identities $\nabla \times \nabla \times \mathbf{F} = \nabla(\nabla \cdot \boldsymbol{F}) - \nabla^2 \boldsymbol{F}$ and $\nabla \cdot (a\boldsymbol{F}) = a\nabla \cdot \boldsymbol{F} + \nabla \mathrm{a} \times \boldsymbol{F}$ to the Maxwell-Faraday and Maxwell-Ampere laws (Eqs. (16)-(17)):

$$\nabla^2 \boldsymbol{E} - \epsilon_0 \mu_0 \epsilon(\boldsymbol{r}) \frac{\partial^2 \boldsymbol{E}}{\partial^2 t} = -\nabla(\nabla \ln(\varepsilon(\boldsymbol{r})) \cdot \boldsymbol{E}) \tag{20}$$

$$\nabla^2 \boldsymbol{H} - \epsilon_0 \mu_0 \epsilon(\boldsymbol{r}) \frac{\partial^2 \boldsymbol{H}}{\partial^2 t} = -\nabla \ln\big(\varepsilon(\boldsymbol{r})\big) \times (\nabla \times \boldsymbol{H}) \tag{21}$$

Since n can be defined as $n(\boldsymbol{r}) = \sqrt{\epsilon(\boldsymbol{r})}$ and is close to 1, the dielectric constant is also close to 1 and the term $\nabla \ln\big(\varepsilon(\boldsymbol{r})\big)$ becomes negligible. The Eqs. (20)-(21) can then be rewritten in the form of wave equations:

$$\nabla^2 \boldsymbol{E} - \epsilon_0 \mu_0 n^2(\boldsymbol{r}) \frac{\partial^2 \boldsymbol{E}}{\partial^2 t} = 0 \tag{22}$$

$$\nabla^2 \boldsymbol{H} - \epsilon_0 \mu_0 n^2(\boldsymbol{r}) \frac{\partial^2 \boldsymbol{H}}{\partial^2 t} = 0 \tag{23}$$

Thus, $\boldsymbol{E}$ and $\boldsymbol{H}$ must solve the same equation known as the 3D wave equation. The solution is in the form of a plane wave expressed as $\boldsymbol{A} = \boldsymbol{A_0} \exp(i\omega t - \boldsymbol{k} \cdot \boldsymbol{r})$, with $A = A_0 \exp(\mathrm{i}(\omega \mathrm{t} - \mathbf{k} \cdot \mathbf{r}))$ the related field amplitude, ω the angular frequency and $\boldsymbol{k}$ the wave vector.

With plane waves, some operators can be simplified:

$$\boldsymbol{\nabla^2 A} = -k^{\boldsymbol{2}} \boldsymbol{A} \text{ and } \frac{\partial^2 \boldsymbol{A}}{\partial^2 t} = -\omega^2 \boldsymbol{A}$$

Replacing in the wave equation:

$$-k^{\boldsymbol{2}} \boldsymbol{A} = -\epsilon_0 \mu_0 n^2(\boldsymbol{r}) \omega^2 \boldsymbol{A}$$

So k and ω must satisfy the following dispersion equation:

$$k = \sqrt{\epsilon_0 \mu_0} n(\boldsymbol{r}) \omega = \frac{n(\boldsymbol{r})}{c} \omega$$

Where, $c = \frac{1}{\sqrt{\epsilon_0 \mu_0}}$.

In addition, $\nabla \times \boldsymbol{A} = -\boldsymbol{ik} \times \boldsymbol{A}$ and $\frac{\boldsymbol{\partial A}}{\boldsymbol{\partial t}} = -\boldsymbol{i\omega A}$. Hence, rewriting the Maxwell-Faraday law (Eq. (16)):

$$-\boldsymbol{ik} \times \boldsymbol{E} = -\boldsymbol{i\omega B}$$

So,

$$\boldsymbol{B} = \frac{\boldsymbol{k} \times \boldsymbol{E}}{\boldsymbol{\omega}}$$

This implies that $\boldsymbol{B}$, $\boldsymbol{E}$, and $\boldsymbol{k}$ are orthogonal and the magnitude of the electric and magnetic fields are related by:

$$E = \frac{cB}{n(\boldsymbol{r})}$$

Especially in vacuum $n(\boldsymbol{r}) = 1$ so:

$$E = cB$$

Then, the wave equations (Eqs.(22)-(23)) can be rewritten in form of Helmholtz equations by replacing the second time derivative of A:

$$[\nabla^2 + \epsilon_0\mu_0\omega^2 n^2(\boldsymbol{r})]\boldsymbol{E} = \boldsymbol{0}$$
$$[\nabla^2 + \epsilon_0\mu_0\omega^2 n^2(\boldsymbol{r})]\boldsymbol{H} = \boldsymbol{0}$$

Finally, let us note $k_0^2 = \epsilon_0\mu_0\omega^2$ (dispersion relation in vacuum):

$$[\nabla^2 + k_0^2 n^2(\boldsymbol{r})]\boldsymbol{E} = \boldsymbol{0} \quad (24)$$
$$[\nabla^2 + k_0^2 n^2(\boldsymbol{r})]\boldsymbol{H} = \boldsymbol{0} \quad (25)$$

Propagation through an interface

To find a unique solution for the electric and magnetic fields, boundaries conditions are needed. Let us consider an interface between a medium 1 and a medium 2 with electromagnetic fields $\boldsymbol{E_1}, \boldsymbol{H_1}$ in the medium 1 and $\boldsymbol{E_2}, \boldsymbol{H_2}$ in the medium 2. The situation is represented in Figure 27 for the electric field. The case of the magnetic field is analogous.

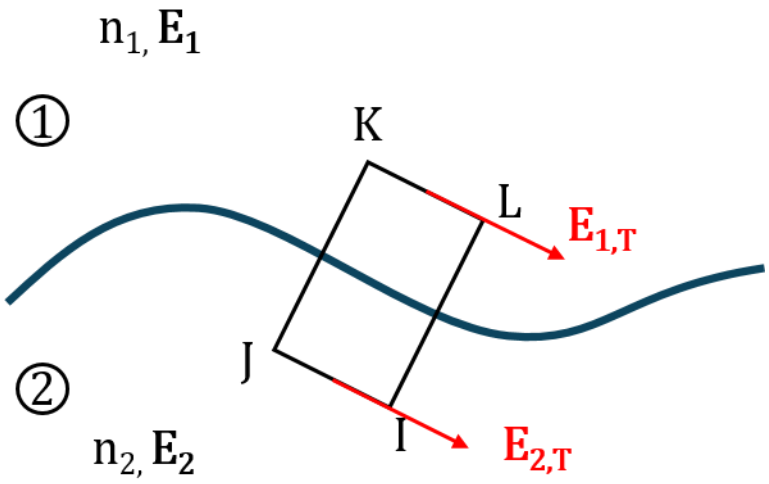

Figure 27: Schematic representation of the considered geometry in order to determine the boundary conditions of the electromagnetic field. The two medium 1 and 2 are characterized with their refractive index n_1 and n_2. The electric field in the medium 1 is $\boldsymbol{E_1}$ and in the medium 2 is $\boldsymbol{E_2}$, the red arrow represents the tangential component $\boldsymbol{E_{1,T}}$ and $\boldsymbol{E_{2,T}}$ in respect to the interface of the electric fields. The loop IJKL define the integration domain for the contour integral and the surface integral.

From Maxwell-Faraday and Maxwell-Ampere equations, the integral on the closed loop IJKL across the interface is:

$$\oint \boldsymbol{E}\cdot d\boldsymbol{l} = \iint \nabla\times\boldsymbol{E}\cdot d\boldsymbol{S} = \iint -\frac{\partial \boldsymbol{B}}{\partial t}\cdot d\boldsymbol{S} = -\frac{\partial}{\partial t}\iint \boldsymbol{B}\cdot d\boldsymbol{S}$$
$$\oint \boldsymbol{H}\cdot d\boldsymbol{l} = \iint \nabla\times\boldsymbol{H}\cdot d\boldsymbol{S} = \iint \frac{\partial \boldsymbol{D}}{\partial t}\cdot d\boldsymbol{S} = \frac{\partial}{\partial t}\iint \boldsymbol{D}\cdot d\boldsymbol{S}$$

When the height of the rectangular contour LI tends to vanish (i.e. $LI \to 0$), the surfaces integrals tend to zero and only the parts of the line integrals parallel to the interface remain:

$$\oint \boldsymbol{E} \cdot d\boldsymbol{l} = \boldsymbol{E} \cdot \boldsymbol{KL} + \boldsymbol{E} \cdot \boldsymbol{IJ} = E_{1,T} \cdot KL + E_{2,T} \cdot IJ = (E_{2,T} - E_{1,T})IJ = 0$$

$$\oint \boldsymbol{H} \cdot d\boldsymbol{l} = \boldsymbol{H} \cdot \boldsymbol{KL} + \boldsymbol{H} \cdot \boldsymbol{IJ} = H_{1,T} \cdot KL + H_{2,T} \cdot IJ = (H_{2,T} - H_{1,T})IJ = 0$$

Where $A_{i,T}$ is the tangential component in respect to the interface of $\boldsymbol{A}$ in the medium i.

Hence, the tangential components of the electric and magnetic fields are continuous across the interface:

$$E_{2,T} = E_{1,T} \quad (26)$$

$$H_{2,T} = H_{1,T} \quad (27)$$

To simplify the problem, we can use the fact that any wave can be decomposed in s and p-polarized waves. The electric field of s-polarized waves, and the magnetic field of p-polarized waves propagating in the (xOz) plane are aligned along the y axis (i.e $E_x = E_z = 0$ for s-polarized waves and $H_x = H_z = 0$ for p-polarized waves).

The Helmholtz equations (Eqs.(24)-(25)) are then reduced to scalar equations:

$$[\nabla^2 + k_0^2 n^2(\boldsymbol{r})]E_y = 0 \text{ for s-polarized waves} \quad (28)$$

$$[\nabla^2 + k_0^2 n^2(r)]H_y = 0 \text{ for p-polarized waves} \quad (29)$$

With s-polarized waves:

$$\nabla \times \boldsymbol{E} = -\frac{\partial E_y}{\partial z}\boldsymbol{e_x}$$

According to the Maxwell-Faraday law (Eq.(16)):

$$-\frac{\partial E_y}{\partial z}\boldsymbol{e_x} = -\mu_0 \frac{\partial \boldsymbol{H}}{\partial t} = -i\mu_0 \omega \boldsymbol{H}$$

So:

$$H_x = \frac{1}{i\mu_0 \omega}\frac{\partial E_y}{\partial z} \quad (30)$$

It implies that the tangential component of the derivative of the electric field is also continuous.

Similar demonstration for a p-polarized wave with the Maxwell-Ampere law (Eq.(17)) gives:

$$E_x = -\frac{1}{i\epsilon_0 \epsilon(\boldsymbol{r})\omega}\frac{\partial H_y}{\partial z} \quad (31)$$

It is worth noting that for both s and p-polarized waves a relation between $\boldsymbol{E}$ and $\boldsymbol{H}$ has been found which means that the propagation of X-ray wavefields can be describe only by one Helmoltz equation (Eq.(28) or Eq.(29)).

Reflexion and transmission coefficients: Fresnel coefficients

From the previous discussions, the Helmholtz equations have been derived and the solution is in the form of plane waves. The complexity of the vectorial problem has been reduced to a scalar problem by considering s and p polarized waves. The boundary conditions i.e. the continuity of the electric and magnetic fields and their derivatives regarding the normal of the interface have been established to determine the unique solution of the problem.

So the system is the following: in the medium 1, the wave field is composed of the incident wave marked with the subscript “i” and the reflected wave with the index “r”. In the medium 2 the wave field is only the transmitted wave noted with the subscript “t”. The transmitted wave is assumed to be completely absorbed in the medium 2 and will not be reflected in the direction to the interface. The situation is represented in Figure 28.

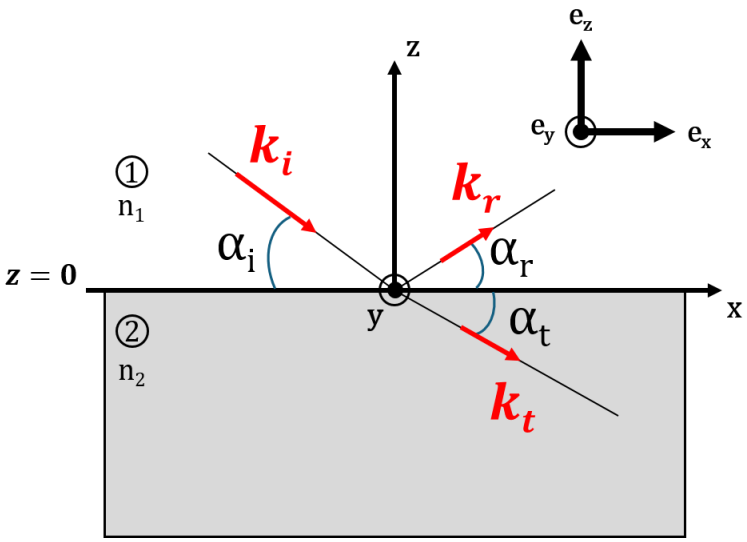

Figure 28: Schematic representation of the Fresnel system composed of a medium 1 with the refractive index n_1 and a medium 2 with the refractive index n_2. The interface between medium 1 and 2 is in the plane (xOy) and located at $z = 0$. The incident wave vector is $\boldsymbol{k_i}$ with the incident angle α_i, the reflected wave vector and angle are marked with the subscribe “r” and the transmitted ones are noted with a “t”.

The three different waves are then described by $\boldsymbol{A_\gamma} = A_{0,\gamma} e^{i(\omega_\gamma t - \boldsymbol{k_\gamma}\cdot\boldsymbol{r})}\boldsymbol{e_y}$ where γ is for “i", “r” or “t”. Let us notice that by construction of the coordinate system, the y component of the incident wave vector is null: $k_{i,y} = 0$.

At the interface ($z = 0$), the continuity of $\boldsymbol{A}$ (Eqs.(26)-(27)) means:

$$A_{0,i}e^{i\omega_i t}e^{-ik_{i,x}x} + A_{0,r}e^{i\omega_r t}e^{-ik_{r,x}x}e^{-ik_{r,y}y} = A_{0,t}e^{i\omega_t t}e^{-ik_{t,x}x}e^{-ik_{t,y}y} \quad (32)$$

This relation is true at any time and for all (x, y) points on the interface, in particular at $t = 0$ and $x = y = 0$ it gives:

$$A_{0,i} + A_{0,r} = A_{0,t} \quad (33)$$

For $t \neq 0$ and $x = y = 0$:

$$A_{0,i}e^{i\omega_i t} + A_{0,r}e^{i\omega_r t} = A_{0,t}e^{i\omega_t t}$$

And by replacing $A_{0,t}$ (Eq. (33)):

$$A_{0,i}e^{i(\omega_i-\omega_t)t} + A_{0,r}e^{i(\omega_r-\omega_t)t} = A_{0,i} + A_{0,r}$$

Which leads to the conservation of the frequency:

$$\omega_i = \omega_t = \omega_r = \omega \quad (34)$$

From this point, the time dependence of the waves amplitude will be removed by considering $t = 0$ as the Helmholtz equations (Eqs. (24)-(25)) to be solved are purely equations in space.

Similarly, for $x = 0$, it leads to the relation $k_{i,y} = k_{r,y} = k_{t,y} = 0$ which means that the reflected and the transmitted waves propagate also in the incident plane.
And for $y = 0$, the relation $k_{i,x} = k_{r,x} = k_{t,x}$ is obtained.

Using the definition of the wavevectors, it ends-up that:

$$k_{i,x} = \frac{n_1\omega}{c}\cos(\alpha_i) = \frac{n_1\omega}{c}\cos(\alpha_r) = k_{r,x}$$

So:

$$\alpha_i = \alpha_r \quad (35)$$

And with the incident and transmitted wavevectors:

$$k_{i,x} = \frac{n_1\omega}{c}\cos(\alpha_i) = \frac{n_2\omega}{c}\cos(\alpha_t) = k_{t,x}$$

The Snell-Descartes law is derived:

$$n_1\cos(\alpha_i) = n_2\cos(\alpha_t) \quad (36)$$

The continuity of the first derivative at the interface (Eqs.(30)-(31)) gives:

$$A_{0,i}\mathrm{n}_1\sin(\alpha_i)\,e^{-ik_{i,x}x} - A_{0,r}\mathrm{n}_1\sin(\alpha_r)\,e^{-ik_{r,x}x} = A_{0,t}\mathrm{n}_2\sin(\alpha_t)e^{-ik_{t,x}x}$$

For $x = 0$:

$$A_{0,i}\,\mathrm{n}_1\sin(\alpha_i) - A_{0,r}n_1\sin(\alpha_r) = A_{0,t}\mathrm{n}_2\sin(\alpha_t)$$

The Fresnel coefficients in amplitude are defined as $r = \frac{A_{0,r}}{A_{0,i}}$ and $t = \frac{A_{0,t}}{A_{0,i}}$ which can then be written:

$$r = \frac{n_1\sin(\alpha_i) - n_2\sin(\alpha_t)}{n_1\sin(\alpha_i) + n_2\sin(\alpha_t)} = \frac{n_1\mathrm{k_{i,z}} - n_2\mathrm{k_{t,z}}}{n_1\mathrm{k_{i,z}} + n_2\mathrm{k_{t,z}}} \quad (37)$$

$$t = 1 + r = \frac{2n_1 \sin(\alpha_i)}{n_1 \sin(\alpha_i) + n_2 \sin(\alpha_t)} = \frac{2n_1 \mathrm{k_{i,z}}}{n_1 \mathrm{k_{i,z}} + n_2 \mathrm{k}_{t,z}} \quad (38)$$

In the following, the Fresnel wavefield will refer to this known system with the amplitude of the wavefield expressed as:

$$A(\boldsymbol{r}, \boldsymbol{k}) = A_0 e^{-ik_x x} e^{-ik_y y} \begin{cases} e^{-ik_{0,z} z} + r e^{ik_{0,z} z} & \text{for } z > 0 \\ t e^{-ik_{1,z} z} & \text{for } z < 0 \end{cases} \quad (39)$$

Where $k_i = \frac{n_i \omega}{c} = n_i k_0$.

The penetration depth of X-ray (Eq. (14)) can be derived by considering the amplitude of the transmitted wave out of the interface:

$$tA_0 e^{-ik_x x} e^{-ik_y y} e^{-ik_{1,z} z} = tA_0 e^{-in_2 k_o \cos(\alpha_t) x} e^{in_2 k_0 \sin(\alpha_t) z}$$

and for $x = 0$:

$$tA_0 e^{in_2 k_0 \sin(\alpha_t) z} \approx tA_0 e^{in_2 k_0 \alpha_t z}$$

.

However, according to the Snell's law (Eq. (36)):

$$n_1 \cos(\alpha_i) = n_2 \cos(\alpha_t)$$

Let's consider the medium 1 as vacuum ($n_1 = 1$), and note $n_2 = n = 1 - \delta - i\beta$ for X-rays. With small angles we can expand the cosines as:

$$1 - \frac{\alpha_i^2}{2} = n\left(1 - \frac{\alpha_t^2}{2}\right) = (1 - \delta - i\beta)\left(1 - \frac{\alpha_t^2}{2}\right)$$

As $\delta, \beta \ll 1$ (see example in Table 3) then $\delta\alpha_t^2$ and $\beta\alpha_t^2$ are negligible and:

$$\alpha_t^2 = \alpha_i^2 - \alpha_c^2 - 2i\beta$$

So:

$$n\alpha_t \approx \alpha_t \approx \sqrt{\alpha_i^2 - \alpha_c^2 - 2i\beta}$$

Hence: $n\alpha_t$ is a complex number that can be written in the form $n\alpha_t = Re(n\alpha_t) + iIm(n\alpha_t)$, thus the transmitted wave amplitude is:

$$tA_0 e^{ik_0 Re(n\alpha_t) z} e^{-k_0 Im(n\alpha_t) z} \quad (40)$$

Finally, the intensity of the transmitted wave in the z direction is given as:

$$\left| tA_0 e^{ik_0 Re(n\alpha_t) z} e^{-k_0 Im(n\alpha_t) z} \right|^2 = t^2 A_0^2 e^{-2k_0 Im(n\alpha_t) z}$$

Which means that the intensity of the transmitted wave decreases exponentially as the wave propagates in the material.

The penetration depth $\Lambda(\alpha_i)$ is defined as the depth where the intensity drops by $1/e$ that finally leads to Eq. (14):

$$\Lambda(\alpha_i) = -\frac{1}{2k_0 Im(n\alpha_t)} = -\frac{1}{2k_0 Im\left(\sqrt{\alpha_i^2 - \alpha_c^2 - 2i\beta}\right)} \quad (41)$$

All the previous formalism provides a rigorous treatment of reflected and transmitted waves through a perfect planar interface. The GISAXS signal arises from a perturbation of this ideal interface.

Green formalism

The GISAXS signal arises from a variation of the dielectric constant. The perturbation of the dielectric constant can be considered by replacing $n^2(\boldsymbol{r})$ by $n^2(\boldsymbol{r}) = n_0^2(\boldsymbol{r}) + \delta n^2(\boldsymbol{r})$ where $n_0(\boldsymbol{r})$ is the refractive index of the medium without perturbation and $\delta n(\boldsymbol{r})$ the perturbation of the refractive index. In the following, the demonstration is restricted to the electric field and analogous demonstration is valid for the magnetic field. The propagation equation is thus:

$$[\nabla^2 + k_0^2 n_0^2(\boldsymbol{r})]\boldsymbol{E}(\boldsymbol{r}) = \delta n^2(\boldsymbol{r}) k_0^2 \boldsymbol{E}(\boldsymbol{r}) \quad (42)$$

The solution of this differential equation is of form $\boldsymbol{E}(\boldsymbol{r}) = \boldsymbol{E}_0(\boldsymbol{r}) + \delta\boldsymbol{E}(\boldsymbol{r})$ with $\boldsymbol{E}_0(\boldsymbol{r})$ the solution in absence of perturbation and $\delta\boldsymbol{E}(\boldsymbol{r})$ the variation of the electric field caused by the perturbation of the refractive index.

The Green formalism can be used to write $\delta\boldsymbol{E}(\boldsymbol{r})$:

$$\delta\boldsymbol{E}(\boldsymbol{r}) = \int \boldsymbol{dr'}\, \boldsymbol{G}(\boldsymbol{r} - \boldsymbol{r'})\delta n^2(\boldsymbol{r'})\boldsymbol{E}(\boldsymbol{r'})$$

With $\boldsymbol{G}(\boldsymbol{r})$ the Green function defined by:

$$[\nabla^2 + k_0^2 n_0^2(\boldsymbol{r})]\boldsymbol{G}(\boldsymbol{r}) = \delta(\boldsymbol{r}) k_0^2$$

$\boldsymbol{E}(\boldsymbol{r}) = \boldsymbol{E}_0(\boldsymbol{r}) + \int \boldsymbol{dr'}\, \boldsymbol{G}(\boldsymbol{r} - \boldsymbol{r'})\delta n^2(\boldsymbol{r'})\boldsymbol{E}(\boldsymbol{r'})$ is hence a solution of the propagation equation. Indeed, by injecting $\boldsymbol{E}(\boldsymbol{r})$ in the propagation equation:

$$\begin{aligned}
&[\nabla^2 + k_0^2 n_0^2(\boldsymbol{r})]\boldsymbol{E}_0(\boldsymbol{r}) + [\nabla^2 + k_0^2 n_0^2(\boldsymbol{r})] \int \boldsymbol{dr'}\, \boldsymbol{G}(\boldsymbol{r} - \boldsymbol{r'})\delta n^2(\boldsymbol{r'})\boldsymbol{E}(\boldsymbol{r'}) \\
&= 0 + \int \boldsymbol{dr'}\, [\nabla^2 + k_0^2 n_0^2(\boldsymbol{r})]\boldsymbol{G}(\boldsymbol{r} - \boldsymbol{r'})\delta n^2(\boldsymbol{r'})\boldsymbol{E}(\boldsymbol{r'}) \\
&= \int \boldsymbol{dr'}\, \delta(\boldsymbol{r} - \boldsymbol{r'}) k_0^2 \delta n^2(\boldsymbol{r'})\boldsymbol{E}(\boldsymbol{r'}) \\
&= \delta n^2(\boldsymbol{r}) k_0^2 \boldsymbol{E}(\boldsymbol{r})
\end{aligned}$$

The Green function in vacuum is:

$$\boldsymbol{G}(\boldsymbol{r} - \boldsymbol{r'}) = \boldsymbol{E_0} \frac{k_0^2}{4\pi} \frac{\exp(-\boldsymbol{i} k_0 |\boldsymbol{r} - \boldsymbol{r'}|)}{|\boldsymbol{r} - \boldsymbol{r'}|} \quad (43)$$

$\boldsymbol{G}(\boldsymbol{r} - \boldsymbol{r'})$ represents the spherical wave emitted by a punctual source located at $\boldsymbol{r'}$ and observed from the position $\boldsymbol{r}$.

If the distance r is much longer than r' as we assume to be the case, then $|\boldsymbol{r} - \boldsymbol{r'}| \approx r$ for the denominator and $|\boldsymbol{r} - \boldsymbol{r'}| \approx r - \boldsymbol{u} \cdot \boldsymbol{r'} \approx r - \frac{\boldsymbol{k_f}}{k_0} \cdot \boldsymbol{r'}$ in the exponential, where $\boldsymbol{u}$ is a unit vector in the direction $\boldsymbol{r} - \boldsymbol{r'}$ and $\boldsymbol{k_f}$ is the scattering wavevector.

So $\boldsymbol{G}(\boldsymbol{r} - \boldsymbol{r'}) \approx \boldsymbol{E_0} \frac{k_0^2}{4\pi} \frac{\exp(-\boldsymbol{i} k_0 r)}{r} \exp\left(i \boldsymbol{k_f} \cdot \boldsymbol{r'}\right)$

In this expression, $\mathbf{E_0} \exp\left(i \boldsymbol{k_f} \cdot \boldsymbol{r'}\right)$ refers to an outgoing wave created at the point in $\boldsymbol{r'}$ by the interaction between the wave coming to this point and the perturbation. The

structure of the emitted wave remains identical to the incident wave (in this case a plane wave) hence the green function can be generalized to:

$$\boldsymbol{G}(\boldsymbol{r}-\boldsymbol{r}') \approx \frac{k_0^2}{4\pi}\frac{\exp(-\boldsymbol{i}k_0 r)}{r}\mathbf{E_0}\left(-\boldsymbol{k_f}, \boldsymbol{r}'\right) \tag{44}$$

Born approximation

The Born expansion consists of reinjecting $\boldsymbol{E}(\boldsymbol{r})$ in itself.

$$\begin{aligned}\boldsymbol{E}(\boldsymbol{r}) = \boldsymbol{E_0}(\boldsymbol{r}) &+ \int \boldsymbol{dr}'\, \boldsymbol{G}(\boldsymbol{r}-\boldsymbol{r}')\delta n^2(\boldsymbol{r}')\boldsymbol{E_0}(\boldsymbol{r}') \\ &+ \int \boldsymbol{dr}' \int \boldsymbol{dr}''\, \boldsymbol{G}(\boldsymbol{r}-\boldsymbol{r}')\delta n^2(\boldsymbol{r}')\boldsymbol{G}(\boldsymbol{r}'-\boldsymbol{r}'')\delta n^2(\boldsymbol{r}'')\boldsymbol{E_0}(\boldsymbol{r}'') \\ &+ \cdots\end{aligned} \tag{45}$$

This gives a series of integral with known terms. The physical meaning of the born expansion is represented in the scheme of Figure 29. For the second order expansion:

- The first term $\boldsymbol{E}_0(\boldsymbol{r})$ is the incident wave reaching $\boldsymbol{r}$
- The second term $\int \boldsymbol{dr}'\boldsymbol{G}(\boldsymbol{r}-\boldsymbol{r}')\delta n^2(\boldsymbol{r}')\boldsymbol{E_0}(\boldsymbol{r}')$ represents the incident wave reaching $\boldsymbol{r}'$ ($\boldsymbol{E_0}(\boldsymbol{r}')$) then interacting with the refractive index perturbation $\delta n(\boldsymbol{r}')$ in $\boldsymbol{r}'$ and then emitting a new wave from $\boldsymbol{r}'$ to $\boldsymbol{r}$ ($\boldsymbol{G}(\boldsymbol{r}-\boldsymbol{r}')$).
- The third term $\int \boldsymbol{dr}' \int \boldsymbol{dr}''\boldsymbol{G}(\boldsymbol{r}-\boldsymbol{r}')\delta n^2(\boldsymbol{r}')\boldsymbol{G}(\boldsymbol{r}'-\boldsymbol{r}'')\delta n^2(\boldsymbol{r}'')\boldsymbol{E_0}(\boldsymbol{r}'')$ represents the incident wave reaching $\boldsymbol{r}''$ ($\boldsymbol{E_0}(\boldsymbol{r}'')$) interacting with the refractive index perturbation $\delta n(\boldsymbol{r}'')$ in $\boldsymbol{r}''$ then emitting a new wave from $\boldsymbol{r}''$ to $\boldsymbol{r}'$ ($\boldsymbol{G}(\boldsymbol{r}'-\boldsymbol{r}'')$) which then interacts again with the refractive index perturbation $\delta n(\boldsymbol{r}')$ in $\boldsymbol{r}'$and finally emits a new wave from $\boldsymbol{r}'$ to $\boldsymbol{r}$ ($\boldsymbol{G}(\boldsymbol{r}-\boldsymbol{r}')$).

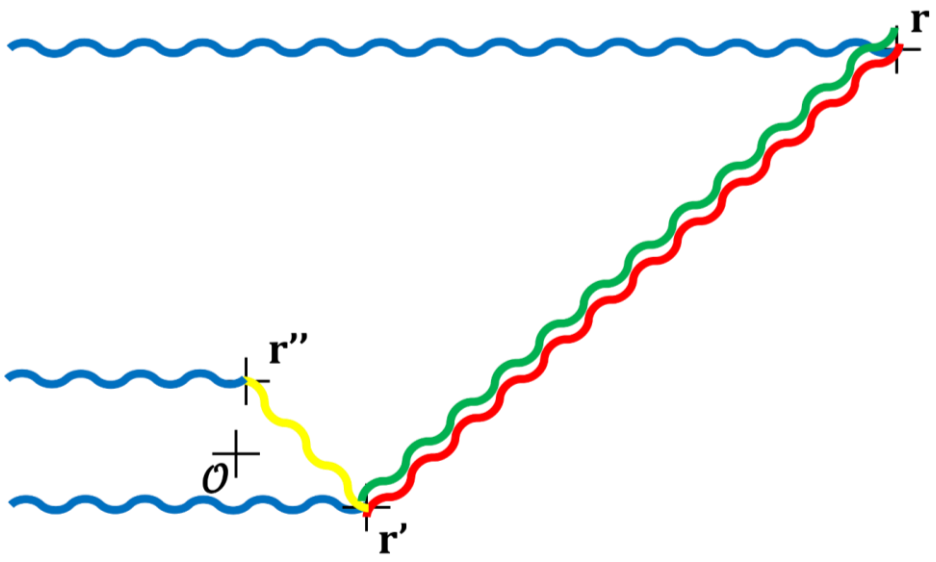

Figure 29: Schematic representation of the Born expansion.

The so called Born approximation (BA) consists to restrain the Born expansion to the first order:

$$\boldsymbol{E}(\boldsymbol{r}) = \boldsymbol{E_0}(\boldsymbol{r}) + \int \boldsymbol{dr'}\, \boldsymbol{G}(\boldsymbol{r}-\boldsymbol{r'})\delta n^2(\boldsymbol{r'})\boldsymbol{E_0}(\boldsymbol{r'}) \tag{46}$$

By introducing the expression of the Green function (Eq. (44)) in Eq. (46) we obtain the general form:

$$\boldsymbol{E}(\boldsymbol{r}) = \boldsymbol{E_0}(\boldsymbol{r}) + \frac{k_0^2}{4\pi}\frac{\exp(-ik_0 r)}{r}\int \boldsymbol{dr'}\, \mathbf{E_0}\big(-\boldsymbol{k_f}, \boldsymbol{r'}\big)\delta n^2(\boldsymbol{r'})\boldsymbol{E_0}(\boldsymbol{r'}) \tag{47}$$

The second term in the right-hand side of the expression is the scattered electric field

$$\boldsymbol{E_s}(\boldsymbol{r}) = \frac{k_0^2}{4\pi}\frac{\exp(-ik_0 r)}{r}\int \boldsymbol{dr'}\, \mathbf{E_0}\big(-\boldsymbol{k_f}, \boldsymbol{r'}\big)\delta n^2(\boldsymbol{r'})\boldsymbol{E_0}(\boldsymbol{r'}) \tag{48}$$

Physically the BA considers the electric field $\boldsymbol{E}(\boldsymbol{r'})$ in $\boldsymbol{r'}$, weakly affected by the field of perturbation (e.g. no reflexion, no absorption…) and thus $\boldsymbol{E}(\boldsymbol{r'})$ is very similar to the incident electric field $\boldsymbol{E_0}(\boldsymbol{r'})$ in $\boldsymbol{r'}$.
Replacing $\boldsymbol{E_0}(\boldsymbol{r'})$ by the planar incident wave expression (i.e. $\boldsymbol{E_0}(\boldsymbol{r'}) = \boldsymbol{E_0}\exp(-i\boldsymbol{k_i}\cdot\boldsymbol{r})$ gives:

$$\boldsymbol{E_s}(\boldsymbol{r}) = \frac{\exp(-ik_0 r)}{r}\boldsymbol{E_0^2}\int d\boldsymbol{r'}\ \exp\big(i\boldsymbol{k_f}\cdot\boldsymbol{r'}\big)\,\delta n^2(\boldsymbol{r'})\exp(-i\boldsymbol{k_i}\cdot\boldsymbol{r})$$

By introducing the wave vector transfer $\boldsymbol{q} = \boldsymbol{k_f} - \boldsymbol{k_i}$, the scattered electric field within the BA is thus proportional to the Fourier transform of the perturbation:

$$\boldsymbol{E_s}(\boldsymbol{r}) = \frac{k_0^2}{4\pi}\frac{\exp(-ik_0 r)}{r}\boldsymbol{E_0^2}\int d\boldsymbol{r'}\ \delta n^2(\boldsymbol{r'})\exp(i\boldsymbol{q}\cdot\boldsymbol{r}) \tag{49}$$

The BA is valid for high incident angles where the reflection coefficient is small but with grazing incidence, reflection comes non-negligible and must be considered in the expression of $\boldsymbol{E}(\boldsymbol{r'})$. This is achieved by the distorted wave Born approximation (DWBA).

Distorted wave Born approximation DWBA

In GISAXS, the incident angle α_i and out-of-plane exit angle α_f are small, which generate multiple reflexion and refraction events as soon as the “perfect” surface is perturbed with the presence of objects or protrusions. The distorted wave Born approximation (DWBA) has been developed to consider those events that are neglected within the BA. The first development of the DWBA theory was devoted to describe the collisions of charged particles, the theoretical description of such system can be found in standard quantum mechanics book [141]. Application of the DWBA to grazing incidence X-ray scattering have been performed by Vineyard [142] in the beginning of 80’s then by Sinha few years later to describe the scattering by deferent systems as rough surfaces [143] or multilayers [144]. Nowadays, the DWBA is commonly used to treat the scattering of X-ray in grazing incidence.

The DWBA considers the surface roughness or the objects on the sample as a perturbation of an ideal system characterized by the Fresnel wavefield (Eq. (39)). In the following, the DWBA will be employed to determine the intensity scattered by a rough surface. This well-known case will illustrate the use of the DWBA and show some of the differences with the simpler BA. In particular it will predict the intense scattering seen in most GISAXS experiments when the exit angle is equal to the critical angle ($\alpha_f = \alpha_c$) known as the Yoneda peak.

Differential scattering cross section

The intensity measured on the detector is the so-called differential scattering cross section $\frac{d\sigma}{d\Omega}$. The definition of the differential scattering cross section is the ratio between the electromagnetic power that has been scattered into the solid angle $d\Omega$ covered by the detector and the incident power.

$$d\sigma = \frac{Scattered\ power\ into\ the\ solid\ angle\ d\Omega}{Incident\ power}$$

The electromagnetic power passing through a surface unit can be calculated using the average value (noted $< \cdots >$) of the Poynting vector $\mathbf{\Pi} = \frac{\boldsymbol{B}\times\boldsymbol{E}}{\mu_0}$.

For the denominator, the incident power is:

$$< \Pi_0 > = \frac{|\boldsymbol{B_0} \times \boldsymbol{E_0}|}{2\mu_0} = \frac{|\boldsymbol{E}_0|^2}{2\mu_0 c} = \frac{E_0^2}{2\mu_0 c}$$

For the numerator, the scattered electric field is:

$$\boldsymbol{E_s}(\boldsymbol{r}) = \frac{k_0^2}{4\pi}\frac{\exp(-ik_0 r)}{r}\int d\boldsymbol{r'}\ \mathbf{E_0}\left(-\boldsymbol{k_f}, \boldsymbol{r'}\right)\delta n^2(\boldsymbol{r'})\ \boldsymbol{E_0}(\boldsymbol{r'})$$

The scattered power is:

$$< \Pi_s >= \frac{|\boldsymbol{B_s} \times \boldsymbol{E_s}|}{2\mu_0} = \frac{|\boldsymbol{E_s}(\boldsymbol{r})|^2}{2\mu_0 c} = \frac{1}{2\mu_0 c}\frac{k_0^4}{16\pi^2 r^2}\left|\int d\boldsymbol{r'}\ \mathbf{E_0}\left(-\boldsymbol{k_f}, \boldsymbol{r'}\right)\delta n^2(\boldsymbol{r'})\ \boldsymbol{E_0}(\boldsymbol{r'})\right|^2$$

This quantity must be multiplied by the considered surface $dA = r^2 d\Omega$. So the numerator is:

$$< \Pi_s > dA = \frac{1}{2\mu_0 c}\frac{k_0^4}{16\pi^2}\left|\int d\boldsymbol{r'}\ \mathbf{E_0}\left(-\boldsymbol{k_f}, \boldsymbol{r'}\right)\delta n^2(\boldsymbol{r'})\ \boldsymbol{E_0}(\boldsymbol{r'})\right|^2 d\Omega$$

The differential scattering cross section can then be written as:

$$\frac{d\sigma}{d\Omega} = \frac{< \Pi_s > dA}{< \Pi_0 >} = \frac{k_0^4}{16\pi^2 E_0^2}\left|\int d\boldsymbol{r'}\ \mathbf{E_0}\left(-\boldsymbol{k_f}, \boldsymbol{r'}\right)\delta n^2(\boldsymbol{r'})\ \boldsymbol{E_0}(\boldsymbol{r'})\right|^2 \qquad (50)$$

Comparison between BA and DWBA: A rough surface case

To illustrate the DWBA and to compare to the BA, let us consider the case of a randomly rough interface.
The rough interface is characterized, by its in-plane profile $z(x,y) = z(\boldsymbol{r}_{\parallel})$ as represented in Figure 30. The medium 1 (above the interface) has a refractive index n_1 and the medium 2 (below the interface) has a refractive index n_2.

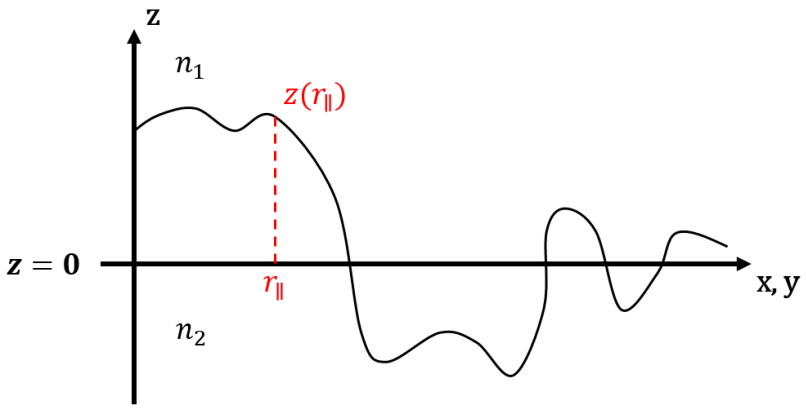

Figure 30: Schematically representation of a rough interface characterized by its in-plane profile $z(\boldsymbol{r}_{\parallel})$. The refractive index in the medium 1 above the surface is n_1 and n_2 in the medium 2 below the interface.

Born Approximation
In the case of the BA, the square of the refractive index is defined as:

$$n(\boldsymbol{r})^2 = n_1^2 + \delta n(\boldsymbol{r})^2 \tag{51}$$

With:

$$\delta n(\boldsymbol{r})^2 = (n_2^2 - n_1^2) \times \begin{cases} 0 \text{ for } z > z(r_{\parallel}) \\ 1 \text{ for } z \leq z(r_{\parallel}) \end{cases} \tag{52}$$

The differential scattering cross section has been derived previously (Eq.(50)) and is:

$$\frac{d\sigma}{d\Omega} = \frac{k_0^4}{16\pi^2 E_0^2} \left| \int d\boldsymbol{r}' \, \mathbf{E_0}(-\boldsymbol{k_f}, \boldsymbol{r}) \delta n^2(\boldsymbol{r}) \, \boldsymbol{E_0}(\boldsymbol{r}) \right|^2$$

Considering the BA, $\mathbf{E_0}(-\boldsymbol{k_f}, \boldsymbol{r}) = \boldsymbol{E_0} e^{i\boldsymbol{k_f}\cdot\boldsymbol{r}}$ and $\boldsymbol{E_0}(\boldsymbol{r}) = \boldsymbol{E_0} e^{-i\boldsymbol{k_i}\cdot\boldsymbol{r}}$ hence the differential scattering cross section is:

$$\frac{d\sigma}{d\Omega} = \frac{k_0^4}{16\pi^2} \left| \int d\boldsymbol{r} \, \delta n^2(\boldsymbol{r}) \, e^{i\boldsymbol{q}\cdot\boldsymbol{r}} \right|^2$$

Where $\boldsymbol{q} = \boldsymbol{k_f} - \boldsymbol{k_i}$ is the wave vector transfer. The scattering cross section is thus proportional to the square modulus of the Fourier transform of the refractive index perturbation.

Replacing $\delta n^2(\boldsymbol{r}')$ by its expression (Eq.(52)) gives:

$$\frac{d\sigma}{d\Omega} = \frac{k_0^4}{16\pi^2} |n_2^2 - n_1^2|^2 \left| \int d\boldsymbol{r} \, e^{i\boldsymbol{q}\cdot\boldsymbol{r}} \right|^2$$

By splitting $\boldsymbol{q}$ and $\boldsymbol{r}$ in parallel and perpendicular components:

$$\frac{d\sigma}{d\Omega} = \frac{k_0^4}{16\pi^2}|n_2^2 - n_1^2|^2 \left| \int d\boldsymbol{r}_\parallel \, e^{i\boldsymbol{q}_\parallel \cdot \boldsymbol{r}_\parallel} \int_{-\infty}^{z(\boldsymbol{r}_\parallel)} dz \, e^{iq_z \cdot r_z} \right|^2$$

The term $\int_{-\infty}^{z(\boldsymbol{r}_\parallel)} dz \, exp(iq_z \cdot r_z)$ can be calculated thanks to an integration by part giving:

$$\int_{-\infty}^{z(\boldsymbol{r}_\parallel)} dz \, e^{iq_z \cdot r_z} = \frac{e^{iq_z z(\boldsymbol{r}_\parallel)}}{iq_z}$$

So:

$$\frac{d\sigma}{d\Omega} = \frac{k_0^4}{16\pi^2 q_z^2}|n_2^2 - n_1^2|^2 \left| \int d\boldsymbol{r}_\parallel \, \frac{e^{iq_z z(\boldsymbol{r}_\parallel)}}{i} \, e^{i\boldsymbol{q}_\parallel \cdot \boldsymbol{r}_\parallel} \right|^2$$

After development of the square modulus of the complex number:

$$\frac{d\sigma}{d\Omega} = \frac{k_0^4}{16\pi^2 q_z^2}|n_2^2 - n_1^2|^2 \int d\boldsymbol{r}_\parallel \, \frac{e^{iq_z z(\boldsymbol{r}_\parallel)}}{i} \, e^{i\boldsymbol{q}_\parallel \cdot \boldsymbol{r}_\parallel} \int d\boldsymbol{r}'_\parallel \, \frac{e^{-iq_z z(\boldsymbol{r}'_\parallel)}}{-i} \, e^{-i\boldsymbol{q}_\parallel \cdot \boldsymbol{r}'_\parallel}$$

With rearrangement of the terms:

$$\frac{d\sigma}{d\Omega} = \frac{k_0^4}{16\pi^2 q_z^2}|n_2^2 - n_1^2|^2 \int d\boldsymbol{r}_\parallel \int d\boldsymbol{r}'_\parallel \, e^{iq_z\left(z(\boldsymbol{r}_\parallel) - z(\boldsymbol{r}'_\parallel)\right)} \, e^{i\boldsymbol{q}_\parallel \cdot (\boldsymbol{r}_\parallel - \boldsymbol{r}'_\parallel)}$$

The difference of height $z(\boldsymbol{r}_\parallel) - z(\boldsymbol{r}'_\parallel)$ depends only on the relative distance between the two points considered $\boldsymbol{r}_\parallel - \boldsymbol{r}'_\parallel$**.** Hence, the 4D integral can be reduced to a 2D integral by changing the variables $\boldsymbol{R}_\parallel = \boldsymbol{r}_\parallel - \boldsymbol{r}'_\parallel$ that consists to move the origin of the space at the point in $\boldsymbol{r}'_\parallel$:

$$\frac{d\sigma}{d\Omega} = \frac{k_0^4}{16\pi^2 q_z^2}|n_2^2 - n_1^2|^2 \int d\boldsymbol{R}_\parallel \, e^{iq_z\left(z(\boldsymbol{R}_\parallel) - z(\boldsymbol{0})\right)} \, \mathrm{e}^{i\boldsymbol{q}_\parallel \cdot \boldsymbol{R}_\parallel} \int d\boldsymbol{r}'_\parallel$$

With $\int d\boldsymbol{r}'_\parallel = A_i$ the illuminated area, the differential scattering cross section is thus:

$$\frac{d\sigma}{d\Omega} = \frac{A_i k_0^4}{16\pi^2 q_z^2}|n_2^2 - n_1^2|^2 \int d\boldsymbol{R}_\parallel \, e^{iq_z\left(z(\boldsymbol{R}_\parallel) - z(\boldsymbol{0})\right)} e^{i\boldsymbol{q}_\parallel \cdot \boldsymbol{R}_\parallel}$$

However, $z(\boldsymbol{R}_\parallel) - z(\boldsymbol{0})$ must be averaged over all the possible choices for the origin, that is to say, the ensemble average (noted with $\langle \cdots \rangle$) for a fixed point in $\boldsymbol{R}_\parallel$, so $e^{iq_z\left(z(\boldsymbol{R}_\parallel) - z(\boldsymbol{0})\right)} \rightarrow \langle e^{iq_z\left(z(\boldsymbol{R}_\parallel) - z(\boldsymbol{0})\right)} \rangle$ hence:

$$\frac{d\sigma}{d\Omega} = \frac{A_i k_0^4}{16\pi^2 q_z^2}|n_2^2 - n_1^2|^2 \int d\boldsymbol{R}_\parallel \, \langle e^{iq_z\left(z(\boldsymbol{R}_\parallel) - z(\boldsymbol{0})\right)} \rangle \, e^{i\boldsymbol{q}_\parallel \cdot \boldsymbol{R}_\parallel}$$

To go further, assumption on the fluctuation of the roughness $(z(\boldsymbol{R}_\parallel) - z(\boldsymbol{0}))$ must be made. For example, the height fluctuation $z(\boldsymbol{r}_\parallel) - z(\boldsymbol{0})$ can be assumed to follow a Gaussian statistic. Indeed, as mentioned in [139], if the roughness is due to a large number of successive independent events (for example the passage of sandpaper), the height will follow a Gaussian statistics because of the central limit theorem.

This assumption means that the ensemble average of $\left(z(\boldsymbol{R}_\parallel) - z(\boldsymbol{0})\right)^2$ is:

$$\langle\Big(z(\boldsymbol{R}_\parallel)-z(\boldsymbol{0})\Big)^2\rangle = g(\boldsymbol{R}_\parallel) = 2\sigma^2\left[1-\mathrm{e}^{-\left(\frac{R_\parallel}{\xi}\right)^{2h}}\right]$$

Where $\sigma^2 = \langle z(\boldsymbol{R}_\parallel)^2\rangle$**,** h determines the irregularity of the surface and its value is strictly in the range of $0 < h < 1$. When $h \to 1$ the surface is smooth and when $h \to 0$, the surface is highly irregular. Finally, ξ is a cut-off length that allows to define two regimes:

$$g(\boldsymbol{R}_\parallel) \propto R_\parallel^{2h}, \text{ if } R_\parallel \ll \xi$$
$$g(\boldsymbol{R}_\parallel) = 2\sigma^2, \text{ if } R_\parallel \gg \xi$$

ξ is sometimes called the correlation length because it acts as the typical length for the loss of correlation between the height of two distant points. Physically it could correspond to the distance between 2 bumps on the surface.

Finally, $g(\boldsymbol{R}_\parallel)$ can be written in terms of height-height correlation $C(\boldsymbol{R}_\parallel) = \langle z(\boldsymbol{R}_\parallel)z(\boldsymbol{0})\rangle$ [143]:

$$\langle\Big(z(\boldsymbol{R}_\parallel)-z(\boldsymbol{0})\Big)^2\rangle = g(\boldsymbol{R}_\parallel) = 2\langle z(\boldsymbol{R}_\parallel)^2\rangle - \boldsymbol{2}\langle z(\boldsymbol{R}_\parallel)z(\boldsymbol{0})\rangle = 2\sigma^2 - 2C(\boldsymbol{R}_\parallel)$$

Since $\langle e^{iq_z\left(z(\boldsymbol{R}_\parallel)-z(\boldsymbol{0})\right)}\rangle = e^{-\frac{1}{2}q_z^2\langle\left(z(\boldsymbol{R}_\parallel)-z(\boldsymbol{0})\right)^2\rangle}$ so:

$$\frac{d\sigma}{d\Omega} = \frac{A_i k_0^4}{16\pi^2 q_z^2}|n_2^2-n_1^2|^2\int d\boldsymbol{R}_\parallel\; e^{-\frac{1}{2}q_z^2\langle(z(\boldsymbol{R}_\parallel)-z(\boldsymbol{0}))^2}e^{i\boldsymbol{q}_\parallel\cdot\boldsymbol{R}_\parallel}$$

Replacing $\langle\Big(z(\boldsymbol{R}_\parallel)-z(\boldsymbol{0})\Big)^2\rangle$ by $2\langle z(\boldsymbol{R}_\parallel)^2\rangle - 2\langle z(\boldsymbol{R}_\parallel)z(\boldsymbol{0})\rangle$**:**

$$\frac{d\sigma}{d\Omega} = \frac{A_i k_0^4}{16\pi^2 q_z^2}|n_2^2-n_1^2|^2 e^{-q_z^2\langle z(\boldsymbol{R}_\parallel)^2\rangle}\int d\boldsymbol{R}_\parallel\, e^{q_z^2\langle z(\boldsymbol{R}_\parallel)z(\boldsymbol{0})\rangle}e^{i\boldsymbol{q}_\parallel\cdot\boldsymbol{R}_\parallel}$$

If the surface is perfectly flat, i.e. $g(\boldsymbol{R}_\parallel) = 0$, hence $\langle z(\boldsymbol{R}_\parallel)z(\boldsymbol{0})\rangle = \langle z(\boldsymbol{R}_\parallel)^2\rangle$ so:

$$\frac{d\sigma}{d\Omega} = \frac{A_i k_0^4}{16\pi^2 q_z^2}|n_2^2-n_1^2|^2\delta(\boldsymbol{R}_\parallel) \qquad (53)$$

The intensity is not null, and this remaining intensity is called the specular scattering or coherent scattering intensity. Physically, on GISAXS pattern it will create an intense scattering rod called the specular rod in the normal to the surface direction and precisely localized (because of the delta function) at $q_\parallel = 0$ (see Figure 26).

For a rough surface, the differential scattering cross section can be written as:

$$\frac{d\sigma}{d\Omega} = \frac{A_i k_0^4}{16\pi^2 q_z^2}|n_2^2-n_1^2|^2 e^{-q_z^2\langle z(\boldsymbol{R}_\parallel)^2\rangle}\int d\boldsymbol{R}_\parallel\,(e^{q_z^2\langle z(\boldsymbol{R}_\parallel)z(\boldsymbol{0})\rangle}+1-1)e^{i\boldsymbol{q}_\parallel\cdot\boldsymbol{R}_\parallel}$$

Then:

$$\frac{d\sigma}{d\Omega} = \frac{A_i k_0^4}{16\pi^2 q_z^2}|n_2^2-n_1^2|^2 e^{-q_z^2\langle z(\boldsymbol{R}_\parallel)^2\rangle}\left[\int d\boldsymbol{R}_\parallel\,(e^{q_z^2\langle z(\boldsymbol{R}_\parallel)z(\boldsymbol{0})\rangle}-1)e^{i\boldsymbol{q}_\parallel\cdot\boldsymbol{R}_\parallel} + \int d\boldsymbol{R}_\parallel\, e^{i\boldsymbol{q}_\parallel\cdot\boldsymbol{R}_\parallel}\right]$$

So:

$$\frac{d\sigma}{d\Omega} = \frac{A_i k_0^4}{16\pi^2 q_z^2} |n_2^2 - n_1^2|^2 e^{-q_z^2 \langle z(\boldsymbol{R}_\parallel)^2 \rangle} \delta(\boldsymbol{R}_\parallel) + \frac{A_i k_0^4}{16\pi^2 q_z^2} |n_2^2 - n_1^2|^2 e^{-q_z^2 \langle z(\boldsymbol{R}_\parallel)^2 \rangle} \int d\boldsymbol{R}_\parallel \, (e^{q_z^2 \langle z(\boldsymbol{R}_\parallel) z(\mathbf{0}) \rangle} - 1) e^{i \boldsymbol{q}_\parallel \cdot \boldsymbol{R}_\parallel} \quad (54)$$

The intensity collected is hence the sum of two terms, the first one is the specular term that differs from the case of flat surface by the factor $e^{-q_z^2 \langle z(\boldsymbol{R}_\parallel)^2 \rangle}$ called the Debye-Waller attenuation factor due to the roughness of the surface. The second term is the diffuse scattering or incoherent part generating intensity out of the specular rod (i.e. for $q_\parallel \neq 0$):

$$\frac{d\sigma}{d\Omega} = \left(\frac{d\sigma}{d\Omega}\right)_{BA\ specular} + \left(\frac{d\sigma}{d\Omega}\right)_{BA\ diffuse} \quad (55)$$

Distorted wave Born approximation

In the case of the DWBA, the refractive index is defined as:

$$n(\boldsymbol{r})^2 = n_0(\boldsymbol{r})^2 + \delta n(\boldsymbol{r})^2 \quad (56)$$

With:

$$n_0(\boldsymbol{r})^2 = \begin{cases} n_1^2 \text{ for } z > 0 \\ n_2^2 \text{ for } z < 0 \end{cases} \quad (57)$$

and

$$\delta n(\boldsymbol{r})^2 = (n_2^2 - n_1^2) \begin{cases} 1 \text{ for } 0 < z < z(r_\parallel) \\ -1 \text{ for } z(r_\parallel) < z < 0 \\ 0 \text{ for } 0 < z(r_\parallel) < z \; or \; \mathrm{z} < z(r_\parallel) < 0 \end{cases} \quad (58)$$

The reference electric field in DWBA is the Fresnel electric field (Eq.(39)):

$$E_0(\boldsymbol{r}, \boldsymbol{k}) = E_0 e^{-i\boldsymbol{k}_{i,\parallel} \cdot \boldsymbol{r}_\parallel} \begin{cases} e^{-ik_{i,0,z}z} + re^{ik_{i,0,z}z} & \text{for } z > 0 \\ te^{-ik_{i,1,z}z} & \text{for } z < 0 \end{cases}$$

The differential scattering cross section is (Eq. (50)):

$$\frac{d\sigma}{d\Omega} = \frac{k_0^4}{16\pi^2 E_0^2} \left| \int d\boldsymbol{r} \, \mathbf{E_0}(-\boldsymbol{k_f}, \boldsymbol{r}) \delta n^2(\boldsymbol{r}) \, \boldsymbol{E_0}(\boldsymbol{r}) \right|^2$$

Injecting $\delta n^2(\boldsymbol{r}')$ (Eq. (58)(50)):

$$\frac{d\sigma}{d\Omega} = \frac{k_0^4}{16\pi^2 E_0^2} |n_2^2 - n_1^2|^2 \left| \int d\boldsymbol{r}_\parallel \left[\int_{\mathbf{0}}^{z(\boldsymbol{r}_\parallel) > \mathbf{0}} dz \; \mathbf{E_0}(-\boldsymbol{k_f}, \boldsymbol{r}) \boldsymbol{E_0}(\boldsymbol{r}) - \int_{z(\boldsymbol{r}_\parallel) < \mathbf{0}}^{\mathbf{0}} dz \; \mathbf{E_0}(-\boldsymbol{k_f}, \boldsymbol{r}) \, \mathbf{E_0}(\boldsymbol{r}) \right] \right|^2$$

Replacing the electric fields:

$$\frac{d\sigma}{d\Omega} = \frac{k_0^4}{16\pi^2}|n_2^2 - n_1^2|^2 \left| \int d\boldsymbol{r}_{\parallel} e^{i(\boldsymbol{k}_{f,\parallel} - \boldsymbol{k}_{i,\parallel})\cdot \boldsymbol{r}_{\parallel}} \left[\int_0^{z(\boldsymbol{r}_{\parallel})>0} dz \left(e^{ik_{f,0,z}z} + r_f e^{-ik_{f,0,z}z} \right) \left(e^{-ik_{i,0,z}z} + r_i e^{ik_{i,0,z}z} \right) + \int_{z(\boldsymbol{r}_{\parallel})<0}^{0} dz - t_f e^{ik_{f,1,z}z}\ t_i e^{-ik_{i,1,z}z} \right] \right|^2$$

Let us note:

$$\begin{array}{l|l} \boldsymbol{k}_{f,\parallel} - \boldsymbol{k}_{i,\parallel} = \boldsymbol{q}_{\parallel} & -k_{f,0,z} - k_{i,0,z} = q_2 \\ k_{f,0,z} - k_{i,0,z} = q_z & -k_{f,0,z} + k_{i,0,z} = q_3 \\ k_{f,0,z} + k_{i,0,z} = q_1 & k_{f,1,z} - k_{i,1,z} = q_t \end{array}$$

Five terms are composing the differential cross scattering, a visualisation of the physical meaning of those terms is given in Figure 31.

vi) $\int_0^{z(\boldsymbol{r}_{\parallel})>0} dz\ e^{iq_z z} = \frac{1}{iq_z}(e^{iq_z z(\boldsymbol{r}_{\parallel})} - 1)$ is the term of Born that corresponds to the scattering by the perturbation as it was alone in vacuum (no surface).

vii) $\int_0^{z(\boldsymbol{r}_{\parallel})>0} dz\ r_i e^{iq_1 z} = r_i \frac{1}{iq_1}(e^{iq_1 z(\boldsymbol{r}_{\parallel})} - 1)$ corresponds to a two stages phenomenon, first the reflexion of the beam on the reference surface then the scattering by the perturbation.

viii) $\int_0^{z(\boldsymbol{r}_{\parallel})>0} dz\ r_f e^{iq_2 z} = r_f \frac{1}{iq_2}(e^{iq_2 z(\boldsymbol{r}_{\parallel})} - 1)$, corresponds to a two stages phenomenon the incident beam is first scattered by the perturbation then the scattered beam is reflected on the reference surface.

ix) $\int_0^{z(\boldsymbol{r}_{\parallel})>0} dz\ r_i r_f e^{iq_3 z} = r_i r_f \frac{1}{iq_3}(e^{iq_3 z(\boldsymbol{r}_{\parallel})} - 1)$, corresponds to a three stages phenomenon: first the incident beam is reflected on the reference surface then scattered by the perturbation then re-reflected by the reference surface.

x) $\int_{z(\boldsymbol{r}_{\parallel})<0}^{0} dz - t_i t_f e^{iq_t z} = -t_i t_f \frac{1}{iq_t}(e^{iq_t z(\boldsymbol{r}_{\parallel})} - 1)$ corresponds to a three stages phenomenon: the incident beam is first refracted, then scattered by the buried perturbation and again refracted at the interface.

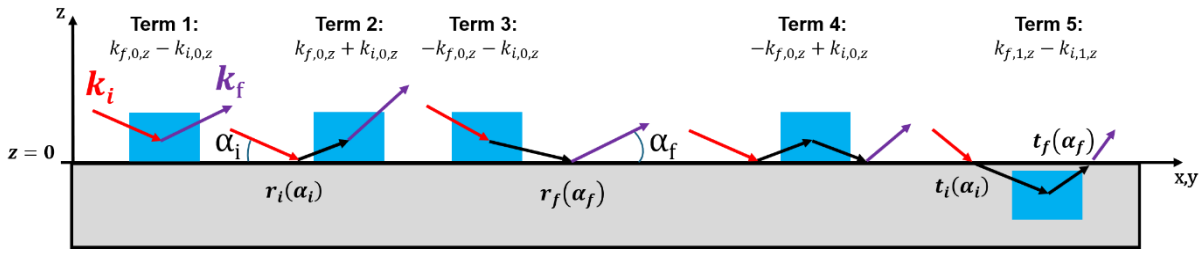

Figure 31: Schematic representation of the multiple reflection and refraction events considered by the DWBA.

So, the differential scattering cross section is:

$$\frac{d\sigma}{d\Omega} = \frac{k_0^4}{16\pi^2}|n_2^2 - n_1^2|^2 \left| \int d\boldsymbol{r}_\parallel \, e^{i\boldsymbol{q}_\parallel \cdot \boldsymbol{r}_\parallel} \left[\frac{1}{iq_z}\left(e^{iq_z z(\boldsymbol{r}_\parallel)} - 1\right) + r_i \frac{1}{iq_1}\left(e^{iq_1 z(\boldsymbol{r}_\parallel)} - 1\right) \right. \right.$$
$$\left. \left. + r_f \frac{1}{iq_2}\left(e^{iq_2 z(\boldsymbol{r}_\parallel)} - 1\right) + r_i r_f \frac{1}{iq_3}\left(e^{iq_3 z(\boldsymbol{r}_\parallel)} - 1\right) - t_i t_f \frac{1}{iq_t}\left(e^{iq_t z(\boldsymbol{r}_\parallel)} - 1\right) \right] \right|^2$$

The rest of the demonstration consists to follow the same procedure than for the BA and can be found in ref. [143]. The calculation gives for the specular intensity quite a similar expression to the case of the simpler BA:

$$\left(\frac{d\sigma}{d\Omega}\right)_{DWBA\ specular} \approx \frac{A_i k_0^4}{16\pi^2 q_z^2}|n_2^2 - n_1^2|^2 |r_i|^2 e^{-q_z^2\langle z(\boldsymbol{R}_\parallel)^2\rangle}\delta(\boldsymbol{R}_\parallel) = |r_i|^2 \left(\frac{d\sigma}{d\Omega}\right)_{BA\ specular}$$

For the diffuse scattered intensity, and considering that the perturbation is inside the medium (e.g. buried bubbles), the DWBA gives:

$$\left(\frac{d\sigma}{d\Omega}\right)_{DWBA\ diffuse} \approx \frac{A_i k_0^4}{16\pi^2 q_z^2}|n_2^2 - n_1^2|^2 |t_i|^2 \left|t_f\right|^2 e^{-q_z^2\langle z(\boldsymbol{R}_\parallel)^2\rangle} \int d\boldsymbol{R}_\parallel \, (e^{q_z^2\langle z(\boldsymbol{R}_\parallel) z(\boldsymbol{0})\rangle} - 1) e^{i\boldsymbol{q}_\parallel \cdot \boldsymbol{R}_\parallel}$$
$$= |t_i|^2 \left|t_f\right|^2 \left(\frac{d\sigma}{d\Omega}\right)_{BA\ diffuse}$$

The difference with the BA is in the factor $|t_i|^2\left|t_f\right|^2$. For large q_z the $|t_i|^2\left|t_f\right|^2 \approx 1$ hence, the DWBA scattered intensity tends to the BA one.

In addition, each transmission coefficient is maximum when the incident or exit angle is equal to the critical angle ($\alpha_{i,f} = \alpha_c$). This gives rise to an intense horizontal scattering in the $\boldsymbol{q}_\parallel$ directions for $\alpha_f = \alpha_c$ called the Yoneda peak (see Figure 25). Below this line ($\alpha_f < \alpha_c$), no intensity is transmitted due to the net drop of the transmitted coefficients (see Figure 24).

DWBA for buried object

Scattering of X-ray on buried objects as He-bubbles must be treated in the DWBA. The Figure 32 illustrates the geometry of the problem. Buried bubbles a depth z_0 are inside a homogenous W material with a surface assumed to be perfectly flat. The perturbation $\delta n^2(\boldsymbol{r})$ in that case, is due to the difference in electron density between the W matrix and the He-bubble.

Let us define n_b the refractive index in the bubble and the bubble shape:
$S(\boldsymbol{r}) = \begin{cases} 1\ inside \\ 0\ outside \end{cases}$.

The refractive index of the problem is $n^2(\boldsymbol{r}) = n_0^2(\boldsymbol{r}) + \delta n^2(\boldsymbol{r}) = n_0^2(\boldsymbol{r}) + \Delta n^2 S(\boldsymbol{r})$ with $n_0(\boldsymbol{r})^2 = \begin{cases} n_1^2 \text{ for } z > 0 \\ n_2^2 \text{ for } z < 0 \end{cases}$ and $\Delta n^2 = n_b^2 - n_2^2$.

In the framework of the DWBA, the Fresnel electric field (Eq. (39)) is chosen as the reference.

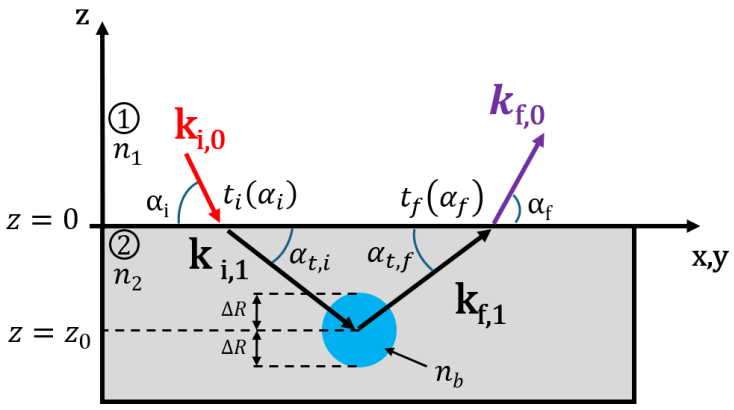

Figure 32: Schematic representation of a buried bubble treated in the DWBA.

The differential scattering cross section given by Eq.(50) is:

$$\frac{d\sigma}{d\Omega} = \frac{k_0^4}{16\pi^2 E_0^2}\left|\int d\boldsymbol{r}\, \mathbf{E_0}(-\boldsymbol{k_f}, \boldsymbol{r})\delta n^2(\boldsymbol{r})\, \boldsymbol{E_0}(\boldsymbol{r})\right|^2$$

Injecting the Fresnel wave field (Eq.(39)) and $\delta n^2(\boldsymbol{r})$:

$$\frac{d\sigma}{d\Omega} = \frac{k_0^4}{16\pi^2}|n_b^2 - n_2^2|^2|t_i|^2\left|t_f\right|^2\left|\int d\boldsymbol{r}\, S(\boldsymbol{r})e^{i(k_{f,1,z}-k_{i,1,z})z}e^{i\boldsymbol{q}_\parallel\cdot\boldsymbol{r}_\parallel}\right|^2$$

Considering that the bubble is located at a depth z_0, the z integral can be written:

$$\int dz\, e^{iq_{t,z}z}S(\boldsymbol{r}) = \int dz\, e^{iq_{t,z}(z-z0)}S(\boldsymbol{r})e^{iq_{t,z}z_0} = e^{iq_{t,z}z_0}\int dz\, e^{iq_{t,z}(z-z0)}S(\boldsymbol{r})$$

With $q_{t,z} = (k_{f,1,z} - k_{i,1,z})$.

By replacing the variable $z' = z - z_0$ and $r' = \sqrt{x^2 + y^2 + z'^2}$:

Then:

$$\frac{d\sigma}{d\Omega} = \frac{k_0^4}{16\pi^2}|n_b^2 - n_2^2|^2|t_i|^2\left|t_f\right|^2\left|\int d\boldsymbol{r}'\, S(\boldsymbol{r}')e^{i\boldsymbol{q}_t\cdot\boldsymbol{r}'}\right|^2\left|e^{iq_{t,z}z_0}\right|^2$$

As seen previously in Eq.(40), the z coordinate of the transmitted wave vectors ($k_{f,1,z}$ and $k_{i,1,z}$) in the medium is complex and is defined as:

$$k_{i,1,z} = -\frac{2\pi}{\lambda}n_2\sin(\alpha_{t,i}) \approx -\frac{2\pi}{\lambda}n_2\alpha_{t,i} \approx -\frac{2\pi}{\lambda}\left[Re(n_2\alpha_{t,i}) + iIm(n_2\alpha_{t,i})\right]$$

$$k_{f,1,z} = \frac{2\pi}{\lambda}n_2\sin(\alpha_{t,f}) \approx \frac{2\pi}{\lambda}n_2\alpha_{t,f} \approx \frac{2\pi}{\lambda}\left[Re(n_2\alpha_{t,f}) + iIm(n_2\alpha_{t,f})\right]$$

The last term can then be rewritten:

$$\left|e^{iq_{t,z}z_0}\right|^2 = \left|e^{i\frac{2\pi}{\lambda}[Re(n_2\alpha_{t,f})+Re(n_2\alpha_{t,i})]z_0}e^{-\frac{2\pi}{\lambda}[Im(n_2\alpha_{t,f})+Im(n_2\alpha_{t,i})]z_0}\right|^2$$

Leading to an exponential damping of the intensity:

$$\left|e^{iq_{t,z}z_0}\right|^2 = e^{\frac{z_0}{\Lambda}}$$

Where, $z_0 < 0$ and $\frac{1}{\Lambda} = \frac{1}{\Lambda(\alpha_i)} + \frac{1}{\Lambda(\alpha_f)}$ with $\Lambda(\alpha_{i,f})$ defined in Eq.(41).

The differential scattering cross section can then be simplified as $\delta n^2(\boldsymbol{r}) = 0$ outside of the bubble hence, only the integral inside the bubble shape remains:

$$\frac{d\sigma}{d\Omega} = \frac{k_0^4}{16\pi^2}|n_b^2 - n_2^2|^2|t_i|^2|t_f|^2 \left| \int_{S(\boldsymbol{r}')} d\boldsymbol{r}'\, e^{i\boldsymbol{q_t}\cdot\boldsymbol{r}'} \right|^2 e^{\frac{z_0}{\Lambda}}$$

Finally, the Eq.(15) is found:

$$\frac{d\sigma}{d\Omega} = \frac{k_0^4}{16\pi^2}|n_b^2 - n_2^2|^2|t_i|^2|t_f|^2|F(\boldsymbol{q_t})|^2 e^{\frac{z_0}{\Lambda}} \quad (59)$$

Where $F(\boldsymbol{q}) = \int_{S(\boldsymbol{r})} d\boldsymbol{r}\, e^{i\boldsymbol{q}\cdot\boldsymbol{r}}$ is the form factor of the bubble and $\boldsymbol{q_t}$ the wave vector transfer in the medium: $\boldsymbol{q_t} = \frac{2\pi}{\lambda}\begin{pmatrix} \cos(\alpha_f)\cos(2\theta_f) - \cos(\alpha_i) \\ \cos(\alpha_f)\sin(2\theta_f) \\ \sqrt{n^2 - \cos^2(\alpha_f)} + \sqrt{n^2 - \cos^2(\alpha_i)} \end{pmatrix}$

The GISAXS intensity measured on the detector, i.e. the differential scattering cross section is hence proportional to the modulus square of the bubble form factor.

The form factor of a variety of shapes have been derived and can be found in ref. [137]. In addition, software as IsGISAXS [145], Born-again [146] and FitGISAXS [147] are able to simulate the GISAXS pattern for a given shape.

We have used the equations and methods presented to investigate the shape of He bubbles in W by GISAXS: it has allowed us to determine the equilibrium shape (see chapter 4) and the growth mechanism of bubbles (see chapter 5).

3.2.3. ESRF – BM32 – INS2

In this study, GISAXS measurements have been performed using the INS2 set-up of the BM32 beam line of the European synchrotron radiation facility (ESRF) in Grenoble (France). The Figure 33 is a representation of the main characteristics of the experimental set-up and the Figure 34 is a picture of the experimental hutch.

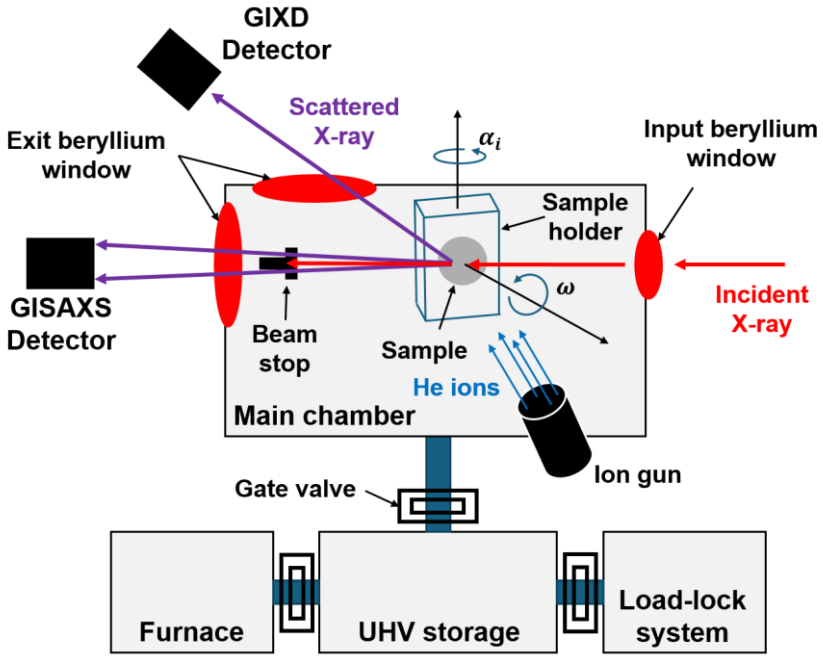

Figure 33: Schematic representation of the INS2 set-up (ESRF - BM32 beam line) used for He implantation and GISAXS measurements.

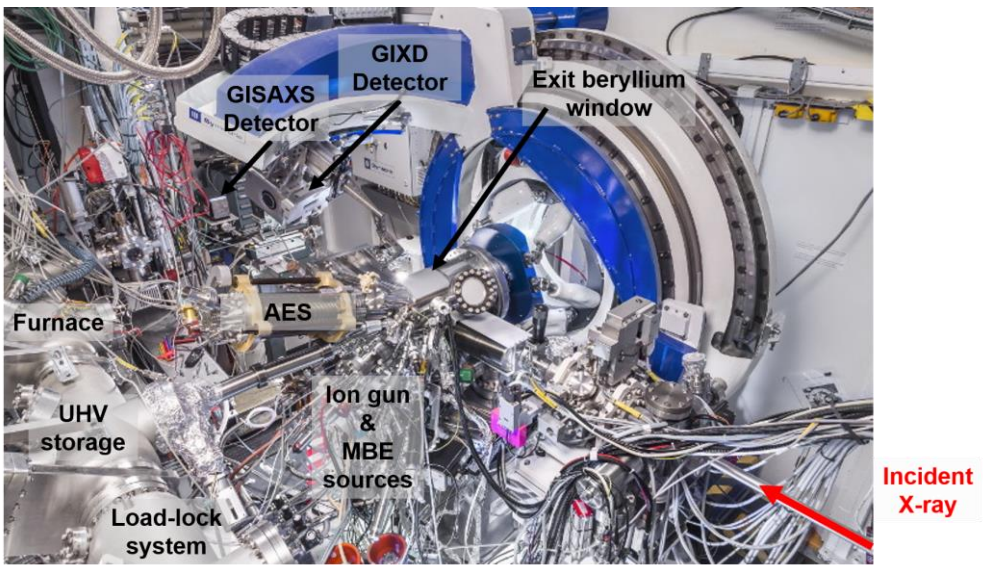

Figure 34: Picture of the INS2 set-up (ESRF - BM32 beam line) used for He implantation and GISAXS measurements.

The setup can operate under ultra-high vacuum (UHV) environment, the load-lock system allows to insert the samples under vacuum. In the main chamber, under UHV conditions, the sample is placed vertically and a W filament placed behind the sample is used to increase the sample temperature up to 1773 K by electron bombardment. The temperature of the sample is recorded thanks to two pyrometers, the first one for low temperature regimes (< 723 K) and the second one for high temperatures (> 723 K). In-situ He irradiation is performed using an ion gun placed in front of the sample (the angle with respect to the normal to the surface is about 30°). He atoms are assumed to be ionized in the first state (He^+). The ion flux on the sample is deduced by measuring the electrical current on the sample holder.

Optics are placed in the X-ray path from the synchrotron storage ring to the main chamber. The X-ray beam is collimated and the different wavelengths are filtered to keep only the desired X-ray energy. In this study either 10 keV ($\lambda = 0.1240$ nm) or 18keV ($\lambda = 0.0689$ nm) have been selected. The beam size is about 300 µm however, due to the grazing incidence in GISAXS configuration, more than the whole sample along the beam path is illuminated. The part of the X-ray beam unused is eliminated by a T-shaped beam stop in Tungsten and placed between the sample and the exit beryllium (Be) window that is transparent to X-ray. In addition, the beam stop suppresses the specularly reflected beam and allows X-ray with small scattering angles to reach the detector. The 2D GISAXS detector is a charge-coupled device (CDD) camera composed of two modules. On GISAXS patterns a black horizontal zone corresponding to a gap between those two modules is visible. The field of view in the $\boldsymbol{q}$ space can be tunned by changing the distance between the sample and the detector from ~800 mm to 2-3 m.
The incidence X-ray beam is fixed while the sample can be inclined to define the incident angle α_i. In addition, the sample can rotate with respect to its surface normal direction allowing to probe in-plane anisotropies.
A diffractometer with a second Be window allows to record the grazing incidence X-ray diffraction (GIXD) and orient the sample with respect to crystallographic axis.

Finally, the main chamber is also equipped with molecular beam epitaxy (MBE) sources (up to 7) for atomic deposition and additional characterization techniques as an Auger spectrometer and a reflection high-energy electron diffraction (RHEED) system.

3.3. Sample preparation

As evidenced during the previous section, surface roughness is of utmost importance due to the potential diffuse scattering than may overlap with the diffuse scattering signal coming from the He bubbles, therefore surface preparation is a key step. The chemical inhomogeneity, due to native oxide on the surface or impurities in the matrix can also induce a perturbation of the refractive index and hence scatter X-rays, therefore creating parasitic signal. In addition, as seen in Chapter 2, the behaviour of He in W can be modified in presence of impurities. Preferential agglomeration of He in the neighbourhood of impurities has been observed. The sample preparation is hence crucial to i) minimize the surface roughness, and ii) eliminate impurities in surface and sub-surface regions.

3.3.1. Samples characteristics

In this work, high purity (>99.999%) W single crystalline samples have been used. The samples were purchased from MaTeck GmbH. The surface samples were oriented along {100}, {110} and {111} crystallographic planes with precision below 0.1°. Samples are either disk-shaped or hat-shaped as shown Figure 35 with 9 mm diameter and 1 mm thickness. Surfaces were mechanically polished to obtain a mirror like aspect (roughness below 0.01 µm according to MaTeck).

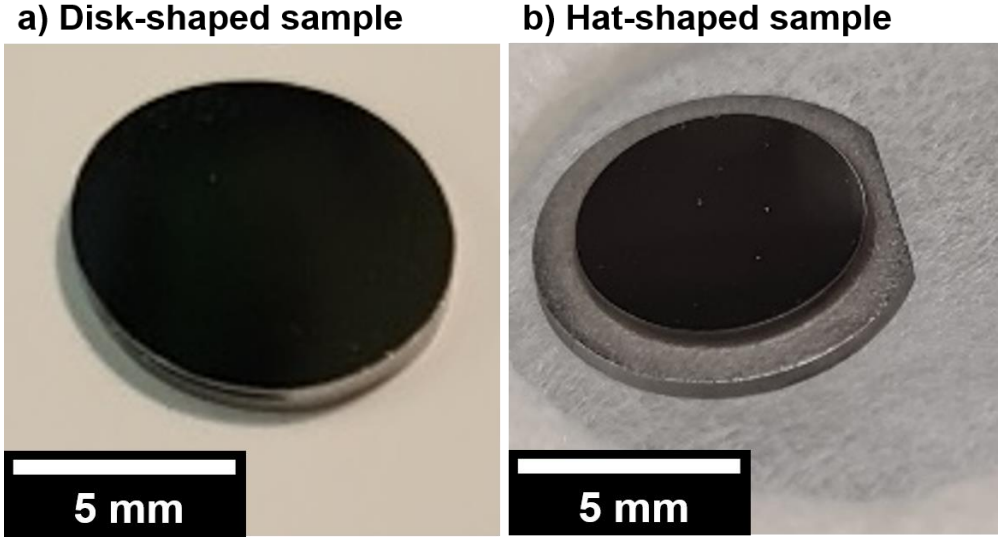

Figure 35: Picture of W single crystalline samples used in this these.

3.3.2. Preparation of clean W crystal

The most common chemical contaminations of tungsten are carbon in the bulk and oxygen at the surface (native oxide). Zakeri et al. [148] have elaborated a procedure to clean W single crystals. The preparation of samples prior GISAXS experiments is based on their protocol. Identical process has been followed for all surface orientations.

Experimental set-up

Several requirements are necessary to prepare clean W crystals: (i) UHV environment is mandatory to avoid air contamination. (ii), high temperature must be achievable. In this case the temperatures is 1273 K for 30 minutes under oxygen exposure. Gas injection (pure oxygen) is performed using a micro-leak valve. This oxidation is followed by a rapid flash up to 2273 K for few seconds. Finally, a non-destructive characterization of the chemistry and morphology in surface is required.

The samples preparation has been performed in the LEEM-PEEM set-up of the CINaM laboratory in Marseille (France). The set-up is represented in Figure 36, the preparation chamber is equipped with a furnace that can heat the sample up to 2273 K. The temperature is monitored thanks to a pyrometer (emissivity ϵ_W = 0.28 [26]). The level of chemical contamination is checked using an Auger spectrometer and the surface morphology is observed using the low-energy electron microscope (LEEM).

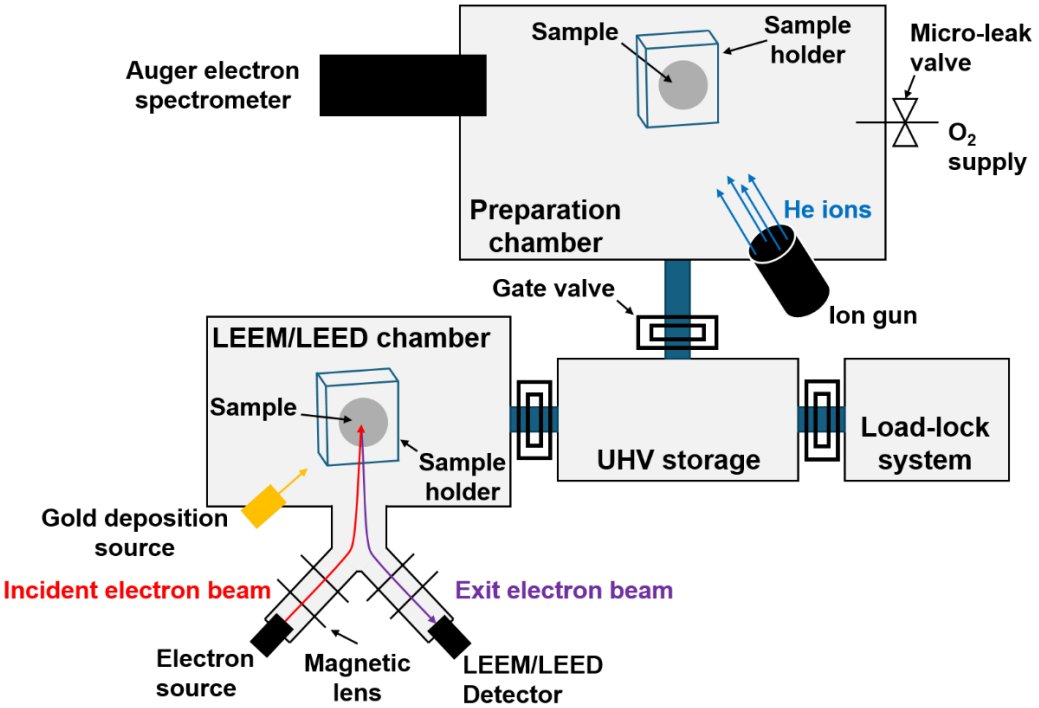

Figure 36: Schematic representation of the LEEM-PEEM set-up in the CINaM laboratory for the sample preparation.

Preparation procedure

The cleaning of W samples consists in a cycling process of two steps:

i) Annealing at 1000°C under O_2 atmosphere for 30 minutes. The pressure of oxygen is adjusted thanks to a micro-leak valve to $P_{O_2} = 10^{-6}$mbar.

ii) UHV flash up to 2000°C for 40 seconds.

After 3 cycles O_2 annealing-flash the level of chemical contamination of carbon and oxygen is checked by Auger-spectroscopy. If oxygen and carbon peaks are below the detection limit (see Figure 37a), the W surface is analysed by LEEM. The imaging of atomic steps and extended terraces is expected at the surface (see Figure 37b). Once both chemical cleanness and surface morphology are acceptable, a 5 nm thick gold layer (Au) is deposited on the sample surface (see Figure 37c and d) to prevent air contamination during transportation to the ESRF.

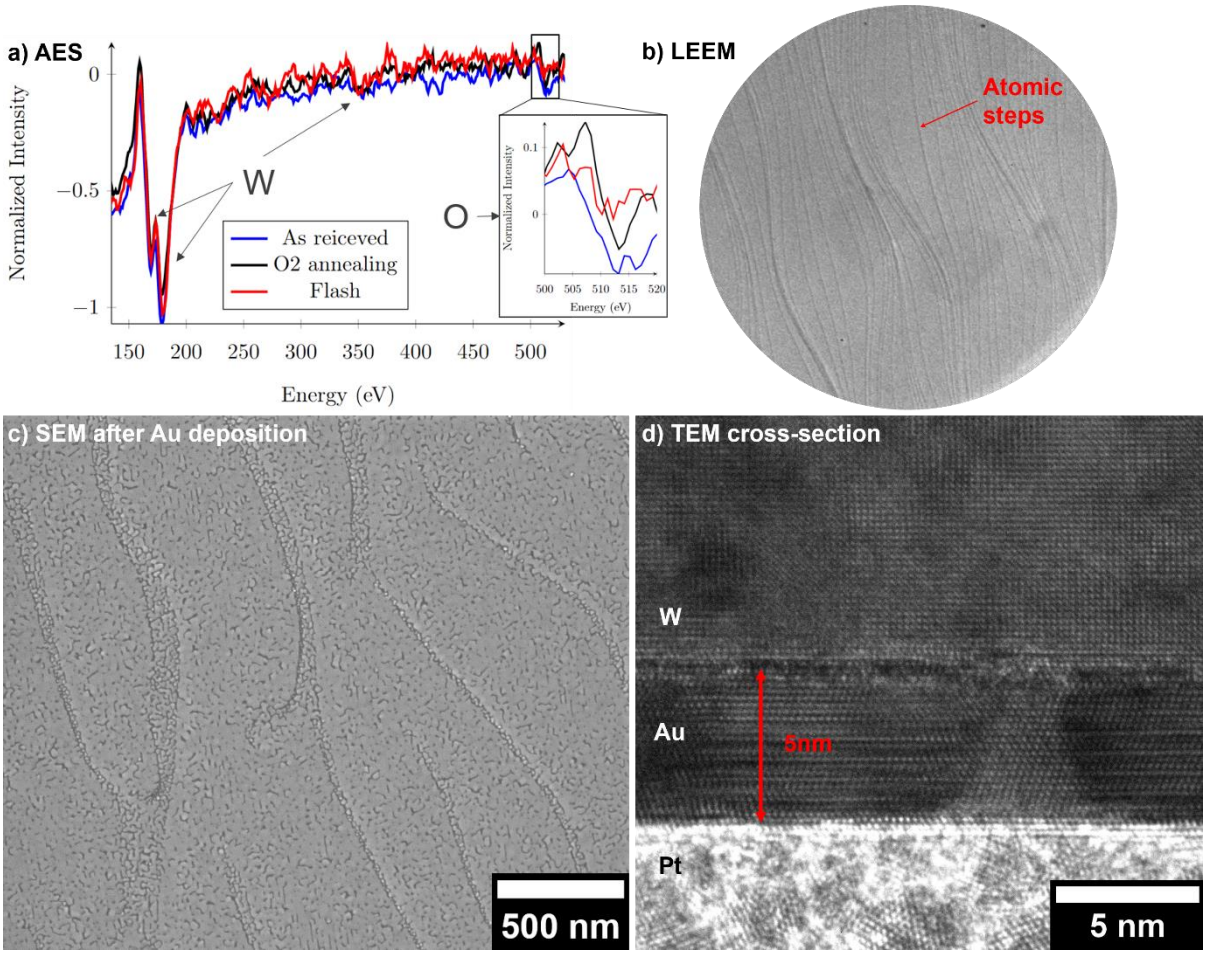

Figure 37: Chemical and morphological characterization of the sample after preparation procedure by Auger spectrometry (a) and low energy electron microscopy (b). Surface imaging after deposition of the Au protective layer by SEM (c) and cross-section TEM characterization of the Au layer by TEM (d).

Final steps prior implantation

Once a sample is introduced in the INS2 set-up, the first step is to remove the gold protective layer from the sample surface. To that end, the sample is heated to 1373 K. Desorption of Au is monitored by GIXD as shown in Figure 38.

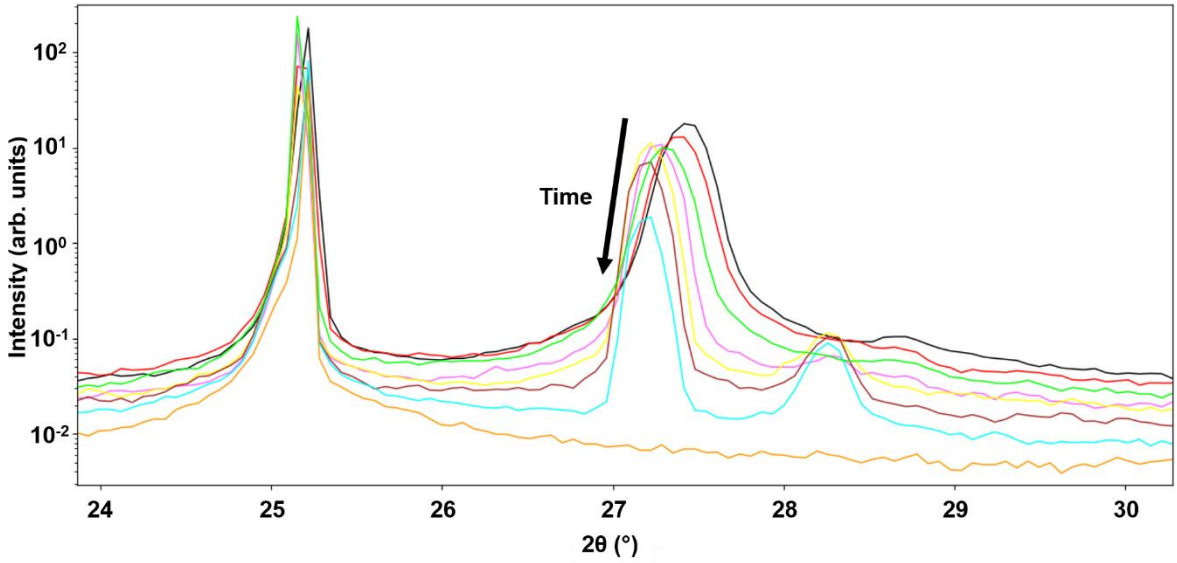

Figure 38: GIXD diffractogram of Au/W(110) at 1373 K. Black line is the initial time. Chronological order is: black, red, green, pink, yellow, brown, cyan and orange. Peak at $2\theta \approx 25°$ corresponds to the W peak of (002) planes and peak at $2\theta \approx 27.4°$ corresponds to the Au layer.

In addition, the complete desorption of the Au layer has been checked by LEEM at several occasions, in the CINaM laboratory as shown Figure 39. The Figure 39a is the coated W with gold before heating, and the bottom part of Figure 39 is three snap-shots recorded during the temperature plateau at 1373 K. When temperature is 1373 K, the gold layer had already started to desorb forming patches with different gold thickness and islands (bottom left image). Then, only a mono-layer of gold remains (bottom and in middle image). Finally, the rest of gold is desorbed with time and a clean W surface is observed (right image).

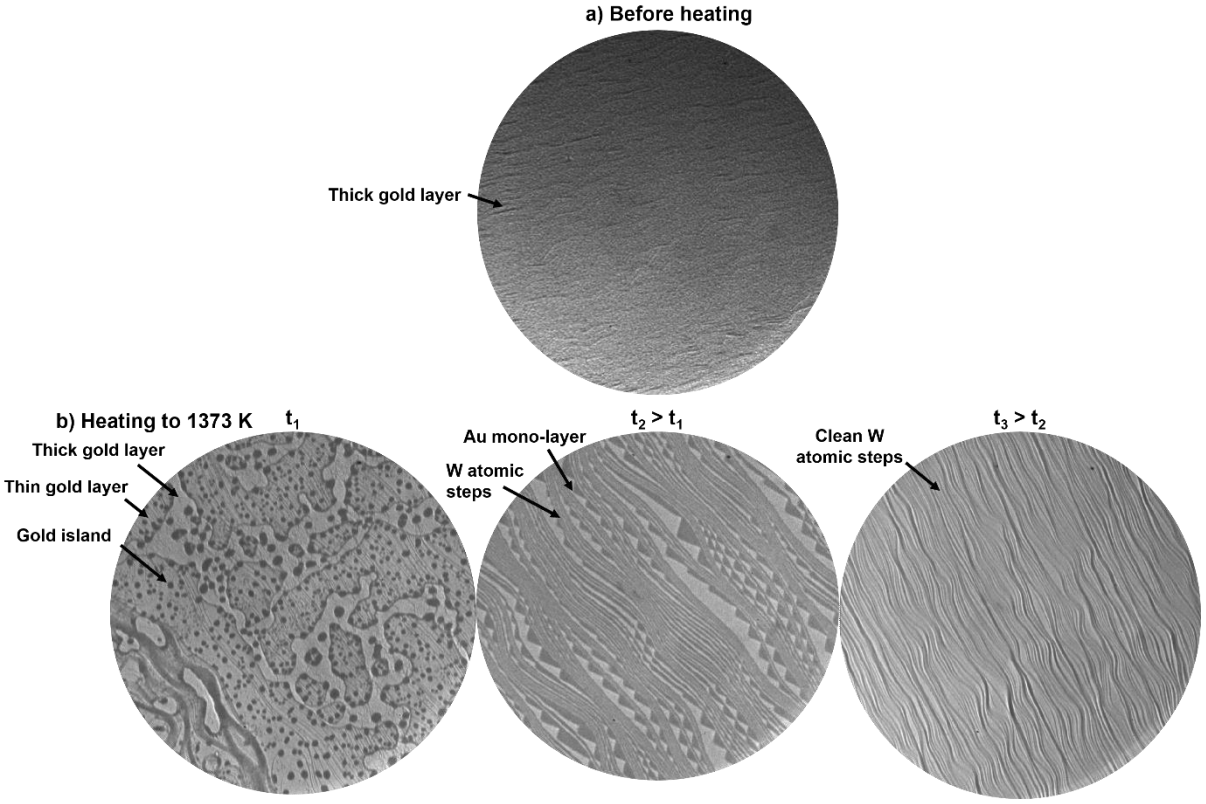

Figure 39: LEEM micrographs of Au/W(110). Before heating (a) a thick Au layer covers the W surface. When temperature reaches 1373 K (b), the thick layer of gold had already started to desorb forming island (dark spots in the left image). Then with time, only a single atomic layer remains (middle image) and finally the gold mono-layer in turn desorbs, leaving a clean W surface.

The last steps before implantation are 1) the orientation of the sample using GIXD and 2) the recording of GISAXS references before implantation.

We also advise to record the position of the direct beam on the GISAXS pattern to identify the position of the reciprocal space origin.

3.4. Transmission electron microscopy

This section is dedicated to the use of TEM to characterize He bubbles in W. The issues in observing buried He bubbles in a W matrix are (i) first to prepare a thin enough lamella to allow transmission of electrons through it. This is mandatory to obtain images of buried bubbles and high resolution of the W matrix with the microscope. (ii) Second, only low contrast is expected especially with small bubbles (diameter of few nanometers). (iii) Third, often bubbles in cross-section are superimposed, which make their characterization very difficult. Finally, (iv) the fourth difficulty is the hiding of bubbles by dislocations loops generated during bubble formation and growth.
The first part of this section is dedicated to the lamella preparation by focused ion beam (FIB). Thin lamellas with thickness around 70 nm have been produced by this technique. Then the second part will address the characterization of bubbles by TEM, where a special microscope setting overcomes most of the difficulties mentioned above.

3.4.1. Thin lamella preparation

In general, thin lamella are prepared either by a chemical approach or by physical etching. The chemical approach consists in eroding the sample by electro-erosion until a hole is formed. This technique guarantees that at the periphery of the hole a region is thin enough to be analysed by TEM. However, the sample is sacrificed and cannot be reused. In some cases, the sample must remain usable after the thin lamella preparation, for example in the case of onerous samples as single crystals or multi-step experiments. The physical etching by FIB is a good alternative method that alters only an area of few microns square. The main drawback of FIB cutting is the generation of crystallographic defects; in particular, dislocation loops are produced.

In this work, thin lamellas were prepared at the CP2M laboratory in Marseille using a FEI Helios 600 nanolab dual beam. A SEM is coupled to the FIB to observe in-situ the fabrication steps. The procedure to extract a thin lamella is presented in Figure 40:
The first step consists in covering the surface of the future lamella with a 3 µm-thick protective layer of platinum (Pt) (see Figure 40a). Since the bubbles are very close to the surface, the Pt layer is designed to prevent alteration of the area of interest during the subsequent etching steps. A 30 keV gallium (Ga) ions beam is then used to excavate both side of the lamella to a depth of few micrometers (see Figure 40b). The sample is tilted to remove the left side and the down part of the lamella (red rectangles 1 and 2 in Figure 40b). The next step consists in attaching a thin pin-manipulator to the protective layer of the lamella by Pt deposition. Once the thin pin-manipulator is stuck, the last side of the lamella is removed (red rectangle 3 in Figure 40b). After that, the lamella is moved to the support grid and Pt deposition is again used to stick the lamella on the grid. The thin pin-manipulator is removed using a Ga beam to cut the Pt sticking layer between the manipulator and the lamella. The last step of the procedure is the

thinning of the lamella. During this step, the energy of the Ga beam is progressively decreased to remove the damaged volume of the lamella that has been generated during the extraction and thinning the lamella to the desired thickness. Careful attention is required to prevent the bending of the lamella. Criterions to stop the thinning are:

i) The transparency to electrons as shown in Figure 40c.
ii) Thickness of approximately 70 nm when measured by the SEM (see Figure 40d).

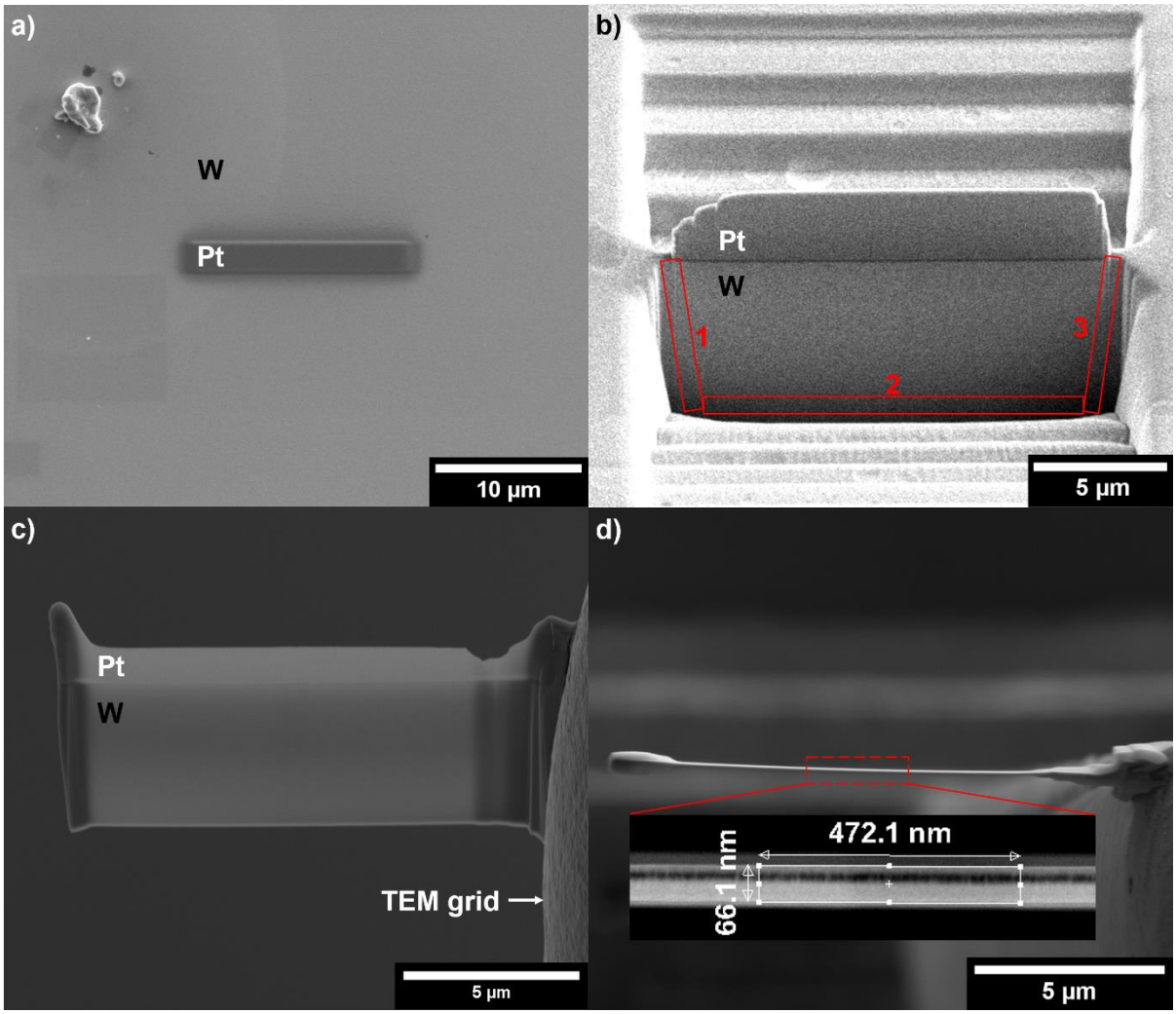

Figure 40: SEM images of the lamella preparation by FIB. In a), a platinum protective layer is deposited to protect the surface of the future lamella. In b), the lamella is pre-formed by etching using a gallium beam. The red rectangles delimit the cut areas to detach the lamella. The last rectangle must be cut once the pin-manipulator is attached to the lamella. In c), the lamella is stuck to the TEM grid and then thinned to obtain electron transparency. In d) is shown the top view of the lamella at the end of the procedure.

3.4.2. Bubble characterisation

This section first introduces the principle of the TEM technique. The interested reader can find more detailed information on the physics in numerous textbooks such as the series written by Edington [149–153] or the complete book of Williams and Carter [154]. In a second step, the specific conditions to characterize gas-bubbles in metal materials will be presented.
In this work two TEM microscopes have been used, a JEOL JEM-2100 F located in the CINaM laboratory (Marseille, France) and a FEI Titan 80-300 located in the CP2M laboratory (Marseille, France).

TEM microscope

The main components of a transmission electron microscope are represented in Figure 41.

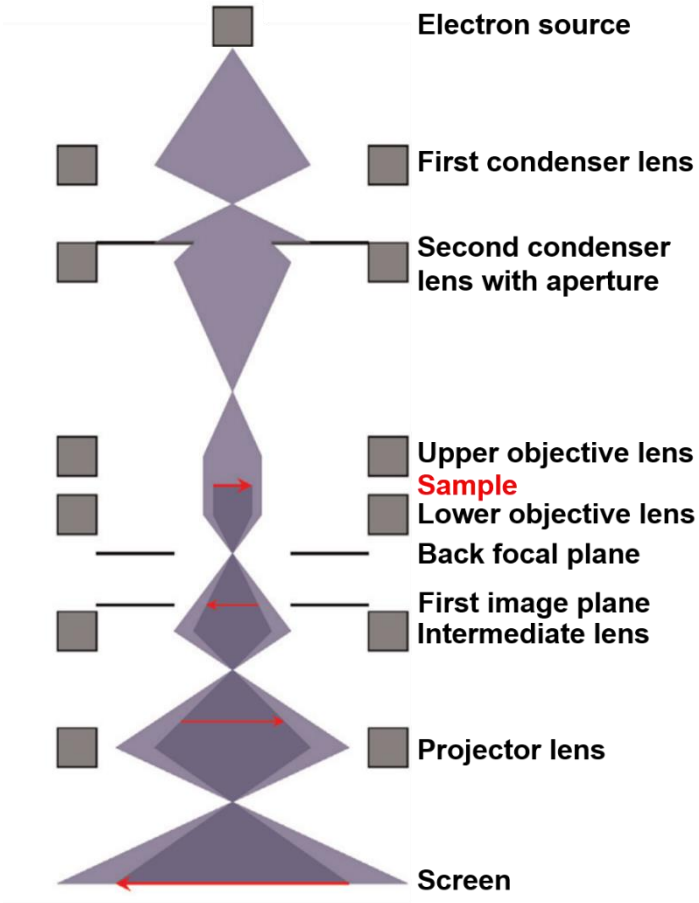

Figure 41: Schematic representation of the main components of a transmission electron microscope. Modified from ref. [155].

An electron beam is generated at the top of the column then accelerated through vacuum to energies in the range of hundreds of keV (200 keV in our case). A series of magnetic lenses (first and second condenser and the upper objective lenses) collimate

the electron beam onto the sample. Then electrons pass through the sample, and magnification is performed by magnetic lenses. plane (or back Fourier plane) is finally projected on a 2D detector.

The scattering process of electrons by the sample may be elastic or inelastic. The elastic scattering of electrons is used for imaging (and high resolution). Inelastic scattering is the basis of the electron energy loss spectroscopy (EELS) technique that gives information on the local chemical composition of a material. In the case of He-bubbles, it has been shown that the He density inside the bubbles can be measured by locally measuring the spectrum of electron energy loss [49,72].
Elastically scattered electrons are in fact diffracted by atomic planes in the sample and a diffraction pattern is created in the back focal plane of the lower objective lens as shown in Figure 42. The contrast in TEM images is due to scattering phenomena that have transformed the uniform incident beam in a non-uniform transmitted beam.

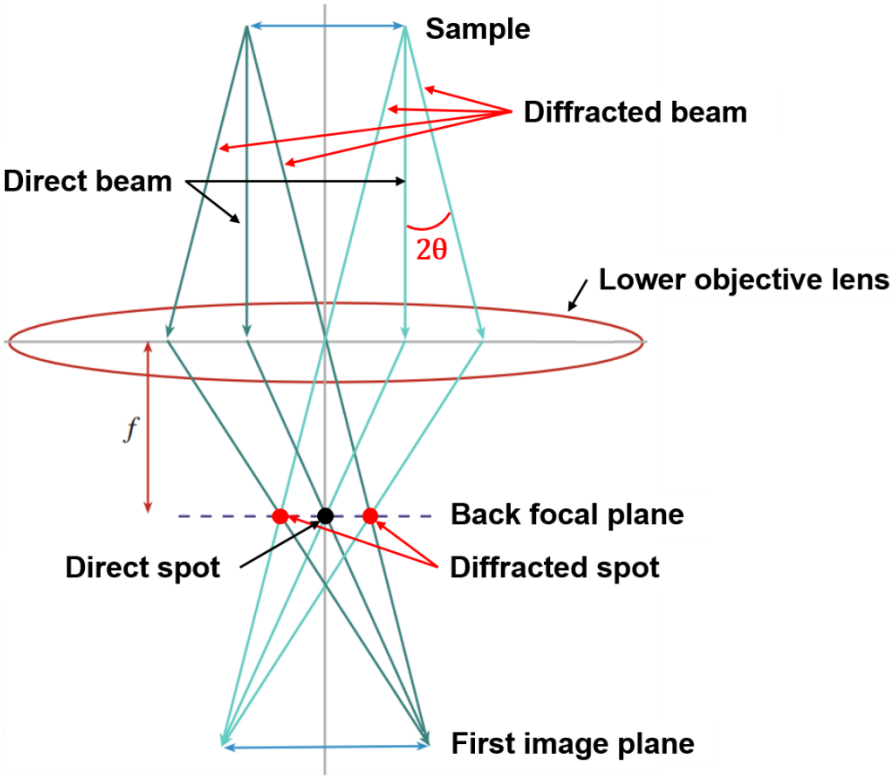

Figure 42: Schematic representation of the formation of the diffracted pattern at the back focal plane and the image of the sample at the first image plane of the lower objective lens. Diffracted spots generated by diffraction with an angle 2θ are represented by red circles and the transmitted spot is shown as a black spot. Modified from ref. [154].

It is worth noticing that both the sample image and the diffraction pattern are generated simultaneously in the TEM. Depending on the settings of the intermediate lens (see Figure 41), two modes are available:

i) **Diffraction mode**, the intermediate lens is adjusted to select the back focal plane of the lower objective lens as object. Then the diffraction pattern is projected by the projector lens onto the viewing screen.

ii) **Image mode**, the object plane of the intermediate lens is this time set to be the first image plane of the lower objective lens. The projector lens will then project the sample image on the screen.

The image of the sample projected on the detector results from an interference of many diffracted beams. Therefore, a selection of spots on the diffraction pattern can be done using the objective aperture located at the back focal plane of the lower objective lens. When the diaphragm is centred on the direct spot and is small enough to exclude all the diffracted spots, the image formed is in bright-field (BF) mode. The crystalline part of the sample will thus appear dark and defect as bubble will appear bright. Instead, if the direct spot is excluded by the diaphragm, images are in dark-field (DF) mode. In this mode, the crystalline part of the sample will appear bright while bubbles will be dark. It may also be interesting to select only a part of the diffracted beams to improve the resolution of the image by removing the electrons away from the optical axis responsible for aberrations.

The diffraction pattern is generated by the whole sample, sometimes it is preferable to restrain the zone that scatters to study a specific area, for example when a lamella is bend or in case of poly-crystalline samples. To this aim, another diaphragm called the “selective area diffraction” (SAD) aperture is placed at the first image plane of the lower objective lens. As shown in Figure 43, a virtual diaphragm is likely positioned at the sample plane and restrain the illumination to the selected area.

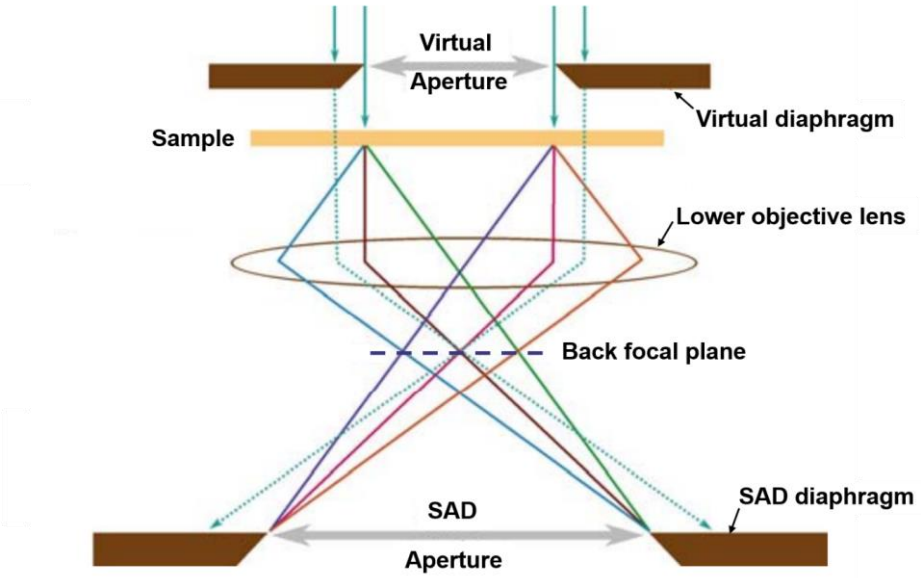

Figure 43: Schematic representation of the use of the SAD aperture to select the diffraction of a precise area. Once the SAD aperture is engaged, a virtual aperture localized at the sample plane (represented slightly above) is acting as a mask and restrains the illuminated area.

Bubble observation

To enhance the contrast on a TEM image, different configurations of the microscope may be used depending on the type of defects. The review in ref. [156] describes different configurations to characterize radiation-damages in metals and in particular voids and gas-bubbles, which is mentioned as well is refs. [152,154]

For large bubbles (diameter more than 5 nm), the structure factor contrast is sufficient to visualize bubbles. This contrast is due to the lower thickness of W to pass through as compared with a filled part (without bubble). Figure 44 is an example of a large bubble visualized without using the objective aperture. The high resolution of the image allows clearly to see the faceting of bubbles that will be studied in chapter 4 and atomic columns of the W matrix.

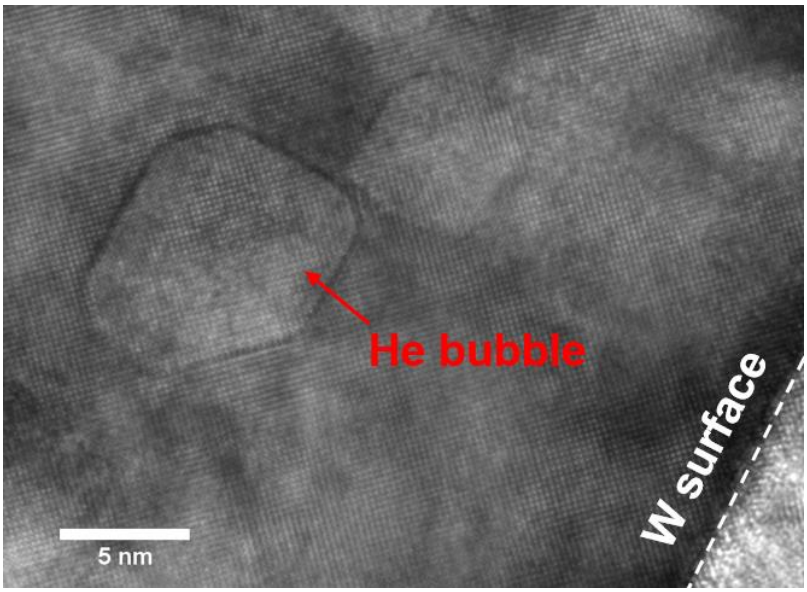

Figure 44: High resolution TEM micrograph of a helium bubble obtained without use of the objective aperture.

To obtain such an image, the sample has been oriented along a zone axis, i.e. the sample has been tilted to align the incident electron beam along a crystallographic direction of the sample. In this case the zone axis is [001].
In practice, this can be done by visualising in diffraction mode the reciprocal space, then tilting the sample to find intense spots series that respect the symmetry of the crystallographic structure. Indexation of the zone axis can be done by comparing with the standard diffraction patterns provided in Appendix.

The structure factor contrast alone is limited, as the thickness of the lamella increases, the contrast is weaker until bubbles become invisible. Therefore, the preparation of the sample to obtain a thin enough lamella is crucial.

Small bubbles (diameter less than 5 nm), are difficult to visualize by the structure factor contrast. Instead, the visualization of small bubbles is performed taking advantage of the phase contrast. The phase contrast also called Fresnel contrast arises from the potential difference between the inner bubble and the W matrix. In addition, observation of small bubbles is easier in kinematical diffraction conditions i.e. by tilting the sample to deviate from the exact Bragg conditions (off a zone axis). Calculation of the phase contrast can be found in ref. [154]. In practice, the observation of small bubbles is performed as follow:

i) Once the sample has been oriented, the objective aperture is engaged to switch to BF mode

ii) In imaging mode, the sample is tilted to enter in kinematical diffraction conditions. The W matrix will alternatively be dark then bright. The tilting is stopped when the W matrix is bright. In general, a tilt of just a few degrees (up to 5°) is enough. Tilting according to the eucentric angle avoid z-readjustment. In addition, as seen in Figure 44, bubbles can be facetted, it is recommended to limit the tilting angle with respect to the zone axis to properly index the crystallographic facet planes.

iii) Bubbles are then observable using either over or under focus conditions.

As shown in Figure 45, bubbles appear bright surrounded by dark fringe in under-focus images and dark surrounded by bright fringes in over-focus conditions. Some of the smallest bubbles as those marked with coloured arrows in Figure 45 are not visible in in-focus condition.

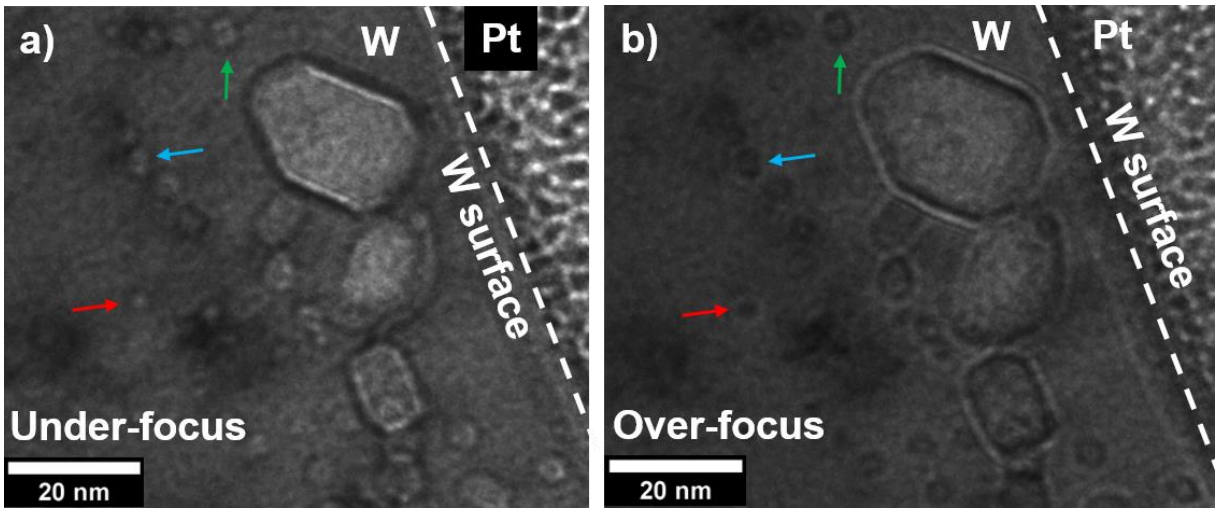

Figure 45: TEM micrograph of He implanted W. In a) the image has been recorded in under-focus conditions, bubbles appear bright surrounded by a dark fringe. In b) the image is in over-focus conditions, bubbles are dark and surrounded by a bright fringe. Each coloured arrow shows the same small bubble in under and over focus conditions.

Size measurements of bubbles must be performed in in-focus conditions. Except for invisible bubbles in in-focus conditions, extrapolation of the bubble size by a series a measurements using different focus values can give an reasonable estimate of the bubble size [157,135].

Characterization of the 3D shape of bubbles will be discussed in chapter 4.

3.5. **Overview of the experimental conditions**

The aim of this work was to investigate separately the effect of different parameters on the formation and behaviour of He bubbles. To that end, we have characterized He bubbles in W using nanoscience methods and techniques. Our approach is based on He implantation in single-crystalline W under well-controlled experimental conditions. In-operando GISAXS measurements in real time during He implantation have been performed to get access to the dynamics of the formation and evolution of bubbles. In combination, post-mortem microscopy measurements have been performed. Essentially, SEM and TEM have been used to characterize samples, giving a precise and direct vision of the final stage.

Three experimental campaigns have been performed with the INS2 set-up (ESRF synchrotron) during this thesis. The impact of the crystal orientation, the temperature and the ion implantation energy on the bubble population has been studied.
In this manuscript, the different samples are labelled using their surface orientation and the implantation conditions, i.e. the temperature and the ion energy. Four samples have been annealed after implantation, in this case, an asterisk is added to their identification label. As example, the (110) single crystal implanted at 1273 K with 2 keV He ions and annealed after implantation is called: $W(110)^{*}_{1273K,2keV}$.

Table 4 summarizes the exposure conditions for the three campaigns with the corresponding sample identification and GISAXS parameters. In addition, a schematic summary of the different experiments is given in Figure 46.

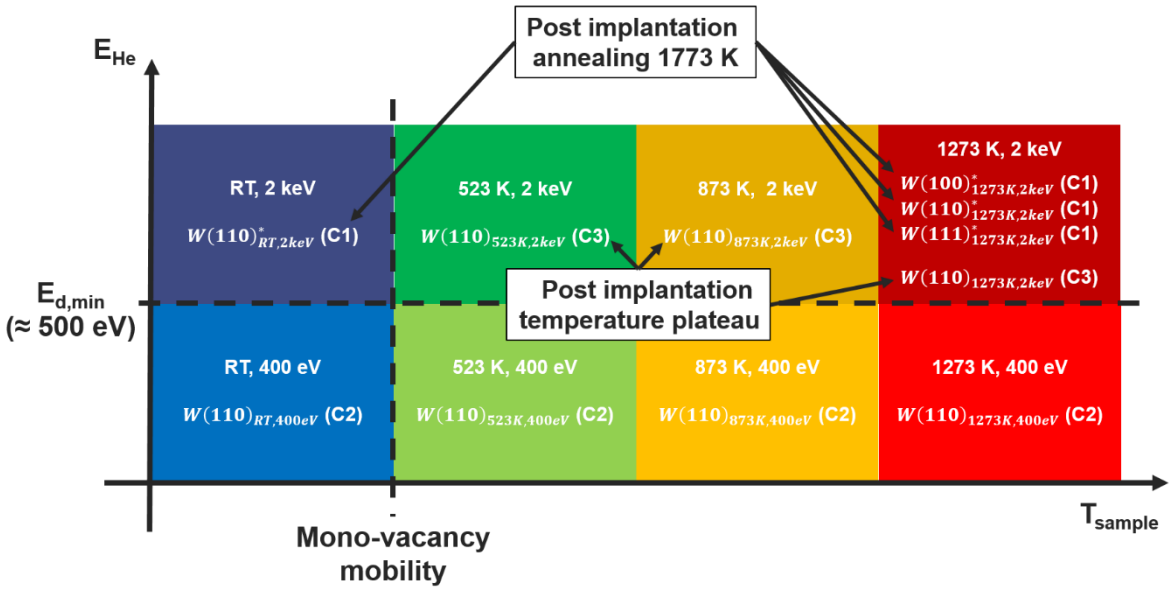

Figure 46: Schematic summary of the different experimental parameters explored in this study.

Surface orientation

Sample surfaces were oriented along {100}, {110} or {111} crystallographic plane with a precision below 0.1°. The effect of the surface orientation has been studied exclusively during the first campaign (C1).

Temperature

The temperature is a key parameter in the bubble kinetic evolution. This parameter has been studied during the three campaigns (C1, C2 and C3). The range of temperature has been chosen to cover different level of vacancies mobility in W. He implantations have been performed at room temperature (RT), 523 K, 873 K and 1273 K.
At RT vacancies are immobile, around 550 K mono-vacancies get mobile and diffuse in the material [158,159]. Progressively at higher temperatures, larger vacancies cluster can migrate. Once diffusing in the material, vacancies can agglomerate forming clusters, being absorbed in bubble or being annihilated at the surface of by Frenkel pair recombination.
The effect of temperature on the evolution of bubbles in absence of He implantation has been studied. During the third campaign (C3) some samples have been maintained at their implantation temperature for several hours after the implantation. Samples implanted during the first campaign (C1) have been annealed up to 1773 K after implantation to reproduce the heating of an ITER component due to transient events. This high temperature allows also getting closer to the thermodynamic equilibrium of bubbles. This condition is a requirement to determine the intrinsic effect that He could have on W.

Implantation energy

For each studied temperature (RT, 523 K, 873 K and 1273 K) at least two implantations conditions with 400 eV and 2 keV He ions have been performed. Those energies have been chosen respectively below and above the threshold displacement energy of W by He (~500 eV, see section 2.1.2). At 400 eV, the production of displacement damages is avoided while at 2 keV displacement damages produced during He implantation are expected. The 400 eV implantations have been performed during the second campaign (C2) and 2 keV implantations have been performed during the first and the last campaigns (C1 and C3).

X-ray parameters

GISAXS analyses were performed to have a statistically significant determination of the size and shape of bubbles in the sample. In-operando GISAXS measurements were performed to have access to the dynamics of processes (growth, shape change…). The X-ray energy was 10 keV (wavelength $\lambda = 0.124$ nm) for the first campaign (C1) and 18 keV (wavelength $\lambda = 0.069$ nm) for the second and third campaigns (C2 and C3). The penetration length of X-ray in the material according to

the incident angle is represented in Figure 22. The critical angle for total external reflexion is $\alpha_c = 0.43°$ at 10 keV and $0.26°$ at 18 keV.

Campaign	Sample ID	Surface orientation	Implantation Energy	Temperature	Flux ($m^{-2}.s^{-1}$) ↓ Fluence (m^{-2})	Temperature treatment after implantation	X-ray energy	Sample-detector distance (mm)
C1	$W(110)^{*}_{RT,2keV}$	{110}	2 keV	RT	2.4×10^{17} ↓ 1.0×10^{22}	Annealing up to 1773 K	10 keV ($\lambda = 0.124$ nm)	1246
	$W(100)^{*}_{1273K,2keV}$	{100}		1273 K				802
	$W(110)^{*}_{1273K,2keV}$	{110}						1286 802 (annealing)
	$W(111)^{*}_{1273K,2keV}$	{111}						1246
C2	$W(110)_{RT,400eV}$	{110}	400 eV	RT	1.0×10^{17} ↓ 4.3×10^{21}	No treatment	18 keV ($\lambda = 0.069$ nm)	1143
	$W(110)_{523K,400eV}$			523 K				
	$W(110)_{873K,400eV}$			873 K				
	$W(110)_{1273K,400eV}$			1273 K				
C3	$W(110)_{523K,2keV}$		2 keV	523 K	1.9×10^{17} ↓ 1.0×10^{22}	Temperature plateau for several hours		823
	$W(110)_{873K,2keV}$			873 K				
	$W(110)_{1273K,2keV}$			1273 K				

Table 4: Experimental parameters of the three experimental campaigns performed in the ESRF synchrotron.

4. Helium bubbles characterization

4.1. Low temperature implantations **121**
4.1.1. Room temperature 121
4.1.2. 523 K implantations 128
4.1.3. 873 K implantations 135

4.2. High temperature implantation and annealing **137**
4.2.1. Non-annealed samples implanted at 1273 K 137
4.2.2. Annealed samples implanted at 1273 K 141

4.3. Equilibrium shape of bubbles **146**
4.3.1. The Wulff theorem 146
4.3.2. Effect of pressurized He on the W surface energy 149
4.3.3. Form factor of the equilibrium shape of bubbles 151

This chapter will present the experimental investigations on the shape evolution of bubbles regarding different experimental conditions. The GISAXS and TEM techniques presented in the previous chapter have been used to characterize the bubble populations. The interest here is to characterize the bubble population at the end of implantation, therefore, post-mortem TEM analysis and GISAXS patterns mainly recorded after implantation will be shown here. The study of the dynamics of bubble formation and evolution will be treated in the next chapter.

This chapter is structured according to the implantation temperature. In the first section implantations at relatively low temperature will be presented i.e. room temperature (RT) then 523 K and finally 873 K. The second section will treat the major change in the bubble shape happening at temperatures higher than 1273K. The implantations at 1273 K and the case of post-implantation annealing up to 1773 K will be described. Finally, in the last section, the extremely high temperature reached during annealing allows to approach the thermodynamic equilibrium. The equilibrium shape of He bubbles in W will be determined and the effect of He on W surface energies will be addressed.

4.1. Low temperature implantations

4.1.1. Room temperature

At RT (~ 300 K) interstitial He clusters, SIA W and dislocation loops may be mobile while vacancies and He_nV_m clusters are immobile. It is worth to mention that the surface of sample $W(110)^*_{RT,2keV}$ implanted with 2 keV He ions was non-intentionally macroscopically damaged before the implantation. A wavy surface is visible with naked eyes. The wavy surface has led to un-controlled and inhomogeneous X-ray incident angle over the sample during GISAXS experiments. Thus, only the TEM characterisation after the post-implantation annealing up to 1773 K of the $W(110)^*_{RT,2keV}$ will be presented (in section 4.3.1).

TEM observations

TEM micrographs for the sample $W(110)_{RT,400eV}$ implanted at RT and low energy (400 eV) is shown in Figure 47.

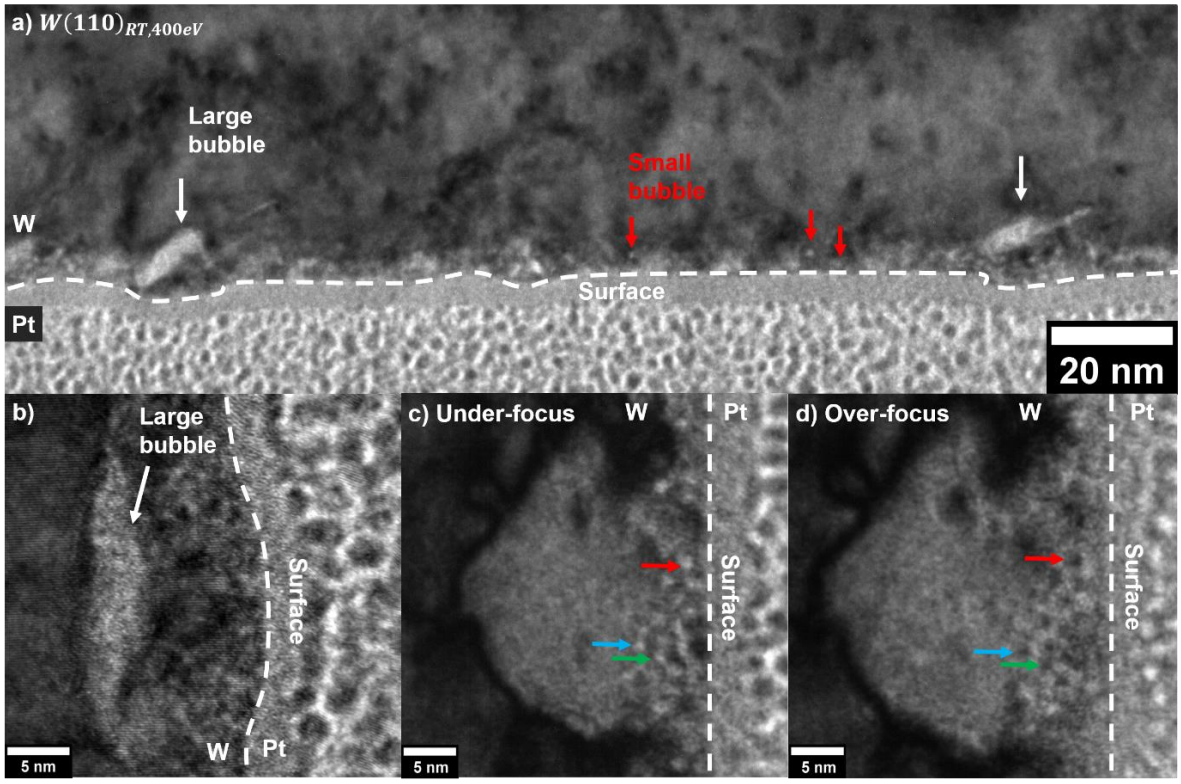

Figure 47: TEM micrograph of $W(110)_{RT,400eV}$ after 400 eV He implantation at room temperature. In a), a large field of view showing the presence of large bubbles (white arrows) and small bubbles (red arrows) within the first dozen of nanometers. In b), high magnification view of a large bubble deforming the surface. c) and d) are respectively the view in under and over focus conditions. Small bubbles are visible in bright (under focus) or dark (over focus) contrast. Some of those small bubbles are pointed with coloured arrows.

Large elongated bubbles with the largest size up to 12 nm have been observed (pointed out with white arrows in Figure 47a). Large bubbles are not specifically oriented in the sample as it could be thought in Figure 47a. For example, a bubble parallel to the surface is shown in Figure 47b. Large bubbles are responsible for surface deformation as seen on Figure 47a and b. In addition, small spherical bubbles with diameter approximately equal to 1 nm are visible. Bubbles are too small to be visualized in in-focus condition. Nevertheless, the observation of those bubbles is possible as presented in section 3.3.2 by setting the microscope in under and over-focus conditions. For example, Figure 47c and d show under and over-focused images where small spherical bubbles (some of them are indicated with coloured arrows) are seen in bright in under-focus and dark in over-focus conditions.

Black contrast like ink stains is visible, this contrast is typical to structural defect as dislocation loops and cloud of SIA. Those defects may have been produced in part by the formation and growth of bubble through the trap mutation and loop punching processes. Some structural defects may have also been generated by the FIB etching during the thin lamella preparation.

A possible explanation of the formation of large bubbles is the growth by successive static coalescence events of small bubbles. Indeed as seen in section 2.2.1., according to MD simulations [85], the neighbourhood of a bubble is occupied by structural defects generated by its growth. This environment is a preferential nucleation site for new bubbles. Thus, once bubbles are formed by He agglomeration and trap-mutation mechanisms, the successive absorption of He atoms makes the bubble grow, that generates a cloud of defect in the surrounding acting as preferential nucleation sites for other bubbles. Once a new bubble is nucleated, the distance to the pre-existing bubble is only a few atomic layers, hence a small increase in the size of the bubbles could be enough to make them coalesced.

GISAXS analysis

To measure 3D shape anisotropies, GISAXS patterns were measured at different azimuths, i.e. by rotating the sample around the normal of the surface (ω angle, see Figure 20) while maintaining the grazing incidence.

Figure 48 shows the GISAXS measurements performed on $W(110)_{\mathrm{RT,400eV}}$ after implantation. Patterns have been selected to correspond to X-ray beams aligned along the $[001]$ (Figure 48a), $[1\bar{1}1]$ (Figure 48b) and $[1\bar{1}0]$ (Figure 48c) direction with 0.47° of incident angle.

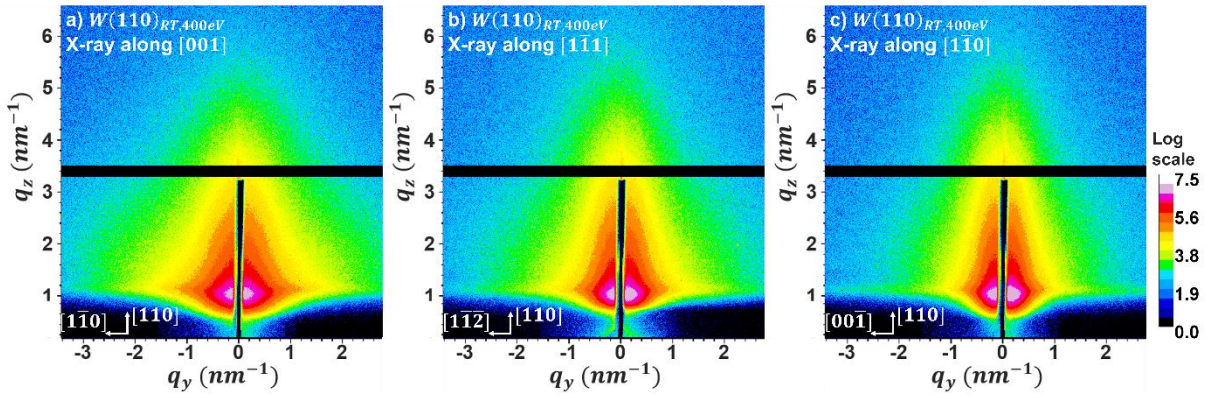

Figure 48 : GISAXS patterns at $\alpha_i = 0.47°$ of $W(110)_{RT,400eV}$ after 400eV He implantation at RT. The X-ray incident beam are aligned along the directions: (a)$[001]$, (b) $[1\bar{1}1]$ and (c) $[1\bar{1}0]$.

The GISAXS patterns show a more extended diffuse scattering in the $[1\bar{1}0]$ direction when the beam is along the $[001]$ direction (Figure 48a) and shrinks when the sample is rotated, until 90° when the X-ray beam is aligned along the $[1\bar{1}0]$ (Figure 48c). The GISAXS pattern is therefore not isotropic as it would be expected for spherical bubbles. The deviation from the expected spherical scattering indicates a strong influence of the large and elongated bubbles seen by TEM. A preliminary interpretation of the different GISAXS patterns is that as the diffuse scattering shrinks in the $[00\bar{1}]$ direction it means that large bubbles are preferably elongated in this direction. While they are contracted in the $[1\bar{1}0]$ direction as seen by the extension the diffuse scattering in this direction.

GISAXS modelling

A more deeper interpretation of GISAXS measurements has been conducted using IsGISAXS software [145]. A model fixing the bubble characteristics must be provided (e.g. the shape, size distribution, depth location…) then experimental data are fitted in the framework of the DWBA to adjust the bubble characteristics. Finally, GISAXS patterns are simulated and compared to experimental patterns.

Thompson et al. [160] have developed a He bubbles model to fit the GISAXS data obtained on polycrystalline samples. In their study, samples were exposed to He plasma in the Large Helical Device (LHD). The sample was maintained at 1073 K, the flux was estimated at $1.0 \times 10^{20}\ m^{-2}s^{-1}$ and the fluence $1.0 \times 10^{23}\ m^{-2}$. Ion energy was contained between 2 keV for the upper limit and below 500 eV for the lower energy. In order to fit their GISAXS measurements and determine the bubbles shape, they have been compared with two models based on different bubbles shapes. 1) spherical bubbles and 2) spheroidal bubbles, i.e. a sphere elongated in the surface plane and compressed in the direction normal to the surface. In the first case the sphere is described by its radius R and in the second case the spheroid is described by its radius R in the surface plane and the height H in the direction normal to the surface. A sphere can be obtained from a spheroid if H=2R, in the present case, the ratio H/R is expected to be lower than 2.

They have also considered that the bubbles diameter (d = 2R) is distributed according to an exponential law given by:

$$P(d,\mu) = \frac{1}{\mu}\exp\left(-\frac{d}{\mu}\right)$$

Where μ is the mean diameter.
They have concluded that bubbles were spheroids with a mean diameter of 0.6 ± 0.1 nm and the ratio $\frac{H}{R} = 1.4$.

In our case, based on TEM observations, we consider that two types of bubbles exist. The first one corresponds to spherical bubbles described by a radius R_1 and the second one to spheroids formed by coalescence defined with an in-plane radius R_2 and the ratio H/R_2. In addition, we will consider the radius distributed by a log normal law given by:

$$P(R,m,\sigma_g) = \frac{1}{Rln(\sigma_g)\sqrt{2\pi}}\exp\left(-\frac{ln^2(R/m)}{ln^2(\sigma_g)}\right)$$

With m the median and σ_g the geometric standard deviation.
This type of distribution has already been reported by TEM in polycrystalline samples exposed to He plasma in Ref. [135].

In order to fit the data, the background must be subtracted. To that end, the reference before implantation is subtracted from the pattern of interest as shown in Figure 49.

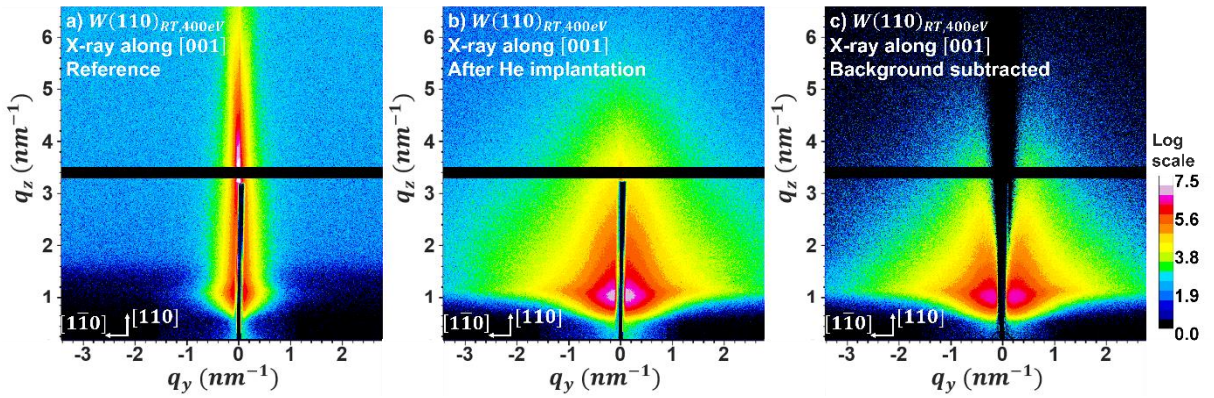

Figure 49: Background subtraction of GISAXS data. The reference pattern recorded before He exposure in a) is subtracted from GISAXS pattern obtained after implantation (b). In c) is the resulting pattern.

The inputs of IsGISAXS are intensity profiles along lines extracted from the experimental patterns. Three cuts represented in Figure 50 have been extracted. In principle cuts can be extracted anywhere but a preferential choice of cut depending on the model used is advised. In our case, the vertical and horizontal cuts have been chosen to better extract the diffuse scattering arising from elongated bubbles and the

45° cut to better fit spherical bubbles. Of course, diffuse scattering generated by both species are present in all the cuts, thus, all cuts are fitted by the two species model. Finally, a particular attention regarding the cuts must been taken to minimize the contributions of the vertical specular scattering and the horizontal Yoneda peak.

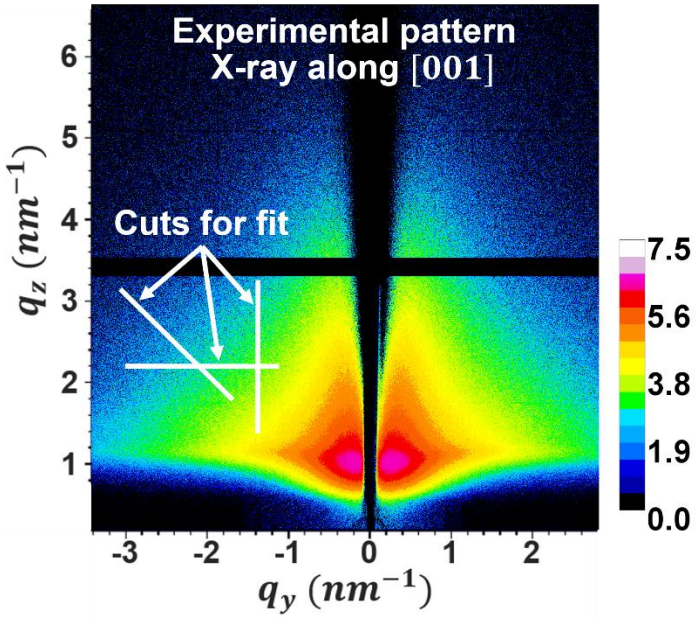

Figure 50 : GISAXS pattern after background subtraction of $W(110)_{RT,400eV}$ recorded at $\alpha_i = 0.47°$. Three intensity profile represented by white lines have been extract for the fit by IsGISAXS.

The starting values of the fitted parameters (e.g. mean size, size distribution, depth …) have been measured by TEM over 40 bubbles. However, due to obvious statistical limitation, the relative proportion of spherical/spheroidal bubbles is difficult to appreciate by TEM. Hence, the starting value of relative proportion has been investigated by generating a set of simulated GISAXS patterns with different spherical/spheroidal repartition (see Figure 51).
The relative proportion has been roughly estimated to 99.9% of small bubbles and 0.1% of large bubbles. This proportion corresponds to one large bubble per a thousand small bubbles that is also roughly their volume ratio (the estimated radius of large bubbles is ten times greater than that of small bubbles). This is consistent with the fact that the scattered intensity is proportional to the volume of the scatterers and both large and small bubbles seem to contribute. The contribution of spheroidal bubbles is hence dominant due to their larger volume, but small spherical bubbles must still be taken into account since their number is very large.

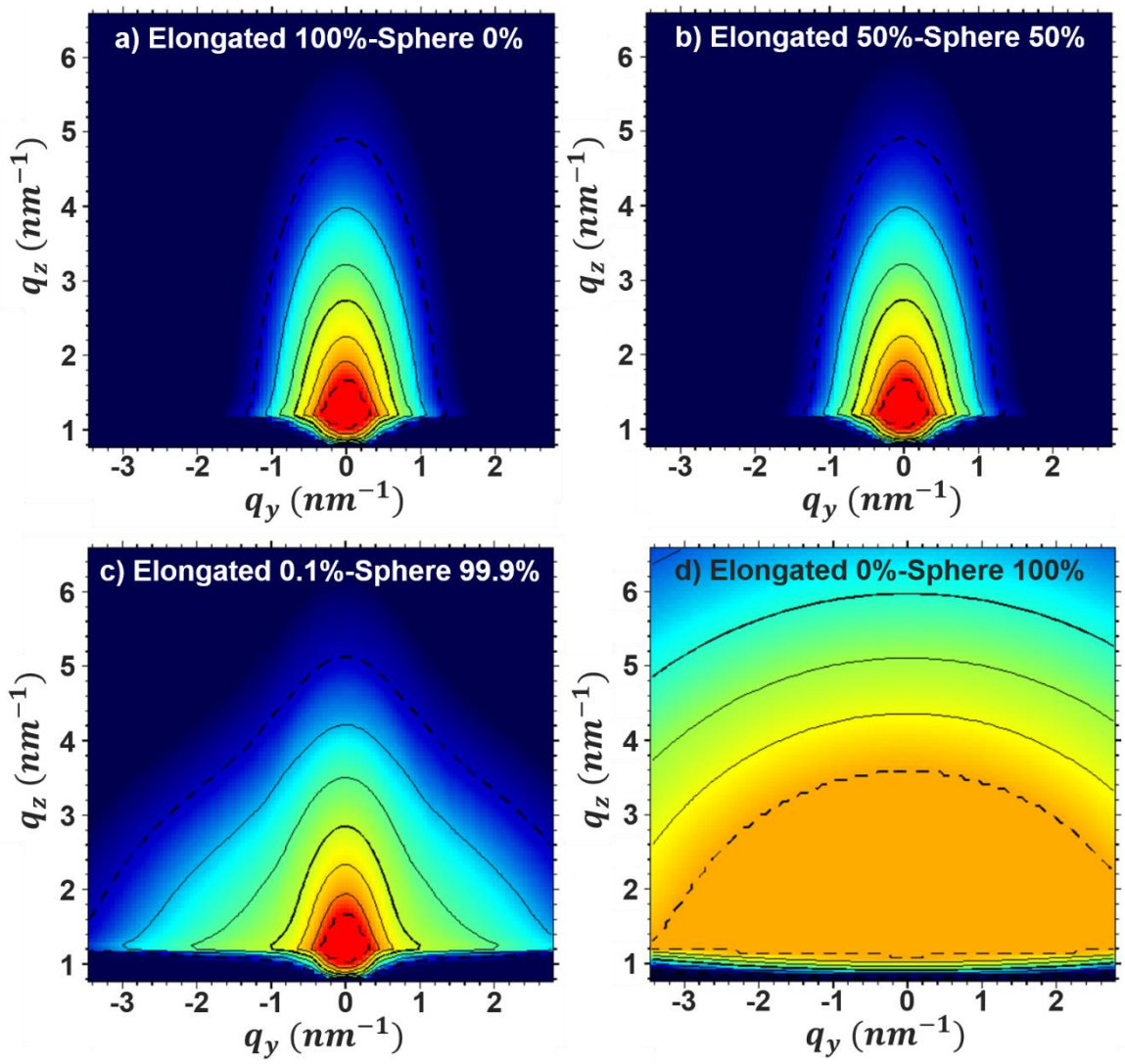

Figure 51: Effect of the proportion between small spherical bubbles and large elongated bubbles. Simulated GISAXS patterns with 100% of elongated bubbles a), 50%-50% of elongated-spherical bubbles b), 0.1%-99.9% elongated-spherical bubbles c) and 100% spherical bubbles in d).

A reasonable fit based on the two species model has been obtained as shown in Figure 52. Table 5 summarises the first guess values measured by TEM and the different parameters after fitting. We deduce that the typical radius of small bubbles is 0.7±1.3 nm and 4.4±1.6 nm for large bubbles. They appear as flattened since H/R=0.56.

		Species 1: spherical bubbles			Species 2: elongated bubbles		
Sample	Parameters	Median radius	Geometric standard deviation	Prop ortion	Median radius	Geometric standard deviation	H/R
$W(110)_{RT,400eV}$	TEM	0.6	1.25	X	6.6	1.3	0.55
	Fit	0.7	1.29	99.8 %	4.4	1.59	0.56

Table 5: Fitted parameters for $W(110)_{RT,400eV}$ after implantation.

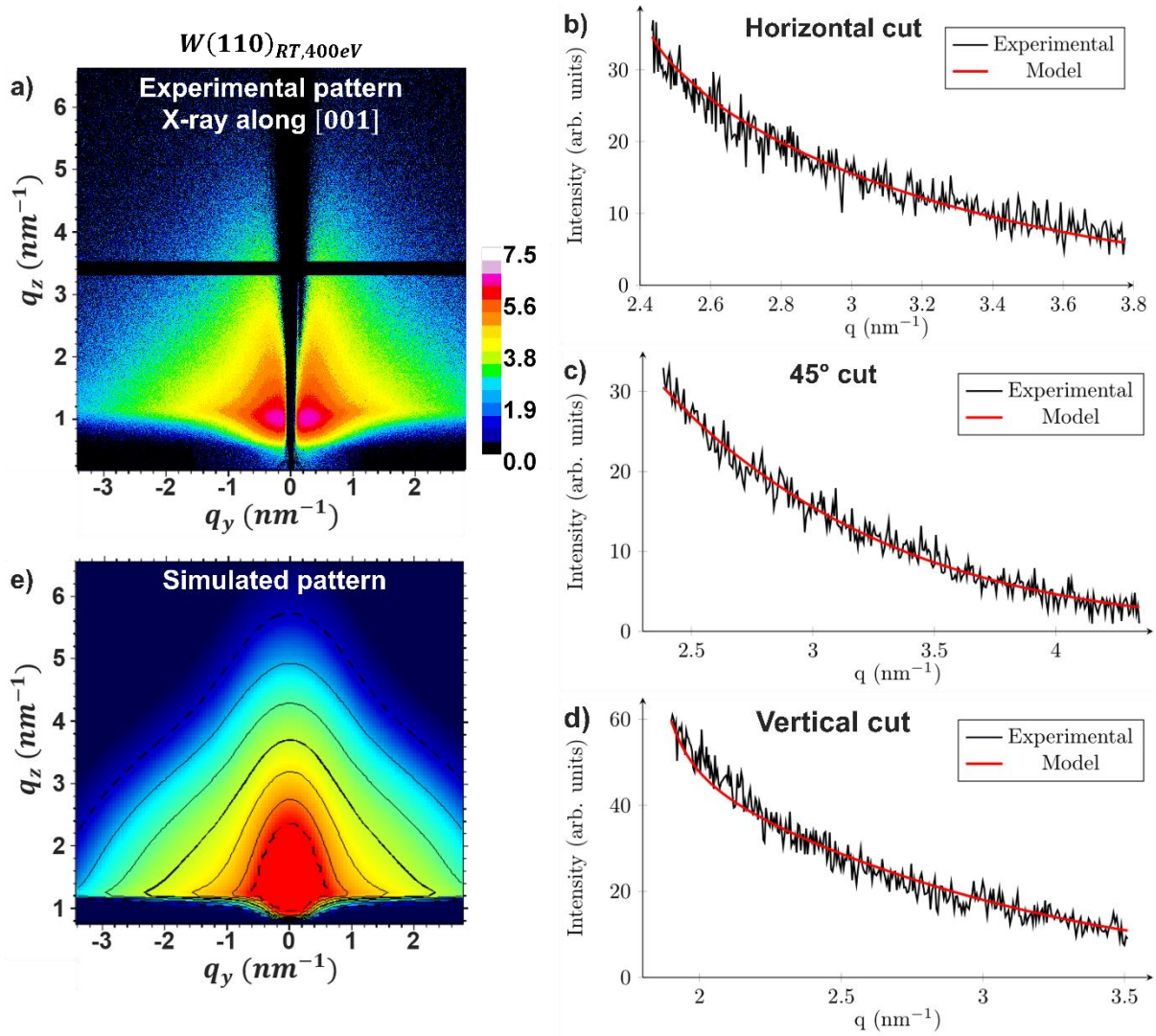

Figure 52: In a) GISAXS pattern after background subtraction of $W(110)_{RT,400eV}$, recorded at $\alpha_i = 0.47°$. Three intensity profiles represented by white lines have been extracted for the fit by IsGISAXS. The experimental profiles in black and the fit obtained in red for the horizontal cut b), 45° cut c) and vertical cut d). In e) is the resulting GISAXS pattern simulated with the fitted parameters.

TEM measurements provide suitable first-estimate values for fitting GISAXS data. In addition, the direct view obtained by TEM is very helpful to build the model that must be used. This highlights the great complementarity between the two techniques.

4.1.2. **523 K implantations**

At 523 K, mono-vacancies are still immobile but the temperature threshold to become mobile is close (573 K) [158].

TEM observations

TEM micrographs of $W(110)_{525K,400eV}$ and $W(110)_{523K,2keV}$ after implantation are shown in Figure 53.

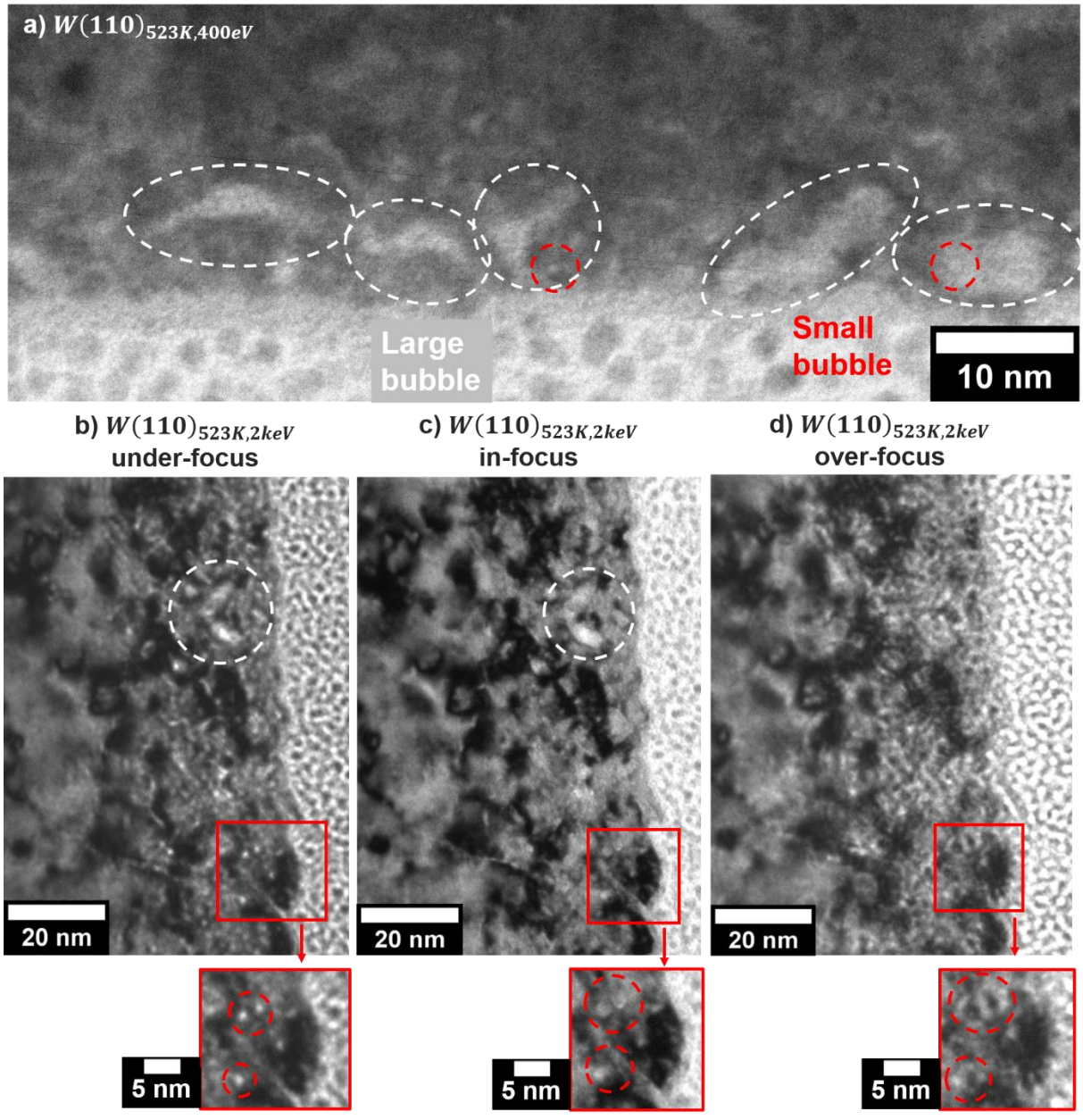

Figure 53: TEM micrographs of $W(110)_{523K,400eV}$(a) and $W(110)_{523K,2keV}$ (b-d) and after implantation at 523K with 400eV and 2 keV He ions respectively. b), c) and d) are TEM images of the same area taken in under-focus, in-focus and over-focus conditions. Large bubbles with size of several nanometers are shown by the white dashed circles and small spherical bubbles are shown by red dashed circles.

Sample $W(110)_{523K,400eV}$ (Figure 53a) is globally similar to the sample $W(110)_{RT,400eV}$ implanted with the same energy at RT. Elongated bubbles are visible (see white circles) and small bubbles with diameter measuring approximately 1 nm are also visible (see red circles). Unfortunately, the precise characterization of large and small bubbles is difficult because of the large thickness of the lamella prepared by FIB. Nevertheless, the bubbles seem to be spatially confined again in an area of approximately 10 nm deep.

In $W(110)_{523K,2keV}$ (Figure 53b-d) numerous dark patches corresponding to crystalline defects are visible. Many small bubbles appearing as white dots in under-focus image and dark dots in over-focus images (see red circles in insets for example). The bubble area is extended up to 40 nanometers deep in this case. Few bubbles have been observed up to 90 nm. Fewer large bubbles have been found in $W(110)_{523K,2keV}$ compared to 400 eV implanted samples (RT and 523 K).

GISAXS analysis

The GISAXS measurements reveal a difference in the bubble population between $W(110)_{523K,400eV}$ (Figure 54a-c) and $W(110)_{523K,2keV}$ (Figure 54d-f).

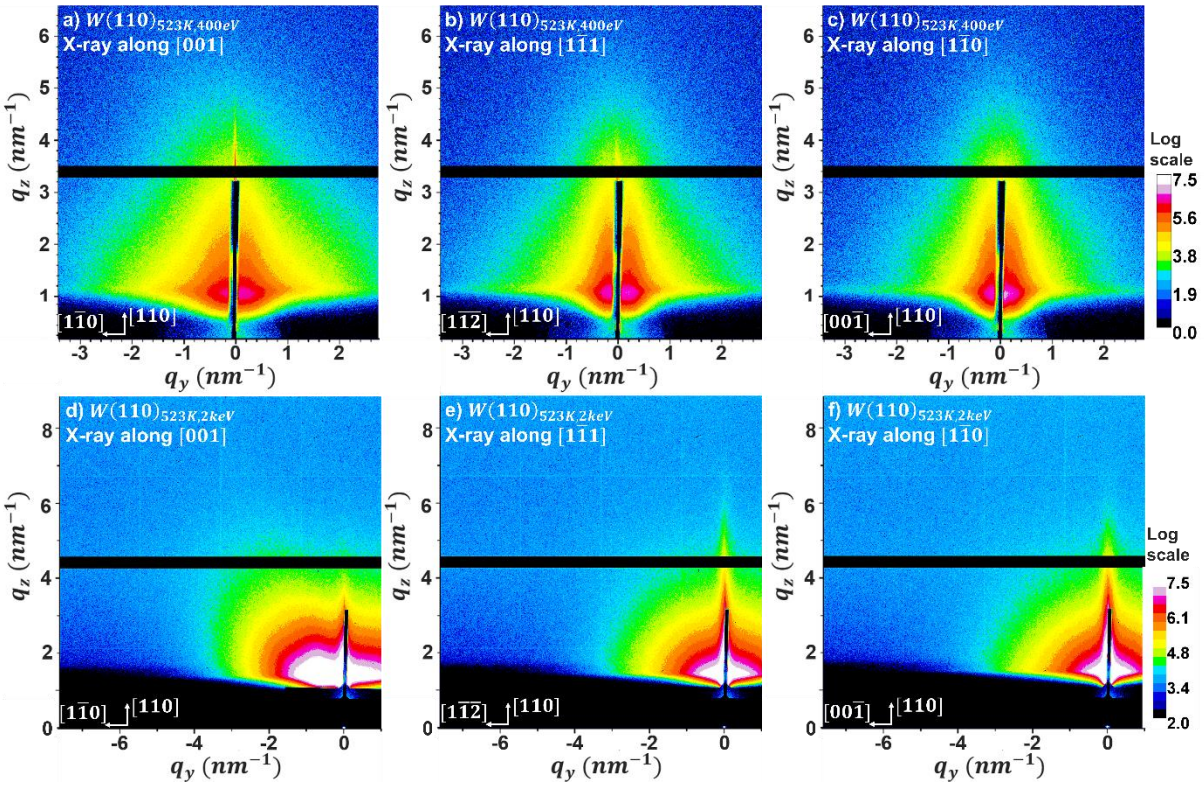

Figure 54: GISAXS patterns recorded at $\alpha_i = 0.47°$ for $W(110)_{523K,400eV}$ after 400eV He implantation and $\alpha_i = 0.6°$ for $W(110)_{523K,2keV}$ after 2 keV He implantation at 523 K. X-ray are aligned along directions: $[001]$ (a) and (d), $[1\bar{1}1]$ (b) and (e) and $[1\bar{1}0]$ (c) and (f).

For $W(110)_{523K,400eV}$, GISAXS patterns show a similar diffuse scattering anisotropy to what has been observed for $W(110)_{RT,400eV}$ implanted at room temperature. For the 2 keV implantation when x-ray are aligned along $[1\bar{1}1]$ and $[1\bar{1}0]$ (Figure 54e and f), the diffuse scattering patterns are isotropic meaning that bubbles are spherical in majority. This is in agreement with the TEM observations (Figure 53b-d) discussed above. However, for x-ray aligned along the $[001]$ direction (Figure 54a) the diffuse scattering seems laterally elongated. The source of this unexpected signal has been investigated by varying the incident angle α_i. For incident angle below the critical angle $\alpha_c = 0.26°$, the penetration depth of the 18 keV x-ray is limited to the extreme surface while, for the incident angle above the critical angle, x-rays can penetrate deeper in the material.
The corresponding GISAXS pattern at $\alpha_i = 0.2°$ (below the critical angle) is shown Figure 55.

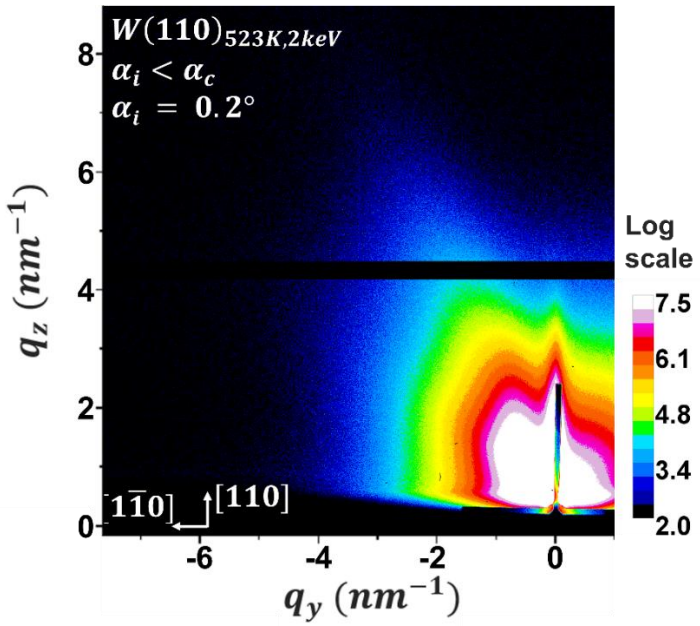

Figure 55: GISAXS pattern of $W(110)_{523K,2keV}$ with X-ray aligned along the $[001]$direction. The patterns have been recorded with incident angle α_i of 0,2° (below the critical angle) to enhance the surface sensitivity.

The signal is still visible at $\alpha_i = 0.2°$ meaning that it arises from the surface. This signal was absent before implantation (Figure 56a) and appeared during the first stages of implantation as seen in Figure 56b recorded few minutes after the ion gun has been activated. The signal is a vertical rod that corresponds to a crystalline flat surface parallel to the surface, the signal is more intense as He is continuously implanted as seen on the Figure 56c recorded 7 minutes later. A possible explanation is the formation of a transient superlattice structure due to surface contamination induced by the He ion gun. The “lattice” constant of the superstructure is given by the relation $d = \frac{2\pi}{\Delta q}$ where Δq is the reciprocal space distance between the position $q_{\parallel} = 0$ and the

vertical unknown rod. We have found $d \approx 4.7$ nm that corresponds to 15 times the lattice constant of W. In literature, surface reconstructions R(15X3) and R(15X12) on W(110) surface in presence of carbon impurity has been reported [161–163]. A reasonable explanation is therefore a transient surface contamination by carbon, which was probably emitted by the ion gun during its start-up phase.

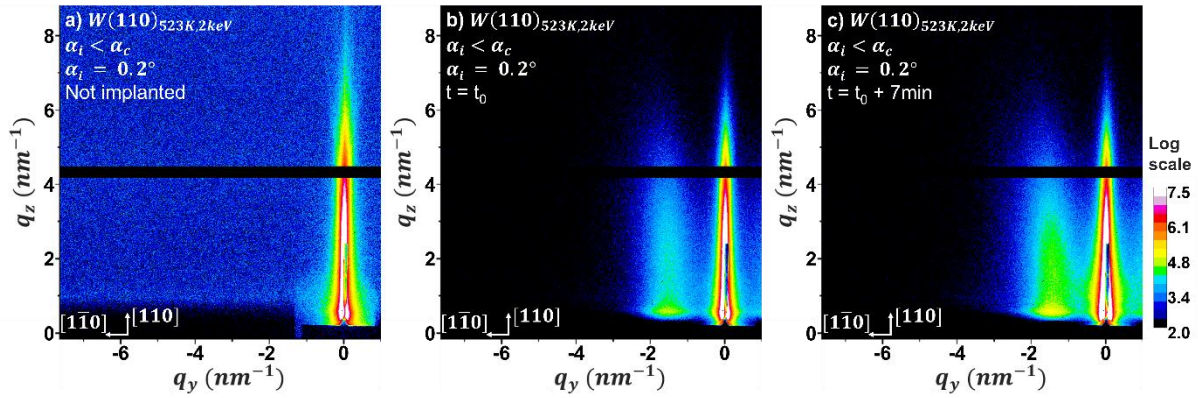

Figure 56: GISAXS patterns of $W(110)_{523K,2keV}$ with X-ray aligned along the [001]direction. The patterns have been recorded with incident angle α_i of 0,2° (below the critical angle) before implantation a), at the beginning of implantation b) and 7 minutes later c).

From TEM and GISAXS analysis it seems that an effect of the implantation energy could be to favour the formation of small spherical bubbles instead of large elongated bubbles. This behaviour may be explained by the following hypothesis: a 2 keV implantation generate a high amount of Frenkel pair defects especially in the He retention area. Bubbles would hence be more diluted by nucleating in vacancies instead of being nucleated at the periphery of a pre-existing bubble. The distance between bubbles will hence be relatively long preventing the static-coalescence events to occur.

GISAXS modelling

Fits of GISAXS data have been performed using the same procedure as described above. The model of two species has been used for both samples. The results of the fits are shown in Figure 57 for $W(110)_{523K,400eV}$ and Figure 58 for $W(110)_{523K,2keV}$. The fitted parameters are shown in Table 6.

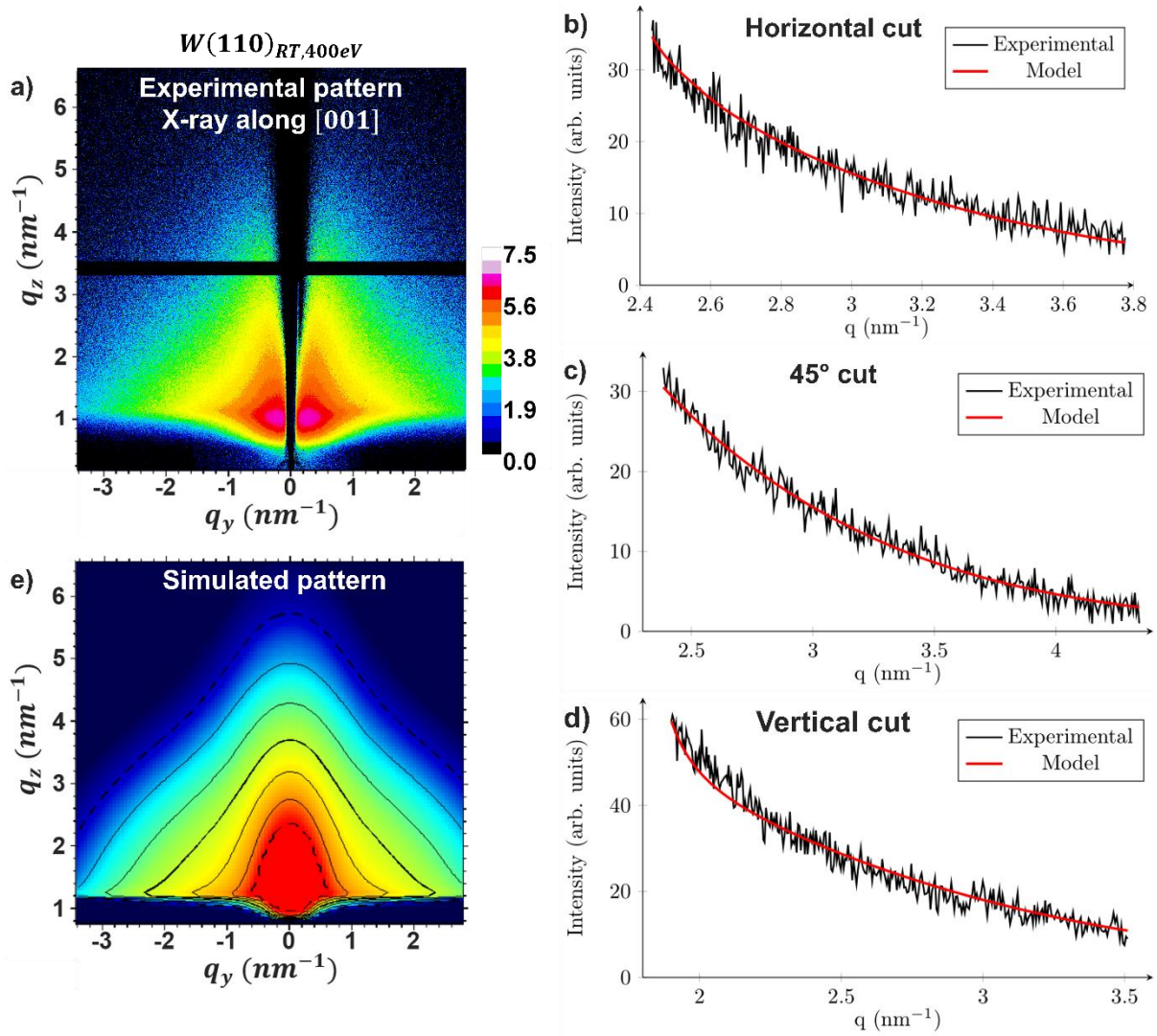

Figure 57: In a) GISAXS pattern after background subtraction of $W(110)_{523K,400eV}$, recorded at $\alpha_i = 0.47°$. Three intensity profile represented by white lines have been extracted for the fit by IsGISAXS. In b), c) and d) are represented the experimental profiles in black and the obtained fit in red. In e) is the resulting GISAXS pattern simulated with the fitted parameters.

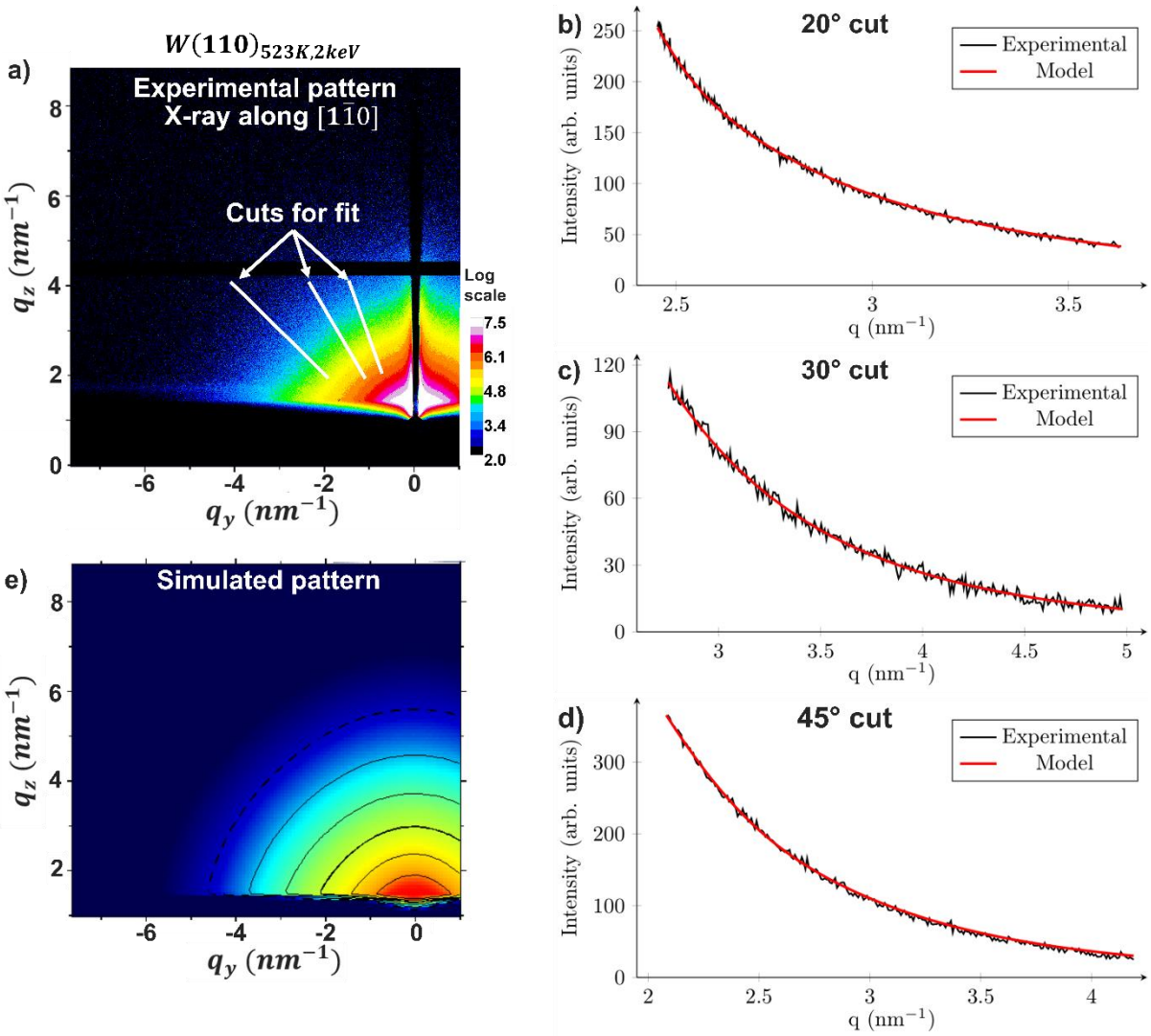

Figure 58: In a) GISAXS pattern after background subtraction of $W(110)_{573K,2keV}$, recorded at $\alpha_i = 0.6°$. Three intensity profiles represented by white lines have been extracted for the fit by IsGISAXS. In b), c) and d) is represented the experimental profiles in black and the fit obtained in red. In e) is the resulting GISAXS pattern simulated with the fitted parameters.

		Species 1: spherical bubbles			Species 2: elongated bubbles		
Sample	Parameters	Median radius	Geometric standard deviation	Proportion	Median radius	Geometric standard deviation	H/R
$W(110)_{523K,400eV}$	Fit	0.8	1.28	99.8%	4.5	1.51	0.59
$W(110)_{523K,2keV}$	TEM	0.8	1.39	X	4.9	1.65	0.63
	Fit	0.5	1.53	99.9%	6.1	1.30	0.68

Table 6: Fitted parameters for $W(110)_{523K,400eV}$ and $W(110)_{523K,2keV}$ after implantation.

For $W(110)_{523K,400eV}$ the median radius of spherical and spheroidal bubbles is globally the same compared to the RT implantation (0.8 nm versus 0.7 nm for spherical bubbles and 4.4 nm versus 4.5 nm for spheroidal bubbles). Consequently, temperature has no effect between RT and 523 K for 400 eV implantation. For the 2 keV case, spherical bubbles are slightly smaller (0.5 nm versus 0.7 nm) while spheroidal bubbles are larger (6.1 nm versus 4.5 nm). However, the proportion of spheroidal bubbles has been decreased in this case. If spheroidal bubbles are formed by static coalescence of spherical bubbles, it would indicate that with high energy implantation less bubbles have coalesced. A reasonable explanation is that with high energy implantation, vacancies acting as preferential nucleation site are generated randomly in the sample. The result is that the distance between bubbles is greater compared to low implantation energy case, preventing bubbles to coalesce. This could also explain why spherical bubbles are smaller as the implanted helium quantity is more diluted.

4.1.3. 873 K implantations

At 873 K vacancies can migrate and agglomerate to form clusters, being annihilated at the surface or absorbed by bubbles.

TEM observations

TEM images of $W(110)_{873K,400eV}$ and $W(110)_{873K,2keV}$ are shown in Figure 59.

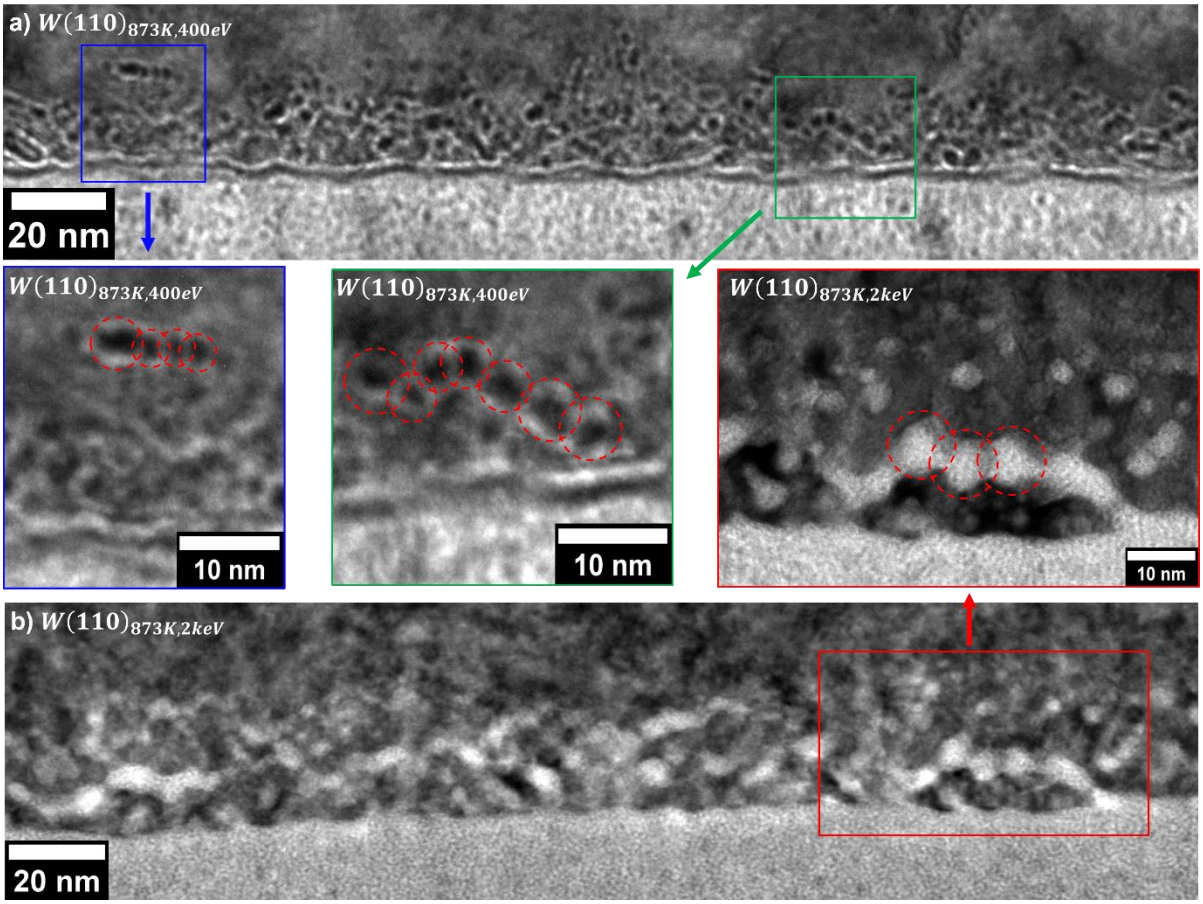

Figure 59: TEM micrographs of $W(110)_{873K,400eV}$(a) and $W(110)_{873K,2keV}$ (b) and after implantation at 873K with 400 eV and 2 keV He ions respectively. Blue and green insets for $W(110)_{873K,400eV}$ and red inset for $W(110)_{873K,2keV}$ show assembly of bubbles in pearl necklace like structures. In those structures, jointed bubbles are highlighted by red dotted circles.

Compared to the previous samples less displacement damages are seen in $W(110)_{873K,400eV}$, probably due to their annihilation after diffusion. Bubbles appear spherical with a diameter around 1.4 nm that is comparable to other 400 eV implanted samples. In addition, as shown in the blue and green insets many bubbles seem organised in line, but interconnection is not clearly visible.

In $W(110)_{873K,2keV}$ isolated bubbles with a diameter in the range 1.4-6 nm have been measured but more frequently bubbles are seen interconnected forming a network

broadly oriented parallel to the surface similarly to a pearl necklace. The red inset shows a closer view of this structure. Spherical bubbles are highlighted with red dotted circles. It seems clear that spherically shaped bubbles are connected by a thin corridor that supports the hypothesis of bubble coalescence. At 873 K, vacancies produced during the high energy implantation process can diffuse and be absorbed by the bubbles, causing them to grow and come into contact with one another. It results the formation of the pearl necklace arrangement seen on Figure 59.

GISAXS analysis

GISAXS measurements for the implanted samples at 873K are shown Figure 60.

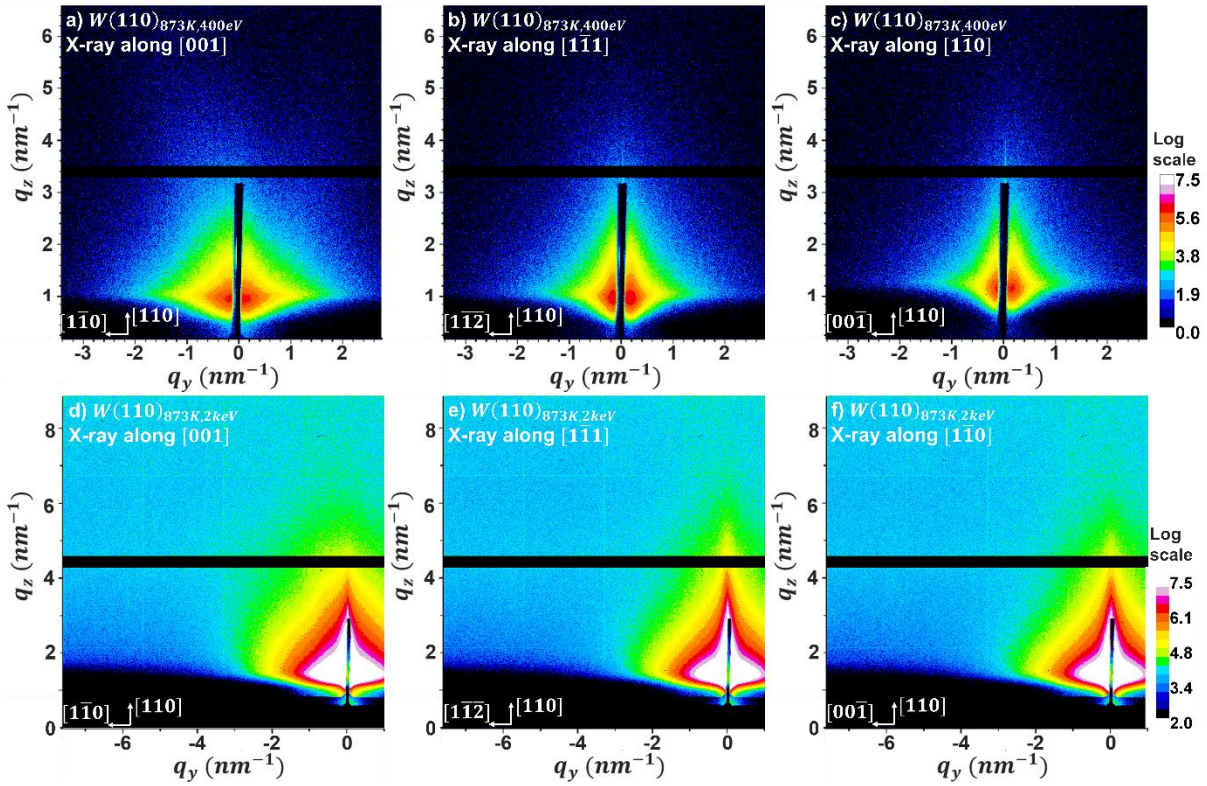

Figure 60: GISAXS patterns recorded at $\alpha_i = 0.47°$ for $W(110)_{873K,400eV}$ after 400eV He implantation and $\alpha_i = 0.6°$ for $W(110)_{873K,2keV}$ after 2 keV He implantation at 873 K. X-ray are aligned along directions: $[001]$ (a) and (d), $[1\bar{1}1]$ (b) and (e) and $[1\bar{1}0]$ (c) and (f).

The diffuse scattering anisotropy seen for other samples is again visible at this temperature. Nevertheless, GISAXS patterns are not identical. The patterns for the 2 keV implantation are more rounded compared to those of the 400 eV implantation.

The network structure formed by bubbles at 873 K is too complex for being reproduced by the simpler model used to fit the GISAXS data for RT and 523 K. Further work must be performed to build a new model.

4.2. High temperature implantation and annealing

At 1273K and above, bubbles have been reported facetted. Temperature has been identified as the key parameter in the formation of facets at the bubble surface. The temperature threshold to pass from rounded to facetted shape has been estimated in literature between 1073 K and 1223 K [114].

Both annealed and non-annealed samples will be presented in this section. First TEM analysis of non-annealed samples will be presented to allow a comparison with the low temperature implantations discussed above. Then, TEM observation of annealed samples will be discussed to go further in the characterization of the bubbles. GISAXS results will be presented in the same way, first non-annealed in the aim of comparison with the previous section then annealed sample for a detailed understanding of the quasi-equilibrium shape.

4.2.1. Non-annealed samples implanted at 1273 K

TEM observations

In our work, increasing the implantation temperature to 1273 K has indeed led to important modifications of bubbles shape. TEM observations of $W(110)_{1273K,400eV}$ and $W(110)_{1273K,2keV}$ after implantation are given in Figure 61.

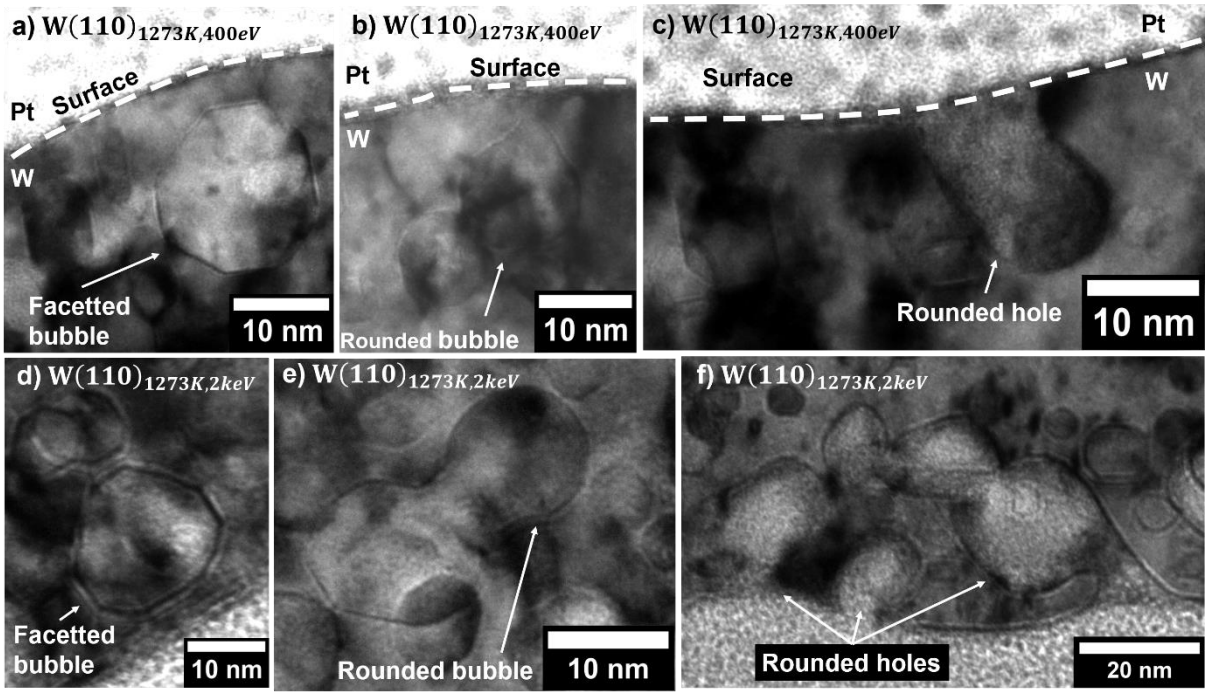

Figure 61: TEM micrographs of $W(110)_{1273K,400eV}$(a-c) and $W(110)_{1273K,2keV}$ (d-f) after implantation at 1273K with 400 eV and 2 keV He ions respectively. Facetted bubbles (a and d) and rounded bubbles (b and e) are formed at this temperature. Rounded holes (c and f) formed by bursting of bubbles are spherical.

Bubbles are visible in the first 20 nm deep in $W(110)_{1273K,400eV}$ and 40 nm in $W(110)_{1273K,2keV}$. Their radius varies from 1.0 to 10.9 nm for the 400 eV implanted sample and from 1.4 to more than 10.6 nm in the 2 keV implanted sample.
Some bubbles are elongated probably due to coalescence as seen in Figure 61e.
As expected at this temperature, some bubbles are facetted (Figure 61a and d). Nevertheless, some bubbles are non-faceted (Figure 61b and e). This means that the thermodynamic equilibrium has not been reached completely. It is worth to notice that both small and large bubbles have been observed either facetted or rounded. No evident size dependence for the formation of facets has been concluded. In addition, as seen in Figure 61c and f, many bubbles burst leaving holes at the surface. Interestingly, all holes observed are non-facetted. The rounded shape of bubbles and holes could correspond to transient shapes arising from a fast kinetic process (bursting and coalescence at the intermediate state).

The presence of He inside bubbles has been checked by energy electron loss spectroscopy (EELS). To that end, the first step consists to turn the microscope in scanning transmission electron microscopy (STEM) mode. STEM is commonly used to identify the difference in composition of a material. In this mode, the contrast shows a difference in atomic number so call Z-contrast (see ref. [154]). In Figure 62 is shown a TEM (Figure 62a) and a STEM (Figure 62b) image of a bubble. In STEM, W matrix appears in bright while the Pt layer on the surface appear dark. Bubbles can be

visualized by STEM thanks to the contrast with the W matrix, meaning that bubbles are either filled with vacuum or another element than W. Finally, the second step consist to perform EELS measurements to identify without doubt the chemical composition of bubbles. Figure 62c is the EELS spectrum obtained in the bubble shown in Figure 62a and b. The red curve is obtained for the measurement in the bubble (spot location represented by a red circle in Figure 62b) and the blue curve for a measurement in the W matrix surrounding the bubble. The bulk W Plasmon peak is visible at 24 eV for both curve and an additional peak at 21.9 eV is visible for the measurement inside the bubble. The additional peak corresponds to the 1s□2p electronic transition of free He atoms [72,164].

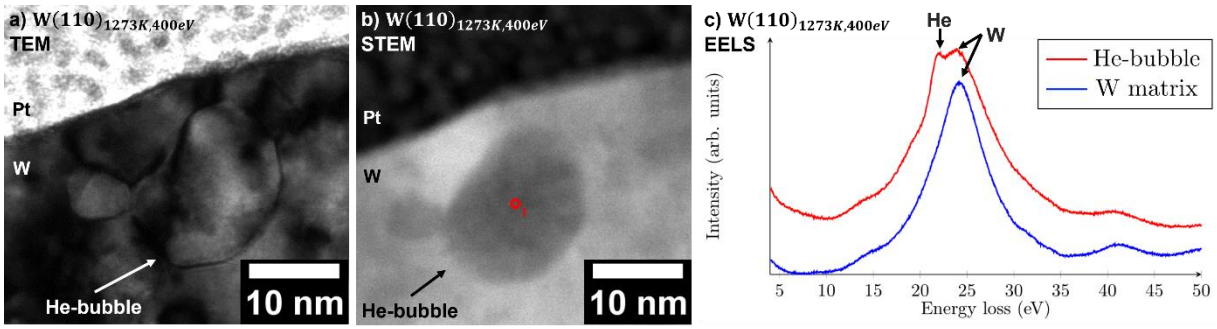

Figure 62: (a) TEM micrograph of a He-bubble. (b) STEM micrograph of the same area, bubble is filled by a lighter element compare to W. The red circle represents the electron spot for the EELS measurement. (c) EELS spectra recorded in the bubble (red curve) and in the W matrix (blue curve).

Bubbles are thus filled by pressurized He that could modify the thermodynamic properties of W surface. It could explain why bubbles turn faceted while holes remain rounded.

GISAXS analysis

GISAXS analyses of both samples are shown in Figure 63. Patterns are significantly different from what has been observed at lower temperature.

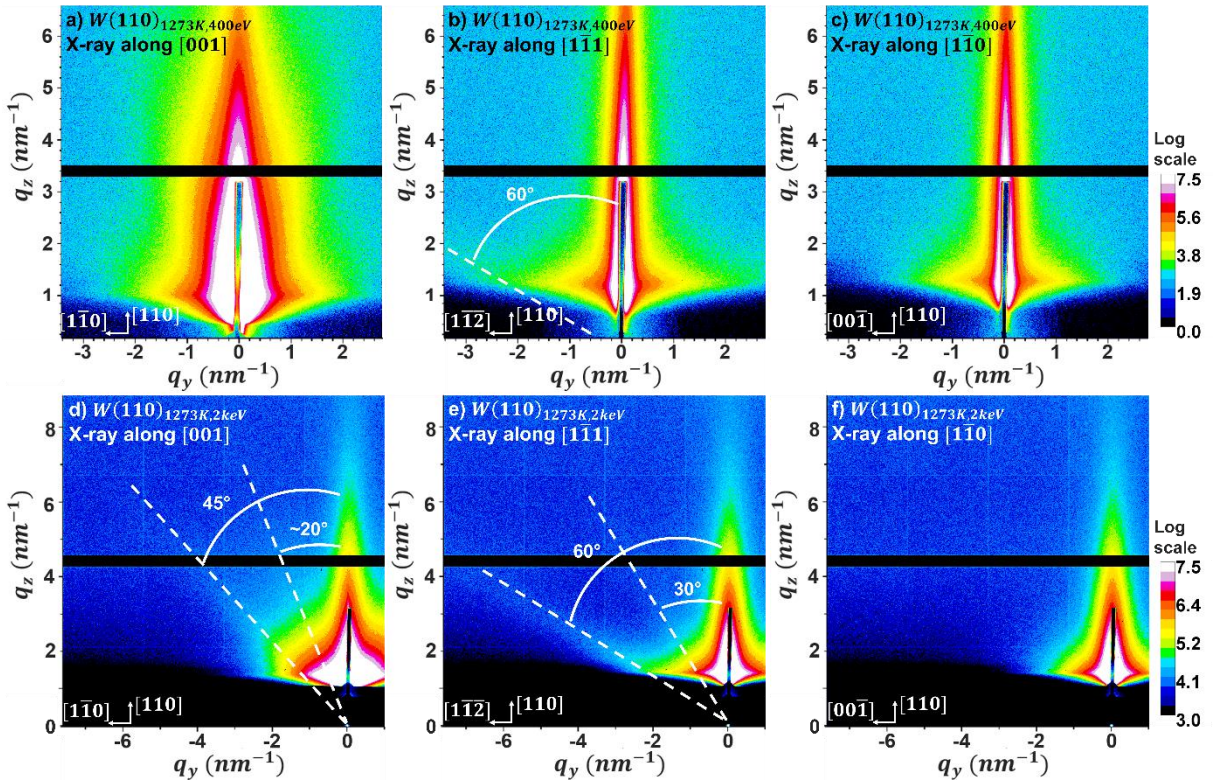

Figure 63: GISAXS patterns recorded at $\alpha_i = 0.47°$ for $W(110)_{1273K,400eV}$ after 400eV He implantation and $\alpha_i = 0.6°$ for $W(110)_{1273K,2keV}$ after 2 keV He implantation at 1273 K. X-ray are aligned along directions: $[001]$ (a) and (d), $[1\bar{1}1]$ (b) and (e) and $[1\bar{1}0]$ (c) and (f). Lateral streaks emanating from facets either on the sample surface or at bubbles surface are highlighted by white dashed lines.

For the 400 eV sample (Figure 63a to c), when the x-ray beam is propagating along the $[1\bar{1}1]$ direction (Figure 63b) a weak lateral streak at an angle of 60° with the surface normal is visible. This lateral streak results from a truncation by well-defined planes corresponding to facets [137].

For the 2 keV implantation (Figure 63d to f), the detector position has been adjusted for a better recording of this signal. The distance between the sample and the detector has been reduced and the detector has been moved to place the reciprocal space origin in the bottom right corner of the detector. When the x-ray beam is aligned in the $[001]$ direction, two lateral streaks are visible forming an angle of 45° and approximately 20° with the normal to the surface. For x-rays aligned along the $[1\bar{1}1]$ direction two more lateral streaks are visible at angle 60° and 30° with the normal to the surface direction. In Figure 63f, i.e. when the incident x-ray beam is along the [110] direction, no specific signal is seen.

The source of the four lateral streaks has been investigated, bubbles facets and surface planes are suspected to produce those signals. Except for the lateral rod at 45°, all other streaks are still visible on GISAXS patterns recorded with a X-ray incident

angle below the critical angle. We believed that some signals are due to both contributions from the sample surface and from the bubbles facets. In this case, it is not possible to clearly establish the source of those signals. A deeper understanding will be provided with annealed samples.

4.2.2. Annealed samples implanted at 1273 K

TEM observations

For annealed samples up to 1773K ($W(100)^{*}_{1273K,2keV}$, $W(110)^{*}_{1273K,2keV}$ and $W(111)^{*}_{1273K,2keV}$), TEM analyses reveal a similar distribution compared to the 2 keV implanted and non-annealed samples. He bubbles are distributed in the first 40 nm deep for all samples. The difference with non-annealed samples is that all bubbles are facetted, and it does not depend on the sample orientation. Some bubbles are elongated that could be due to coalescence as seen previously.

In Figure 64 is shown a series of TEM micrographs from the sample $W(100)^{*}_{1273K,2keV}$. TEM shown micrographs are representative for all annealed samples.

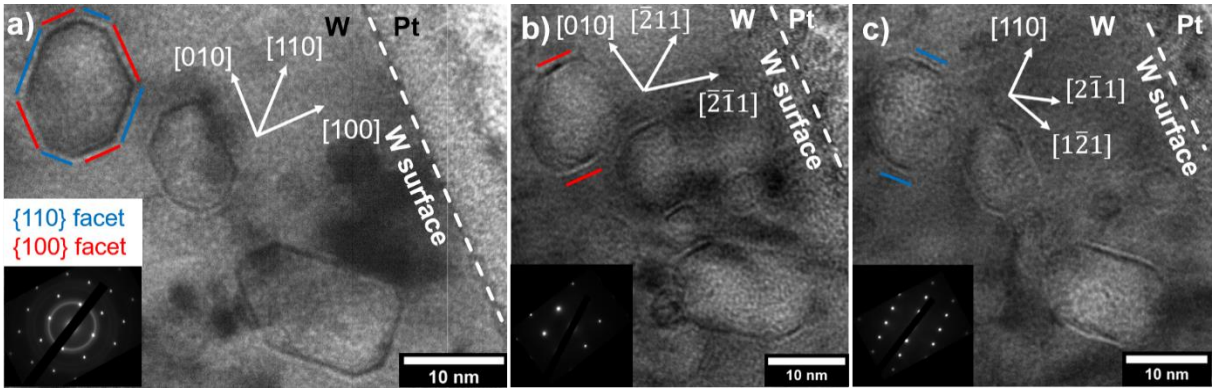

Figure 64: TEM micrograph of $W(100)^{*}_{1273K,2keV}$ implanted at 1273 K with 2 keV He ions then annealed to 1773 K. The tree images show the same area from close to the [001] zone axis (a), close to then [102] zone axis (b) and close to the [113] zone axis (c). Bubbles are faceted with {110} (in blue) and {100} (in red) planes.

Figure 64a has been recorded close to the [001] zone axis as shown by the diffractogram in the inset. Bubbles surface is composed of {110} and {100} planes marked respectively in blue and red. All other {hk0} planes are not detected meaning that {hk0} facets are absent (e.g. {210}, {310} …). In Figure 64b is shown the same area after tilting the sample close to the zone axis [102]. The {100} plane at the surface of the bubbles is again visible. However, the bubble edge is rounded everywhere else. This result indicates that $\{h\ 2k\ \bar{k}\}$-type facets with *h≠0* are absent (e.g $\{12\bar{1}\}$, $\{22\bar{1}\}$ …). Finally, the Figure 64c shows a TEM micrograph considering the [113] zone axis. The

{110} facets are visible, but again the other parts of the edges are rounded indicating no other facet exists with normal vector perpendicular to the [113] direction (e.g. {301}, {211} …). Similarly, only {100} and {110} facets are observed for other samples oriented along the [110] and [111] directions implanted at 1273 K ($W(110)^*_{1273\mathrm{K,2keV}}$ and $W(111)^*_{1273\mathrm{K,2keV}}$) as well as in the [110] oriented sample implanted at RT then annealed ($W(110)^*_{\mathrm{RT,2keV}}$).

GISAXS analysis

In the same manner as what has been done previously, GISAXS patterns were measured at different azimuths for all three W single crystals, i.e. by rotating the sample around the normal to the surface (ω angle, see Figure 65). The aim is to find all facets in the samples. In addition, a 3D iso-intensity surface map has been obtained from the compilation of the 2D patterns recorded after azimuthal rotation (see the right part of Figure 65).

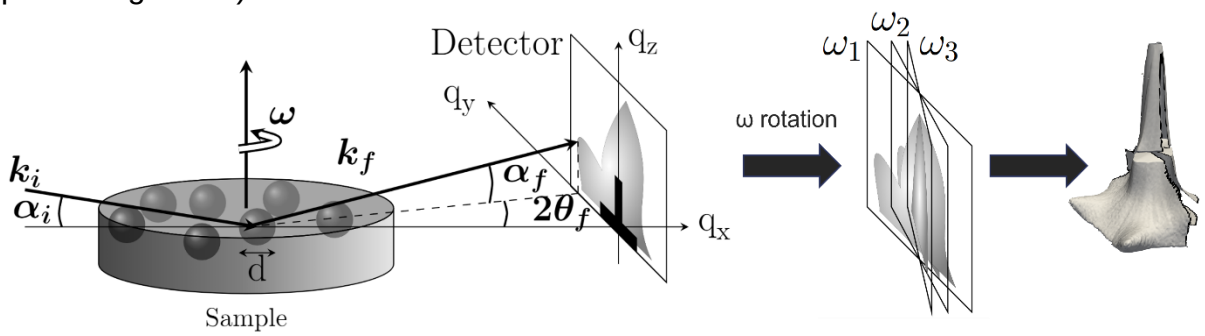

Figure 65: Schematic representation of the GISAXS geometry. ω is the azimuthal angle that defines the probing direction. The right part is a 3D iso-intensity surface map obtained from the compilation of 2D patterns recorded after azimuthal rotation.

Figure 66 shows the iso-intensity surface maps for implanted $W(100)^*_{1273K,2keV}$, $W(110)^*_{1273K,2keV}$ and $W(111)^*_{1273K,2keV}$ single crystals recorded after annealing up to 1773 K and some particular GISAXS patterns.

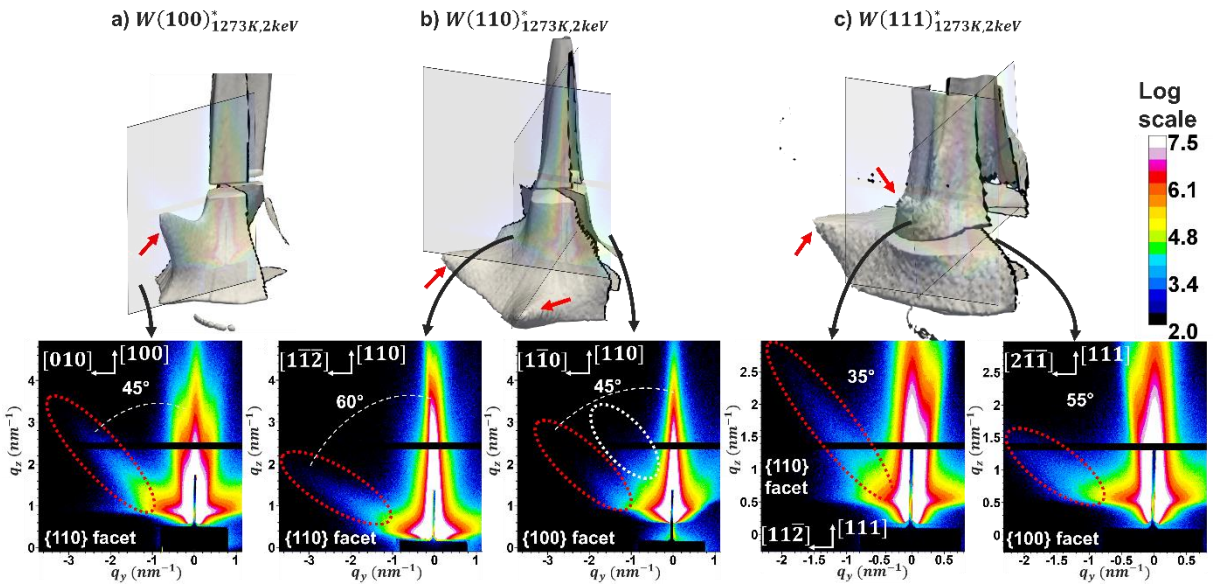

Figure 66: Up: Reconstruction of iso-intensity surface map recorded during azimuthal scan at $\alpha_i = 0.6°$, after 2 keV He implantation and UHV annealing up to 1773 K, for a) $W(100)^{*}_{1273K,2keV}$, b) $W(110)^{*}_{1273K,2keV}$ and c) $W(111)^{*}_{1273K,2keV}$. Below: particular GISAXS patterns corresponding to a cut of the 3D map. Lateral rods on GISAXS patterns are due to X-ray scattering on He-bubbles facets (red dashed circle). Corresponding facets are {110} and {100}. On $W(110)^{*}_{1273K,2keV}$ (b) the twin rod of {100}-type facet (white dashed circle) is due to multiple scattering on surface morphologies and buried bubble internal surface.

Iso-intensity surface maps show lateral streaks highlighted with red arrows and red ellipses in precise directions of the reciprocal space. These diffuse scattering streaks result from the truncation of the bubbles by well-defined planes corresponding to facets [137]. The inclination angle between the diffuse scattered intensity and the surface normal depends on the relative orientation of the facets with the surface of the single crystal (e.g. 45° for {110} facets on (100)-oriented W). As seen by TEM, two types of facets exist presumably at the bubbles surface: the {100} and the {110} facets. We have not observed streaks corresponding to facets other than {100} and {110} ones. In addition, no spherical bubbles are observed as no 3D isotropic scattering is recorded.

The origin of these lateral streaks has been investigated by varying the incident angle α_i. For this experiment the critical angle α_c is equal to $0.4°$.
The corresponding GISAXS pattern at $\alpha_i = 0.2°$ and $\alpha_i = 0.6°$ for the sample $W(100)^{*}_{1273K,2keV}$ are shown in Figure 67.
For $\alpha_i = 0.2°$ (Figure 67) the penetration depth of X-rays is $\Lambda \approx 1.5$ nm and for $\alpha_i = 0.6°$ (Figure 67b), the penetration depth is approximately 40nm.

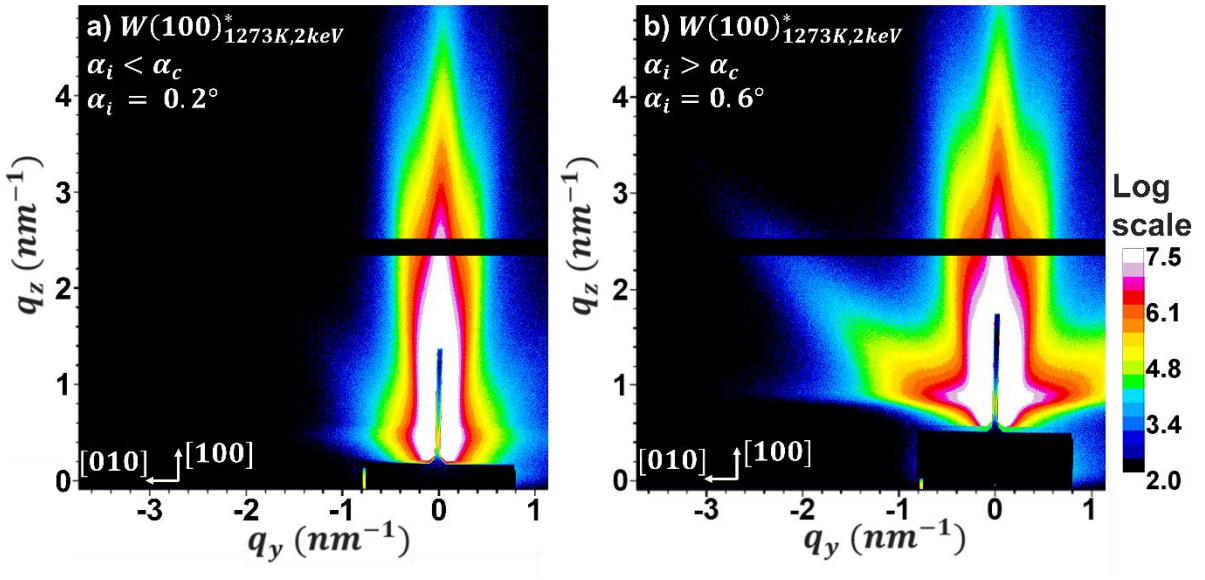

Figure 67: GISAXS patterns for $W(100)^*_{1273K,2keV}$ after post implantation annealing up to 1773 K. Recorded at the azimuthal angle ω to visualize the signal from a {110} facets. a) corresponds to an incident angle α_i of 0.2° (below the critical angle), and b) 0.6°(above the critical angle).

The diffuse scattering streak is visible only for $\alpha_i = 0.6°$ meaning clearly that the signal arises from bubbles located below the surface. The origin of the diffuse scattering streaks for other samples (red ellipses in bottom part of Figure 66) have also been checked and the same conclusion has been found. The bubbles are hence faceted by {100} and {110} planes.

Let us note two particularities, 1) In the case of $W(100)^*_{1273K,2keV}$ the X-ray diffuse scattering on {100} facets is expected to produce scattering rods at 90° with respect to the vertical ($\alpha_f = 0°$) which is located below the critical angle that defines the limit where intensity can be transmitted. Hence, {100} facet on $W(100)^*_{1273K,2keV}$ cannot be measured. 2) On $W(110)^*_{1273K,2keV}$ a twin lateral scattering rod of {100}-type is visible (see white ellipse in GISAXS pattern of Figure 66). This doubling effect is due to multiple scattering processes occurring at the sample surface and below the surface that can be described within the Distorted Wave Born Approximation (DWBA). It combines X-ray diffuse scattering due to holes formed at the surface by bubble bursting and also buried bubbles. Indeed, as shown by scanning electron microscopy (SEM) in Figure 68, the surface of $W(110)^*_{1273K,2keV}$ is not flat. Holes due to bubbles bursting, appearing in black on the SEM micrograph, pave the surface. In addition, elongated surface structures due to surface healing are observable.

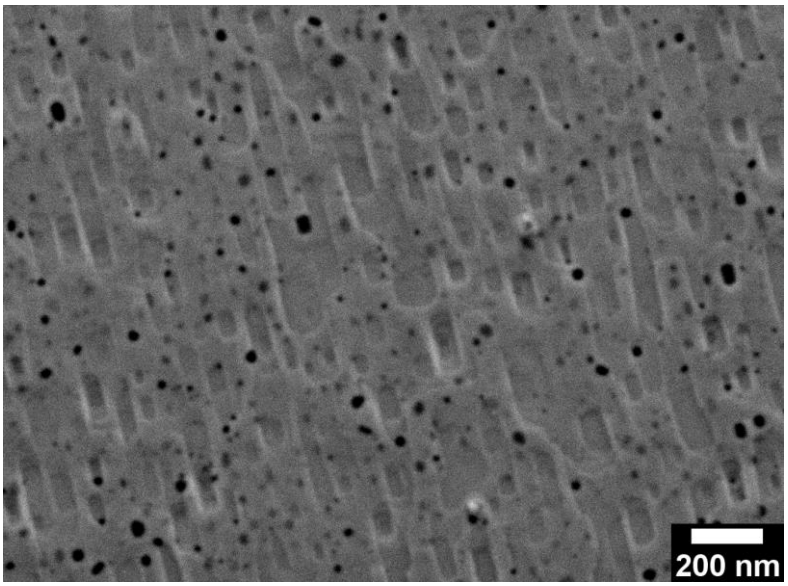

Figure 68: SEM micrograph of $W(110)^{*}_{1273K,2keV}$ surface after 2 keV He implantation and UHV annealing up to 1773 K.

The average size d of a facet can be deduced measuring the full width at half maximum (FWHM) of the diffuse scattering streak of the corresponding facet noted Δq and approximated as:

$$d = \frac{2\pi}{\Delta q}$$

Even though this equation does not give a quantitative value of the facet size, it provides a good estimate and allows close comparison between samples.

In Table 7 the sizes d of {110} and {100} facets measured by GISAXS for each W crystals are shown (except for $W(100)^{*}_{1273K,2keV}$ where only the {110} facet can be measured). The uncertainty on the measurement is mostly due to the fit quality of the intensity profile along the streak width. In our case, the uncertainty on the sizes *d* is evaluated at maximum 5% of the measured length.

Sample	Average length of facet by GISAXS (in nm)	
	d_{100}	d_{110}
$W(100)^{*}_{1273K,2keV}$	X	9.1 ± 0.5
$W(110)^{*}_{1273K,2keV}$	9.2 ± 0.5	11.3 ± 0.6
$W(111)^{*}_{1273K,2keV}$	13.6 ± 0.7	13.6 ± 0.7

Table 7: GISAXS measurements of facet length of bubbles in $W(100)^{*}_{1273K,2keV}$, $W(110)^{*}_{1273K,2keV}$, $W(111)^{*}_{1273K,2keV}$ after 2 keV He implantation at 1273 K and annealed up to 1773 K

4.3. Equilibrium shape of bubbles

4.3.1. The Wulff theorem

The standard method for determining the equilibrium shape of an object (bulk or void in a crystal) is given by the so called γ-plot or Wulff-plot based on the Wulff theorem [165]. The mathematical background of the Wulff theorem will not be discussed in this manuscript, the interested reader can find a formal demonstration in standard books as ref. [166].
The Wulff theorem predicts the equilibrium shape of an object by minimizing its total surface energy at constant volume. In crystals, due to surface energy anisotropy, facets of well-defined crystallographic orientations are formed to minimize the total surface energy. The Wulff theorem shows that the surface energy of a plane (γ_{hkl}) is proportional to the distance h_{hkl} from the centre of the crystal to this facet. For two different (hkl) planes, let say $(h_1k_1l_1)$ and $(h_2k_2l_2)$:

$$\gamma_{h_1k_1l_1} = h_{h_1k_1l_1} \cdot C$$
$$\gamma_{h_2k_2l_2} = h_{h_2k_2l_2} \cdot C$$

where C is a constant independent of the volume of the crystal.

If surface energies are known, the γ-plot consist in drawing the different (hkl) planes with respect to their respective geometry. The first type of plane $(h_1k_1l_1)$ fixes arbitrary the distance $h_{h_1k_1l_1}$ then, the second type of plane $(h_2k_2l_2)$ is drawn with respect to angles between $(h_1k_1l_1)$ and $(h_2k_2l_2)$ planes and at a distance from the centre given by $h_{h_2k_2l_2} = \frac{\gamma_{h_2k_2l_2}}{\gamma_{h_1k_1l_1}} h_{h_1k_1l_1}$. The same procedure must be followed until a sufficient representative number of (hkl)-type planes have been considered. The crystal shape corresponds to the inner contour obtained. Figure 69 is an example of a γ-plot in 2D in [001] zone axis. The (100) and (110) planes are represented respectively in red and blue. Their surface energies are low enough to form facets on the crystal surface. In addition, (210)-type planes with a higher surface energy has been represented in green to illustrate the exclusion from the equilibrium shape of high energy planes.

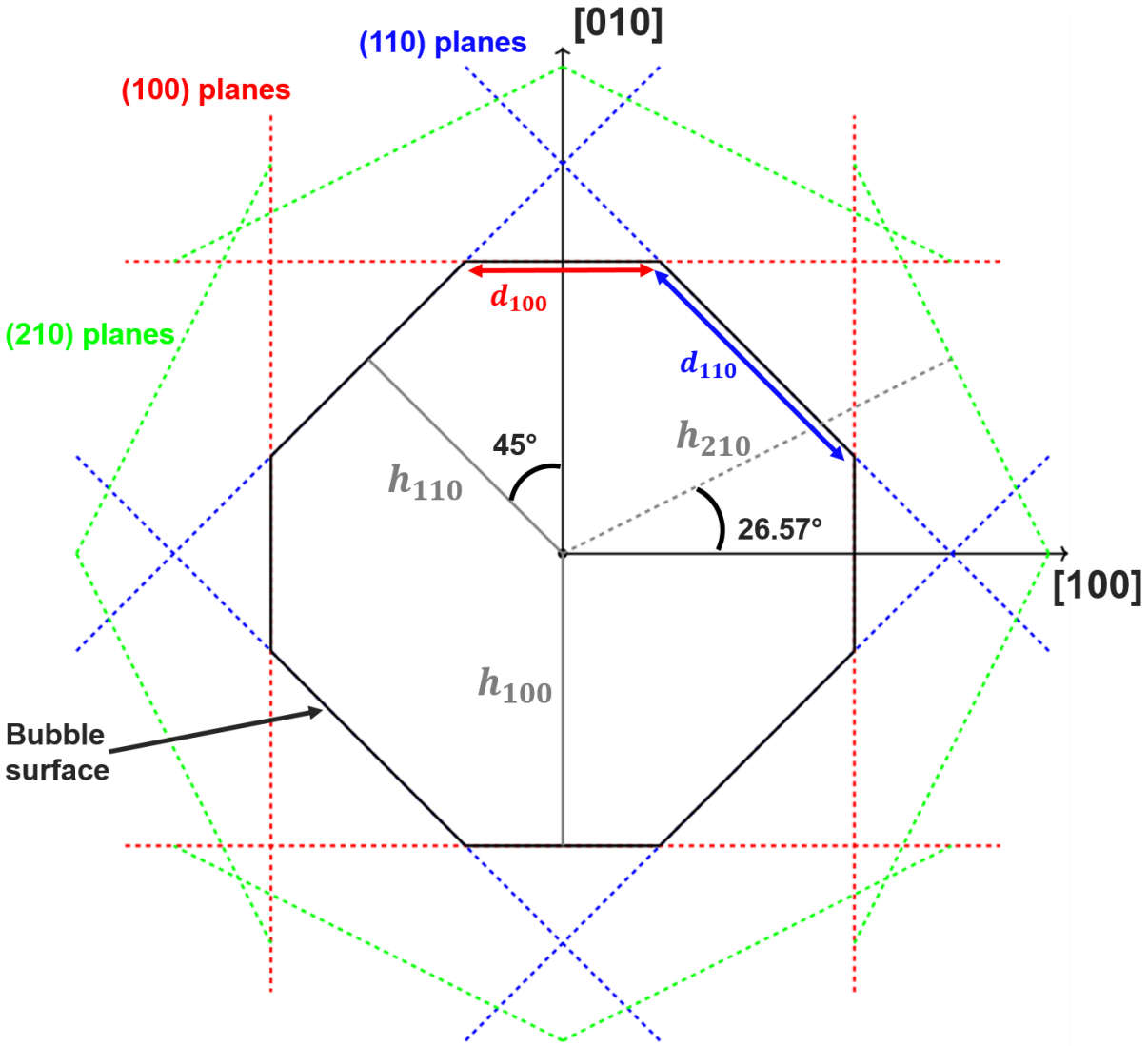

Figure 69: γ-plot in the zone axis [001]. Crystallographic planes are represented by dashed line, (100) planes are represented in red, (110) planes in blue and (210) planes in green. The final shape of the bubble is determined by the inner contour represented by black lines.

In our study, we aim at determining how the pressurized He in bubbles affect the W surface energies. In other terms, if the equilibrium shape is known, thus by construction of the γ-plot, then the surface energies ratio ($\frac{\gamma_{100}}{\gamma_{110}}$) in presence of pressurized He can be deduced.

From Figure 69, by geometric construction, the following relation between the facets length d_{100} and d_{110} and the distances h_{100} and h_{110} can be found:

$$h_{100} = \frac{d_{100}}{2} + \frac{d_{110}}{\sqrt{2}}$$

$$h_{110} = \frac{d_{100}}{\sqrt{2}} + \frac{d_{110}}{2}$$

According to the Wulff theorem:

$$\frac{\gamma_{100}}{\gamma_{110}} = \frac{h_{100}}{h_{110}}$$

Hence:

$$\frac{\gamma_{100}}{\gamma_{110}} = \frac{d_{100} + \sqrt{2}d_{110}}{\sqrt{2}d_{100} + d_{110}}$$

In Table 8 is shown the $\frac{\gamma_{100}}{\gamma_{110}}$ energetic ratio obtained by GISAXS. We can evaluate the $\frac{\gamma_{100}}{\gamma_{110}}$ ratio as 1.03 ± 0.03 by GISAXS.

Sample	$\frac{\gamma_{100}}{\gamma_{110}}$
$W(100)^*_{1273K,2keV}$	X
$W(110)^*_{1273K,2keV}$	1.04 ± 0.02
$W(111)^*_{1273K,2keV}$	1.02 ± 0.02

Table 8: Energetic ratio between {100} and {110} W surfaces with pressurized He.

The simulated Wulff bubble shape corresponding to this ratio is given in Figure 70, the visualization is performed using the Wulffpack software [167].

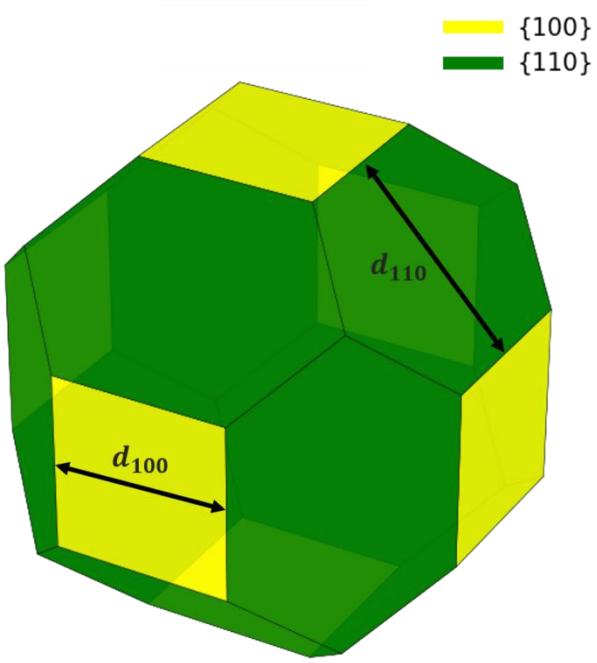

Figure 70: Wulff construction generated by the energetic ratio deduced by GISAXS. Black arrows represent the lengths used in the energetic ratio calculation.

4.3.2. Effect of pressurized He on the W surface energy

Our experimental result can be compared with the literature. Only a few experimental investigations on the equilibrium shape of pure W have been found. Kuporosov and Shuppe [168] have heated a spherical W sample to 2500 K for 30 to 50 hours. After heat treatment they have found {100}, $\{110\}$, $\{111\}$ and $\{211\}$ facets. Weise and Richter [169] have studied the formation of a single crystal by chemical transport reaction. They have found similarly {100}, $\{110\}$, and $\{211\}$ facets but did not mention the presence of {111} facets.

More commonly, surface energies can be calculated by simulations and equilibrium shape deduced using the Wulff theorem. Density Functional Theory (DFT) [117,170–172] or Molecular dynamics (MD) [107,173] simulations have been used to calculate the surface energy of different orientations of W crystals. Figure 71 combines different energetic ratios $\frac{\gamma_{100}}{\gamma_{110}}$ determined from the literature and the deduced Wulff shapes. A large discrepancy between the values has been found, corresponding to very different expected bubble shapes.

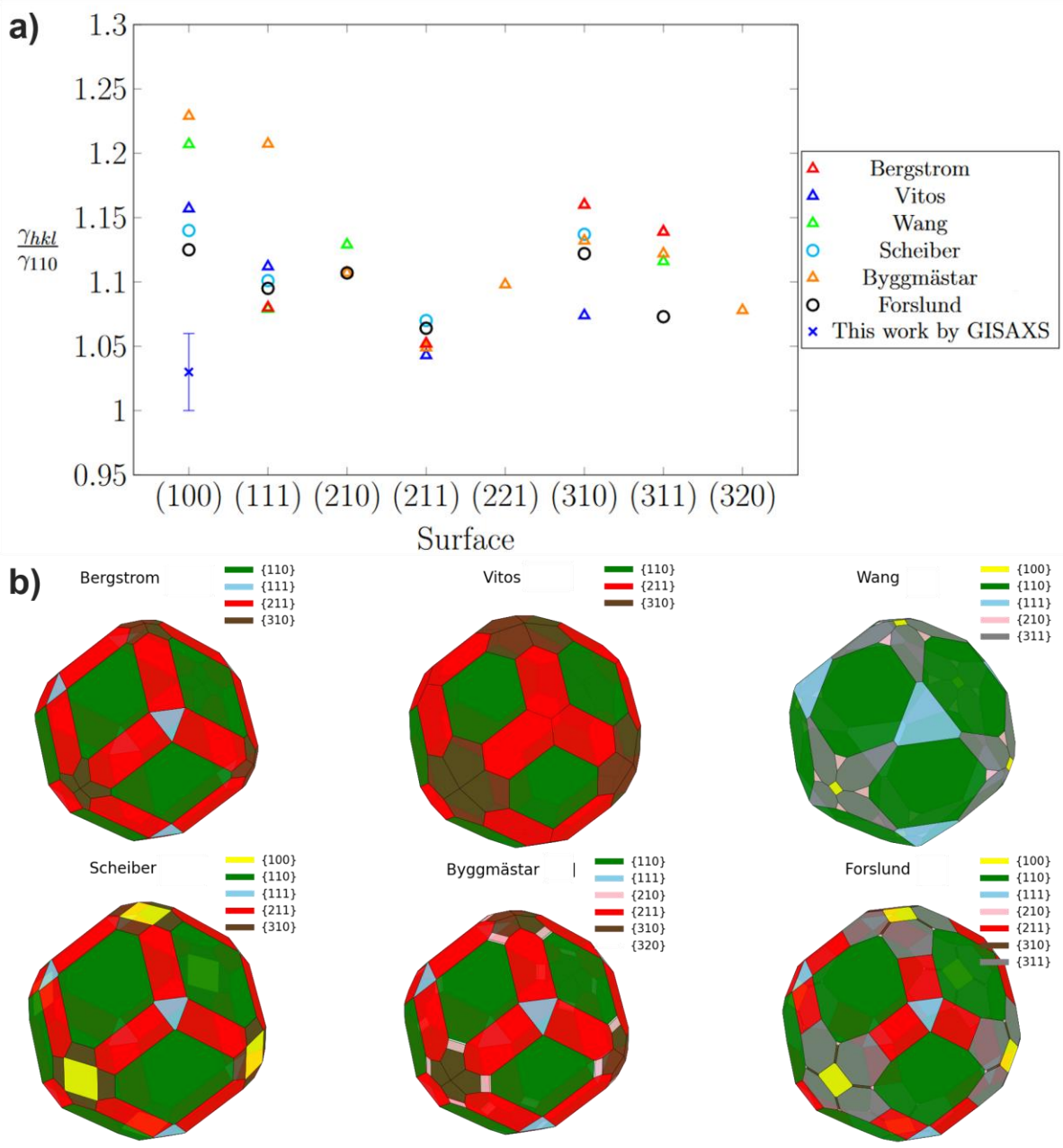

Figure 71:a) Energetic ratio deduced by DFT or MD simulations for various surface orientations, circle marks are for coupled approach considering temperature effect. b) Wulff constructions generated using the energetic ratio of a).

The studies coupling DFT to quasi-harmonic approximation (QHA) in [172] or MD in [107] aim at taking into account the effect of temperature on surface energies. In all cases, the {100} facet appears on the equilibrium shape generated at 1773 K. According to their studies the $\frac{\gamma_{100}}{\gamma_{110}}$ energetic ratio decreases as the temperature increases, therefore the {100} facet size is expected to increase with temperature. From the calculations, the {211} is the second most dominant facet of the Wulff shape

at 0 K, but it is reported to shrink when the temperature increases (see [172]). Therefore, the lack of {211} facets in our high-temperature experimental observations is not in disagreement with the simulations. Let us note that DFT simulations do not lead to a consensus, and that predicting an equilibrium shape at a given temperature from simulations performed at 0 K is delicate. Furthermore, most calculations neglect the W-He interaction. Recent approaches combining QHA-DFT [172] or MD-DFT [107] to take into account temperature dependence show a closer agreement to our experimental observations.

4.3.3. Form factor of the equilibrium shape of bubbles

For GISAXS analysis, the form factor plays a major role. The form factor is defined as a finite integral over the volume V of the bubble:

$$F_b(\boldsymbol{q}) = \int_V e^{i\boldsymbol{q}\cdot\boldsymbol{r}}\, \boldsymbol{dr}$$

For this reason, the form factor of the bubble can be constructed as a sum of known form factor of simpler geometries. For instance, the bubble can be decomposed in seven parts, a cube at its center and six truncated square based pyramids on the cube faces. The Figure 72 is a schematic representation of such construction.

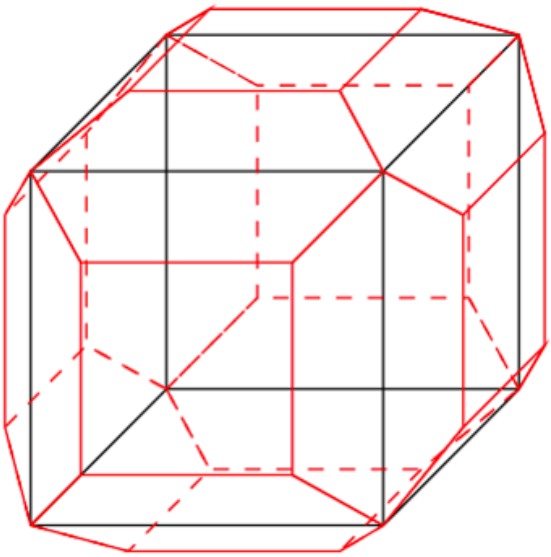

Figure 72: Schematic representation of the decomposition of the bubble shape in a cube (in black) at its center and six truncated square based pyramids (in red) located on the cube faces.

A cube is defined only by its side $2R$ and a truncated square based pyramid is defined by the side $2R$ of its base, the angle α between the base and the lateral inclined faces

and H the height in the z-direction. The Figure 73 is a schematic representation of an individual cube and a truncated square based pyramid.

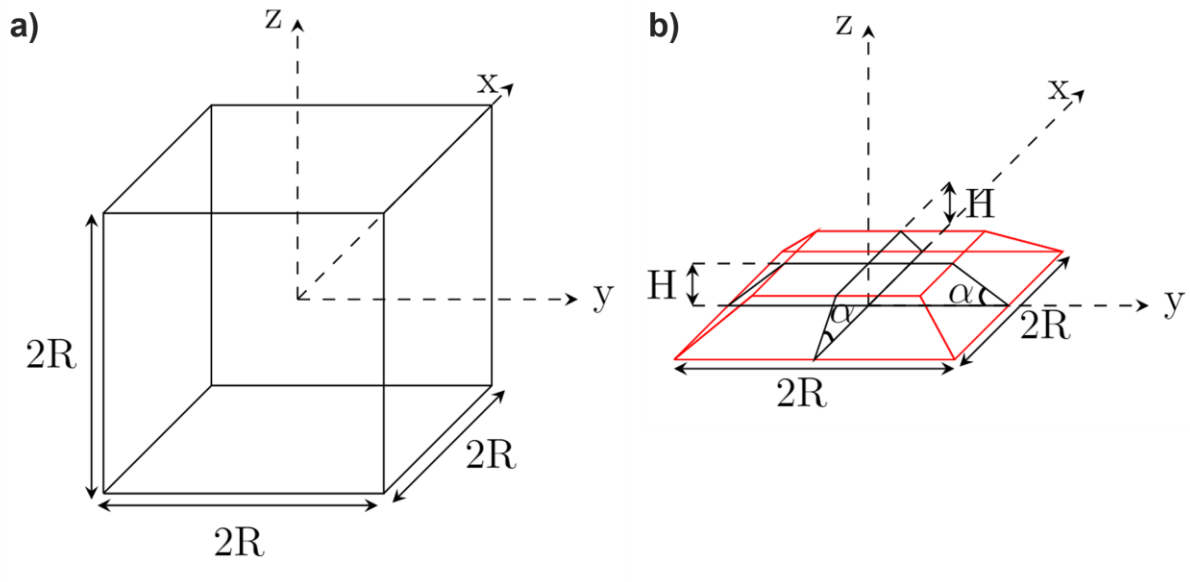

Figure 73: Schematic representation of a cube of side $2R$ (a) and a truncated square based pyramid with a base side $2R$, α the angle with lateral faces and H the height (b).

The form factor of a cube of side $2R$ is given by:

$$F_c(\boldsymbol{q}, 2R) = \int_V e^{i\boldsymbol{q}\cdot\boldsymbol{r}}\, \boldsymbol{dr}$$

$$= \int_{-R}^{R} e^{iq_x x}\, dx \int_{-R}^{R} e^{iq_y y}\, dy \int_{-R}^{R} e^{iq_z z}\, dz$$

Each integral is of the same form:

$$\int_{-R}^{R} e^{iq_x x}\, dx = \left[\frac{1}{iq_x} e^{iq_x x}\right]_{-R}^{R} = \frac{1}{iq_x}\left[e^{iq_x R} - e^{-iq_x R}\right] = \frac{2i\sin(q_x R)}{iq_x} = 2R\,sinc(q_x R)$$

Hence:

$$F_c(\boldsymbol{q}, 2R) = V_c\, sinc(q_x R) sinc\left(q_y R\right) sinc(q_z R)$$

With $V_c = (2R)^3$ the volume of the cube.

The form factor of a truncated square based pyramid can be found in [137]:

$$F_p(\boldsymbol{q}, 2R, H, \alpha)$$

$$= \frac{H}{q_x q_y}\Big[K_1 \cos\Big((q_x - q_y)R\Big) + K_2 \sin\Big((q_x - q_y)R\Big) - K_3 \cos\Big((q_x + q_y)R\Big)$$

$$- K_4 \sin\Big((q_x + q_y)R\Big)\Big]$$

With:

$$K_1 = sinc(q_1 H) e^{iq_1 H} + sinc(q_2 H) e^{-iq_2 H}$$

$$K_2 = isinc(q_1 H) e^{iq_1 H} - isinc(q_2 H) e^{-iq_2 H}$$

$$K_3 = sinc(q_3 H)e^{iq_3 H} + sinc(q_4 H)e^{-iq_4 H}$$
$$K_4 = isinc(q_3 H)e^{iq_3 H} - isinc(q_4 H)e^{-iq_4 H}$$

And:

$$q_1 = \frac{1}{2}\left[\frac{q_x - q_y}{\tan(\alpha)} + q_z\right]$$
$$q_2 = \frac{1}{2}\left[\frac{q_x - q_y}{\tan(\alpha)} - q_z\right]$$
$$q_3 = \frac{1}{2}\left[\frac{q_x + q_y}{\tan(\alpha)} + q_z\right]$$
$$q_4 = \frac{1}{2}\left[\frac{q_x + q_y}{\tan(\alpha)} - q_z\right]$$

The form factor of the bubble is hence:

$$\begin{aligned} F_b = {} & F_c(\boldsymbol{q}, 2R) \\ & + F_{p1}(q_x, q_y, q_z, R, H, \alpha)e^{iq_z R} \\ & + F_{p2}(-q_x, q_y, -q_z, R, H, \alpha)e^{-iq_z R} \\ & + F_{p3}(q_x, -q_z, q_y, R, H, \alpha)e^{iq_y R} \\ & + F_{p4}(q_x, q_z, -q_y, R, H, \alpha)e^{-iq_y R} \\ & + F_{p5}(-q_z, q_y, q_x, R, H, \alpha)e^{iq_x R} \\ & + F_{p6}(q_z, q_y, -q_x, R, H, \alpha)e^{-iq_x R} \end{aligned}$$

The pyramid on the top of the cube has been translated by R in positive z direction, this is translated by the term $e^{iq_z R}$. For pyramid that have been rotated, for example the pyramid on the right side of the cube the form factor is transformed $F_{p3}(q_x, q_y, q_z, R, H, \alpha) \rightarrow F_{p3}(q_x, -q_z, q_y, R, H, \alpha)$ for the rotation then the translation is applied with the term $e^{iq_y R}$.

Within the equilibrium shape of bubbles a relation between $2R, H, \alpha$ and the measured length d_{110} and d_{100} can be found.

First, from the definition of the energetic ratio: $d_{100} = d_{110}\frac{\frac{\gamma_{100}}{\gamma_{110}} - \sqrt{2}}{1 - \sqrt{2}\frac{\gamma_{100}}{\gamma_{110}}}$

Between α corresponds to the angle between (100) and (110) planes, hence $\alpha = 45°$. From the construction of the pyramids the length of a lateral face is half the length of a {110} bubble facet. Thus, $\cos(\alpha) = \frac{R - d_{100}/2}{d_{110}/2} = \frac{\sqrt{2}}{2}$ and $\sin(\alpha) = \frac{H}{d_{110}/2} = \frac{\sqrt{2}}{2}$.

So:

$$R = \frac{d_{110}}{2}\left(\frac{1}{\sqrt{2}} + \frac{\frac{\gamma_{100}}{\gamma_{110}} - \sqrt{2}}{1 - \sqrt{2}\frac{\gamma_{100}}{\gamma_{110}}}\right)$$
$$H = \frac{d_{110}}{2\sqrt{2}}$$

With $\frac{\gamma_{100}}{\gamma_{110}} = 1.03 \pm 0.03$:

$$R \approx 0.774\ d_{110}$$
$$H \approx 0.354\ d_{110}$$

The bubble form factor has been uploaded to the IsGISAXS software and Figure 74 shows the simulated patterns that have been generated based on {110} facet length measured by GISAXS (Table 7).

The patterns have been simulated for azimuth angles seen in Figure 66 allowing to detect facets. The diffuse scattering streaks due to bubbles facets are well reproduced meaning that the form factor seems adequate. However, intensity fluctuation along streaks is visible. This seems to remain even for broad distribution for example, the Figure 74 has been generated for a log normal distribution of the bubble radius with a geometric standard deviation $\sigma_g = 1.5$. Further work to analyse this behaviour must be performed.

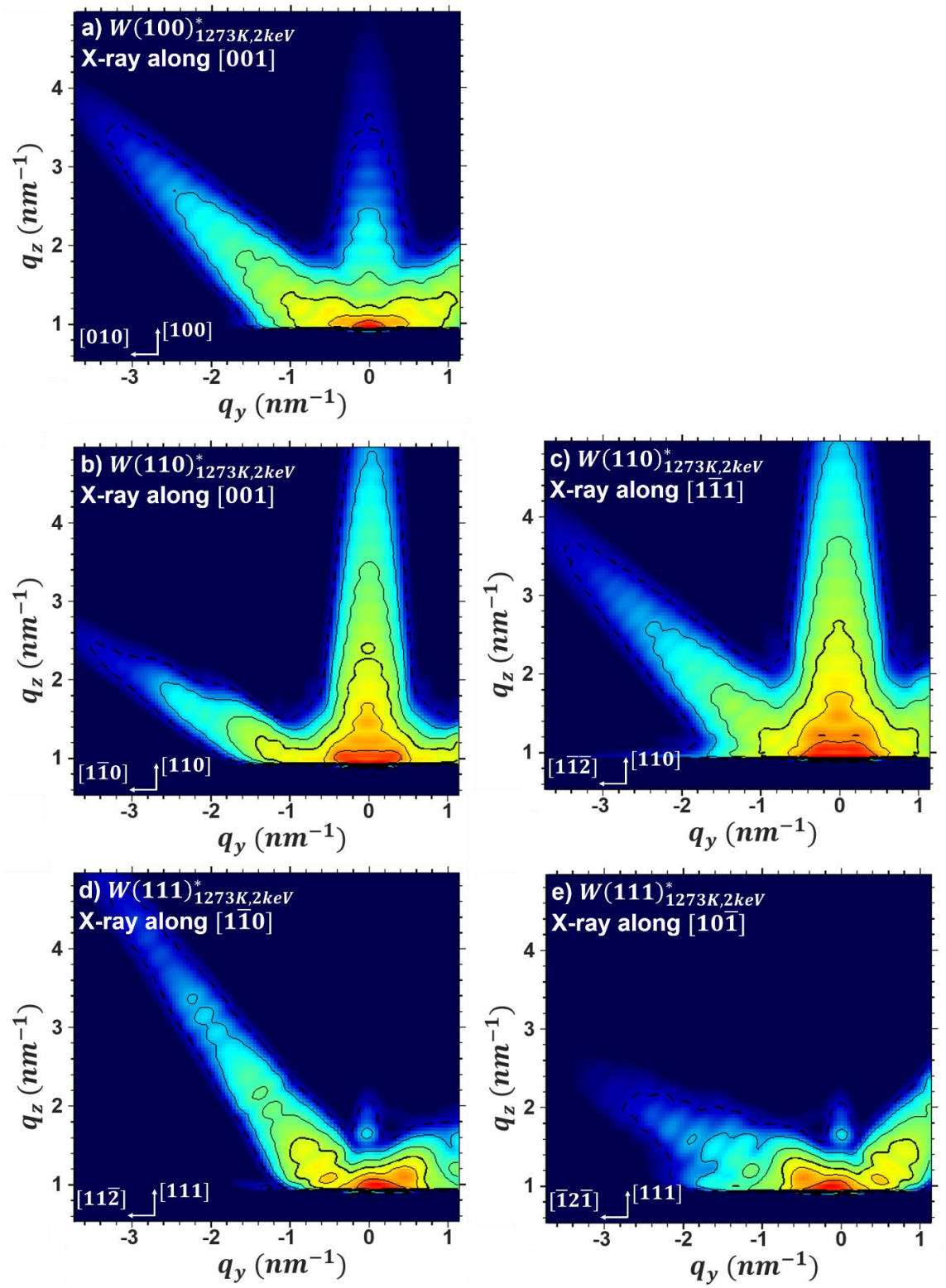

Figure 74: Simulated GISAXS patterns of the equilibrium shape of bubbles for $W(100)^*_{1273K,2keV}$, $W(110)^*_{1273K,2keV}$ and $W(111)^*_{1273K,2keV}$ using different crystallographic directions of the incoming x-ray beam.

5. Growth of bubbles

5.1. Low temperatures 159

5.2. High temperature 162

5.2.1. Experimental observations 162

5.2.2. Growth mechanism 164

5.2.3. Bubble diffusion coefficient 169

In the previous chapter the bubble populations have been characterized by the coupled approach combining TEM and GISAXS analysis. The shape of the bubbles has been drastically affected by the temperature, at relatively low temperature (< 1273 K) bubbles are rounded being described by sphere or spheroidal shapes. At High temperature (> 1273 K) bubbles are truncated by well-defined crystallographic planes, changing the shape from rounded to facetted. In this chapter, will be presented the investigations on the size evolution of bubbles. *In-operando* GISAXS measurements have been performed in real time during He implantation in order to record the dynamics of the bubble evolution.

In the first half of this chapter will be discussed the case of non-facetted bubbles formed at low temperatures (<1273 K).

The second half of this chapter will deal with the case of facetted bubbles formed at high temperature (>1273 K). From the evolution of GISAXS signal during implantation, the growth mechanism of bubbles will be investigated.

5.1. Low temperatures

GISAXS patterns recorded before implantation, after approximately 10%, 50% and 100% of the total fluence are shown in Figure 75 for $W(110)_{RT,400eV}$ implanted at RT with 400eV ions, in Figure 76 for $W(110)_{523K,400eV}$ (top) and $W(110)_{523K,2keV}$ (bottom) implanted at 523K with 400eV and 2keV energies respectively and in

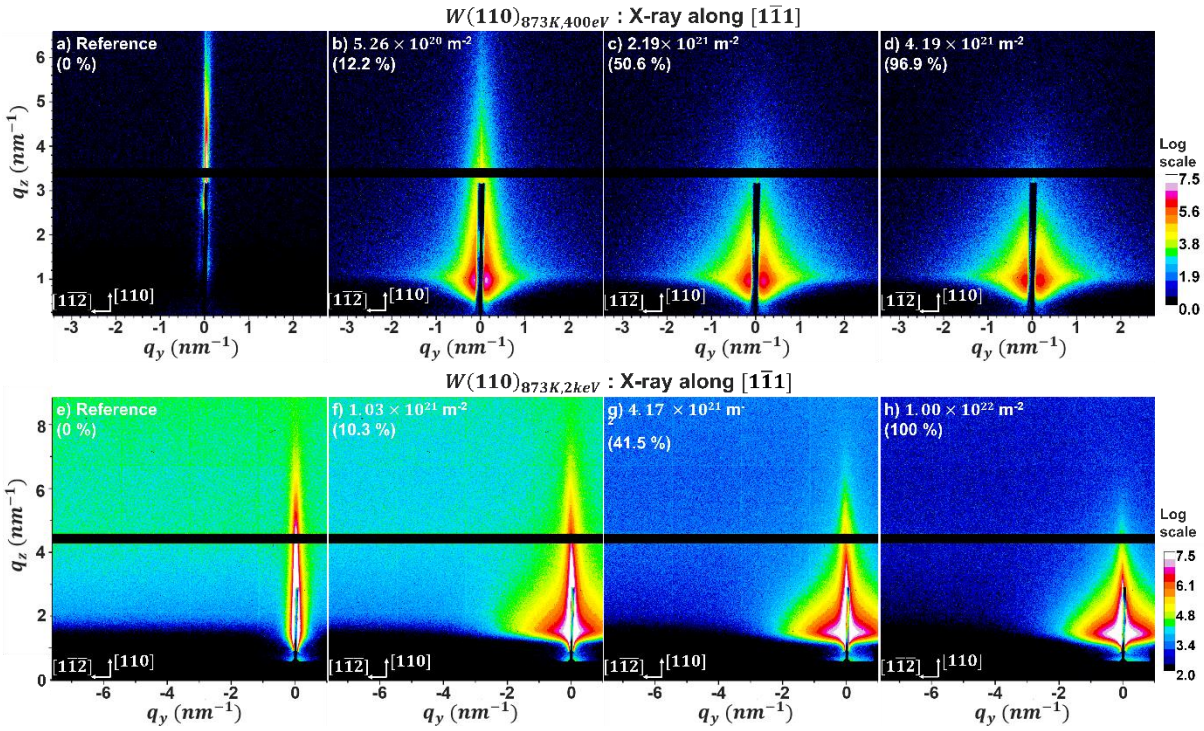

Figure 77 for $W(110)_{873K,400eV}$ (top) and $W(110)_{873K,2keV}$ (bottom) irradiated at 873K with 400eV and 2keV He ions respectively.

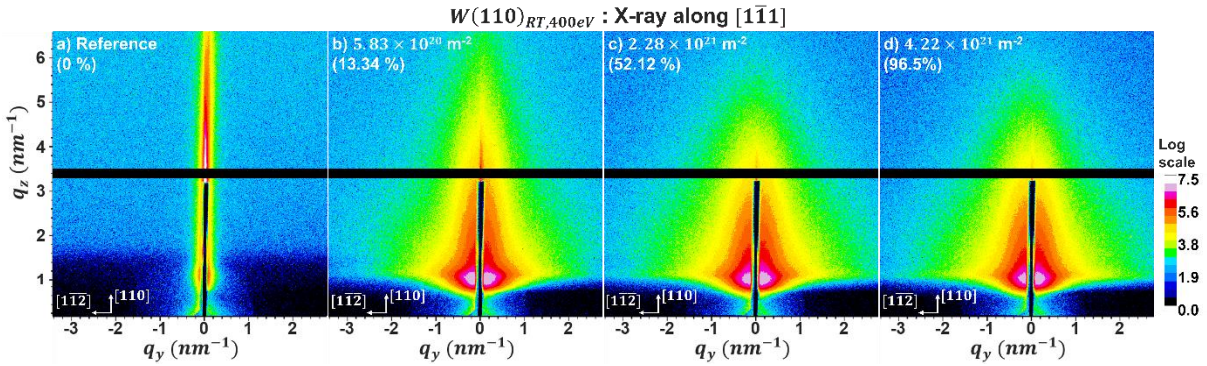

Figure 75: GISAXS patterns recorded at $\alpha_i = 0.47°$ for $W(110)_{RT,400eV}$ implanted with 400 eV ions at RT. The incident X-ray beam is aligned along the $[1\bar{1}1]$ direction. The patterns correspond to the reference state before implantation (a), approximately 10% of the final fluence (b), 50% of the total fluence (c) and 100% of the reached fluence (d).

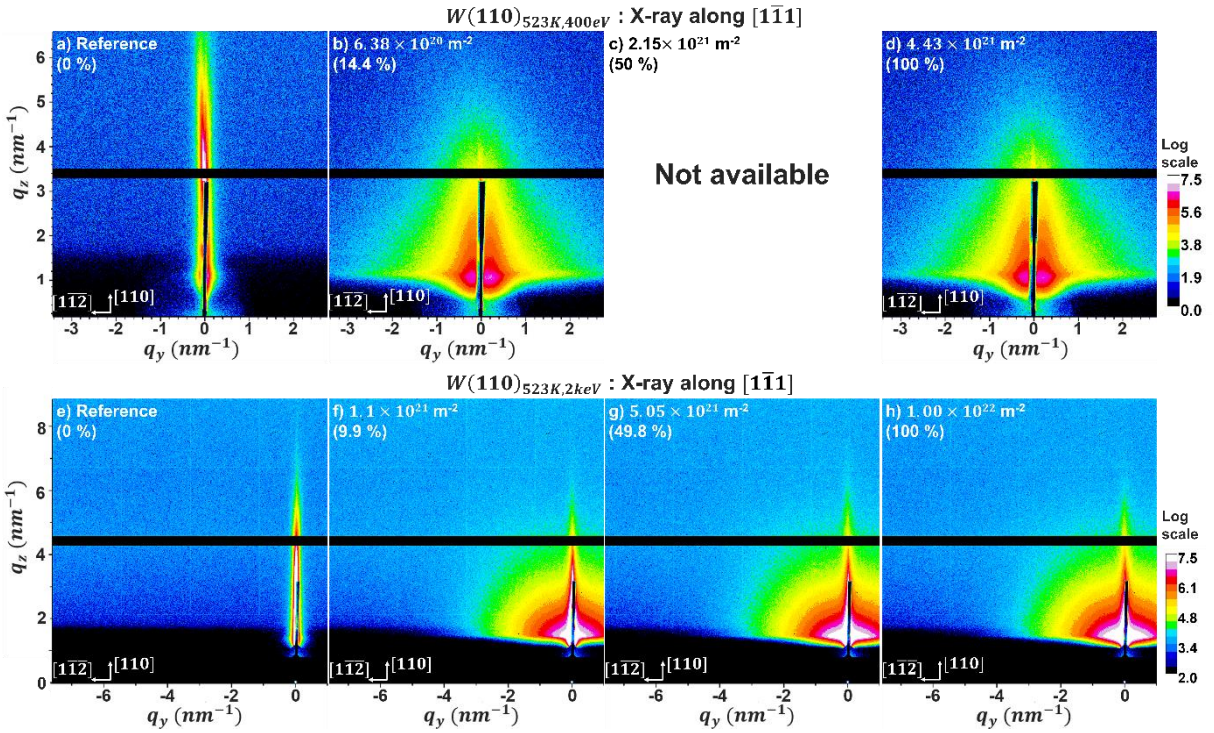

Figure 76: GISAXS patterns recorded at $\alpha_i = 0.47°$ for $W(110)_{523K,400eV}$ implanted with 400 eV ions (top) and at $\alpha_i = 0.6°$ for $W(110)_{523K,2keV}$ implanted with 2 keV ions (bottom) at 523K. The X-ray incident beam is aligned along the $[1\bar{1}1]$ direction. The patterns correspond to the reference state before implantation (a and e), approximately 10% of the final fluence (b and f), 50% of the total fluence (c and g) and 100% of the reached fluence (d and h).

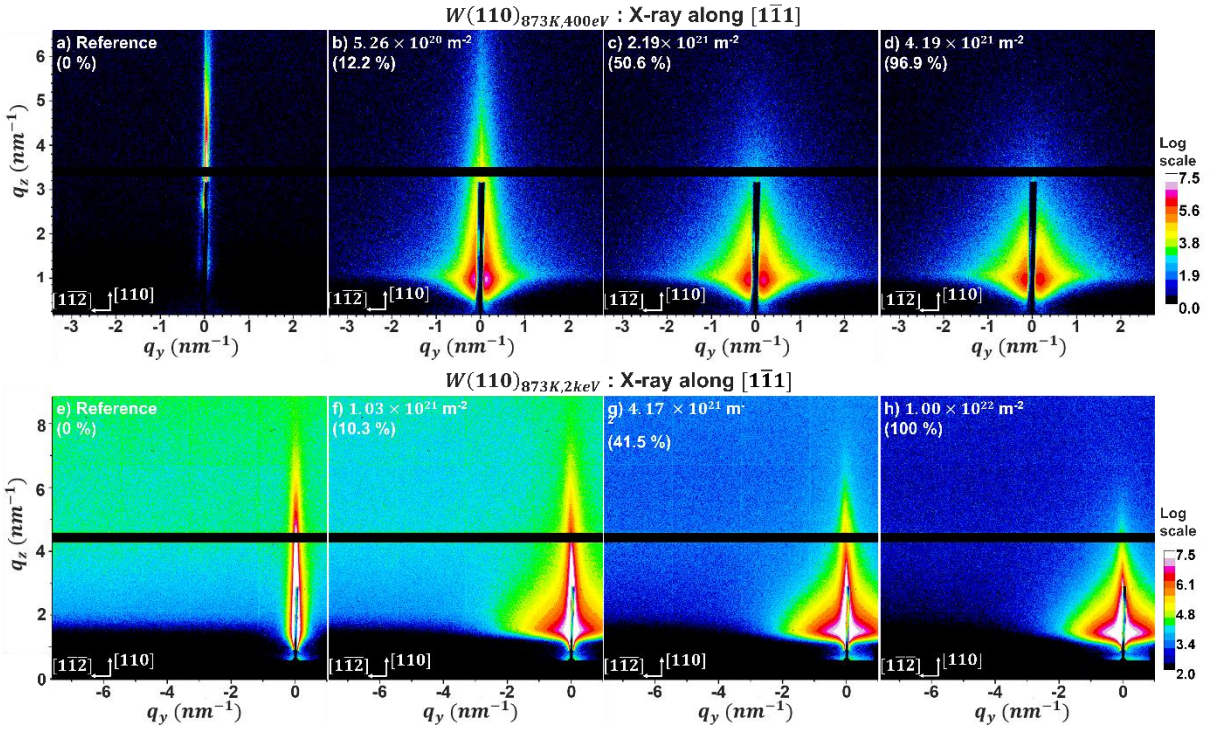

Figure 77: GISAXS patterns recorded at $\alpha_i = 0.47°$ for $W(110)_{873K,400eV}$ implanted with 400 eV ions (top) and at $\alpha_i = 0.6°$ for $W(110)_{873K,2keV}$ implanted with 2 keV ions (bottom) at 873K. The X-ray incident beam is aligned along the $[1\bar{1}1]$ direction. The patterns correspond to the reference before implantation (a and e), approximately 10% of the final fluence (b and f), 50% of the total fluence (c and g) and 100% of the reached fluence (d and h).

For all samples, the bubble signal appears very quickly after the beginning of implantation, patterns recorded at 10% of the final fluence show already the off-specular signal corresponding to spherical and spheroidal bubbles discussed in Chapter 4. In first approach, the shape of GISAXS patterns are very similar all along implantation no matter the temperature or implantation energy used meaning that the shape of bubbles remains identical of what has been found in chapter 4 i.e. spheres and spheroids.

From first analysis by IsGISAXS of the evolution of the two species, it appears that the size distribution of the bubbles starts broad and get more and more thin as more bubbles are generated. Based on molecular dynamics simulations in ref. [85], once the first bubbles are created, they grow by absorbing new implanted He atoms and eject W atoms in interstitial positions. The cloud of self-interstitial atoms thus formed generates local deformations of the lattice, causing compression at the cloud location and relaxation in the surrounding area, which attract He atoms and promote further bubble formation. We think that once the initial bubble reaches a critical size, the dense cloud of self-interstitial atoms generates many preferential nucleation sites at the periphery of the initial bubble dragging the majority of incoming He atoms. This mechanism would hence prevent the initial bubble to grow further as being difficult for a He atom to reach the bubble. We believe that this mechanism occurs repeatedly for second bubbles formed at the periphery of the initial one and successively for all bubbles generated. This mechanism would thus lead to the formation of a dense packed bubbles group in onion like structure with all bubbles with the same critical size. The effect of temperature could help to remove some of interstitial atoms and thus preserve a path for incoming He atoms. However, this first hint needs to be confirmed. In perspective, a deeper analysis involving more fits of the data by the 2 species model at different fluences could provide the evolution of the size distribution of bubbles and confirm these first results.

5.2. High temperature

5.2.1. Experimental observations

GISAXS patterns of $W(110)_{1273K,400eV}$ implanted at 1273K with 400 eV are shown Figure 78.

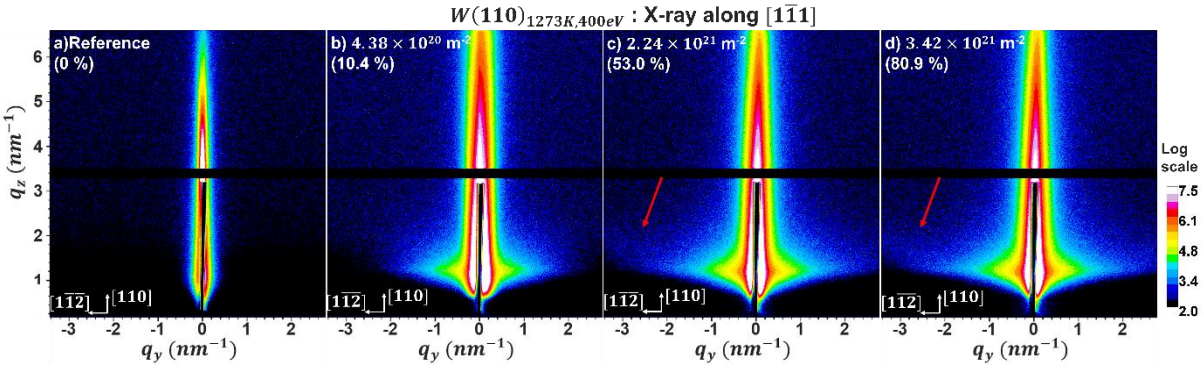

Figure 78:GISAXS patterns recorded at $\alpha_i = 0.47°$ for $W(110)_{1273K,400eV}$ implanted with 400 eV ions at 1273K. The incident X-ray beam is aligned along the $[1\bar{1}1]$ direction. The patterns correspond to the reference state before implantation (a), approximately 10% of the final fluence (b), 50% of the total fluence (c) and 100% of the reached fluence (d).

At this temperature, GISAXS patterns vary during implantation. At low fluence (Figure 78a) no lateral streaks due to facets are visible, while at half the implantation (Figure 78b) facets from bubbles surface are progressively growing as seen by the progressive apparition of the lateral rod (pointed with red arrow). The signal of facets is more and more intense as the implanted dose increases. This could correspond to an increase of the concentration of faceted bubbles or due to the increase of the facet size due to the growth of bubbles.

The same behaviour has been observed for two different samples implanted with 2 keV ions as shown in Figure 79.

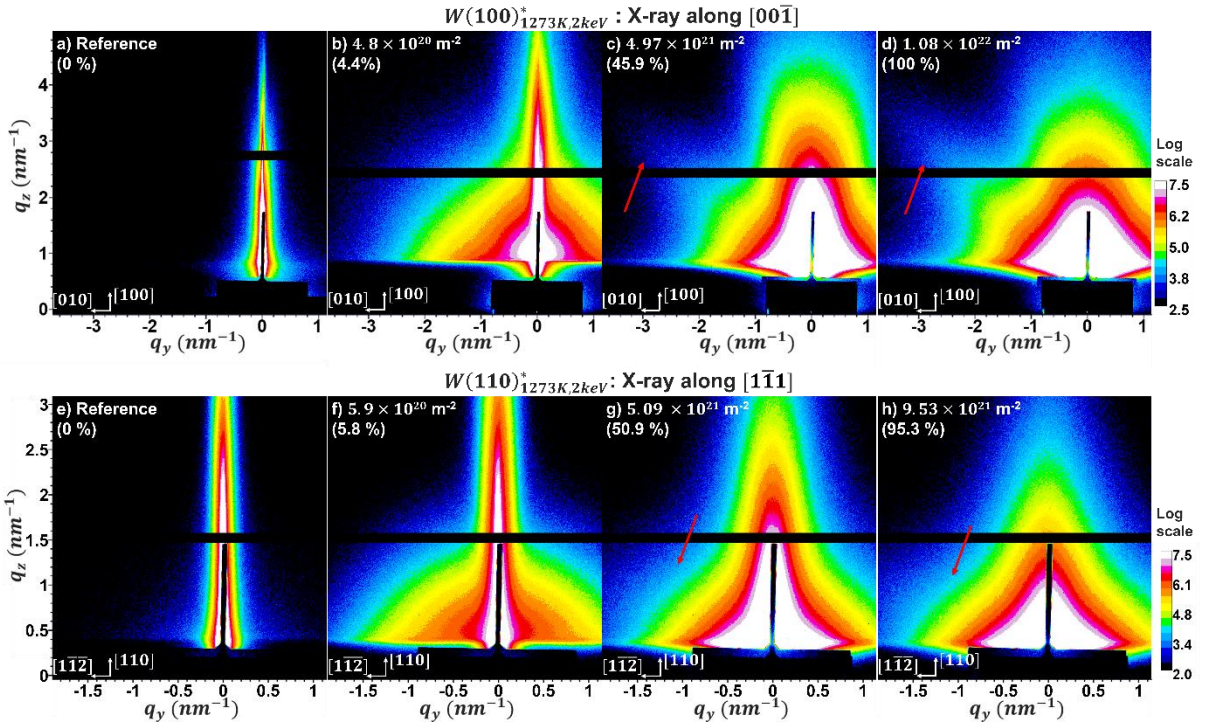

Figure 79: GISAXS patterns recorded at $\alpha_i = 0.6°$ for $W(100)^*_{1273K,2keV}$ (top row), $W(110)^*_{1273K,2keV}$(bottom row) implanted with 2 keV ions at 1273K. The patterns correspond to the early stage of implantation (a and d), 50% of the total fluence (b and e) and 100% of the reached fluence (c and f).

The reference state before implantation is shown in the first column of Figure 79. In the first time of implantation (second column of Figure 79) a diffuse scattering signal appears, this signal is rather similar for both samples and isotropic, indicating the presence of spherical bubbles buried below the sample. The specular rod becomes broader as the fluence increases as shown in the second column of Figure 79. This behaviour can be assigned to an increase of the surface roughness during He implantation. This arises presumably from surface damages caused by the 2 keV He ions and bubbles bursting at the surface. In addition, a lateral rod highlighted by a red arrow is more and more pronounced with implantation.

5.2.2. Growth mechanism

The average size d_{110} of the {110} facet is given by $d_{110} = \frac{2\pi}{\Delta q}$ where Δq is the full width at half maximum (FWHM) of the diffuse scattering rod. Even though this formula does not give a quantitative value of the facet size, it provides a good estimate and allows close comparison between samples. The size evolution of the facets has been measured for $W(100)^{*}_{1273\mathrm{K,2keV}}$ and $W(110)^{*}_{1273\mathrm{K,2keV}}$. The experimental uncertainty on GISAXS measurements lies on the fit quality of the intensity profile along the rod width. When the facet size is small (< 2 nm), the rod is broad and the ratio between the scattered intensity and the background is not favourable. In this case, the maximum relative uncertainty on the facet size is 40%. When facets are larger, (> 2nm) the relative uncertainty decreases rapidly and tends to 5%.

Assuming that the bubbles have reached a quasi-equilibrium shape at 1273 K [174], the bubble radius R (defined here as the half distance between two opposite {100} facets) is given by:

$$R = \frac{d_{100}}{2} + \frac{\sqrt{2}}{2} d_{110}$$

where d_{hkl} is the size of the hkl facet.

Furthermore, d_{100} can be directly estimated from the {110} facet size and surface energy anisotropy ratio ($\gamma_{100}/\gamma_{110}$) derived in section 4.3.1 as $\frac{\gamma_{100}}{\gamma_{110}} = \frac{d_{100}+\sqrt{2}d_{110}}{\sqrt{2}d_{100}+d_{110}}$, this leads to:

$$d_{100} = d_{110} \frac{\frac{\gamma_{100}}{\gamma_{110}} - \sqrt{2}}{1 - \frac{\gamma_{100}}{\gamma_{110}}\sqrt{2}}$$

Finally, the radius is:

$$R = \frac{d_{110}}{2}\left(\sqrt{2} + \frac{\frac{\gamma_{100}}{\gamma_{110}} - \sqrt{2}}{1 - \frac{\gamma_{100}}{\gamma_{110}}\sqrt{2}}\right)$$

Thus, the variations of {110} facet size and bubble radius are correlated by a simple linear relation. Let us note that it has been estimated in section 4.3.1 that $\gamma_{100}/\gamma_{110} = 1.03$ (see also ref. [174]).

Figure 80 represents the bubble radius evolution measured by *in-operando* GISAXS considering the two crystallographic orientations of the surface. As seen in Figure 80a, bubble growth occurs in three steps and is identical for both crystallographic orientations. First, the bubble radius is below the detection limit (<0.5 nm) for a so-called incubation time. Then, once the fluence reaches approximately 5.80×10^{20} m^{-2} the bubble radius increases drastically up to around 4 nm beyond which the growth

rate slows down significantly. We propose two possible explanations for the observed incubation time.

The first possible scenario has been proposed by Trinkaus *et al.* [175]. The incubation phase corresponds to a regime during which bubbles are not stable and spontaneously form and dissociate. Then, since the He concentration in the W matrix continuously increases during He implantation, a critical bubble size is finally reached, above which the bubbles are stable and can grow. In our experiments, the fluence needed to overpass the incubation phase is around 5.80×10^{20} m^{-2} and the critical bubble radius would be between 0 and 1.2 ± 0.3 nm.
The second probable scenario has been proposed by Curiotto *et al.* and is based on KMC simulations [176]. The diffusion of facetted voids of different sizes in a bcc solid has been simulated. It has been shown that the diffusion coefficient first increases with the void size, reaches a maximum and then decreases to follow classical scaling power laws for diffusion of 3D objects. In our experiment, if the MC of bubble is the governing coarsening mechanism, the motion of small bubbles is initially hampered due to a low diffusion coefficient, until their size increases sufficiently for the diffusion coefficient to reach its maximum strongly favouring the coalescence phenomenon. This moment might correspond to the incubation time. Then, since the bubble size increases the diffusion coefficient decreases continuously limiting drastically the number of coalescence events.

To determine whether OR or MC is governing the coarsening mechanism, the radius evolution of the bubbles has been compared to theoretical predictions according to the long-time regime of void growth (see Figure 80).

The expected radius evolution by OR mechanism has been derived by Greenwood [130] and is $R(t) \propto t^{\frac{1}{2}}$.

For the MC mechanism, Goodhew and Tyler [128] have derived the time dependence of the mean bubble radius assuming that the volume of bubbles is conserved after coalescence. They have found the following radius variation:

$$\frac{dR(t)}{dt} = \frac{8\pi c D_b}{3R(t)}$$

with D_b the bubble diffusion coefficient that depends on the transport process (given in Table 9) and c the volume fraction of bubbles in the sample (assumed to be constant).

Elementary processes	Bubble diffusion coefficient: D_b	
Vapor transport	$D_{b,vap} = \frac{D_g P \Omega^2 q}{k_B T R(t)^3}$	D_g: diffusion coefficient of metal atom in the bubble gas P: vapor pressure of the metal Ω: the atomic volume q: deviation of the bubble gas from ideal gas T: temperature k_B: the Boltzmann constant
Volume transport	$D_{b,vol} = \frac{D_v \Omega}{R(t)^3}$	D_v: diffusion coefficient of vacancy in the metal matrix
Surface transport	$D_{b,surf} = \frac{4 D_s \Omega^2}{\alpha_s^2 R(t)^4}$	D_s : surface coefficient diffusion the metal atom α_s : jump distance of the moving atom
Ledge nucleation regime	$D_{b,ledge} = \frac{\pi D_s R(t)}{6\alpha_s} exp\left(\frac{-\pi R(t) \varepsilon}{2 k_B T}\right)$	ϵ : ledge energy formation

Table 9: Bubble diffusion coefficient regarding the elementary processes of the bubble motion, from ref. [128].

After integration, scaling power laws can be deduced for the bubble radius $R(t) = A t^{\frac{1}{n}}$ with $n = 5$ for vapour and volume transports and $n = 6$ for surface transport. The prefactor A contains all the constants and is different for each transport regime.

For the ledge nucleation regime, the time dependence of the radius is hence $R(t) = \frac{ln(Bkt)}{k}$ where $B = \frac{8\pi^2 c D_s}{18\alpha_s}$ and $k = \frac{\pi\varepsilon}{2k_B T}$ are constants. The time scale in the expressions has been shifted to consider the incubation time τ such that $t \rightarrow t - \tau$. In other words, the experimental points have been fitted by power law functions expressed by $R(t) = A(t-\tau)^{\frac{1}{n}}$ (A and τ are fitted parameters) except for the ledge nucleation limited regime case where $R(t) = \frac{ln(Bk(t-\tau)+1)}{k}$. In such a way, when $t = \tau$ the radius is $R(t = \tau) = 0$ nm.

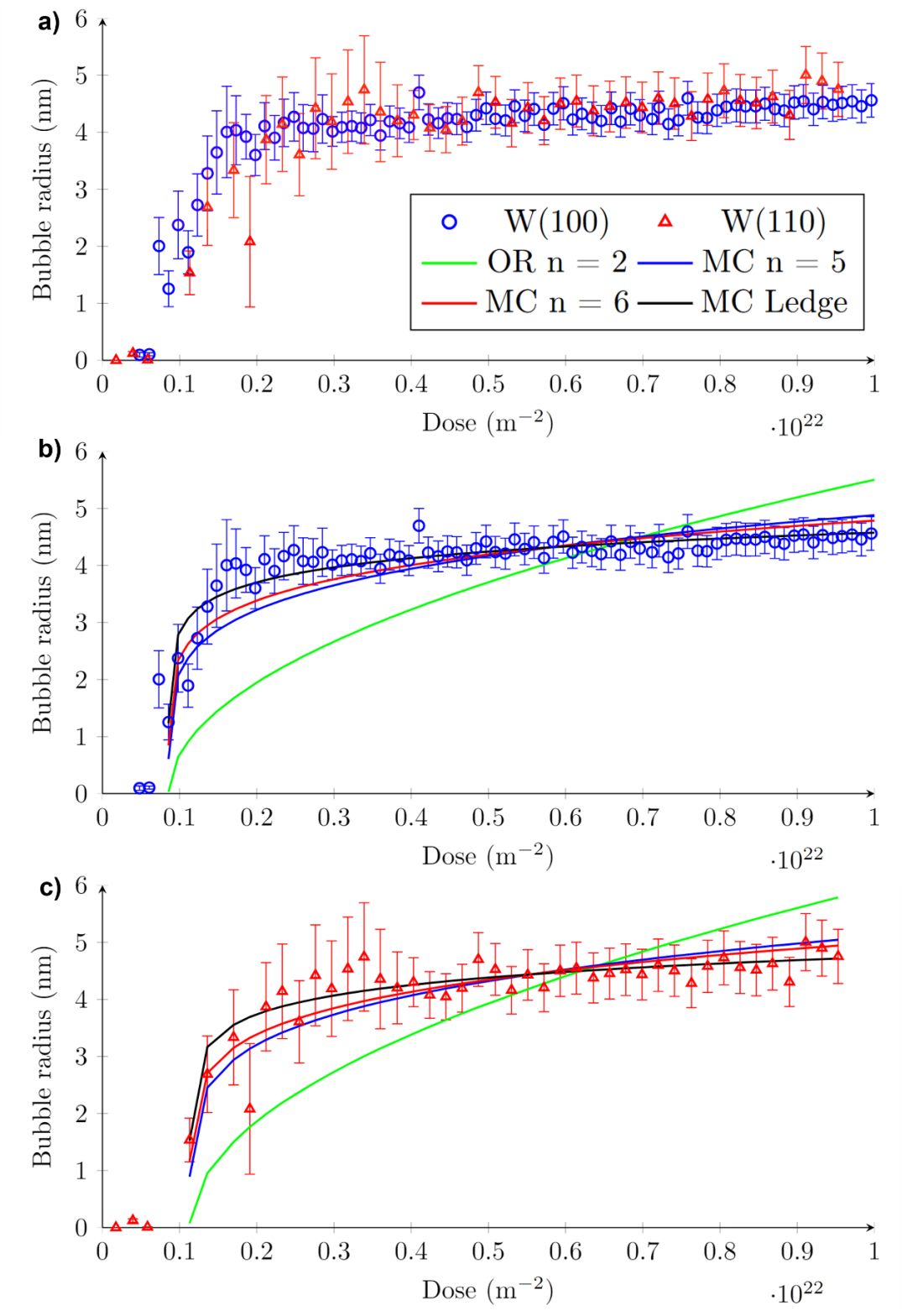

Figure 80: The experimental bubble radius evolution in $W(100)^{*}_{1273K,2keV}$ (blue dots) and $W(110)^{*}_{1273K,2keV}$ (red triangles) during 2 keV He implantation at 1273 K by in-situ GISAXS analysis. The full line curves represent the fit corresponding the different growing mechanisms. In green Ostwald ripening, in blue is the non-distinguishable case of migration-coalescence by vapour or volume diffusion, in red the migration-coalescence limited by surface diffusion and in black the ledge nucleation migration-coalescence regime.

The best fit is obtained for bubble growth with a limiting elementary mechanism of bubble motion by the ledge nucleation mechanism at the bubble facets (black curve). OR (green lines) clearly does not overlap the experimental data and other MC mechanisms are not as satisfactory (blue and red curves) as the ledge nucleation-based process. Let us note that the models of radius evolution are based on the assumption of a constant bubble volume fraction. This implies that the time scale for the increase of c is much longer than the growth rate of He bubbles and we can assume a weak effect of the concentration increase.

The fitted parameters for the ledge nucleation regime are given in Table 10. Assuming that the diffusivity of W atoms at the bubbles inner surface does not depend on the initial surface orientation (i.e. B constant), we can deduce the ledge energy ε that is about 2.63±0.04 × 10^{-11} J.m^{-1}.

Sample	B (nm.s^{-1})	ε (in J.m^{-1})
$W(100)^{*}_{1273\mathrm{K},2\mathrm{keV}}$	0.69	2.67×10^{-11}
$W(110)^{*}_{1273\mathrm{K},2\mathrm{keV}}$	0.69	2.59×10^{-11}

Table 10: Fit parameters for the ledge nucleation limited growth.

For comparison the ledge energy ε has also been reported for the W surface in vacuum and lies in between 2.18×10^{-10} and 4.95×10^{-10} J.m^{-1} at 0 K under vacuum [177]. The deduced value of the ledge energy ε from GISAXS analysis is thus an order of magnitude smaller. This difference could result from the influence of the sample temperature (1273 K) and He atoms trapped inside the bubbles that may reduce the ledge nucleation energy barrier. Indeed, it has been shown [85] that W atoms could be expelled from their crystallographic positions in pressurized He bubbles. This type of mechanism clearly indicates that the mobility of W atoms may be strongly enhanced at the surface of He bubbles and favour the nucleation of ledges on facets by reducing the energy barrier. A growth mechanism based on coalescence is supported by our TEM observations. Coalescence of bubbles was clearly observed several times as shown in Figure 81 (see red arrows).

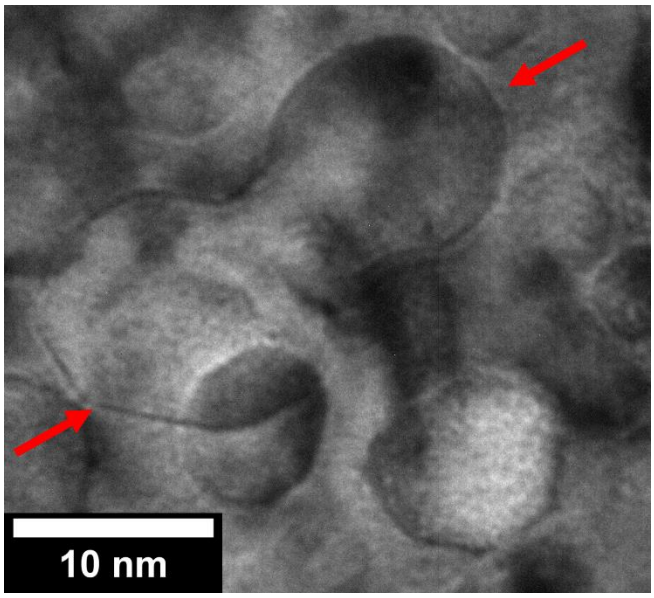

Figure 81: TEM micrograph of $W(110)_{1273K,2keV}$ implanted with 2 keV He ion at 1273 K and after post-implantation temperature plateau at 1273 K during 11 hours. Two bubbles marked by the red arrows are coalescing.

5.2.3. **Bubble diffusion coefficient**

The extraction of the bubbles radius as function of time by the migration coalescence mechanism allows us to estimate the evolution of the bubble diffusion coefficient over time if the volume fraction of bubbles is known. Indeed, rewriting the expression of $D_{b,ledge}$ (Table 9) with the expressions of B and k, the bubble radius dependence of the diffusion coefficient $D_{b,ledge}$ is given by:

$$D_{b,ledge} = \frac{3}{8\pi c} BR(t) exp\left(-kR(t)\right)$$

where $R(t)$ is experimentally measured and B and k are deduced by the previous fit.

Since *c* can be estimated by TEM analysis it should be possible to quantify the bubbles' diffusion coefficient. In order to do so, TEM analysis has been performed on an extra $W(110)_{1273\mathrm{K},2\mathrm{keV}}$ sample. The sample has been implanted in the same conditions then maintained at 1273 K during 11 hours after implantation allowing bubble to grow and to be easily visible by TEM. The parameter c is expected to stay constant during the whole plateau as the bubble growth is described by the constant volume model. The bubble radius measured by GISAXS at the end of the temperature plateau is 7.08±0.35 nm.Bubbles in the volume represented by the red dashed rectangle in Figure 82 were counted manually. The area is limited in depth at 40 nm that corresponds to the maximum penetration of X-ray at $\alpha_i = 0.6°$.

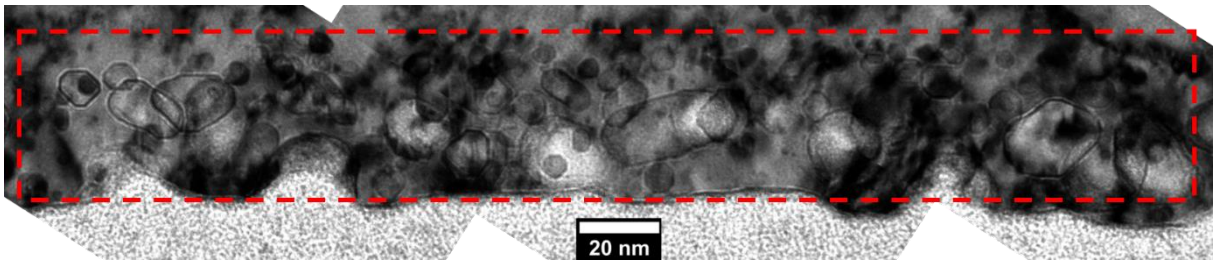

Figure 82: TEM micrograph of $W(110)_{1273K,2keV}$ implanted with 2keV He ion at 1273 K and after post-implantation temperature plateau during 11 hours. The bubble density has been estimated in the area delimited by the red dashed rectangle.

This number is probably under-estimated and experimental errors could result in missing small bubbles, due to bubble overlap and possibly truncated bubble at the lamella surfaces. The estimated bubble density is 1.04×10^{23} m^{-3}. The volume fraction c expressed as the product of the bubble volume (R^3) and density [128] is c = 0.11. It means around 11% of the volume is filled with bubbles.

Figure 83 shows the evolution of D_b as a function of He dose. The sharp decrease of D_b from 10^{-2} to 10^{-4} $nm^2.s^{-1}$ with the implanted dose is clear evidence that the bubble diffusion coefficient drops: it is dominated by its exponential decay.

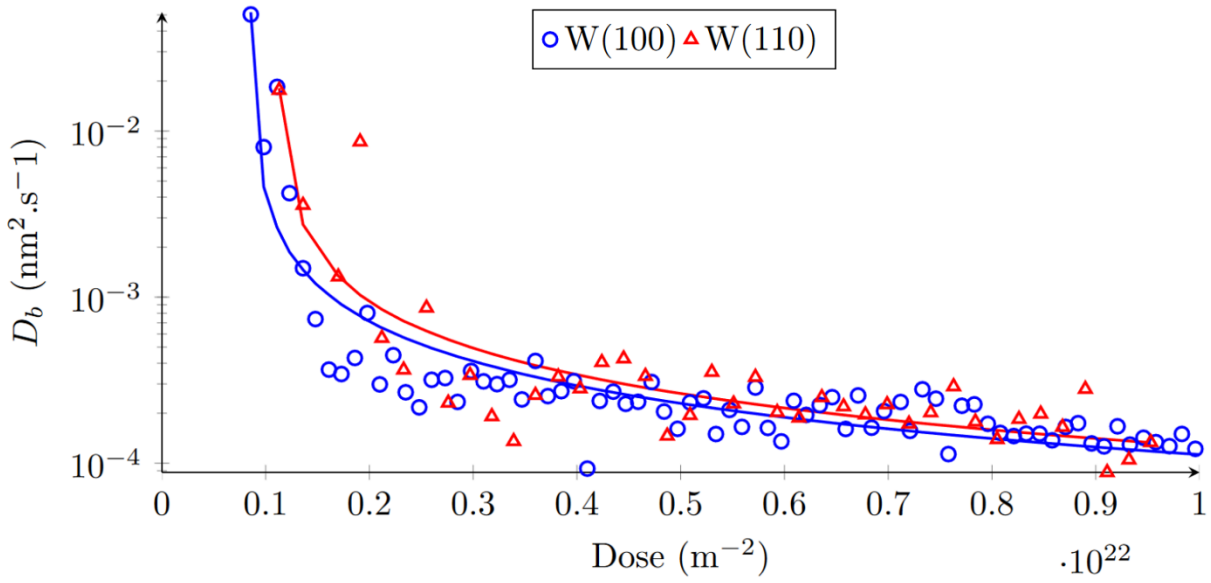

Figure 83: Bubble diffusion coefficient evolution during the bubble growth by migration-coalescence limited by ledge nucleation in $W(100)^*_{1273K,2keV}$ (blue) and $W(110)^*_{1273K,2keV}$ (red). Dot representations of the diffusion coefficient (blue circle, red triangle) are deduced from the experimental measurements of the bubble radius and full lines are deduced from the bubble radius prediction by the best fit.

We can estimate that D_b decreases by two orders of magnitude during implantation, indicating that the bubbles are much less mobile as they grow. At some point, the mobility of bubbles is too low and coalescence is less frequent resulting in a very slow evolution of the bubble size.

Conclusion

This chapter summarises the main results of this work and how these results can contribute to a better understanding of the interaction between tungsten and helium. The limitations of this study will be reviewed and perspectives for future work will be drawn.

The aim of this study was to clarify the role of different parameters influencing the formation of helium bubbles in tungsten. One of the objectives of this work was to access to the dynamics of the phenomena involved in the evolution of bubbles. To that end, we have characterized the bubble formation and evolution in real time during implantation by *in-operando* grazing incidence small angle X-ray scattering (GISAXS). Samples were also analysed by transmission electron microscopy (TEM) after implantation.

Main results and contribution to the field

Temperature and the presence of vacancies in the tungsten matrix are key parameters. Below 873 K, in absence of vacancies, bubbles formed are either spherical and small (approximately 1 nm in diameter) or larger and spheroidal (few nanometers on the longest side). The mechanism suggested for the formation of spheroidal bubbles is the static coalescence of spherical bubbles. In absence of available nucleation site (vacancies), new bubbles are preferentially nucleated at the neighbourhood of pre-existing bubbles, thus, spherical bubbles are closely packed. This theory derived from simulations in the literature seems to be confirmed experimentally here. In addition, the behaviour of bubbles observed for high energy (2keV, that generates vacancies) and low temperature (523 K, where vacancies annihilation is limited) implantation seems also to point into this direction. In such conditions, the large majority of bubbles are spherical and spaced apart. The distance between bubbles is greater because preferential nucleation sites (vacancies) are available directly from the implantation process. The occurrence of coalescence events is therefore limited. If the temperature is raised further (e.g. from 873 K), vacancies are able to migrate and be annihilated or absorbed in bubbles. It results that spherical bubbles are formed, then they can grow by vacancies absorption until they touch each other and coalesce forming pearl necklace like structures. This study at low temperatures (≤ 873 K) gives a plausible explanation for the formation of elongated bubbles also referred as platelets and pearl necklace like structures.

For higher temperatures (e.g. 1273 K), the shape of bubbles is composed of facets as already reported in the literature. In agreement with most results found in the literature, {110} -type facets have been observed. The presence of {100}-type facets is also

observed which is a new result. The thermodynamic equilibrium has been approached by raising the temperature up to 1773 K. At this temperature and for all the three studied crystalline orientations (100), (110) and (111), bubbles remain facetted by {100} and {110}-type facets. The surface energy anisotropy between (100) and (110) surface has been estimated to $\gamma_{100}/\gamma_{110} = 1.03 \pm 0.03$ using the Wulff theorem. The deduced surface energy anisotropy found is lower when compared with simulated data for pure tungsten. This is a clear evidence of an impact of pressurized helium on thermodynamic properties of tungsten.

The growth mechanism of facetted bubbles has been investigated. The time evolution of the bubble radius has been measured by *in-operando* GISAXS in real time during implantation. A close comparison with analytical modelling of the growth process has been performed. Ostwald ripening and four different regimes of migration-coalescence have been considered. The growth kinetics obtained experimentally suggests a growth dominated by the migration-coalescence of bubbles during which the bubble motion is hindered by the nucleation of ledges at the bubble facet surface. The size dependence of the diffusion coefficient of bubbles has been derived. The diffusion coefficient decreases exponentially with the bubble radius limiting collision frequency and coalescence. This is a valuable information for implantation of bubble motion in simulation models.

Limitations and perspectives

The major limitation of this work is the low flux obtained during implantation ($\sim 10^{17}$ $m^{-2}s^{-1}$). This has allowed to study the early stage of the formation of bubbles but in comparison to a D-T discharge in ITER, the maximum fluence in our experiment will be reached in a dozen of seconds in ITER. To fill this gap, it is recommended to perform plasma implantation to increase the flux of implanted helium ions.

Our approach based on nanoscience using in-operando GISAXS and post-mortem TEM characterisation have permitted to identify the impact of temperature, vacancies and crystalline orientation of the surface in model samples. The results obtained in this work are valuable resources for the modelling of the bubble behaviour in tungsten. In future it is now recommended to increase the sample complexity, e.g. adding grain boundaries to the microstructure or adding impurities such as oxygen present in fusion devices or carbon in order to get closer to a real plasma facing component.

Appendix

This appendix includes some of the most standard diffraction pattern obtained by electron diffraction in bcc single crystal by a TEM. The diffraction patterns have been reproduced from ref. [150]

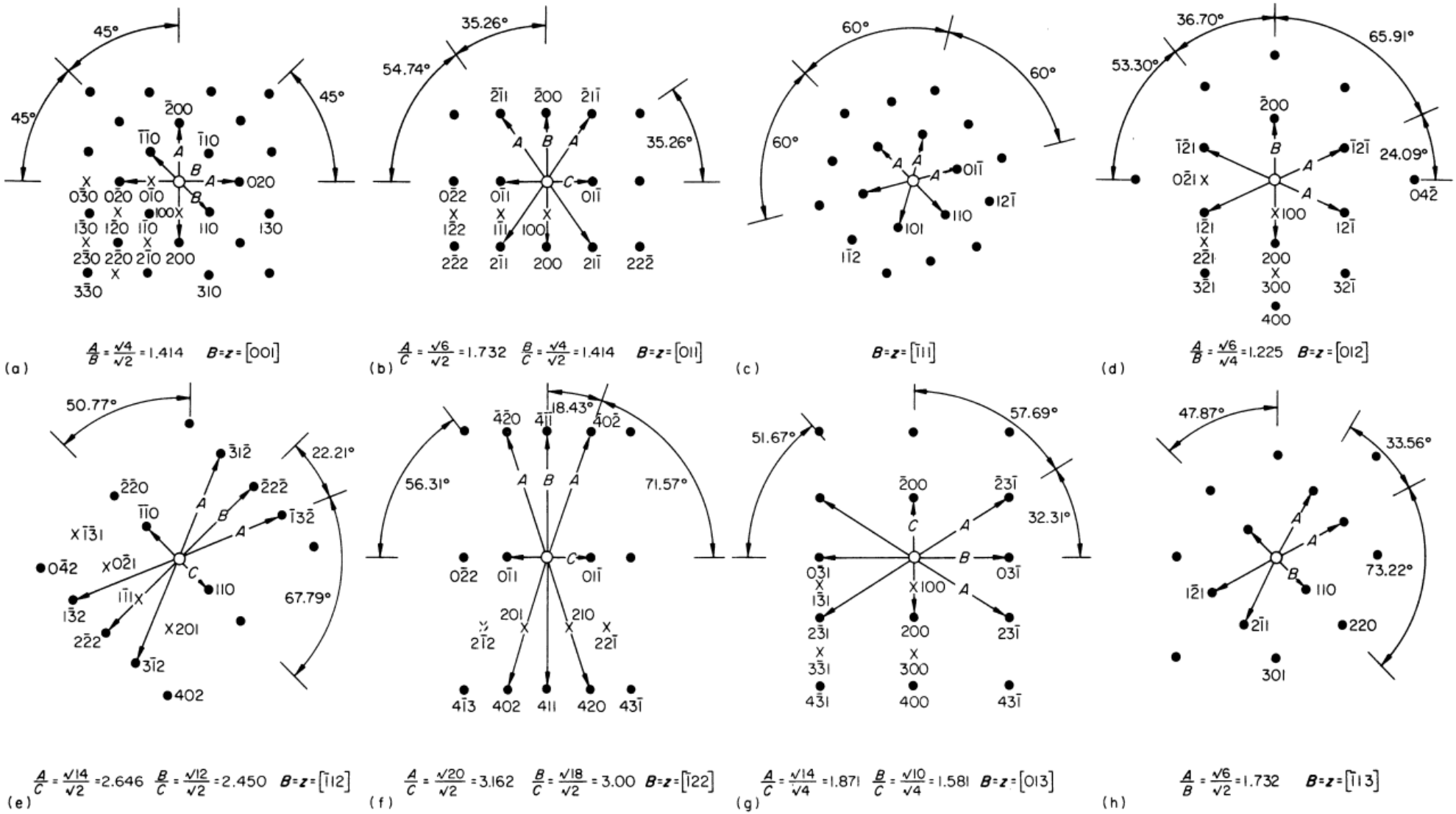
45°
45°
45°
$\bar{2}00$
$\bar{1}10$
$1\bar{1}0$
A
B
A
020
B
$0\bar{3}0$ $0\bar{2}0$ $0\bar{1}0$ 100 110 130
$1\bar{3}0$ $1\bar{2}0$ $1\bar{1}0$
$2\bar{3}0$ $2\bar{2}0$ $2\bar{1}0$ 200
$3\bar{3}0$ 310
(a) $\frac{A}{B} = \frac{\sqrt{4}}{\sqrt{2}} = 1.414$ $B = z = [001]$
35.26°
54.74°
35.26°
$2\bar{1}1$ $\bar{2}00$ $2\bar{1}\bar{1}$
A B A
C
$0\bar{2}2$ $0\bar{1}1$ 011
$1\bar{2}2$ $1\bar{1}1$ 100
$2\bar{2}2$ $2\bar{1}1$ 200 $2\bar{1}\bar{1}$ $22\bar{2}$
(b) $\frac{A}{C} = \frac{\sqrt{6}}{\sqrt{2}} = 1.732$ $\frac{B}{C} = \frac{\sqrt{4}}{\sqrt{2}} = 1.414$ $B = z = [011]$
60°
60°
60°
A A A
$01\bar{1}$
110
$12\bar{1}$
101
$1\bar{1}2$
(c) $B = z = [\bar{1}11]$
36.70°
53.30°
65.91°
24.09°
$\bar{2}00$
$\bar{1}2\bar{1}$ $\bar{1}2\bar{1}$
B
A A
$0\bar{2}1$ 100 $12\bar{1}$
$1\bar{2}1$ $12\bar{1}$
$2\bar{2}1$ 200 $32\bar{1}$
$3\bar{2}1$ 300
400
$04\bar{2}$
(d) $\frac{A}{B} = \frac{\sqrt{6}}{\sqrt{4}} = 1.225$ $B = z = [012]$
50.77°
22.21°
67.79°
$\bar{3}1\bar{2}$
$\bar{2}2\bar{0}$ $\bar{2}2\bar{2}$
$\bar{1}10$
A B A
$\bar{1}3\bar{2}$
$\bar{1}3\bar{1}$
$0\bar{4}2$ $0\bar{2}1$
C
110
$1\bar{1}1$
$1\bar{3}2$
$2\bar{2}2$
201
$3\bar{1}2$
402
(e) $\frac{A}{C} = \frac{\sqrt{14}}{\sqrt{2}} = 2.646$ $\frac{B}{C} = \frac{\sqrt{12}}{\sqrt{2}} = 2.450$ $B = z = [\bar{1}12]$
56.31°
18.43°
71.57°
$4\bar{2}0$ $4\bar{1}1$ $40\bar{2}$
A B A
C
$0\bar{2}2$ $0\bar{1}1$ 011
201 210
$2\bar{1}2$ $22\bar{1}$
$4\bar{1}3$ 402 411 420 $43\bar{1}$
(f) $\frac{A}{C} = \frac{\sqrt{20}}{\sqrt{2}} = 3.162$ $\frac{B}{C} = \frac{\sqrt{18}}{\sqrt{2}} = 3.00$ $B = z = [\bar{1}22]$
51.67°
57.69°
32.31°
$\bar{2}00$ $\bar{2}3\bar{1}$
C
A
B
$03\bar{1}$
$0\bar{3}1$
100
$1\bar{3}1$
$2\bar{3}1$ 200 $23\bar{1}$
$3\bar{3}1$ 300
$4\bar{3}1$ 400 $43\bar{1}$
(g) $\frac{A}{C} = \frac{\sqrt{14}}{\sqrt{4}} = 1.871$ $\frac{B}{C} = \frac{\sqrt{10}}{\sqrt{4}} = 1.581$ $B = z = [013]$
47.87°
33.56°
73.22°
A
A
B
110
$1\bar{2}1$
$2\bar{1}1$
220
301
(h) $\frac{A}{B} = \frac{\sqrt{6}}{\sqrt{2}} = 1.732$ $B = z = [\bar{1}13]$

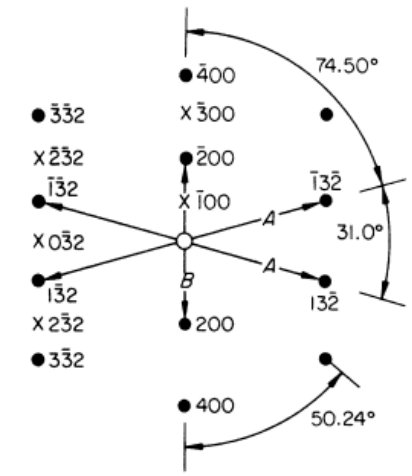

(i) $\frac{A}{B} = \frac{\sqrt{14}}{\sqrt{4}} = 1.871$ $B = z = [023]$

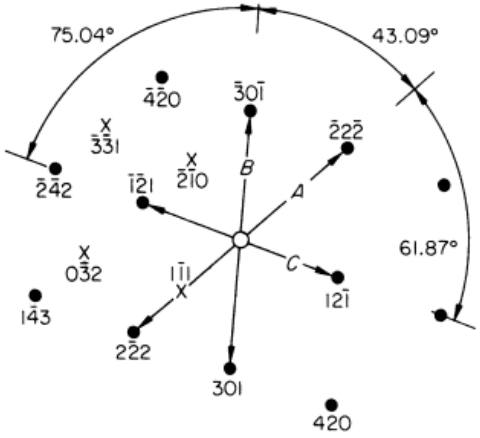

(j) $\frac{A}{C} = \frac{\sqrt{12}}{\sqrt{6}} = 1.414$ $\frac{B}{C} = \frac{\sqrt{10}}{\sqrt{6}} = 1.291$ $B = z = [\bar{1}23]$

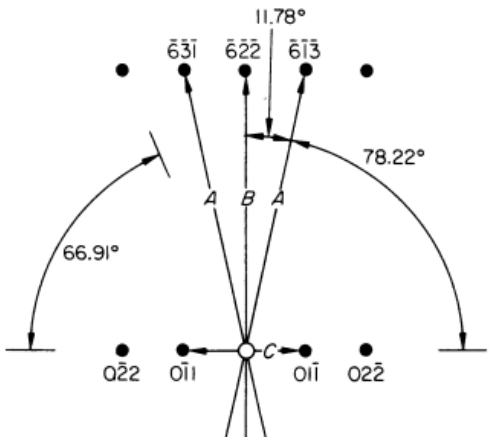

(k) $\frac{A}{C} = \frac{\sqrt{46}}{\sqrt{2}} = 4.796$ $\frac{B}{C} = \frac{\sqrt{44}}{\sqrt{2}} = 4.690$

$B = z = [\bar{2}33]$

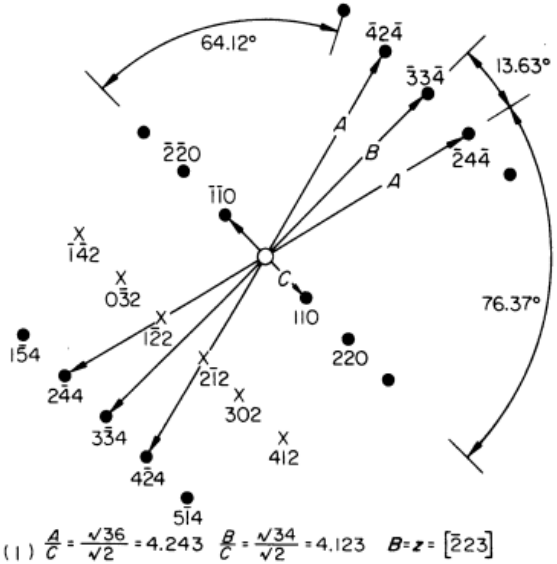

(l) $\frac{A}{C} = \frac{\sqrt{36}}{\sqrt{2}} = 4.243$ $\frac{B}{C} = \frac{\sqrt{34}}{\sqrt{2}} = 4.123$ $B = z = [\bar{2}23]$

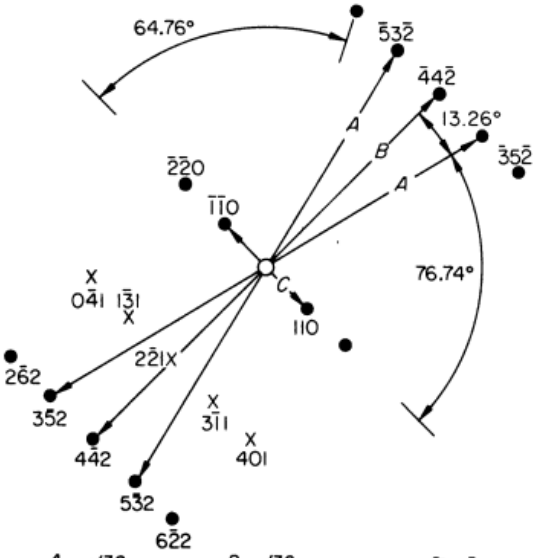

(m) $\frac{A}{C} = \frac{\sqrt{38}}{\sqrt{2}} = 4\ 359$ $\frac{B}{C} = \frac{\sqrt{36}}{\sqrt{2}} = 4\ 243$ $B = z = [\bar{1}14]$

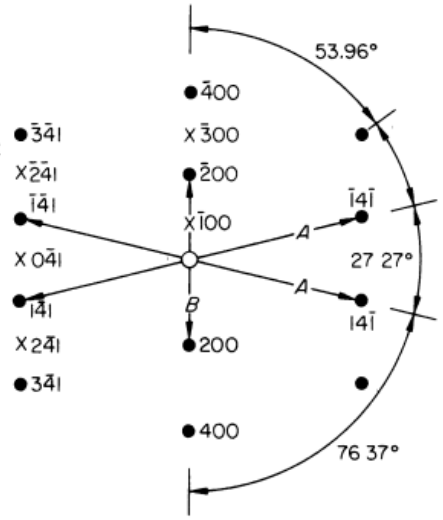

(n) $\frac{A}{B} = \frac{\sqrt{18}}{\sqrt{4}} = 2\ 121$ $B = z = [014]$

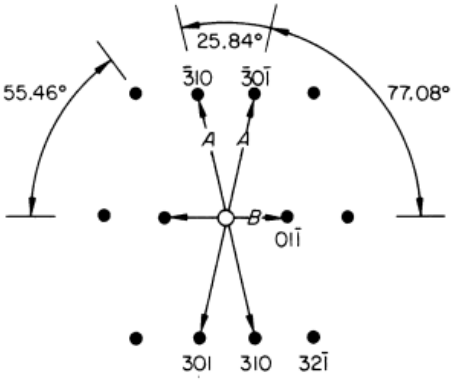

(o) $\frac{A}{B} = \frac{\sqrt{10}}{\sqrt{2}} = 2.236$ $B = z = [\bar{1}33]$

References

[1] H. Ritchie and P. Rosado, Energy Mix, Our World in Data (2020).

[2] A. Köhn-Seemann and J. Hillairet, alfkoehn/fusion_plots: Second release of the fusion plot package (new plots added), (2021).

[3] L. L. Lucas and M. P. Unterweger, Comprehensive review and critical evaluation of the half-life of tritium, J. Res. Natl. Inst. Stand. Technol. **105**, 541 (2000).

[4] M. Ni, Y. Wang, B. Yuan, J. Jiang, and Y. Wu, Tritium supply assessment for ITER and DEMOnstration power plant, Fusion Engineering and Design **88**, 2422 (2013).

[5] J. D. Lawson, Some Criteria for a Power Producing Thermonuclear Reactor, Proc. Phys. Soc. B **70**, 6 (1957).

[6] A. B. Zylstra et al., Burning plasma achieved in inertial fusion, Nature **601**, 542 (2022).

[7] J.-L. Miquel, C. Lion, and P. Vivini, The Laser Mega-Joule : LMJ & PETAL status and Program Overview, J. Phys.: Conf. Ser. **688**, 012067 (2016).

[8] IAEA bulletin, *Fusion Energy* (2021).

[9] V. Bykov et al., Structural analysis of W7-X: Overview, Fusion Engineering and Design **84**, 215 (2009).

[10] A. Iiyoshi et al., Overview of the Large Helical Device project, Nucl. Fusion **39**, 1245 (1999).

[11] *Fundamentals of Magnetic Thermonuclear Reactor Design* (Elsevier, 2018).

[12] J. Bucalossi et al., The WEST project: Testing ITER divertor high heat flux component technology in a steady state tokamak environment, Fusion Engineering and Design **89**, 907 (2014).

[13] S. Ishida, P. Barabaschi, and Y. Kamada, Overview of the JT-60SA project, Nucl. Fusion **51**, 094018 (2011).

[14] S. Wu, An overview of the EAST project, Fusion Engineering and Design **82**, 463 (2007).

[15] Y.-K. Oh et al., Commissioning and initial operation of KSTAR superconducting tokamak, Fusion Engineering and Design **84**, 344 (2009).

[16] R. Delaporte-Mathurin and Nicolasialovega, RemDelaporteMathurin/fusion-world: Patch 0.4.1, (2022).

[17] G. F. Matthews et al., JET ITER-like wall—overview and experimental programme, Phys. Scr. **T145**, 014001 (2011).

[18] J. Mailloux et al., Overview of JET results for optimising ITER operation, Nucl. Fusion **62**, 042026 (2022).

[19] B. J. Green and I. I. T. A. P. Teams, ITER: burning plasma physics experiment, Plasma Phys. Control. Fusion **45**, 687 (2003).

[20] R. Aymar, P. Barabaschi, and Y. Shimomura, The ITER design, Plasma Phys. Control. Fusion **44**, 519 (2002).

[21] the ITER Organization, Domestic Agencies and ITER Collaborators et al., Innovations in Technology and Science R&D for ITER, J Fusion Energ **38**, 11 (2019).

[22] R. Mitteau, P. Stangeby, C. Lowry, and M. Merola, Heat loads and shape design of the ITER first wall, Fusion Engineering and Design **85**, 2049 (2010).

[23] R. Mitteau, R. Eaton, A. Gervash, V. Kuznetcov, V. Davydov, and R. Rulev, Allowable heat load on the edge of the ITER first wall panel beryllium flat tiles, Nuclear Materials and Energy **12**, 1067 (2017).

[24] G. De Temmerman, T. Hirai, and R. A. Pitts, The influence of plasma-surface interaction on the performance of tungsten at the ITER divertor vertical targets, Plasma Phys. Control. Fusion **60**, 044018 (2018).
[25] R. Neu, R. Dux, A. Geier, O. Gruber, A. Kallenbach, K. Krieger, H. Maier, R. Pugno, V. Rohde, and S. Schweizer, Tungsten as plasma-facing material in ASDEX Upgrade, Fusion Engineering and Design **65**, 367 (2003).
[26] E. Lassner and W.-D. Schubert, *Tungsten: Properties, Chemistry, Technology of the Element, Alloys, and Chemical Compounds* (Springer US, Boston, MA, 1999).
[27] J. Roth et al., Recent analysis of key plasma wall interactions issues for ITER, Journal of Nuclear Materials **390–391**, 1 (2009).
[28] V. Philipps, Tungsten as material for plasma-facing components in fusion devices, Journal of Nuclear Materials **415**, S2 (2011).
[29] R. Delaporte-Mathurin, Hydrogen Transport in Tokamaks, Université Sorbonne Paris nord, 2022.
[30] G. Federici et al., Plasma–material interactions in current tokamaks and their implications for next step fusion reactors, Nucl. Fusion **41**, 1967 (2001).
[31] M. Rieth, R. Doerner, A. Hasegawa, Y. Ueda, and M. Wirtz, Behavior of tungsten under irradiation and plasma interaction, Journal of Nuclear Materials **519**, 334 (2019).
[32] J. Amano and D. N. Seidman, Diffusivity of 3He atoms in perfect tungsten crystals, Journal of Applied Physics **56**, 983 (1984).
[33] P. E. Lhuillier, T. Belhabib, P. Desgardin, B. Courtois, T. Sauvage, M. F. Barthe, A. L. Thomann, P. Brault, and Y. Tessier, Trapping and release of helium in tungsten, Journal of Nuclear Materials **416**, 13 (2011).
[34] M. J. Banisalman, S. Park, and T. Oda, Evaluation of the threshold displacement energy in tungsten by molecular dynamics calculations, Journal of Nuclear Materials **495**, 277 (2017).
[35] K. D. Hammond, Helium, hydrogen, and fuzz in plasma-facing materials, Mater. Res. Express **4**, 104002 (2017).
[36] F. W. Meyer, He-ion induced surface morphology change and nanofuzz growth on hot tungsten surfaces, J. Phys. B: At. Mol. Opt. Phys. **52**, 012001 (2019).
[37] M. J. Baldwin and R. P. Doerner, Formation of helium induced nanostructure 'fuzz' on various tungsten grades, Journal of Nuclear Materials **404**, 165 (2010).
[38] D. Nishijima, M. Miyamoto, H. Iwakiri, M. Ye, N. Ohno, K. Tokunaga, N. Yoshida, and S. Takamura, Micron-Bubble Formation on Polycrystal Tungsten due to Low-Energy and High-Flux Helium Plasma Exposure, Mater. Trans. **46**, 561 (2005).
[39] N. Ohno, Y. Hirahata, M. Yamagiwa, S. Kajita, M. Takagi, N. Yoshida, R. Yoshihara, T. Tokunaga, and M. Tokitani, Influence of crystal orientation on damages of tungsten exposed to helium plasma, Journal of Nuclear Materials **438**, S879 (2013).
[40] S. Kajita, N. Yoshida, and N. Ohno, Tungsten fuzz: Deposition effects and influence to fusion devices, Nuclear Materials and Energy **25**, 100828 (2020).
[41] M. Tokitani, S. Kajita, S. Masuzaki, Y. Hirahata, N. Ohno, and T. Tanabe, Exfoliation of the tungsten fibreform nanostructure by unipolar arcing in the LHD divertor plasma, Nucl. Fusion **51**, 102001 (2011).
[42] S. Cui, M. Simmonds, W. Qin, F. Ren, G. R. Tynan, R. P. Doerner, and R. Chen, Thermal conductivity reduction of tungsten plasma facing material due to helium plasma irradiation in PISCES using the improved 3-omega method, Journal of Nuclear Materials **486**, 267 (2017).
[43] S. Qu et al., Thermal conductivity measurement of the He-ion implanted layer of W using transient thermoreflectance technique, Journal of Nuclear Materials **484**, 382 (2017).

[44] M. Cui, T. Shen, L. Pang, Y. Zhu, P. Jin, C. Liu, X. Fang, and Z. Wang, He ion implantation induced He bubbles and hardness in tungsten, Nuclear Materials and Energy **15**, 232 (2018).
[45] W. Qin, Y. Wang, M. Tang, F. Ren, Q. Fu, G. Cai, L. Dong, L. Hu, G. Wei, and C. Jiang, Microstructure and hardness evolution of nanochannel W films irradiated by helium at high temperature, Journal of Nuclear Materials **502**, 132 (2018).
[46] M. A. T. Thompson, K. Song, G. De Temmerman, H. Chen, N. Kirby, J. Bradby, D. Bhattacharyya, C. Hoang, and C. S. Corr, Identifying microstructural changes responsible for retarded grain growth during tungsten recrystallization after helium plasma exposure, Journal of Nuclear Materials **559**, 153448 (2022).
[47] E. Bernard et al., Tritium retention in W plasma-facing materials: Impact of the material structure and helium irradiation, Nuclear Materials and Energy **19**, 403 (2019).
[48] M. Ialovega, E. Bernard, R. Bisson, C. Martin, R. Sakamoto, A. Kreter, E. Hodille, T. Angot, and C. Grisolia, Hydrogen trapping in tungsten: impact of helium irradiation and thermal cycling, Phys. Scr. **T171**, 014066 (2020).
[49] M. Miyamoto, K. Sano, T. Sawae, M. Haruta, and H. Kurata, Effect of helium irradiation on the hydrogen isotope retention in tungsten by in situ TEM and STEM-EELS analysis, Nuclear Materials and Energy **36**, 101484 (2023).
[50] C. Grisolia et al., Tritium absorption and desorption in ITER relevant materials: comparative study of tungsten dust and massive samples, Journal of Nuclear Materials **463**, 885 (2015).
[51] G. M. Wright et al., Comparison of tungsten nano-tendrils grown in Alcator C-Mod and linear plasma devices, Journal of Nuclear Materials **438**, S84 (2013).
[52] G. M. Wright, D. Brunner, M. J. Baldwin, R. P. Doerner, B. Labombard, B. Lipschultz, J. L. Terry, and D. G. Whyte, Tungsten nano-tendril growth in the Alcator C-Mod divertor, Nucl. Fusion **52**, 042003 (2012).
[53] M. Rasiński et al., FIB line marking as a tool for local erosion/deposition/fuzz formation measurements in ASDEX Upgrade during the He campaign, Nuclear Materials and Energy **37**, 101539 (2023).
[54] S. Brezinsek et al., Surface modification of He pre-exposed tungsten samples by He plasma impact in the divertor manipulator of ASDEX Upgrade, Nuclear Materials and Energy **12**, 575 (2017).
[55] A. Hakola et al., Helium plasma operations on ASDEX Upgrade and JET in support of the non-nuclear phases of ITER, Nucl. Fusion **64**, 096022 (2024).
[56] E. Tsitrone et al., Investigation of plasma wall interactions between tungsten plasma facing components and helium plasmas in the WEST tokamak, Nucl. Fusion **62**, 076028 (2022).
[57] M. J. Baldwin and R. P. Doerner, Helium induced nanoscopic morphology on tungsten under fusion relevant plasma conditions, Nucl. Fusion **48**, 035001 (2008).
[58] M. J. Baldwin, R. P. Doerner, D. Nishijima, K. Tokunaga, and Y. Ueda, The effects of high fluence mixed-species (deuterium, helium, beryllium) plasma interactions with tungsten, Journal of Nuclear Materials **390–391**, 886 (2009).
[59] S. Kajita, S. Takamura, N. Ohno, D. Nishijima, H. Iwakiri, and N. Yoshida, Sub-ms laser pulse irradiation on tungsten target damaged by exposure to helium plasma, Nucl. Fusion **47**, 1358 (2007).
[60] M. Y. Ye and S. Takamura, Study of hot tungsten emissive plate in high heat flux plasma on NAGDIS-I, Nucl. Mater. **241–243**, 1243 (1997).
[61] S. Takamura, N. Ohno, D. Nishijima, and S. Kajita, Formation of Nanostructured Tungsten with Arborescent Shape due to Helium Plasma Irradiation, Plasma and Fusion Research **1**, 051 (2006).

[62] S. Kajita, W. Sakaguchi, N. Ohno, N. Yoshida, and T. Saeki, Formation process of tungsten nanostructure by the exposure to helium plasma under fusion relevant plasma conditions, Nucl. Fusion **49**, 095005 (2009).
[63] P. McCarthy, D. Hwangbo, M. Bilton, S. Kajita, and J. W. Bradley, Enhanced fuzzy tungsten growth in the presence of tungsten deposition, Nucl. Fusion **60**, 026012 (2020).
[64] O. El-Atwani, K. Hattar, J. A. Hinks, G. Greaves, S. S. Harilal, and A. Hassanein, Helium bubble formation in ultrafine and nanocrystalline tungsten under different extreme conditions, Journal of Nuclear Materials **458**, 216 (2015).
[65] D. Dasgupta, R. D. Kolasinski, R. W. Friddle, L. Du, D. Maroudas, and B. D. Wirth, On the origin of 'fuzz' formation in plasma-facing materials, Nucl. Fusion **59**, 086057 (2019).
[66] M. Li, J. Wang, and Q. Hou, Molecular dynamics studies of temperature effects on low energy helium bombardments on tungsten surfaces, Journal of Nuclear Materials **423**, 22 (2012).
[67] V. Borovikov, A. F. Voter, and X.-Z. Tang, Reflection and implantation of low energy helium with tungsten surfaces, Journal of Nuclear Materials **447**, 254 (2014).
[68] A. Dunand, M. Minissale, T. Angot, and R. Bisson, Flux dependence of helium retention in clean W(1 1 0): Experimental evidence for He self-trapping, Nuclear Materials and Energy **34**, 101324 (2023).
[69] D. Nishijima, T. Sugimoto, H. Iwakiri, M. Y. Ye, N. Ohno, N. Yoshida, and S. Takamura, Characteristic changes of deuterium retention on tungsten surfaces due to low-energy helium plasma pre-exposure, Journal of Nuclear Materials **337–339**, 927 (2005).
[70] S. Sharafat, A. Takahashi, Q. Hu, and N. M. Ghoniem, A description of bubble growth and gas release of helium implanted tungsten, Journal of Nuclear Materials **386–388**, 900 (2009).
[71] M. Yamagiwa, S. Kajita, N. Ohno, M. Takagi, N. Yoshida, R. Yoshihara, W. Sakaguchi, and H. Kurishita, Helium bubble formation on tungsten in dependence of fabrication method, Journal of Nuclear Materials **417**, 499 (2011).
[72] M. Ialovega et al., Helium-induced morphology evolution in tungsten under thermal treatment, Nucl. Fusion **62**, 126022 (2022).
[73] N. Juslin and B. D. Wirth, Interatomic potentials for simulation of He bubble formation in W, Journal of Nuclear Materials **432**, 61 (2013).
[74] J. Wang, Y. Zhou, M. Li, and Q. Hou, Atomistic simulations of helium behavior in tungsten crystals, Journal of Nuclear Materials **427**, 290 (2012).
[75] C. S. Becquart and C. Domain, Migration Energy of He in W Revisited by *Ab Initio* Calculations, Phys. Rev. Lett. **97**, 196402 (2006).
[76] C. S. Becquart and C. Domain, An object Kinetic Monte Carlo Simulation of the dynamics of helium and point defects in tungsten, Journal of Nuclear Materials **385**, 223 (2009).
[77] Y. J. Feng, T. Y. Xin, Q. Xu, and Y. X. Wang, Factors driving stable growth of He clusters in W: first-principles study, Nucl. Fusion **58**, 076024 (2018).
[78] X.-C. Li, X. Shu, P. Tao, Y. Yu, G.-J. Niu, Y. Xu, F. Gao, and G.-N. Luo, Molecular dynamics simulation of helium cluster diffusion and bubble formation in bulk tungsten, Journal of Nuclear Materials **455**, 544 (2014).
[79] Y. L. Zhou, J. Wang, Q. Hou, and A. H. Deng, Molecular dynamics simulations of the diffusion and coalescence of helium in tungsten, Journal of Nuclear Materials **446**, 49 (2014).
[80] Y.-W. You, X.-S. Kong, X. Wu, C. S. Liu, J. L. Chen, and G.-N. Luo, Bubble growth from clustered hydrogen and helium atoms in tungsten under a fusion environment, Nucl. Fusion **57**, 016006 (2017).

[81] Y.-W. You, D. Li, X.-S. Kong, X. Wu, C. S. Liu, Q. F. Fang, B. C. Pan, J. L. Chen, and G.-N. Luo, Clustering of H and He, and their effects on vacancy evolution in tungsten in a fusion environment, Nucl. Fusion **54**, 103007 (2014).
[82] X.-C. Li, Y.-N. Liu, Y. Yu, G.-N. Luo, X. Shu, and G.-H. Lu, Helium defects interactions and mechanism of helium bubble growth in tungsten: A molecular dynamics simulation, Journal of Nuclear Materials **451**, 356 (2014).
[83] Y. Oda, A. M. Ito, A. Takayama, and H. Nakamura, First-Principles Study on Migration of Vacancy in Tungsten, Plasma and Fusion Research **9**, 3401117 (2014).
[84] C. S. Becquart, M. F. Barthe, and A. De Backer, Modelling radiation damage and He production in tungsten, Phys. Scr. **T145**, 014048 (2011).
[85] R. Kobayashi, T. Hattori, T. Tamura, and S. Ogata, A molecular dynamics study on bubble growth in tungsten under helium irradiation, Journal of Nuclear Materials **463**, 1071 (2015).
[86] M. Li, J. Cui, J. Wang, and Q. Hou, Molecular dynamics simulations of cumulative helium bombardments on tungsten surfaces, Nuclear Instruments and Methods in Physics Research Section B: Beam Interactions with Materials and Atoms **337**, 45 (2014).
[87] F. Sefta, K. D. Hammond, N. Juslin, and B. D. Wirth, Tungsten surface evolution by helium bubble nucleation, growth and rupture, Nucl. Fusion **53**, 073015 (2013).
[88] H. Xie, N. Gao, K. Xu, G.-H. Lu, T. Yu, and F. Yin, A new loop-punching mechanism for helium bubble growth in tungsten, Acta Materialia **141**, 10 (2017).
[89] H. Iwakiri, K. Yasunaga, K. Morishita, and N. Yoshida, Microstructure evolution in tungsten during low-energy helium ion irradiation, Journal of Nuclear Materials **283–287**, 1134 (2000).
[90] L. Sandoval, D. Perez, B. P. Uberuaga, and A. F. Voter, Growth Rate Effects on the Formation of Dislocation Loops Around Deep Helium Bubbles in Tungsten, Fusion Science and Technology **71**, 1 (2017).
[91] K. D. Hammond and B. D. Wirth, Crystal orientation effects on helium ion depth distributions and adatom formation processes in plasma-facing tungsten, Journal of Applied Physics **116**, 143301 (2014).
[92] D. Donovan, D. Buchenauer, J. Whaley, and R. Friddle, Characterization of a compact ECR plasma source and its applications to studies of helium ion damage to tungsten, Phys. Scr. **T167**, 014040 (2016).
[93] O. El Atwani, K. Unal, W. S. Cunningham, S. Fensin, J. Hinks, G. Greaves, and S. Maloy, In-Situ Helium Implantation and TEM Investigation of Radiation Tolerance to Helium Bubble Damage in Equiaxed Nanocrystalline Tungsten and Ultrafine Tungsten-TiC Alloy, Materials **13**, 794 (2020).
[94] L. Hu, K. D. Hammond, B. D. Wirth, and D. Maroudas, Interactions of mobile helium clusters with surfaces and grain boundaries of plasma-exposed tungsten, Journal of Applied Physics **115**, 173512 (2014).
[95] K. D. Hammond, L. Hu, D. Maroudas, and B. D. Wirth, Helium impurity transport on grain boundaries: Enhanced or inhibited?, EPL **110**, 52002 (2015).
[96] L. Hu, K. D. Hammond, B. D. Wirth, and D. Maroudas, Dynamics of Small Mobile Helium Clusters Near a Symmetric Tilt Grain Boundary of Plasma-Exposed Tungsten, Fusion Science and Technology **71**, 36 (2017).
[97] K. D. Hammond, D. Maroudas, and B. D. Wirth, Helium aggregation and surface morphology near grain boundaries in plasma-facing tungsten, Journal of Applied Physics **135**, 235103 (2024).
[98] H.-B. Zhou, Y.-L. Liu, Y. Zhang, S. Jin, and G.-H. Lu, First-principles investigation of energetics and site preference of He in a W grain boundary, Nuclear Instruments and

Methods in Physics Research Section B: Beam Interactions with Materials and Atoms **267**, 3189 (2009).
[99] E. Bernard, R. Sakamoto, M. Tokitani, S. Masuzaki, H. Hayashi, H. Yamada, and N. Yoshida, Temperature impact on the micro structure of tungsten exposed to He irradiation in LHD, Journal of Nuclear Materials **484**, 24 (2017).
[100] K. Wang, M. E. Bannister, F. W. Meyer, and C. M. Parish, Effect of starting microstructure on helium plasma-materials interaction in tungsten, Acta Materialia **124**, 556 (2017).
[101] L. Hu, K. D. Hammond, B. D. Wirth, and D. Maroudas, Dynamics of small mobile helium clusters near tungsten surfaces, Surface Science **626**, L21 (2014).
[102] A. Bakaev, D. Terentyev, P. Grigorev, M. Posselt, and E. E. Zhurkin, Ab initio study of interaction of helium with edge and screw dislocations in tungsten, Nuclear Instruments and Methods in Physics Research Section B: Beam Interactions with Materials and Atoms **393**, 150 (2017).
[103] R. J. Kurtz and H. L. Heinisch, The effects of grain boundary structure on binding of He in Fe, Journal of Nuclear Materials **329–333**, 1199 (2004).
[104] C. S. Becquart and C. Domain, A density functional theory assessment of the clustering behaviour of He and H in tungsten, Journal of Nuclear Materials **386–388**, 109 (2009).
[105] L. Yang and B. D. Wirth, Energetics of hydrogen and helium-vacancy complexes in bulk and near surfaces of tungsten: First-principles study, Journal of Applied Physics **123**, 215104 (2018).
[106] S. E. Donnelly, The density and pressure of helium in bubbles in implanted metals: A critical review, Radiation Effects **90**, 1 (1985).
[107] A. Forslund and A. Ruban, *Ab initio* surface free energies of tungsten with full account of thermal excitations, Phys. Rev. B **105**, 045403 (2022).
[108] K. D. Hammond, S. Blondel, L. Hu, D. Maroudas, and B. D. Wirth, Large-scale atomistic simulations of low-energy helium implantation into tungsten single crystals, Acta Materialia **144**, 561 (2018).
[109] K. D. Hammond, D. Maroudas, and B. D. Wirth, Theoretical Model of Helium Bubble Growth and Density in Plasma-Facing Metals, Sci Rep **10**, 2192 (2020).
[110] C. A. Walsh, J. Yuan, and L. M. Brown, A procedure for measuring the helium density and pressure in nanometre-sized bubbles in irradiated materials using electron-energy-loss spectroscopy, Philosophical Magazine A **80**, 1507 (2000).
[111] X. Yi, K. Arakawa, D. Nguyen-Manh, F. Ferroni, P. Liu, W. Han, F. Wan, and S. G. Roberts, A study of helium bubble production in 10 keV He+ irradiated tungsten, Fusion Engineering and Design **125**, 454 (2017).
[112] O. El-Atwani, J. E. Nathaniel, A. C. Leff, B. R. Muntifering, J. K. Baldwin, K. Hattar, and M. L. Taheri, The role of grain size in He bubble formation: Implications for swelling resistance, Journal of Nuclear Materials **484**, 236 (2017).
[113] X. Huang, C. Lv, and H. Chu, Anomalous shape effect of nanosized helium bubble on the elastic field in irradiated tungsten, Sci Rep **11**, 830 (2021).
[114] O. El-Atwani, W. S. Cunningham, D. Perez, E. Martinez, J. R. Trelewicz, M. Li, and S. A. Maloy, Temperature threshold for preferential bubble formation on grain boundaries in tungsten under in-situ helium irradiation, Scripta Materialia **180**, 6 (2020).
[115] R. W. Harrison, G. Greaves, J. A. Hinks, and S. E. Donnelly, A study of the effect of helium concentration and displacement damage on the microstructure of helium ion irradiated tungsten, Journal of Nuclear Materials **495**, 492 (2017).
[116] F. Zhu, D. Wang, W. Wang, J. Wu, X. Ma, Z. Xie, and Z. Zhang, Microstructure and mechanical property evolution of He-implanted nanochannel W film under post-annealing, Journal of Nuclear Materials **572**, 154065 (2022).

[117] Z. J. Bergstrom, D. Perez, and O. El-Atwani, Helium bubble facetation in tungsten thin films, Scripta Materialia **220**, 114918 (2022).
[118] R. S. Barnes and D. J. Mazey, The migration and coalescence of inert gas bubbles in metals, Proc. R. Soc. Lond. A **275**, 47 (1963).
[119] G. W. Greenwood and M. V. Speight, AN ANALYSIS OF THF. D~FUSIO~ OF FISSION GAS BUBBLES AND ITS EFFECT ON THE B~VIOUR OF REACTOR FUELS, (n.d.).
[120] R. S. Barnes, A theory of swelling and gas release for reactor materials, Journal of Nuclear Materials **11**, 135 (1964).
[121] M. V. Speight, The migration of gas bubbles in material subject to a temperature gradient, Journal of Nuclear Materials **13**, 207 (1964).
[122] E. M. Baroody, Calculations on the Collisional Coalescence of Gas Bubbles in Solids, Journal of Applied Physics **38**, 4893 (1967).
[123] M. E. Gulden, Migration of gas bubbles in irradiated uranium dioxide, Journal of Nuclear Materials **23**, 30 (1967).
[124] K. Ono, S. Furuno, K. Hojou, T. Kino, K. Izui, O. Takaoka, N. Kubo, K. Mizuno, and K. Ito, In-situ observation of the migration and growth of helium bubbles in aluminum, Journal of Nuclear Materials **191–194**, 1269 (1992).
[125] F. A. Nichols, Kinetics of diffusional motion of pores in solids, Journal of Nuclear Materials **30**, 143 (1969).
[126] L. E. Willertz and P. G. Shewmon, Diffusion of helium gas bubbles in gold and copper foils, Metall Trans **1**, 2217 (1970).
[127] S. K. Tyler and P. J. Goodhew, Direct evidence for the Brownian motion of helium bubbles, Journal of Nuclear Materials **92**, 201 (1980).
[128] P. J. Goodhew and S. K. Tyler, Helium bubble behaviour in b. c. c. metals below 0.65Tm, Proc. R. Soc. Lond. **A**, 151 (1981).
[129] K. Y. Chen and J. R. Cost, Coalescence of helium bubbles in aluminum, Journal of Nuclear Materials **52**, 59 (1974).
[130] G. W. Greenwood and A. Boltax, The role of fission gas re-solution during post-irradiation heat treatment, Journal of Nuclear Materials **5**, 234 (1962).
[131] H. Schroeder and P. F. P. Fichtner, On the coarsening mechanisms of helium bubbles — Ostwald ripening versus migration and coalescence, Journal of Nuclear Materials **179–181**, 1007 (1991).
[132] B. N. Singh and H. Trinkaus, An analysis of the bubble formation behaviour under different experimental conditions, Journal of Nuclear Materials **186**, 153 (1992).
[133] D. Cui, Z. Cao, K. Pei, Y. Ding, Y. Li, Y. Dong, and G. Ran, Dynamic behavior of helium bubbles in Fe9Cr1.5W0.4Si F/M steel at elevated temperature, Journal of Nuclear Materials **585**, 154629 (2023).
[134] M. Miyamoto, S. Mikami, H. Nagashima, N. Iijima, D. Nishijima, R. P. Doerner, N. Yoshida, H. Watanabe, Y. Ueda, and A. Sagara, Systematic investigation of the formation behavior of helium bubbles in tungsten, Journal of Nuclear Materials **463**, 333 (2015).
[135] S. H. B. Teo, M. A. Thompson, M. Bilokur, D. Bhattacharyya, and C. S. Corr, Investigating the temperature dependence of helium bubble dynamics in plasma exposed tungsten via in-situ TEM annealing, Materialia **35**, 102110 (2024).
[136] X-ray database site web: https://henke.lbl.gov/optical_constants/pert_form.html, X-ray database, (2024).
[137] G. Renaud, R. Lazzari, and F. Leroy, Probing surface and interface morphology with Grazing Incidence Small Angle X-Ray Scattering, Surface Science Reports **64**, 255 (2009).

[138] J. Als-Nielsen and D. McMorrow, *Elements of Modern X-Ray Physics* (2011).
[139] J. Daillant and A. Gibaud, editors , *X-Ray and Neutron Reflectivity: Principles and Applications* (Springer, New York, 1999).
[140] R. Guinebretière and P. Goudeau, *Rayons X et Matière 4*, ISTE (2015).
[141] A. Messiah, *Quantum Mechanics*, Vol. 2 (1965).
[142] G. H. Vineyard, Grazing-incidence diffraction and the distorted-wave approximation for the study of surfaces, Phys. Rev. B **26**, 4146 (1982).
[143] S. K. Sinha, E. B. Sirota, S. Garoff, and H. B. Stanley, X-ray and neutron scattering from rough surfaces, Phys. Rev. B **38**, 2297 (1988).
[144] S. K. Sinha, X-ray diffuse scattering as a probe for thin film and interface structure, J. Phys. **4**, 1543 (1994).
[145] R. Lazzari, *IsGISAXS* : a program for grazing-incidence small-angle X-ray scattering analysis of supported islands, J Appl Crystallogr **35**, 406 (2002).
[146] A. Nejati, M. Svechnikov, and J. Wuttke, BornAgain, software for GISAS and reflectometry: Releases 1.17 to 20, EPJ Web Conf. **286**, 06004 (2023).
[147] D. Babonneau, *FitGISAXS* : software package for modelling and analysis of GISAXS data using IGOR Pro, J Appl Crystallogr **43**, 929 (2010).
[148] Kh. Zakeri, T. R. F. Peixoto, Y. Zhang, J. Prokop, and J. Kirschner, On the preparation of clean tungsten single crystals, Surface Science **604**, L1 (2010).
[149] J. W. Edington, *The Operation and Calibration of the Electron Microscope* (Macmillan Education UK, London, 1974).
[150] J. W. Edington, *Electron Diffraction in the Electron Microscope* (Macmillan Education UK, London, 1975).
[151] J. W. Edington, *Interpretation of Transmission Electron Micrographs* (Macmillan Education UK, London, 1975).
[152] J. W. Edington, *Typical Electron Microscope Investigations* (Macmillan Education UK, London, 1976).
[153] K. C. Thompson-Russell and J. W. Edington, *Electron Microscope Specimen Preparation Techniques in Materials Science* (Macmillan Education UK, London, 1977).
[154] D. B. Williams and C. B. Carter, *Transmission Electron Microscopy: A Textbook for Materials Science*, 2nd ed (Springer, New York, 2008).
[155] A. Lubk and F. Röder, Semiclassical TEM image formation in phase space, Ultramicroscopy **151**, 136 (2015).
[156] M. L. Jenkins, Characterisation of radiation-damage microstructures by TEM, Journal of Nuclear Materials **216**, 124 (1994).
[157] A. Xu, M. Saleh, T. Wei, T. Palmer, H. Huang, and D. Bhattacharyya, Investigating the effect of helium ion irradiation on deformation behaviour of Ni-Mo-Cr alloy via in-situ micro-tensile testing, Journal of Nuclear Materials **567**, 153812 (2022).
[158] A. Debelle, M. F. Barthe, and T. Sauvage, First temperature stage evolution of irradiation-induced defects in tungsten studied by positron annihilation spectroscopy, Journal of Nuclear Materials **376**, 216 (2008).
[159] J. Heikinheimo, K. Mizohata, J. Räisänen, T. Ahlgren, P. Jalkanen, A. Lahtinen, N. Catarino, E. Alves, and F. Tuomisto, Direct observation of mono-vacancy and self-interstitial recovery in tungsten, APL Materials **7**, 021103 (2019).
[160] M. Thompson, R. Sakamoto, E. Bernard, N. Kirby, P. Kluth, D. Riley, and C. Corr, GISAXS modelling of helium-induced nano-bubble formation in tungsten and comparison with TEM, Journal of Nuclear Materials **473**, 6 (2016).
[161] D. F. Ollis and M. Boudart, Surface and bulk carburization of tungsten single crystals, Surface Science **23**, 320 (1970).

[162] K. J. Sunderland and A. J. Slavin, Thermal decomposition of thr (15X3)R14° two-dimensional carbide on the W(110) surface, Surface Science **233**, 89 (1990).
[163] M. Bode, R. Pascal, and R. Wiesendanger, STM study of carbon-induced reconstructions on W(110): strong evidence for a surface lattice deformation, Surface Science **344**, 185 (1995).
[164] B. Evin, E. Leroy, M. Segard, V. Paul-Boncour, S. Challet, A. Fabre, and M. Latroche, Investigation by STEM-EELS of helium density in nanobubbles formed in aged palladium tritides, Journal of Alloys and Compounds **878**, 160267 (2021).
[165] G. Wulff, Zur Frage der Geschwindigkeit des Wachsthums und der Auflösung der Krystallflächen., Z. Kristallogr. – Cryst. Mater. **34**, 449 (1901).
[166] T. L. Einstein, *Equilibrium Shape of Crystals*, in (2015), pp. 215–264.
[167] J. Rahm and P. Erhart, WulffPack: A Python package for Wulff constructions, JOSS **5**, 1944 (2020).
[168] V. V. Kuporosov and G. N. Shuppe, Form of tungsten crystals in nearly equilibrial conditions, Sov. Phys. Crystallogr. **28**, 552 (1983).
[169] A. A. Chernov, editor , *Рост Кристаллоь / Rost Kristallov / Growth of Crystals: Volume 12* (Springer US, Boston, MA, 1984).
[170] L. Vitos, A. V. Ruban, H. L. Skriver, and J. Kollár, The surface energy of metals, Surface Science **411**, 186 (1998).
[171] J. Wang and S.-Q. Wang, Surface energy and work function of fcc and bcc crystals: Density functional study, Surface Science **630**, 216 (2014).
[172] D. Scheiber, O. Renk, M. Popov, and L. Romaner, Temperature dependence of surface and grain boundary energies from first principles, Phys. Rev. B **101**, 174103 (2020).
[173] J. Byggmästar, A. Hamedani, K. Nordlund, and F. Djurabekova, Machine-learning interatomic potential for radiation damage and defects in tungsten, Phys. Rev. B **100**, 144105 (2019).
[174] L. Corso, S. Curiotto, E. Bernard, M. Cabie, C. Martin, L. Martinelli, F. Cheynis, P. Muller, and F. Leroy, Tungsten evolution under helium irradiation: Shape of bubbles by TEM and in-situ GISAXS analysis, Nuclear Materials and Energy **37**, 101533 (2023).
[175] H. Trinkaus and B. N. Singh, Helium accumulation in metals during irradiation – where do we stand?, Journal of Nuclear Materials **323**, 229 (2003).
[176] S. Curiotto, P. Müller, F. Cheynis, L. Corso, E. Bernard, and F. Leroy, Size-dependent diffusion of 3D nanovoids in a bcc solid, Applied Physics Letters **123**, 241603 (2023).
[177] H.-C. Jeong and E. D. Williams, Steps on surfaces: experiment and theory, Surface Science Reports **34**, 171 (1999).
[178] L. Corso, S. Curiotto, F. Cheynis, P. Muller, E. Bernard, M. Cabie, C. Martin, and F. Leroy, Real-time helium bubble growth in tungsten by in-situ GISAXS, Nuclear Materials and Energy **42**, 101894 (2025).